Fundamental optical properties of single semiconductor nanocrystals at cryogenic temperatures

Elise Prin

université de BORDEAUX

THÈSE PRÉSENTÉE

POUR OBTENIR LE GRADE DE

DOCTEUR
DE L'UNIVERSITÉ DE BORDEAUX

ÉCOLE DOCTORALE SCIENCES PHYSIQUES ET DE L'INGENIEUR

LASERS, MATIÈRE ET NANOSCICENCES

Par **Elise PRIN**

Propriétés optiques fondamentales de nanocristaux de semi-conducteurs individuels aux températures cryogéniques.

Fundamental optical properties of single semiconductor nanocrystals at cryogenic temperatures.

Sous la direction de : **Philippe TAMARAT**
Co-directeur : **Brahim LOUNIS**

Soutenue le vendredi 27 septembre 2024

Membres du jury :

Mme. Maria CHAMARRO	Professeure	Sorbonne Université	Rapporteure
Mme. Carole DIEDERICHS	Professeure	Sorbonne Université	Rapporteure
M. Jérôme CAYSSOL	Professeur	Université de Bordeaux	Président du jury
M. Jean-Pierre HERMIER	Professeur	Université VSQ	Examinateur
M. Philippe TAMARAT	Professeur	Université de Bordeaux	Directeur de thèse
M. Brahim LOUNIS	Professeur	Université de Bordeaux	Co-directeur de thèse

Propriétés optiques fondamentales de nanocristaux de semi-conducteurs individuels aux températures cryogéniques.

Résumé : Les nanocristaux de semi-conducteurs présentent des propriétés optiques et électroniques remarquables en raison du confinement quantique de leurs porteurs de charge, ce qui les rend avantageux pour diverses applications en optoélectronique, dans les dispositifs émetteurs de lumière et dans les technologies basées sur le spin. La compréhension de la physique de l'exciton de bord de bande, dont la recombinaison est à l'origine de leur photoluminescence, est cruciale pour le développement de ces applications. Cette thèse porte sur l'étude expérimentale des propriétés optiques des nanocristaux de phosphure d'indium et de pérovskites d'halogénure de plomb. En utilisant une méthode de spectroscopie de magnéto-photoluminescence sur des nanocristaux uniques à basse température, nous révélons des empreintes spectrales très sensibles à la morphologie des nanocristaux et élucidons la structure fine de l'exciton de bord de bande et les énergies de liaison des complexes de charge. Dans les nanocristaux d'InP/ZnS/ZnSe, l'évolution des spectres et des déclins de luminescence sous champ magnétique montrent l'existence d'un niveau d'exciton noir situé à moins d'un millielectronvolt en dessous du triplet brillant de l'exciton, résultats étayés par un modèle tenant compte de l'anisotropie de forme du cœur d'InP. Dans les pérovskites d'halogénure de plomb, nous démontrons que l'état fondamental de l'exciton est noir et se situe plusieurs millielectronvolts en dessous des sous-niveaux d'exciton brillants les plus bas, résolvant ainsi le débat sur l'ordre des niveaux brillants et noirs de l'exciton dans ces matériaux. En combinant nos résultats avec des mesures spectroscopiques sur divers composés de nanocristaux de pérovskite, nous établissons des lois d'échelle universelles qui relient l'éclatement de la structure fine de l'exciton et les énergies de liaison du trion et du biexciton à l'énergie de l'exciton de bord de bande dans les nanostructures de pérovskite d'halogénure de plomb, quelle que soit leur composition chimique. Enfin, des analyses préliminaires de spectroscopie sur des nano-bâtonnets de pérovskite avec un grand rapport d'aspect suggèrent leur potentiel en tant qu'émetteurs de lumière quantique grâce à leur émission composée d'une raie unique.
Mots-clés : nanocristaux de semi-conducteurs, magnéto-photoluminescence, spectroscopie sur point unique, structure fine de l'exciton

---

Fundamental optical properties of single semiconductor nanocrystals at cryogenic temperatures.

Abstract: Semiconductor nanocrystals exhibit outstanding optical and electronic properties due to the quantum confinement of their charge carriers, making them valuable for various applications in opto-electronics, light-emitting devices, and spin-based technologies. Understanding the physics of the band-edge exciton, whose recombination is at the origin of their photoluminescence, is crucial for developing these applications. This thesis focuses on the experimental study of the optical properties of indium phosphide and lead halide perovskites nanocrystals. Using magneto-photoluminescence spectroscopy on single nanocrystals at low temperatures, we reveal spectral fingerprints highly sensitive to nanocrystal morphologies and elucidate the entire band-edge exciton fine structure and charge-complex binding energies. In InP/ZnS/ZnSe nanocrystals, the evolution of photoluminescence spectra and decays under magnetic fields show evidence of a ground dark exciton level lying less than a millielectronvolt below the bright exciton triplet, findings supported by a model accounting for the shape anisotropy of the InP core. In lead halide perovskites, we demonstrate that the ground exciton state is dark and lies several millielectronvolts below the lowest bright exciton sublevels, resolving the debate on the bright-dark exciton level ordering in these materials. Combining our results with spectroscopic measurements on various perovskite nanocrystal compounds, we establish universal scaling laws relating exciton fine structure splitting, trion and biexciton binding energies to the band-edge exciton energy in lead-halide perovskite nanostructures, regardless of their chemical composition. Lastly, preliminary spectroscopy analyses on perovskite nanorods with a high aspect ratio suggest their potential as candidates for quantum light emitters due to their characteristic single emission line.
Keywords: semiconductor nanocrystals, magneto-photoluminescence, single-dot spectroscopy, exciton fine structure

---

Laboratoire Photonique, Numérique et Nanosciences
UMR 5298, Université de Bordeaux, 33400 Talence, France.

Remerciements

Ce travail de thèse a été réalisé au sein du Laboratoire Photonique, Numérique et Nanosciences (LP2N), unité mixte de recherche du Centre National de la Recherche Scientifique, de l'Université de Bordeaux et de l'Institut d'Optique Graduate School. Je tiens à remercier le directeur du laboratoire, Laurent Cognet, pour m'avoir accueilli au sein de son laboratoire, ainsi que les équipes techniques et administratives.

Je remercie également sincèrement Maria Chamarro et Carole Diederichs d'avoir accepté d'être rapporteures de ce manuscrit, ainsi que Jérôme Cayssol et Jean-Pierre Hermier d'avoir pris part au jury de soutenance.

Je souhaite remercier mes directeurs de thèse, Philippe Tamarat et Brahim Lounis, de m'avoir offert l'opportunité de réaliser ce projet au sein de leur groupe, dans de si bonnes conditions expérimentales. Je remercie Philippe pour sa disponibilité, sa patience et sa bienveillance, qui ont été des sources de motivation pendant ces trois années. Je remercie également Brahim pour son exigence, ses conseils et son enthousiasme. J'ai énormément appris à leurs côtés, aussi bien sur le plan théorique qu'expérimental, et j'ai grandement bénéficié de leur expertise et de leur rigueur scientifique.

Un grand merci à tous les membres du groupe Nanophotonique, passés et présents, pour leur aide et leur soutien, sans qui les heures passées à observer des nanocristaux dans le noir, sous le bruit du cryostat, auraient paru encore plus longues. En particulier, merci à Mathias et Malo, avec qui j'ai eu la chance de partager tous les hauts et les bas de cette aventure. Votre solidarité a été une force précieuse pour avancer. Merci également à Sidd pour la relecture de ce manuscrit et ces nombreux conseils, ainsi qu'à Lei, Hanna, Quentin, Simon, Romane, Robin, Jitendra et Xuyang. Je tiens aussi à remercier Thibault pour le travail réalisé durant son stage au sein du groupe.

Je veux également remercier tous ceux qui ont rendu bien plus agréable ces trois années et ces plus de 600 allers-retours au restaurant du CNRS (et tout autant de pauses-café) : merci beaucoup Luisa, Célia, Vincent, Quentin, Geovan, J-B G. et Naveen, pour votre amitié.

Ces trois ans intenses ont été ponctués de moments de pause essentiels. Merci à Luisa, Mathias, Maxime, Benjamin, Luuk et Paul pour les pauses musicales, et Katia pour m'avoir motivée à continuer l'escalade.

Enfin, je tiens à remercier mes parents et mes sœurs pour le soutien et la confiance qu'ils m'ont apportés tout au long de mes études, ainsi que pour leur présence à ma soutenance.

Contents

List of Figures

List of Tables

Résumé de la thèse en Français

Introduction

La miniaturisation des composants électroniques au cours des dernières décennies a conduit à l'étude des semi-conducteurs à l'échelle nanométrique. Parmi eux, les nanocristaux de semi-conducteurs possèdent au moins une dimension à l'échelle de quelques nanomètres. Lorsque les trois dimensions d'un nanocristal sont suffisamment petites pour confiner les fonctions d'onde des électrons, on les appelle communément des boîtes quantiques. Les nanocristaux diffèrent grandement de leurs équivalents massifs en raison du confinement quantique des porteurs de charge, ce qui induit une modification de leurs propriétés physiques et leur confère des propriétés optiques particulières.

Malgré l'intérêt croissant pour ces matériaux dans les dispositifs optoélectroniques et les technologies d'affichage, des incertitudes subsistent quant à l'origine de leurs propriétés optiques. En effet, leur photoluminescence provient de la recombinaison de l'exciton de bord de bande, nécessitant une compréhension approfondie. En particulier, l'étude des états noirs dans la structure fine de l'exciton est cruciale pour les applications dans les technologies quantiques, y compris pour la manipulation cohérente des qubits de spin. Dans les nanocristaux de perovskite, l'ordre des sous-niveaux brillants et noirs dans la structure fine de l'exciton reste un sujet de débat, dont la connaissance est pourtant cruciale pour le développement de sources de lumière quantique et de technologies basées sur le spin.

Le travail présenté dans cette thèse participe à l'étude de la structure fine de l'exciton, et autres complexes de charges participant à la photoluminescence (comme les trions et biexcitons), dans différents nanocristaux de semi-conducteurs. L'objectif est d'améliorer notre compréhension globale du système complexe que constitue un nanocristal de semi-conducteur, notamment dans les cas particuliers des nanocristaux d'InP/ZnSe/ZnS et de pérovskites d'halogénure de plomb. Pour cela, nous utilisons une méthode de spectroscopie de magnéto photoluminescence sur nanocristaux uniques, à basse température.

Chapitre 1 - Propriétés optiques et électroniques de nanocristaux de semi-conducteurs

Ce chapitre fournit une base théorique pour comprendre les structures électroniques et les propriétés optiques des nanocristaux de semi-conducteurs.

Propriétés électroniques

Lorsqu'un photon est absorbé dans un semi-conducteur, un électron passe directement de la bande de valence à la bande de conduction, entraînant la création d'un trou. Les trous sont des quasi-particules dotées d'une charge élémentaire positive $+e$, représentant l'absence d'un électron dans un niveau d'énergie. Par conséquent, ce processus de photo-excitation induit la

création d'une paire électron-trou interagissant par le biais de l'interaction coulombienne. Cette paire est une quasi-particule appelée **exciton**.

Le rayon des nanocristaux est proche du rayon de Bohr de l'exciton. Les limites physiques du matériau contraignent alors l'exciton dans l'espace. Le mouvement de l'électron est ainsi limité à des niveaux d'énergie discrets, ce qui conduit à une quantification des niveaux d'énergie. Les nanocristaux présentent donc un comportement optique analogue à celui des atomes. La recombinaison de l'exciton conduit à l'émission d'un photon, elle est à l'origine de la photoluminescence des nanocristaux de semi-conducteurs.

La structure fine de l'exciton de bord de bande du **CdSe** et de l'**InP** avec une structure cristalline cubique ou hexagonale peut être décrite avec le modèle de Pidgeon et Brown. Dans ces nanocristaux, l'émission de photons provient du niveau d'énergie d'exciton le plus bas $1S_{h,3/2}$ $1S_e$. Ce niveau est construit à partir de l'état $1S_e$ de l'électron dans la bande de conduction et de l'état $1S_{h,3/2}$ du trou dans la bande de valence. L'état $1S_e$ est doublement dégénéré en raison de la projection du spin de l'électron $\pm\frac{1}{2}$, et l'état $1S_{h,3/2}$ avec son moment angulaire total de 3/2 est quadruplement dégénéré avec les projections $\frac{3}{2}, \frac{1}{2}, -\frac{1}{2}, -\frac{3}{2}$. Par conséquent, dans l'approximation sphérique où les bandes d'énergie sont supposées être sphériquement isotropes, pour un nanocristal sphérique avec un réseau cristallin cubique, l'exciton de bord de bande est huit fois dégénéré. Trois facteurs principaux peuvent lever cette dégénérescence en cinq états excitoniques : l'**anisotropie du champ cristallin**, l'**anisotropie de la forme du cristal** et l'**interaction d'échange électron-trou**. En tenant compte de ces trois facteurs, il est possible de déterminer le diagramme des niveaux d'énergie de la structure fine de l'exciton. Celui-ci est présenté Fig. 1.

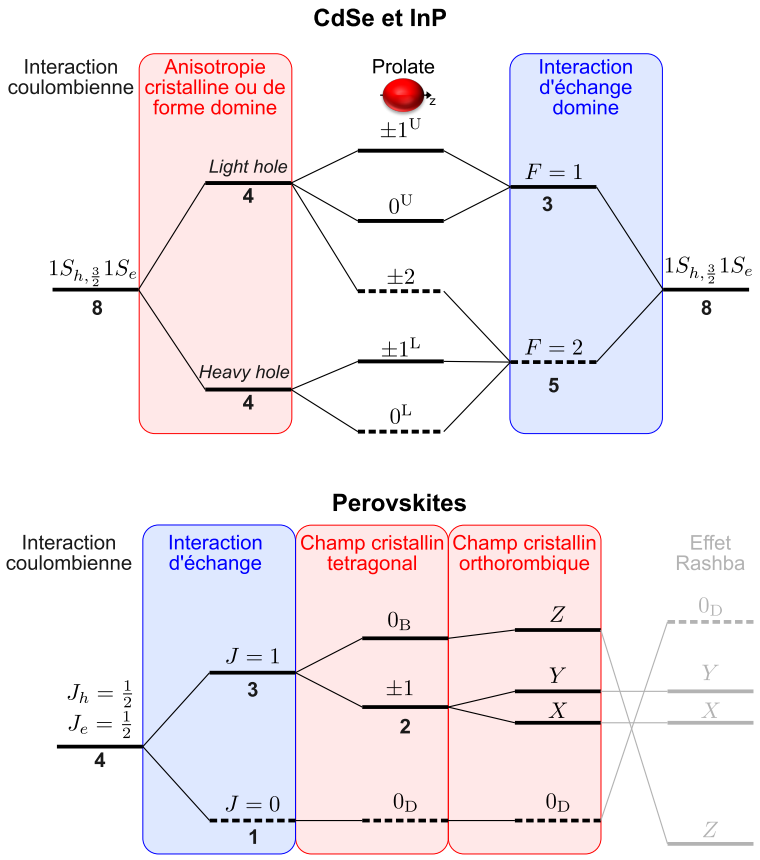

Figure 1: Diagrammes d'énergie de la structure fine de l'exciton dans le cas de nanocristaux de CdSe et d'InP et dans le cas des perovskites.

Les **pérovskites à halogénure de plomb** sont une famille de cristaux avec la formule

$APbX_3$ où X est un anion halogénure et A un cation. La structure cristalline des pérovskites peut être décrite comme un arrangement tridimensionnel d'octaèdres $(PbX_6)^{-4}$ partageant leurs coins. Elles possèdent une bande de valence de type s et une bande de conduction de type p, à l'inverse des semi-conducteurs avec des phases cristallines de type zinc-blende et wurtzite, comme le CdSe et l'InP. Ainsi, dans les pérovskites à halogénure de plomb, le couplage spin-orbite se produit dans la bande de conduction plutôt que dans la bande de valence. Cette disposition des bords de bande joue un rôle important dans leurs propriétés optoélectroniques. Dans les pérovskites, l'exciton de bord de bande est donc formé d'un trou avec un moment angulaire $J_h = 1/2$ et d'un électron avec un moment angulaire $J_e = 1/2$, liés par une interaction coulombienne, donnant un niveau d'énergie d'exciton quatre fois dégénéré. Le diagramme d'énergie de l'exciton dans ces systèmes est également représenté Fig. 1.

Afin d'expliquer la forte photoluminescence des pérovskites à basse température une hypothèse a été émise suggérant que l'état d'énergie le plus bas dans les nanocristaux de pérovskite était en fait le triplet brillant avec $J = 1$. Cette inversion de l'ordre des niveaux d'énergie serait justifiée par la présence d'un fort **effet Rashba**, qui diviserait davantage les sous-niveaux et pourrait inverser l'ordre singulet/triplet, comme représenté en gris Fig. 1. Au début de cette thèse, le débat concernant l'état fondamental du $CsPbBr_3$ persistait en raison de l'absence de signature de l'état noir.

Propriétés optiques de nanocristaux de semi-conducteurs

Les spectres de photoluminescence des nanocristaux de semi-conducteurs sont directement liés à la force d'oscillateur des états de l'exciton. Le niveau excitonique le plus bas en énergie dans l'InP et le CdSe (0^{L} ou ± 2) et dans les perovskites (0_D) est toujours un état noir, non optiquement actif. Cependant, une recombinaison radiative à partir de ces états peut se produire sous l'effet d'un champ magnétique externe, par le biais d'un couplage magnétique entre état noir et états brillants.

Pour interpréter correctement les spectres de photoluminescence provenant d'un nanocristal, il faut également tenir compte de l'émission provenant d'autres complexes de charges comme les trions et le biexciton qui présentent des signatures spectrales distinctes. Un **trion** peut être formé lorsqu'un exciton est créé en présence d'un porteur de charge non apparié dans le cœur du nanocristal et d'un porteur de charge piégé à sa surface ou dans un défaut. Il est composé de deux trous dans la bande de valence et d'un électron dans la bande de conduction (trion $X+$ positif) ou d'un trou dans la bande de valence et de deux électrons dans la bande de conduction (trion $X-$ négatif). Le **biexciton** est composé de deux électrons et deux trous. Sa recombinaison conduit à la formation d'un exciton et à l'émission d'un photon, d'une énergie différente de celle produite par la recombinaison de l'exciton en raison de l'énergie de liaison.

Lors de l'excitation optique de nanocristaux uniques, des phénomènes photo-physiques singuliers apparaissent, comme la **diffusion spectrale**, caractérisée par un déplacement dynamique aléatoire d'une ligne spectrale. En fonction du temps d'acquisition, elle peut entraîner un élargissement de la raie de photoluminescence, ce qui conduit à un écart par rapport aux valeurs théoriques de la largeur de raie. Ce phénomène a été principalement étudié pour les nanocristaux de CdSe et il est attribué à une combinaison de deux mécanismes. Il peut être dû à une fluctuation du champ électrique dans l'environnement local du nanocristal, ou activé par la libération d'un excès d'énergie d'excitation suite à l'absorption d'un photon. Un autre phénomène, appelé **clignotement de la photoluminescence**, est caractérisé par une intermittence d'émission dans la photoluminescence de nanocristaux individuels. Il résulte d'un processus aléatoire de charge et de décharge sous illumination constante. Si le nanocristal est chargé, le porteur supplémentaire déclenche un processus connu sous le nom de **recombinaison Auger** non radiative.

Phonons dans les nanocristaux

Les interactions exciton-phonon influencent fortement les spectres d'émission de photoluminescence. Ces interactions peuvent élargir les spectres d'absorption et sont à l'origine du mélange thermique entre les états de la structure fine des excitons par le biais de phonons optiques. Les interactions des porteurs de charge avec les phonons ont un impact sur leur relaxation et leur mobilité dans les nanocristaux.

Comme les modes de phonon sont directement liés au mouvement des différentes liaisons atomiques dans le cristal, leurs énergies ne dépendent que de la composition chimique du nanocristal et ne devraient pas dépendre de sa taille ou de sa forme. Chaque semi-conducteur possède des modes de phonon caractéristiques ayant des impacts distincts sur la dynamique de recombinaison des excitons.

Il y a néanmoins de nouveau phénomènes physiques apparaissant dans les nanocristaux, n'existant pas dans les cristaux massifs, notamment l'existence de phonons de surface dont la fréquence est liée à la taille du nanocristal, ainsi que l'effet "*phonon bottleneck*" ou **goulot d'étranglement de phonon**. Ce dernier décrit l'inhibition de la thermalisation de l'électron assisté par les phonons lorsque les écarts d'énergie entre les niveaux discrets de l'électron sont plus grands que les énergies des modes de phonons disponibles.

Il existe deux contributions principales à l'interaction entre les excitons et les phonons. La première est le couplage des excitons aux modes acoustiques, confinés par le potentiel de déformation ou l'interaction piézoélectrique. La seconde contribution est le couplage des excitons aux modes optiques via l'interaction de Frölich. Cette interaction décrit la relation entre les particules chargées et les phonons dans un cristal, qui résulte de la polarisation du réseau par des particules chargées créant un champ électrique qui peut se coupler aux vibrations du réseau.

L'étude de l'interaction phonon-exciton dans les pérovskites d'halogénure de plomb reste un domaine de recherche actif. Les pérovskites étant des matériaux mous et ioniques, on s'attend à une interaction plus forte entre excitons et phonons comparée aux nanocristaux de CdSe ou d'InP. En effet, les pérovskites d'halogénure de plomb font partie de la famille des *phonons-glass electron-crystals* (PGEC). Dans ces matériaux, le sous-réseau PbX_3^- forme un réseau cristallin où les cations A^+ peuvent tourner facilement. Dans un tel système polaire, le couplage avec les modes optiques longitudinaux est plus important que ceux avec les phonons acoustiques en raison des fortes interactions de Frölich et de l'importante anharmonicité du réseau.

Chapitre 2 - Méthodes expérimentales

Ce chapitre décrit les différentes méthodes expérimentales utilisées tout au long de cette thèse sur plusieurs types de nanocristaux.

Synthèse chimique de nanocristaux de semi-conducteurs

La synthèse de nanocristaux colloïdaux a connu des avancées importantes au cours des deux dernières décennies. Les domaines d'amélioration comprennent l'obtention de nanocristaux de plus petite taille, la garantie d'une homogénéité de leurs tailles, le maintien d'une grande stabilité avec un minimum de défauts, et l'optimisation de leur rendement quantique. Les différents échantillons de nanocristaux de semi-conducteurs utilisés dans cette thèse ont été synthétisés par des groupes de recherche collaborateurs.

Les mesures de rendement quantique sont un outil important pour évaluer et optimiser l'efficacité des processus de photoluminescence et pour faciliter le développement et la caractérisation des nanocristaux de semi-conducteurs en vue de leurs applications futures. Le rendement quantique d'un échantillon de nanocristaux correspond au rapport entre le nombre de photons

émis et le nombre de photons absorbés. Pour quantifier le rendement quantique des nanocristaux de semi-conducteurs en solution, nous utilisons une méthode de mesure relative, qui nécessite l'utilisation d'un échantillon de référence avec un rendement quantique connu, émettant dans la même gamme de longueur d'onde que les nanocristaux étudiés. Le rendement quantique est calculé en comparant l'intensité de fluorescence intégrée de l'échantillon avec la solution de référence, en tenant compte de l'indice de réfraction des solvants utilisés pour chaque solution.

Spectroscopie de photoluminescence sur nanocristaux uniques

L'utilisation de la spectroscopie de photoluminescence sur nanocristaux uniques constitue une méthode adéquate pour examiner les caractéristiques optiques des nanocristaux, sans moyennage.

Dans cette thèse, nous utilisons un système de microscopie confocal dont le montage expérimental est représenté Fig. 2.

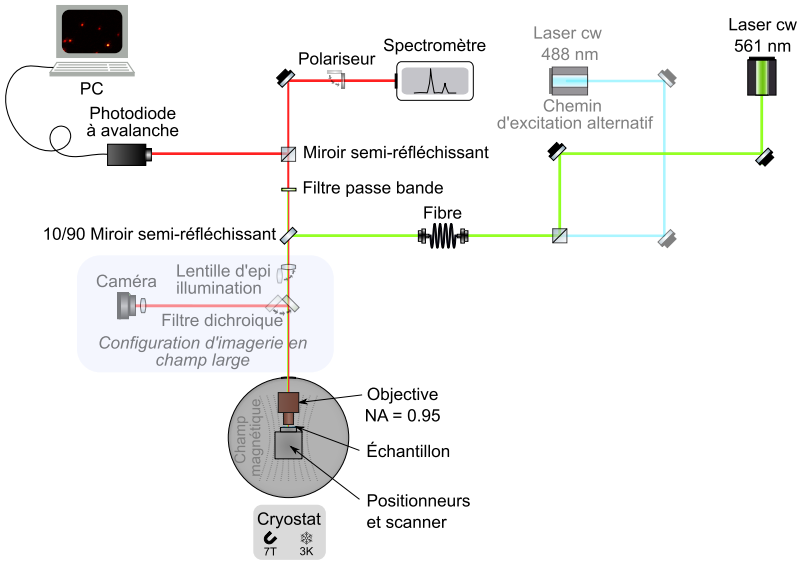

Figure 2: Schéma optique simplifié du montage de spectroscopie sur nanocristaux unique à basse température.

Nous utilisons un cryostat fonctionnant en cycle fermé, pouvant atteindre des températures inférieures à 3 K. Une solution de nanocristaux dans un polymère est préparée avec une concentration massique comprise entre 2 et 3 wt%, et déposée par enduction centrifuge sur une lame de saphir préalablement nettoyée à l'aide d'un nettoyeur à plasma. L'échantillon est en suite placé sur une tour piézoélectrique sur la platine optique du cryostat et excité par un laser. Pour obtenir des images confocales, l'échantillon est scanné à l'aide d'un scanner piézoélectrique.

Nous utilisons également un champ magnétique externe pour mener des études de spectroscopie magnéto-optique. Pour ce faire, nous utilisons des bobines placées autour de l'échantillon dans le cryostat. Ces bobines constituent un aimant supraconducteur en configuration Helmholtz, capable de générer un champ magnétique allant jusqu'à 7 T à l'emplacement de l'échantillon.

Chapitre 3 - Structure fine de l'exciton de bord de bandes dans des nanocristaux d'InP

Ce chapitre explore les propriétés optiques fondamentales de nanocristaux d'InP/ZnSe/ZnS en utilisant une méthode de spectroscopie de magnéto photoluminescence résolue en fréquence et

en temps. Nous présentons les résultats obtenus à partir de mesures sur nanocristaux uniques et proposons un modèle théorique pour les interpréter.

Mesures d'ensemble

Le spectre d'absorbance d'un ensemble de nanocristaux d'InP/ZnSe/ZnS à température ambiante est caractérisé par un pic d'absorption à 2,02 eV et une augmentation de l'absorbance à des énergies supérieures à 2,8 eV, causée par la coquille de ZnSe. Le spectre d'émission de photoluminescence a un profil gaussien avec une largeur de raie de 126 meV, ce qui indique un degré élevé d'uniformité des noyaux d'InP. Des mesures des spectres de photoluminescence d'ensemble de nanocristaux ont aussi été réalisées, en baissant la température de 250 à 3,4 K. À mesure que la température diminue, les positions des pics de photoluminescence présentent un décalage bleu jusqu'à 50 K. Ce décalage est attribué à la contraction du cristal qui induit un effet de confinement quantique plus important. Pour étudier la stabilité de la photoluminescence des échantillons de nanocristaux, nous avons également mesuré leur rendement quantique. Une diminution significative des rendements a été observée après le transport des échantillons. Cette baisse est probablement due à l'oxydation des noyaux d'InP à l'interface cœur/coquille, car l'InP a tendance à s'oxyder en présence d'eau ou d'air.

Une première évaluation de la dynamique de recombinaison des excitons dans ces nanocristaux peut être déduite de l'évolution du déclin de luminescence en fonction de la température. Proche de la température ambiante, la durée de vie de la photoluminescence est courte ($\sim$ 20 ns), ce qui est comparable à celle des nanocristaux de CdSe. À des températures cryogéniques, le déclin de luminescence devient multi-exponentiel, avec une composante longue de $\sim 1\ \mu s$ à 3,4 K. Ce comportement est une signature de la redistribution thermique des populations entre un état d'exciton fondamental noir à longue durée de vie et les états brillants voisins.

Spectroscopie sur nanocristaux uniques

Nous avons effectué des mesures de spectroscopie sur nanocristaux uniques afin d'étudier la structure fine de l'exciton de bord de bande de ces nanocristaux et de s'affranchir des inhomogénéités de taille et de forme. En champ nul, le spectre de photoluminescence d'un nanocristal est composé de deux raies sans phonon (ZPL), comme le montre la Fig. 3 **a)**. À titre d'exception, le nanocristal dont les spectres de photoluminescence sont présentés dans la Fig. 3 **b)** présente une seule ZPL en champ nul. Les éclatements des doublets sans champ magnétique sont répartis entre 0 et 1,1 meV. L'absence de corrélation entre ces valeurs et les énergies d'émission suggère que l'éclatement du doublet ne dépend pas de la taille du nanocristal mais provient de l'anisotropie de sa forme.

Lorsqu'un champ magnétique externe est appliqué à l'échantillon en configuration Faraday, une troisième ligne émerge à plus basse énergie et gagne en poids avec l'augmentation du champ, comme le montre les Fig. 3 **a)** et **b)**. L'apparition d'une nouvelle raie unique sous l'effet d'un champ magnétique est caractéristique du couplage magnétique entre état noir et état brillant. Les trois ZPL révélées par la spectroscopie de magnéto-photoluminescence sont donc attribuées à l'état noir de plus basse énergie de l'exciton (0^{L}) et au doublet d'exciton brillant ($\pm 1^{\mathrm{L}}$) éclaté par l'anisotropie de forme du nanocristal en deux sous-niveaux (X et Y).

Afin de reproduire théoriquement nos résultats expérimentaux, nous modélisons la structure fine de l'exciton du bord de bande avec un hamiltonien de spin incluant l'effet de l'anisotropie de forme sur l'énergie de la bande de valence mais négligeant l'effet de l'anisotropie sur l'interaction

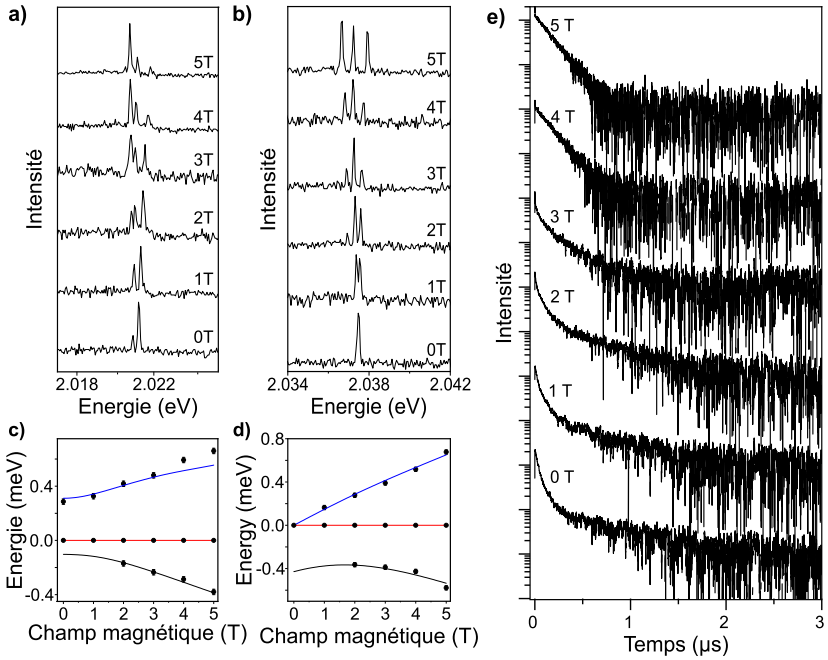

Figure 3: a) et **b)** Evolution des spectres de photoluminescence de deux nanocristaux d'InP en fonction du champ magnétique. **c)** et **d)** Positions relatives des raies sans phonons par rapport à la raie de l'état brillant de plus basse énergie, modélisées en prenant compte l'anisotropie de forme du nanocrystal. **e)** Courbes de déclin de luminescence en fonction du champ magnétique.

d'échange :

$$\hat{H} = -\eta(\hat{\boldsymbol{\sigma}}.\hat{\boldsymbol{J}}) - \frac{\Delta}{2}\left(\hat{J}_z^2 - \frac{5}{4}\right) + \frac{C}{\sqrt{3}}\left(\hat{J}_x^2 - \hat{J}_y^2\right) + \mu_B \frac{g_e}{2}(\hat{\boldsymbol{\sigma}}.\boldsymbol{B}) - \mu_B g_h(\hat{\boldsymbol{J}}.\boldsymbol{B}) \qquad (1)$$

Nos résultats sur une variété de nanocristaux uniques montrent que l'état magnétiquement brillant de l'exciton est l'état noir 0^L, ce qui indique un régime prolate des noyaux d'InP ($\mu_z > 0$). Les valeurs des éclatements noirs/brillants vont de 300 à 600 μeV, ce qui correspond à la structure fine de nanocristaux légèrement prolates avec $\mu_z < 0{,}03$. Les éclatements X-Y ont une valeur moyenne de 400 μeV, indiquant une faible anisotropie de forme dans le plan (x, y) avec $\mu_{x,y} \sim 0{,}003$. Ces résultats soulignent l'intérêt de la spectroscopie sur nanocristaux uniques pour dévoiler les déviations subtiles dans la morphologie de nanocristaux et confirment que les cœurs de nanocristaux d'InP préparés avec cette méthode de synthèse sont uniformes et quasiment sphériques.

Chapitre 4 - Structure fine de l'exciton de bord de bandes dans des nanocristaux de pérovskites à halogénure de plomb

Ce chapitre examine les propriétés de nanocristaux de pérovskites à halogénure de plomb. Bien que d'intenses efforts expérimentaux et théoriques aient été employés pour explorer leurs propriétés uniques, la physique des complexes de charge de bord de bande dans ces matériaux, dont la recombinaison est à l'origine de la photoluminescence, n'est toujours pas totalement connue. Par exemple, l'ordre des sous-niveaux brillants et noirs dans la structure fine de l'exciton était un sujet de débat au début de ma thèse de doctorat.

Les échantillons de $CsPbBr_3$ et de $CsPb(BrCl)_3$ utilisés dans cette étude ont été préparés par Y. Berezovska, A. Moskalenko, M. I. Bodnarchuk et M. V. Kovalenko à l'ETH Zurich.

Structure fine de l'exciton de bord de bande

À basse température (3,5 ± 0,3 K) et sous une excitation laser continue d'une longueur d'onde de 488 nm (2,54 eV), les spectres de photoluminescence des nanocristaux de $CsPbBr_3$ sont caractérisés par trois ZPL, correspondant à la recombinaison du triplet brillant de l'exciton, comme montré Fig. 4 **a)** et **b)**. Leur émission est répartie entre 2,3 et 2,35 eV, c'est-à-dire dans la bande interdite du $CsPbBr_3$ massique à basse température. Tous les triplets observés dans cette étude sont non dégénérés, ce qui est cohérent avec le fait que, pour des cristaux de cette taille, l'éclatement du triplet est principalement déterminé par la structure cristalline anisotrope du nanocristal.

L'ajout d'un champ magnétique externe révèle l'ensemble de la structure fine de l'exciton de bord bande de ces nanocristaux. Alors que les trois raies du triplet s'éclatent davantage sous l'effet du champ, une raie décalée vers le rouge apparaît, comme le montre la Fig. 4 **a)**. L'émergence de cette raie est la marque d'un mélange induit par le champ entre un état optiquement interdit et un état brillant voisin. Cette raie est attribuée à l'état noir de l'exciton, qui se situe entre 3,6 meV et 5 meV en dessous du niveau du triplet brillant. Ces résultats invalident les modèles récents de structure fine d'exciton qui prédisent une inversion des niveaux d'exciton noir/brillant pour les nanocristaux de $CsPbBr_3$ faiblement confinés, causée par l'effet Rashba. La forte luminescence des nanocristaux de pérovskites à halogénure de plomb à basse température peut alors être interprétée comme la signature d'une relaxation assistée par phonons réduite vers l'exciton fondamental noir, même si les éclatements noirs/brillants coïncident avec les énergies des phonons LO.

Propriétés magnétiques des trions et biexcitons

L'application d'un champ magnétique permet également d'étudier l'émission du trion. Un exemple de spectre complet obtenu à 7 T est présenté Fig. 4 **b)**. La trace spectrale de ce nanocristal montre que les raies du singulet et du triplet subissent des variations d'intensité. Étant donné que les nanocristaux sont soit neutres, soit chargés, les caractéristiques spectrales des excitons et des trions sont mesurées sur des spectres d'émission différents. Les sauts spectraux survenant lors de ces changements d'émission sont fréquents et peuvent entraîner une dispersion des énergies de liaison des trions mesurés. Les trions sont en effet très sensibles à l'environnement diélectrique local et aux redistributions de charge à la surface du nanocristal. Les variations d'intensité du doublet et du faisceau d'excitons sont anti-corrélées, ce qui prouve qu'ils appartiennent à des complexes de charge différents du même nanocristal. Dans l'ensemble, les résultats obtenus indiquent que la réponse magnétique des trions dans les nanocristaux de pérovskite est presque isotrope, indépendante de leur taille et de leur composition chimique. Le décalage vers le rouge de la raie du trion par rapport à l'exciton fournit une mesure de son énergie de liaison et montre une corrélation avec l'énergie de recombinaison des excitons.

Nos études spectroscopiques révèlent également l'empreinte spectrale des transitions biexciton-exciton. En effet, l'augmentation de l'intensité d'excitation entraîne l'apparition d'un triplet qui est décalé vers le rouge par rapport au triplet brillant de l'exciton indiquant une interaction attractive. Les variations temporelles de l'intensité de photoluminescence du biexciton sont corrélées avec celles de l'exciton. Comme dans le cas de l'émission de trions, l'énergie de liaison des biexcitons est corrélée avec l'énergie de recombinaison des excitons.

Pour renforcer ces résultats, nous avons également mené des études spectroscopiques magnéto-optiques sur des nanocristaux de $CsPb(ClxBr_{1-x})_3$ d'une taille moyenne de $\sim$ 30 nm. Ces pérovskites suivent les mêmes comportements que le $CsPbBr_3$ en termes d'ordre des sous-niveaux d'excitons et de signes d'interactions au sein des complexes de charge trion et biexciton.

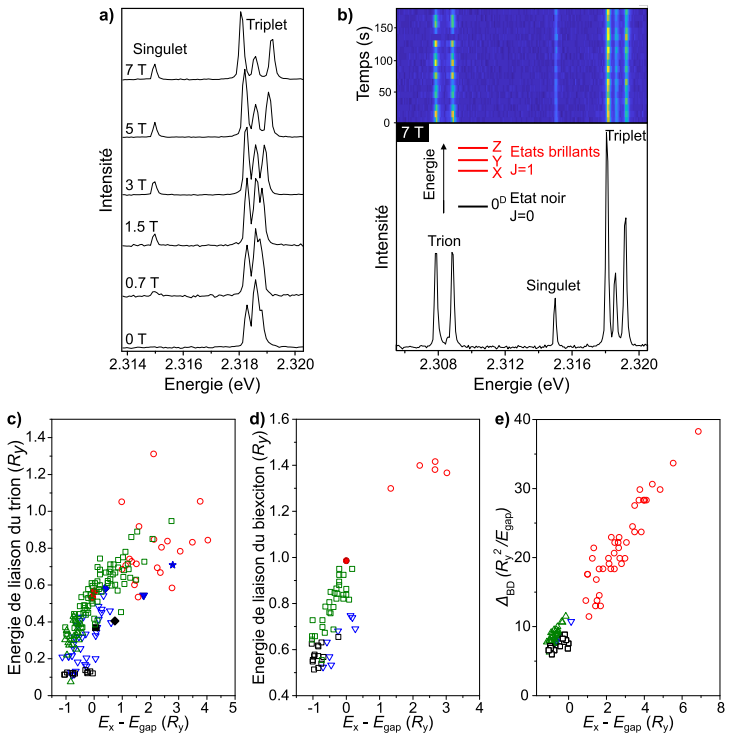

Figure 4: a) Évolution des spectres de photoluminescence en fonction du champ magnétique avec apparition de l'état noir sur un nanocristal de $CsPbBr_3$. **b)** Trace spectral et spectre de photoluminescence à 7 T d'un nanocristal de $CsPbBr_3$. **c)** Évolution des énergies de liaison des trions en unités Ry, **d)** énergies de liaison des biexcitons en unités Ry et **e)** énergies d'éclatements entre états noirs et brillant en unités Ry^2/E_{gap}, en fonction de l'énergie de recombinaison des excitons exprimée en unités Ry après soustraction de la bande interdite.

Lois d'échelle des énergie de complexes de charges.

Nous désirons maintenant donner une image générale et prédictive de l'éclatement des états noir/brillant de l'exciton ainsi que des énergies de liaison du trion et du biexciton dans les nanocristaux de pérovskite d'halogénure de plomb de diverses compositions. Nous nous basons pour cela sur des données spectroscopiques sur nanocristaux uniques recueillies dans cette étude et dans des rapports antérieurs. Nous nous basons sur l'hamiltonien $\mathcal{H}$ décrivant les énergies cinétiques et coulombienne des porteurs de charge dans un nanocristal, où le potentiel de confinement avec des barrières infinies est pris à zéro :

$$\begin{aligned}\mathcal{H} &= \mathcal{H}_{\text{kin}} + \mathcal{H}_{\text{Coul}} \\ &= \sum_A \frac{-\hbar^2}{2m^* a_{\text{B}}^2} \frac{1}{\left(L_{\text{eff}}/a_{\text{B}}\right)^2} \hat{\nabla}_{\text{A}}^2 + \sum_{A<B} \frac{e^2}{4\pi\varepsilon_0 \varepsilon a_{\text{B}}} \frac{c_{\text{A}} c_{\text{B}}}{\left(L_{\text{eff}}/a_{\text{B}}\right)} \frac{1}{|\hat{r}_{\text{A}} - \hat{r}_{\text{B}}|} \\ &= R_y \left(\sum_{\text{A}} \frac{-1}{2\left(L_{\text{eff}}/a_{\text{B}}\right)^2} \hat{\nabla}_{\text{A}}^2 + \frac{2}{\left(L_{\text{eff}}/a_{\text{B}}\right)} \sum_{A<B} c_{\text{A}} c_{\text{B}} \frac{1}{|\hat{r}_{\text{A}} - \hat{r}_{\text{B}}|} \right),\end{aligned} \tag{2}$$

où L_{eff} est la taille effective de confinement du nanocristal, $\hat{\nabla}_i$ et $\hat{r}_i$ les opérateurs de Nabla sans dimension (normalisé à L_{eff}) où i sont les coordonnées des porteurs de charges ($i = A, B...$), c_i les signes de leurs charges avec une valeur absolue e, et $R_y = \hbar^2/(m^* a_{\text{B}}^2)$ l'énergie de Rydberg de l'exciton massif, ε étant la constante diélectrique du pérovskite. Cette normalisation en unités de Rydberg rend les énergies d'interaction indépendantes du matériau et montre que les énergies de liaison des trions et des biexcitons sont essentiellement déterminées par le régime de confinement

quantique, c'est-à-dire le rapport sans dimension L_{eff}/a_B. Cela permet de mettre en lumière les lois universelles reliant les énergies de liaison expérimentales des trions et des biexcitons en unités de Rydberg à l'énergie de recombinaison des excitons E_{X}, une fois la bande interdite du matériau soustraite comme montré Fig. 4 **c)** et **d)**. En effet, les points expérimentaux se répartissent le long d'une ligne de tendance allant de la limite du matériau massif (abscisse proche de -1) au régime de fort confinement (abscisse de plusieurs unités), quelle que soit la composition des pérovskites.

Au-delà du débat sur l'ordre des états noirs et brillants de l'exciton et sur son origine dans les pérovskites à halogénure de plomb, les lois révélées par spectroscopie sur nanocristaux uniques offrent une image prédictive des énergies d'interaction au sein des complexes de charge photogénérés dans ces matériaux. Elles ouvrent également la voie au développement de modèles précis d'interactions de complexes de charge dans les pérovskites d'halogénure de plomb qui partagent une physique commune et forment une classe unique de semi-conducteurs.

Chapitre 5 - Conclusion et perspectives

Les travaux réalisés dans le cadre de cette thèse ont été consacrés à l'étude des propriétés optiques de nanocristaux de semi-conducteurs, en particulier à l'étude de la structure fine des excitons de bord de bande. Ce travail expérimental s'appuie principalement sur une méthode de spectroscopie de photoluminescence magnéto-optique à basse température sur des nanocristaux uniques, permettant d'obtenir des empreintes spectrales hautement résolues de la structure fine des excitons dans différents échantillons de nanocristaux. Dans l'ensemble, les résultats obtenus sur les nanocristaux d'InP et de pérovskites à halogénure de plomb démontrent les avantages de cette méthode de spectroscopie comme outil pour mieux comprendre la structure fine de l'exciton de bord de bande dans ces matériaux.

Une des perspectives des nanocristaux de semi-conducteurs est leur utilisation comme source quantique. En effet, les sources produisant des photons indiscernables jouent un rôle fondamental dans diverses technologies photoniques. Les nanocristaux de pérovskite présentent un potentiel prometteur en tant qu'émetteurs quantiques, grâce à leur stabilité, à leur facilité de synthèse et aux progrès réalisés ces dernières années pour mieux contrôler leur forme, leur homogénéité de taille et leur rapport d'aspect. En théorie, ils peuvent générer des photons uniques à la demande grâce à une excitation pulsée du nanocristal, suivie d'un filtrage spectral de la lumière émise afin d'isoler un photon possédant les propriétés souhaitées. La cascade biexciton-exciton pourrait aussi être exploitée pour générer des paires de photons corrélés. Notamment, les nano-bâtonnets de $CsPbBr_3$ avec un grand rapport d'aspect sont de potentiels candidats grâce à leur émission de photoluminescence composée d'une raie unique. Les nanocristaux de semi-conducteurs sont globalement prometteurs en tant qu'alternatives aux dispositifs actuellement disponibles dans les nouvelles technologies, comme dans les technologies quantiques, les panneaux solaires, les photodetecteurs et les diodes électroluminescentes.

En conclusion, après la découverte du confinement quantique dans les nanocristaux de semi-conducteurs au début des années 1980, il reste encore beaucoup à explorer en ce qui concerne leurs propriétés optiques et leur stabilité. Cette exploration est cruciale pour leur utilisation dans diverses applications en optoélectronique et dans les technologies exploitant les sources de lumières quantiques, ou la manipulation cohérente de qubits de spin.

Introduction

Historical and scientific context

Semiconductor devices form the basis of all modern electronics. Over the past few decades, the miniaturization of electronic components has driven the study of nanoscale semiconductors. Among them are semiconductor nanocrystals that typically possess at least one dimension on the scale of a few nanometers. Nanocrystals differ greatly from their bulk equivalent due to the quantum confinement of their charge carriers, which induces modification of their physical properties and gives them attractive optical properties for nanoscale applications. Their energy levels are discrete, as those of an atom, resulting in tunable absorption and emission spectra based on their size. When all three dimensions of a nanocrystal are small enough to confine the wavefunctions of electrons, they are commonly referred to as quantum dots. The advanced abilities of modern chemistry enable the creation of complex designed structures, facilitating diverse applications of quantum dot-based size-adjustable electronics. Semiconductor nanocrystals exhibit high fluorescence yield; electron-hole pairs (excitons) created as a result of light excitation recombine radiatively, emitting photons. The energy of the emitted photons is determined by the energy difference between the discrete levels of the conduction-band electron and the valence-band hole, whose positions depend on the shape and size of the nanocrystal.

The size dependence of the optical properties of semiconductor nanocrystals was demonstrated in the 1980s by Al. Efros and A. Ekimov at the Ioffe Institut, Russia, on semiconductor nanocrystals in glass matrices [1, 2] and simultaneously in liquid colloids by L. Brus at Bell Labs, USA [3]. The chemical synthesis of colloidal nanocrystals marked the beginning of a new era in the field, their solution form making them easier to handle. Initial experimental studies focused on $CdSe$ nanocrystals. Among various synthesis methods was an organo-metallic synthesis for CdE (where E = S, Se, Te) developed in 1993 at MIT, USA, by M. Bawendi and his group [4]. This method is based on differentiating the nucleation step and the growth of nuclei in time, allowing for better control of their sizes.

On the theoretical side, one of the first models to describe the excitonic structure in these systems was developed for $CdSe$ with hexagonal lattice structures by Al. Efros and A. Rodina. They showed that the lowest exciton state split into five levels due to the crystal field, the crystal shape anisotropy, and the electron-hole exchange interaction [5].

In 2023, M. Bawendi, L. Brus, and A. Ekimov were awarded the Nobel Prize in chemistry "*for the discovery and synthesis of quantum dots*", highlighting the significance of their work in the field of nanotechnology.

Historically, $CdSe$-based nanocrystals have been the center point of nanocrystal study. However, the implementation of semiconductor nanocrystals in commercial optoelectronic devices requires non-toxic materials. InP-based nanocrystals have emerged as a promising alternative

to $CdSe$ due to their lower toxicity and similar optical properties. Since their first synthesis and characterization in the 1990s [6], improvements in their synthesis using safe and inexpensive precursors, along with precise control over their size and quality, give them advantageous characteristics for applications in new technologies. Bare InP core nanocrystals exhibit low photoluminescence efficiency, but the implementation of core/shell systems such as $InP/ZnS/ZnSe$ has proven to be competitive. They have found application in diverse technological domains, including nanocrystal-based light-emitting devices [7, 8], solar cells [9], photocatalysts [10, 11], and bioimaging [12].

More recently, easy chemical synthesis of perovskite nanocrystals has shown promising results, as these materials present strong and stable photoluminescence with high quantum yield and demonstrate high tolerance to defects. Their first significant synthesis breakthrough occurred in 2015 by Protesescu et al. [13]. Their variety of composition, shapes, and sizes (allowing for tunability of electronic structure, bandgap, and absorption spectra) offer the possibility of a broad emission range. This flexibility opens up exciting prospects for the development of high-performance solar cells [14], laser [15] as well as for use in detectors [16].

The bright emission and size-tunable optical properties of nanocrystal semiconductors make them promising candidates for applications in optoelectronics. However, it is essential to acknowledge that both InP and perovskite nanocrystals face challenges that must be addressed for successful integration into practical devices. Issues concerning long-term stability, toxicity, and scalability need careful consideration to ensure the sustainable and widespread implementation of these nanocrystals.

Motivation

Despite the growing interest in these materials for optoelectronic devices and display technologies, there are still uncertainties regarding the origin of their optical properties. The photoluminescence in these materials comes from the recombination of the band-edge exciton, which requires an in-depth understanding. In particular, mapping the dark states within the exciton fine structure is crucial for potential applications in quantum technologies, including coherent manipulation of long-lived spin qubits [17, 18]. Recent progress in the colloidal synthesis of strongly emitting perovskite nanocrystals offers opportunities for tunable light sources, such as light-emitting diodes and lasers [19]. In these materials, the ordering of bright and dark sublevels within the exciton fine structure remains a topic of debate, yet crucial for developing quantum light sources [20, 21, 22] and spin-based technologies [23, 24, 25].

The work presented in this thesis contributes to the study of the fine structure of the exciton and charge complexes in $InP/ZnSe/ZnS$ and lead halide perovskites nanocrystals, such as nearly bulk $CsPbBr_3$ and $CsPb(BrCl)_3$, at the individual scale. The aim is to improve our global understanding of the intricate system that is a colloidal semiconductor nanocrystal.

Method

The distinctive size-dependent characteristics of semiconductor nanocrystals pose challenges for their accurate study. Variations in emission properties among nanocrystals within a sample arise from small differences in their size and shape, leading to ensemble averaging and obscuring the unique properties of individual nanocrystals. To investigate the fundamental optical properties of single zinc-blende $InP/ZnSe/ZnS$ and lead halide perovskites nanocrystals, and to reveal their entire band-edge exciton fine structure, we use frequency- and time-resolved

magneto-photoluminescence spectroscopy on single nanocrystals. To do so, we use a homemade scanning confocal microscopy setup at low temperatures with a magnetic field up to 7 T. Adding a magnetic field allows for the splitting of degenerate states through Zeeman splitting and for revealing hidden dark states. Operating at low temperatures favors the observation of narrow emission lines, unveiling spectroscopic signatures capable of probing the fundamental physical mechanisms inherent in a semiconductor system at the nano-scale. This enables us to observe and analyze the influence of nanocrystal size, shape, and crystal structure, facilitating a deeper understanding of their electronic structure through the application of theoretical models. Detecting narrow emission lines also reveals the recombination of other charge complexes such as trions and biexcitons.

Organization of the thesis

The outline of this manuscript is given hereafter.

Chapter 1

The opening chapter of this thesis aims to present the electronic and optical properties of semiconductor nanocrystals, laying a theoretical groundwork. Starting from bulk crystal properties, we then describe the effect of quantum confinement in nanocrystals. After deriving the particle-in-a-box model and the multiband effective mass approximation, we present the fine structure of the band-edge exciton energy levels in these nanostructures. Initially focusing on $CdSe$ and InP nanocrystals, we extend our analysis to the case of lead halide perovskite nanocrystals. In the second part, we describe the particular optical properties of these systems, beginning with the recombination dynamics of the exciton and other complexes of charges. We also discuss the spectral diffusion phenomenon and blinking effect, characteristic of these systems. Finally, we introduce the notion of phonons in nanocrystals, starting from lattice vibrations in a bulk crystal to the impact of exciton-phonon coupling on the photoluminescence emission of nanocrystals.

Chapter 2

The second chapter presents the different experimental methods employed throughout this work. We start with a brief overview of synthesis techniques and quantum yield measurement methods. We then detail the experimental configuration of our single nanocrystal photoluminescence spectroscopy setup operating at low temperatures and with a magnetic field. This encompasses the preparation of samples, along with the description of the different components of the experiment, including the cryostat, piezoelectric positioners and scanner, excitation sources, and coils. We also present our methods of imaging, spectroscopy, polarization analysis, and lifetimes measurements.

Chapter 3

This chapter investigates the optical properties of single $InP/ZnSe/ZnS$ nanocrystals. We start by presenting the results obtained on an ensemble of nanocrystals, including the absorbance and photoluminescence emission, quantum yield measurements, temperature-dependent photoluminescence spectra, and decay curves. We then perform single nanocrystal photoluminescence spectroscopy with a magnetic field, revealing the three lower exciton states and showing that the lower state is dark. In parallel, we develop a theoretical model to interpret these results, accounting for the InP core shape anisotropy.

Chapter 4

The fourth chapter of this manuscript is devoted to the spectroscopic study of lead halide perovskites nanocrystals. We start by describing the structural and optical properties of both $CsPbBr_3$ and $CsPb(BrCl)_3$ samples. We then present the spectroscopy results obtained on the band-edge exciton fine structure of nearly-bulk $CsPbBr_3$ and of $CsPb(BrCl)_3$ nanocrystals, including the emission spectra from the recombination of the exciton bright triplet, and evidence of the magnetic brightening of the dark ground state. We also study the optical properties of other complexes of charges such as trions and biexcitons. By combining our experimental results with those obtained on various perovskite nanocrystals, we develop universal scaling laws establishing correlations between the exciton fine structure splitting, the trion and biexciton binding energies, and the band-edge exciton energy in lead-halide perovskite nanostructures, regardless of their chemical composition.

Chapter 5

Following these results, we give some conclusions and perspectives on this work. We provide preliminary spectroscopy results on nanorods of $CsPbBr_3$ for two different dimensions. We show that their exciton fine structure is very sensitive to their aspect ratio, and we demonstrate the potential of $CsPbBr_3$ nanorods with high aspect ratio as promising candidates for quantum emitters.

Chapter 1

Electronic and Optical Properties of Semiconductor Nanocrystals

This chapter provides a theoretical foundation for understanding electronic structures and optical properties of semiconductor nanocrystals.

We start by summarizing the theoretical models employed to describe the electronic structures in nanocrystals of $CdSe$ and InP, followed by a comparison with lead halide perovskite nanocrystals such as $CsPbBr_3$ and $CsPbCl_3$. The second part of this chapter is devoted to describing the optical properties proper to semiconductor nanocrystals. Finally, in the third part of this chapter, we introduce the notion of phonons in the context of these systems.

1.1 Electronic properties of semiconductor nanocrystals

As a basis for this thesis, we begin this chapter with the necessary concepts to comprehend the electronic structure of a nanocrystal.

1.1.1 Properties of bulk crystal and effective mass approximation

At an atomic level, the properties of semiconductor nanocrystals are similar to those of crystalline bulk materials. Therefore, we start by reporting the properties of bulk semiconductor crystals. The hybridization of atomic orbitals within a crystal lattice results in a description of the energy levels as bands. Consequently, electrons within a crystal lattice can be studied as free electrons subject to a periodic potential. According to the Bloch theorem, the wavefunctions of a single electron in an ideal and infinite crystal are written [26]:

$$\Psi_{nk}(\vec{r}) = u_{nk}(\vec{r})e^{i\vec{k}.\vec{r}} \tag{1.1}$$

where Ψ_{nk} is the wavefunction depending on the position $\vec{r}$, u_{nk} is a function containing the periodicity of the crystal lattice, n is the band index, and $\vec{k}$ is the wave vector. Within the **effective mass approximation**, we assume that the energies of these wavefunctions represented in a band diagram have simple parabolic shapes near their maxima or minima (i.e. k close to 0) as illustrated in Fig. 1.1 **a)**. The concept of effective mass allows for the inclusion of the periodic potential felt by the electron and hole in the crystal lattice, which corresponds graphically to the curvature of the band when $k = 0$. In this approximation, one can consider electrons as free particles with an effective mass m^*. The dispersion relation for the conduction band is then written:

$$E_{\mathrm{k}}^{\mathrm{c}} = \frac{\hbar^2 k^2}{2m_c^*} + E_{\mathrm{g}} \tag{1.2}$$

and for the valence band:

$$E_{\mathrm{k}}^{\mathrm{v}} = -\frac{\hbar^2 k^2}{2m_v^*} \tag{1.3}$$

where m_c^* and m_v^* are the effective masses of the electron in the conduction band and the valence band, respectively, $\hbar$ the reduced Planck constant, and E_g the semiconductor band gap energy. These energies are expressed relative to the top of the valence band.

1.1.2 Quantum confinement effect

When a photon is absorbed in direct-gap semiconductors, an electron is promoted directly from the valence band to the conduction band. In this process, a hole, the electron counterpart, is produced. Holes are quasiparticles with a positive elementary charge $+e$, as they represent the absence of an electron within an energy level. Therefore, this photo-excitation process induces the creation of an electron-hole pair interacting through the Coulomb interaction, as illustrated in Figure 1.1 **b)**. This paired entity is a quasiparticle called an exciton.

When the size of the semiconductor structure becomes comparable to or smaller than the natural length scale of the electron-hole pair, given by the Bohr radius of the exciton in the bulk material, there is an effect of quantum confinement. The physical limits of the material constrain the charge carriers in the three spatial directions. The motion of the electron is, therefore, restricted to discrete energy levels, leading to a quantization of the bulk band energies. As a result, nanocrystals exhibit optical behavior analogous to that of atoms (they are sometimes referred to as artificial atoms). The recombination of the exciton leads to the emission of a photon and is at the origin of the photoluminescence of semiconductor nanocrystals.

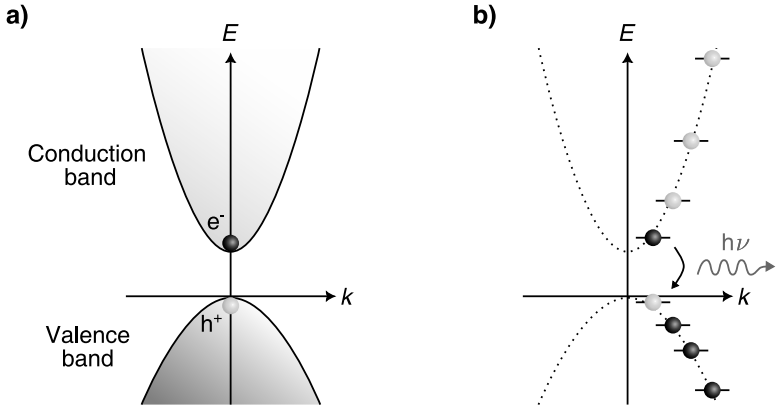

Figure 1.1: a) Simplified band diagram for a two-band model in a bulk semiconductor. e^- is the electron and h^+ the hole. **b)** In a semiconductor nanocrystal, the confinement of the charges in a three-dimensional potential well leads to the discretization of the band diagram. The electron-hole pair recombination leads to the emission of a photon of energy $h\nu$.

1.1.3 Quantum confinement regimes

Nanocrystals exhibit different confinement regimes depending on their size and their chemical composition. To estimate the degree of confinement in a nanocrystal, we define its exciton Bohr radius a_{X} with the general formula:

$$a_{\mathrm{X}} = \varepsilon \frac{m}{m^*} a_0 \tag{1.4}$$

with ε the dielectric constant of the semiconductor material, m the rest mass of the electron, and a_0 the Bohr radius of the hydrogen atom $a_0 = \frac{4\pi\epsilon_0\hbar^2}{m_0 e^2} \approx 0.53$ Å. There are three main confinement regimes, which significantly influence the electronic and optical properties of a nanocrystal.

In the **strong confinement regime**, the radius of the nanocrystal is smaller than the exciton Bohr radius. The confinement energy dominates over the Coulomb interaction between electron and hole. Properties such as bandgap energy, emission wavelength, and absorption spectrum are highly size-dependent. This regime is typical in very small nanocrystals (below 10 nm). In the **weak confinement regime**, the size of the nanocrystal is larger than the exciton Bohr radius but still small enough to exhibit some quantum effects, though less pronounced compared to the strong confinement regime. The confinement energy is smaller than the Coulomb interaction. This regime applies to larger nanocrystals (usually tens of nanometers). The **intermediate confinement regime** is a transitional regime between strong and weak confinement. The size of the nanocrystal is comparable to the exciton Bohr radius; therefore, the Coulomb interaction and confinement energy are of similar magnitudes. While size-dependent properties are still observable, they do not show as marked a change as in the strong confinement regime.

1.1.4 Particle-in-a-box model

A simple method to describe the size dependence of electronic properties in semiconductor nanocrystals is to use the **particle in a box model**. In this model, the particles are confined in a sphere surrounded by a constant potential with an infinite potential barrier. The exciton wavefunction can be written as:

$$\psi(\vec{r}_e, \vec{r}_h) = \psi_e(\vec{r}_e)\psi_h(\vec{r}_h) \tag{1.5}$$

The diameter of the nanocrystal is usually ten times or more than the lattice parameter, which implies that the crystal structure of the nanocrystals can be viewed as similar to bulk material and the effective mass approximation is still valid. Using Equation 1.1, the wavefunction of the electron or hole can be described as a linear combination of Bloch functions:

$$\Psi_n(\vec{r}) = \sum_k c_{nk} u_{nk}(\vec{r}) e^{i\vec{k}.\vec{r}} \tag{1.6}$$

c_{nk} are the expansion coefficients, satisfying the boundary conditions of the nanocrystals. Assuming that the functions $u_{n\vec{k}}(\vec{r})$ have a weak dependency on the wavevector $\vec{k}$, we can consider $u_{n\vec{k}}(\vec{r}) = u_{n\vec{0}}(\vec{r})$ and we obtain [27]:

$$\Psi_n(\vec{r}) \approx u_{n0}(\vec{r})\phi_n(\vec{r}), \tag{1.7}$$

$\phi_n(\vec{r})$ is the envelope function:

$$\phi_n(\vec{r}) = \sum_k c_{nk} e^{i\vec{k}.\vec{r}}. \tag{1.8}$$

The periodic function $u_{n0}(\vec{r})$ varies at the scale of the lattice parameter. The problem is reduced to determining the envelope functions and can then be solved using the solutions of a particle inside a sphere of radius a. The envelope function $\phi_n(\vec{r})$ varies at the scale of nanocrystal size and obeys the following Schrödinger equation:

$$\left[-\frac{\hbar^2}{2m^*}\nabla^2 + V(r)\right]\phi(\vec{r}) = E\phi(\vec{r}). \tag{1.9}$$

$\phi(\vec{r})$ is the electron (or the hole) wavefunction and $V(r)$ is a spherical potential well of radius a, with a potential barrier approximated as infinitely high and defined by:

$$V(r) = \begin{Bmatrix} 0 & \text{if} & r < a \\ \infty & \text{if} & r > a \end{Bmatrix}. \tag{1.10}$$

Solving the Schrödinger equation gives the wavefunction of the particle [28]:

$$\phi_{n,\ell,m}(r,\theta,\phi) = C\frac{j_\ell(k_{n,\ell}r)Y_\ell^m(\theta,\phi)}{r} \tag{1.11}$$

where C is a normalization constant, $Y_\ell^m(\theta,\phi)$ is a spherical harmonic function, and $j_\ell(k_{n,\ell},r)$ is the spherical Bessel function of order ℓ. $k_{n,\ell} = \alpha_{n,\ell}/a$ is determined by the limit condition $\Psi_n(r=a)=0$ with $\alpha_{n,\ell}$ the n^{th} zero of $j_\ell(k_{n,\ell}r)$. The corresponding energies in the parabolic approximation are written [28, 3]:

$$E_{n,\ell} = \frac{\hbar^2 k_{n,\ell}^2}{2m^*} = \frac{\hbar^2\alpha_{n,\ell}^2}{2m^*a^2} \tag{1.12}$$

The energies expressed in Eq. 1.12 are similar to the kinetic energy of a free particle, except that the limit conditions of the spherical potential lead to a quantification of the wavevector $k_{n,\ell}$. These energies strongly depend on the nanocrystal size as they are proportional to $1/a^2$. The electron and hole energy levels can be represented by orbitals identified by quantum numbers n, ℓ, m, analogous to an atomic system.

The model presented does not account for the Coulomb interaction between the electron and the hole, varying in $1/a$. Its inclusion in the exciton energies expressions differs depending on the confinement regime. Using Eq. 1.11, Eq. 1.12 and Eq. 1.7, the exciton states can be written as:

$$\begin{aligned} \Psi_X(\vec{r_e},\vec{r_h}) &= \Psi_e(\vec{r_e})\Psi_h(\vec{r_h}) \\ &= u_c\phi_e(\vec{r_e})u_v\phi_e(\vec{r_e}) \\ &= C\left[u_c\frac{j_{L_e}(k_{n_e,L_e}r_e)Y_{L_e}^{m_e}}{r_e}\right]\left[u_v\frac{j_{L_h}(k_{n_h,L_h}r_h)Y_{L_h}^{m_h}}{r_h}\right] \end{aligned} \tag{1.13}$$

In a strong confinement regime, the nanocrystal is sufficiently small for the quadratic confinement term to dominate, and the electron and hole can be treated independently. Therefore, we approximate the energy of an excitonic state by the sum of the energies of the electron in the conduction band and the hole in the valence band. Each of these particles is described with the particle-in-a-box model:

$$E_X(n_hL_hn_eL_e) = E_g + \frac{\hbar^2}{2a^2}\left[\frac{\alpha^2_{n_h,L_h}}{m_h^*} + \frac{\alpha^2_{n_e,L_e}}{m_e^*}\right] - E_C. \tag{1.14}$$

The electron-hole Coulomb term is added as a first energy correction E_{C}, which slightly lowers the energy levels of the exciton. As an example, using first-order perturbation theory to obtain the expression of the Coulomb correction for pair states with the electron in the $1S$ energy level gives [29]:

$$E_{\text{C}} = -1.8\frac{e^2}{\epsilon a}. \tag{1.15}$$

Eq. 1.15 shows the proportionality in $1/a$ of the Coulomb attraction. For the first state of the

exciton $1S_e1S_h$, with $\alpha_{1,0} = \pi$ the energy can then be expressed:

$$E_X(1S_e1S_h) = E_g + \frac{\hbar^2\pi^2}{2m_X^* a^2} - 1.8\frac{e^2}{\epsilon a} \tag{1.16}$$

This expression first approximates the size dependence of the exciton energy levels [30].

1.1.5 Multiband effective mass approximation

So far, the valence and conduction bands have been described with a simple parabolic band dispersion. However, the band structure of semiconductors is more complex. This simplified model only allows for a qualitative understanding of the optical properties of semiconductor nanocrystals, as it fails to consider the mixing between subbands of the hole states. For instance, in the case of $CdSe$, the valence band is poorly described by this approximation as it comes from the hybridization of the Se $4p$ atomic orbitals and is 6-fold degenerate at $k = 0$. The search for a better description to assess the actual band structure of semiconductor nanocrystals led to the development of various models.

To describe these systems correctly, one must consider the type of semiconductor (wide gap or narrow gap), the multiplicity of the semiconductor bands (valence band in the case of $CdSe$ and InP and conduction band in the case of perovskites), the symmetries of the crystal structures, the size of the nanocrystal (leading to different confinement regimes), and its shape anisotropy. The following part will mention different models adapted to various situations.

Case of $CdSe$ nanocrystals

The case of $CdSe$ nanocrystals with a zinc-blende crystal structure, which derives from a face-centered cubic structure, is similar to an ideal diamond-like structure. The bands are still described as parabolic; however, at $k = 0$ the valence band is split into two p subbands: one with an angular momentum $J = 1/2$ $\left(p_{1/2}\right)$ called the **split-off-hole** (so) subband and one with $J = 3/2$ $\left(p_{3/2}\right)$. For $k \neq 0$ the $p_{3/2}$ is further split by the spin-orbit interaction into two subbands: $J_m = \pm 3/2$ called the **heavy-hole** (hh) subband and $J_m = \pm 1/2$ called the **light-hole** (lh) subband as shown in Fig. 1.2 **a)**. This model adds a first level of complexity to the simple parabolic model. However, in the case of $CdSe$ with a wurzite crystal structure, the hexagonal lattice does not have inversion symmetry. The crystal field will induce a splitting that further lifts the degeneracy of the heavy-hole and light-hole when $k = 0$, as represented in Fig. 1.2 **b)**. In the following parts of this chapter, $CdSe$ nanocrystals will be considered in their wurtzite crystal structure and InP nanocrystals in their zinc-blende crystal structure.

$k.p$ perturbation theory

The $k.p$ method has been developed with the objective of a better description of the bulk band structure [31]. By substituting Bloch wavefunctions (as defined in Eq 1.1) into the Schrödinger equation, one will obtain a Hamiltonian H_k that can be expressed as a sum of the unperturbed Hamiltonian H_0 corresponding to the Hamiltonian at $k = 0$, and the perturbation Hamiltonian $H_k^{'}$ containing a "$k.p$" term. The $k.p$ perturbation theory is semi-empirical as the energy $E_n(k = 0)$ needs to be known. The bulk bands are then expanded analytically around $k = 0$ to the second order of k. This method is applied in the Luttinger-Kohn and Kane models presented thereafter.

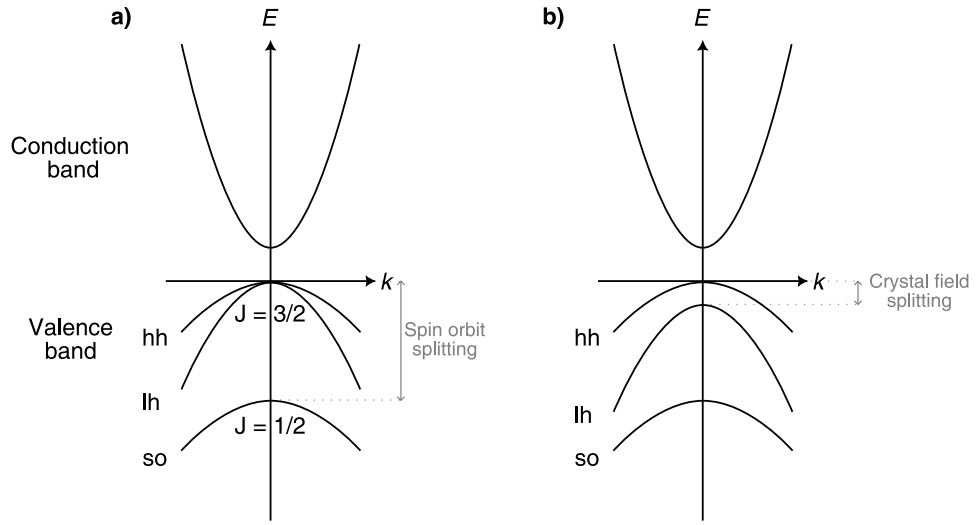

Figure 1.2: Band structure **a)** for zinc-blende $CdSe$ **b)** for wurtzite $CdSe$ nanocrystals. hh is the heavy hole subband, lh the light hole subband and so the split-off band. The crystal field of the hexagonal crystal structure split the hh and lh subbands at $k = 0$

Luttinger-Kohn model

Deriving from the $k.p$ perturbation theory, this model starts to include the valence band degeneracy. It takes into account six valence bands (hh, lh, so and their spin counterpart) but still neglects the crystal field and the coupling between valence and conduction bands. Viewing the hole and electron independently, this model applies to semiconductors with wide bandgap [32].

Kane model

In the context of narrow-gap semiconductors, it becomes necessary to account for the interaction between valence and conduction bands, which is precisely addressed in the Kane model. This model also provides a more accurate representation of deviations from the ideal parabolic behavior of the bands [33].

Pidgeon and Brown (PB) model

The Pidgeon and Brown (PB) model (or 8-band model) is a multiband effective mass approximation derived from the Kane model [34]. It has been developed for $InSb$ and can generally be used for zinc-blende semiconductors. It takes into account the nonparabolicity of electron and light hole band dispersion. The Pidgeon and Brown model elucidates the characteristics of the energy band structure near the Γ point of the Brillouin zone. The following sub-section will be based on this model.

1.1.6 Fine structure of the band-edge exciton energy levels

The development of photoluminescence spectroscopy at low temperatures on individual nanocrystals allows access to their photoluminescence properties. Therefore, a comprehensive understanding of the semiconductor nanocrystal excitonic fine structure is crucial to interpret the photoluminescence spectra accurately and to develop spin manipulation in quantum dot semiconductors.

The following part describes the model developed by Efros and Rosen in 1996 [35] to understand the fine structure of the band edge exciton in the case of direct-gap semiconductors with

cubic or hexagonal lattice structure within the Pidgeon and Brown model. This model holds for $CdSe$ and InP; the specific case of lead halide perovskites will be described afterward.

In these semiconductors, at the Γ point of the Brillouin zone, the lowest conduction state is characterized by an s-like symmetry with an orbital Bloch function S. In contrast, the highest valence band is characterized by a p-like symmetry with orbital Bloch functions X, Y, Z. The inclusion of spin degeneracy doubles the number of states. In semiconductor nanocrystals, the emission of photons comes from the lowest exciton energy level $1S_{h,3/2}$ $1S_e$. This level is constructed from the $1S_e$ state of the electron in the conduction band and the $1S_{h,3/2}$ state from the hole in the valence band. The $1S_e$ state is two-fold degenerate due to electron spin projection $\pm\frac{1}{2}$, and the $1S_{h,3/2}$ state with its total angular momentum of 3/2 is four-fold degenerate with projections $\frac{3}{2}, \frac{1}{2}, -\frac{1}{2}, -\frac{3}{2}$. The Bloch functions of the fourfold degenerate valence band Γ_8 are [34]:

$$\begin{aligned}
|+\frac{3}{2}\rangle &= -|\uparrow\rangle \frac{X+iY}{\sqrt{2}} \\
|+\frac{1}{2}\rangle &= \sqrt{\frac{2}{3}}|\uparrow\rangle Z - |\downarrow\rangle \frac{X+iY}{\sqrt{6}} \\
|-\frac{1}{2}\rangle &= \sqrt{\frac{2}{3}}|\downarrow\rangle Z + |\uparrow\rangle \frac{X-iY}{\sqrt{6}} \\
|-\frac{3}{2}\rangle &= |\downarrow\rangle \frac{X-iY}{\sqrt{2}}
\end{aligned} \tag{1.17}$$

and the Bloch functions of the doublets of conduction band Γ_7:

$$\begin{aligned}
|+\frac{1}{2}\rangle &= \frac{1}{\sqrt{3}}\left[|\uparrow\rangle Z + |\downarrow\rangle (X+iY)\right] \\
|-\frac{1}{2}\rangle &= \frac{1}{\sqrt{3}}\left[-|\downarrow\rangle Z + |\uparrow\rangle (X-iY)\right]
\end{aligned} \tag{1.18}$$

Therefore, in the spherical approximation where the energy bands are assumed to be spherically isotropic, for a spherical nanocrystal with a cubic crystal lattice, the band-edge exciton is eight times degenerate. There are three main factors that can lift this degeneracy and split the eight excitonic states into five states:

- The crystal field anisotropy
- The crystal shape anisotropy
- The electron-hole exchange interaction

Considering these three factors, we can determine the energy level diagram of the exciton fine structure.

Crystal field splitting

The crystal field splitting leads to the splitting of the hh and lh subbands at $k = 0$ as shown in Fig. 1.2 **b)**. It can be considered a perturbation [36]. The splitting due to the hexagonal lattice structure is then written:

$$\Delta_{\text{int}} = \Delta_{\text{cr}}\nu(\beta) \tag{1.19}$$

where Δ_{cr} is the crystal field splitting corresponding to the energy difference between the hh and lh subbands, $\beta = m_{lh}/m_{hh}$ is the ratio of the light-to-heavy hole effective mass and $\nu(\beta)$ is a dimensionless function depending only on β as defined in Ref. [36]. For $CdSe$ nanocrystals in a wurtzite phase, the crystal structure is hexagonal based and possesses a uniaxial symmetry

as shown in Fig 1.3 **a)**. The crystal field splitting of wurtzite $CdSe$ is $\Delta_{cr}^{\mathrm{CdSe}} = 25$ meV [35]. In the case of InP nanocrystals in a zinc-blende phase shown in Fig 1.3 **b)**, the crystal structure is cubic based and possesses symmetry in the 3-space directions, therefore $\Delta_{cr}^{\mathrm{InP}} = 0$.

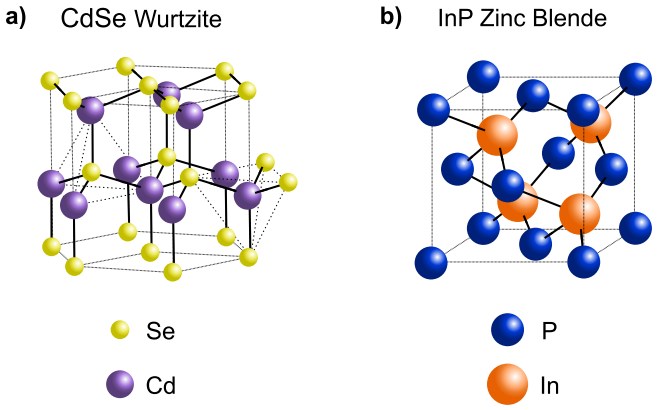

Figure 1.3: Crystal structure representations of **a)** $CdSe$ wurtzite nanocrystals and **b)** InP zinc-blende nanocrystals.

Crystal shape splitting

Experimentally, nanocrystals are rarely perfectly spherical and are usually distorted during the crystal growth process. To take into account the non-sphericity of nanocrystals, their shape is described as an ellipsoidal with a major axis (long axis) of radius c and a minor axis (short axis) of radius b, as represented in Fig. 1.4.

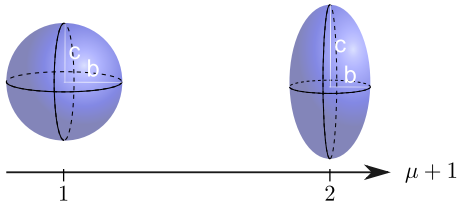

Figure 1.4: Scheme of the ellipsoidal distortion of a spheroidal nanocrystal as a function of the aspect ratio.

The deviation from the spherical shape can be expressed by defining the aspect ratio of a nanocrystal:

$$\mu + 1 = \frac{c}{b} \tag{1.20}$$

with μ the ellipticity of the nanocrystal. $\mu > 0$ corresponds to prolate nanocrystals and $\mu < 0$ to oblate nanocrystals. By keeping the same volume as a spherical nanocrystal of radius $a = b = c$, the effective radius a^* is defined as:

$$\begin{aligned} a^* &= (b^2 c)^{\frac{1}{3}} \\ \Rightarrow a^* &= b(\mu + 1)^{\frac{1}{3}} \end{aligned} \tag{1.21}$$

The shape splitting arising from this non-sphericity is calculated in the first-order perturbation theory:

$$\Delta_{\mathrm{sh}} = \mu u(\beta) \frac{\hbar^2 \varphi^2(\beta)}{m_{\mathrm{hh}}(a^*)^2} \tag{1.22}$$

with $u(\beta)$ and $\varphi(\beta)$ being two dimensionless functions describing the dependence in β as defined

in Ref. [36]. The net splitting of the exciton energy levels can then be written as the sum of crystal field splitting and shape splitting:

$$\Delta = \Delta_{sh} + \Delta_{int} = \mu u(\beta)\frac{\hbar^2\varphi^2(\beta)}{m_{\rm hh}(a^*)^2} + \Delta_{\rm cr}\nu(\beta). \tag{1.23}$$

Electron-hole exchange interaction

The exchange interaction for excitons in semiconductors was first studied by Pikus in 1971 [37]. This interaction is primarily due to the Pauli exclusion principle, which states that two fermions cannot occupy the same quantum state simultaneously. The interaction between the spin of the electron and the spin of the hole changes the mean value of the distance between the two particles when their wavefunctions overlap. The electron-hole exchange interaction conserves the angular momentum of the two particles. It is given by [38]:

$$\hat{H}_{exchange} = -\varepsilon_{\rm exch}\Omega_0(\sigma^e.\sigma^h)\delta(r_e - r_h) \tag{1.24}$$

σ^i are the electron and hole Pauli operators, $\varepsilon_{\rm exch}$ is the exchange strength constant and Ω_0 the volume of the unit cell. The exchange interaction contains a short-range component that decays exponentially in the bulk lattice constant and a long-range component that decays as a power law and extends over several lattice constants [39]. In bulk semiconductors, as the exciton wavevector approaches zero, the long-range interaction is at the source of a nonanalytic behavior of the exciton dispersion which is why 'long-range' and 'short-range' are sometimes referred to as nonanalytic and analytic portions of the exchange interaction. As a first approximation, we start by only considering the short-range interaction.

The short-range exchange interaction between electrons and holes leads to further splitting of the exciton energy level due to an enhanced overlap between electrons and holes. For cubic lattice structure (InP in zinc-blende phase), this splitting can be expressed as [35]:

$$\hbar\omega_{\rm TF} = \frac{8}{3\pi}\left(\frac{a_0}{a_{\rm X}}\right)^3\varepsilon_{\rm exch}, \tag{1.25}$$

and in the case of a hexagonal lattice structure ($CdSe$ in wurtzite phase):

$$\hbar\omega_{\rm TF} = \frac{2}{\pi}\left(\frac{a_0}{a_{\rm X}}\right)^3\varepsilon_{\rm exch}. \tag{1.26}$$

These three factors lifting the degeneracy of the $1S_{h,3/2}$ $1S_e$ split the eight degenerate excited energy levels into five levels. Each of these five energy states is labeled by the exciton total angular momentum projection ($F_m = m_{J_h} + S_z$) along the nanocrystal main symmetry axis. The superscripts U (for upper) and L (for lower) are used to differentiate levels with the same angular momentum but different energies. The five resulting energy levels are therefore labeled: $F = 2, 1^{\rm L}, 1^{\rm U}, 0^{\rm L}, 0^{\rm U}$ and are represented in Fig 1.5. The levels resulting from the heavy hole valence band are the 2 and $1^{\rm L}$ levels. The ones resulting from the light-hole valence band are the $1^{\rm U}$and $0^{\rm U,L}$ levels.

Fig. 1.5 shows the splitting of the band edge exciton fine structure with two limits. When the anisotropy (coming from the crystal structure or shape) dominates and the electron-hole exchange interaction is negligible, the energy levels are split into two fourfold degenerate states. When the exchange interaction dominates, usually when the nanocrystal is very small and therefore the quantum confinement is strong, the energy levels are split into one 3-fold and one 5-fold degenerate states. The middle diagram corresponds to the case where the two effects are included and the energy levels are split into five sublevels. The order of the levels in this figure

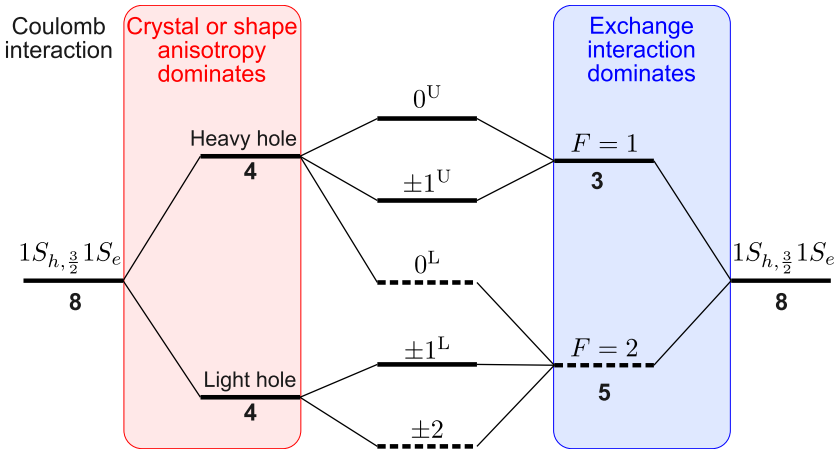

Figure 1.5: Energy diagram of the exciton fine structure of a semiconductor nanocrystal in the case of an oblate deformation. On the left, in red, the crystal or shape anisotropy split the sublevels. On the right in blue, the sublevels are split by the exchange interaction. Between these two limits, the energy levels are split into five sublevels, their order here corresponds to an oblate deformation. The dotted lines show the non-optically active states.

corresponds to an oblate deformation. The radiative recombinations from the band-edge states $F = 0^{L}$ and ±2 are not allowed in the electric dipole approximation. In the case of $F = \pm2$, the transition from this state is one-photon forbidden as an emitted photon cannot have an angular momentum projection of ±2. The transition oscillator strength from level 0^{L} is calculated later in this chapter. These two optically passive states will be referred to as dark states, whereas $F = \pm1^{L}, \pm1^{U}, 0^{U}$ are optically active in the electric dipole approximation and are called optically bright states.

To write the energy of these five exciton levels as a function of nanocrystal size and shape, one must solve the secular equation:

$$det(\hat{E} - E_{|F|}) = 0 \tag{1.27}$$

where $\hat{E}$ is the matrix elements of the perturbation matrix that associate anisotropy perturbations and exchange interaction. The perturbation matrix is given below, in the case of a uni-axial deformation [35]:

	↑, 3/2	↑, 1/2	↑, -1/2	↑, -3/2	↓, 3/2	↓, 1/2	↓, -1/2	↓, -3/2
↑, 3/2	$-\frac{3\eta^{SR}+\Delta}{2}$	0	0	0	0	0	0	0
↑, 1/2	0	$\frac{-\eta^{SR}+\Delta}{2}$	0	0	$-i\sqrt{3}\eta^{SR}$	0	0	0
↑, -1/2	0	0	$\frac{\eta^{SR}+\Delta}{2}$	0	0	$-i2\eta^{SR}$	0	0
↑, -3/2	0	0	0	$\frac{3\eta^{SR}-\Delta}{2}$	0	0	$-i\sqrt{3}\eta^{SR}$	0
↓, 3/2	0	$i\sqrt{3}\eta^{SR}$	0	0	$\frac{3\eta^{SR}-\Delta}{2}$	0	0	0
↓, 1/2	0	0	$i2\eta^{SR}$	0	0	$\frac{\eta^{SR}+\Delta}{2}$	0	0
↓, -1/2	0	0	0	$i\sqrt{3}\eta^{SR}$	0	0	$\frac{-\eta^{SR}+\Delta}{2}$	0
↓, -3/2	0	0	0	0	0	0	0	$-\frac{3\eta^{SR}+\Delta}{2}$
Levels	$+2$	$+1^{U}$	0^{U}	-1^{L}	$+1^{L}$	0^{L}	-1^{U}	-2

η^{SR} is the electron-hole short-range exchange term:

$$\eta^{\mathrm{SR}} = \left(\frac{a_X}{a}\right)^3 \hbar\omega_{\mathrm{TF}}\chi(\beta) \tag{1.28}$$

with $\chi(\beta)$ a dimensionless scaling function written in terms of the electron and hole radial wave functions. Solving the secular equation gives five exciton levels with the wave functions Ψ_F:

$$\begin{aligned}
\Psi_0^{U,L} &= \frac{1}{\sqrt{2}}\left[\mp i\Psi_{\uparrow,-1/2} + \Psi_{\downarrow,1/2}\right] \\
\Psi_1^{U,L} &= \mp iC^+\Psi_{\uparrow,1/2} + C^-\Psi_{\downarrow,3/2} \\
\Psi_{-1}^{U,L} &= \mp iC^-\Psi_{\uparrow,-3/2} + C^+\Psi_{\downarrow,-1/2} \\
\Psi_{-2} &= \Psi_{\downarrow,-3/2} \\
\Psi_2 &= \Psi_{\uparrow,-3/2},
\end{aligned} \tag{1.29}$$

with

$$\begin{aligned}
C^{\pm} &= \sqrt{\frac{\sqrt{f^2+d} \pm f}{2\sqrt{f^2+d}}} \\
f &= \frac{-2\eta^{\mathrm{SR}} + \Delta}{2} \\
d &= 3(\eta^{\mathrm{SR}})^2.
\end{aligned} \tag{1.30}$$

These five excitonic states have the energies:

$$\begin{aligned}
E_0^{\mathrm{U,L}} &= \frac{\eta^{\mathrm{SR}}}{2} + \frac{\Delta}{2} \pm 2\eta^{\mathrm{SR}} \\
E_1^{\mathrm{U,L}} &= \frac{\eta^{\mathrm{SR}}}{2} \pm \sqrt{\frac{(2\eta^{\mathrm{SR}} - \Delta)^2}{4} + 3(\eta^{\mathrm{SR}})^2} \\
E_2 &= -\frac{3\eta^{\mathrm{SR}}}{2} - \frac{\Delta}{2}
\end{aligned} \tag{1.31}$$

In these equations, the "Upper level" corresponds to the $+$, and the "Lower level" to the $-$. The expression of Δ is given in Eq. 1.23.

Fig. 1.6 shows the energy levels splitting for spheroidal nanocrystals of $CdSe$ with a wurtzite structure and of InP with a zinc-blende structure as a function of their aspect ratio. All parameters for these plots can be found in Table 1.1. In both cases, the energy level order and the level splitting strongly depend on the aspect ratio. In the case of a wurtzite crystal structure, the band-crossing happens at $\mu \neq 0$.

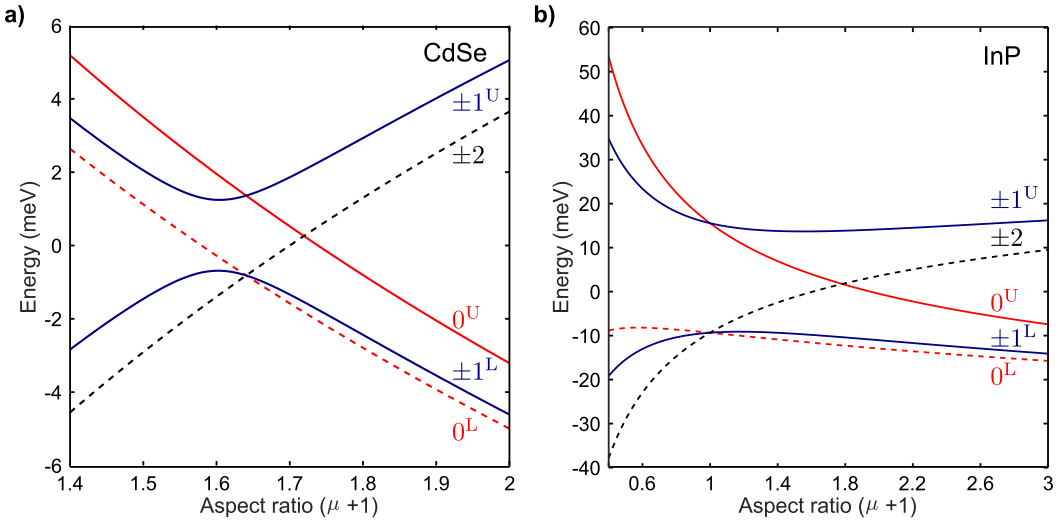

Figure 1.6: Energy levels as a function of aspect ratio of a spheroidal nanocrystal calculated **a)** for a wurtzite $CdSe$ nanocrystal with a radius of 27 Å **b)** for a zinc-blende InP nanocrystal with a radius of 16.5 Å. Dotted lines indicate non-optically active states. All parameters are given in Table 1.1. The long-range component of the exchange interaction is not taken into account in these calculations.

	CdSe (Wurtzite)	InP (Zinc-blende)
β	0.28 [35]	0.15 [40, 41, 42]
a_{X}	56 Å [35]	96 Å[43]
Δ_{cr}	25 meV [35]	0 meV
$\nu(\beta)$	0.94 [35]	0.57 [35]
$\varphi(\beta)$	4.59 [35]	5.3 [35]
$\chi(\beta)$	0.77 [35]	0.78 [35]
$u(\beta)$	-0.26 [35]	-0.02 [35]
$\hbar\omega_{\mathrm{TF}}$	0.13 meV [35]	0.04 meV [43]
m_{hh}	$1.4m_0$*	$0.6m_0$*
b	27 Å	16.5 Å
$\bar{\chi}$	0.02 [44]	0.1 [44]
ϵ_{in}	6.20 [45]	9.61 [40]
ϵ_{out}	1	1
$\hbar\omega_{\mathrm{LT}}$	0.95 meV [44]	0.1 meV [46]
ξ	0.85 [44]	0.58 [44]
$(Q_0^{(1)})^2$	0.93 [44]	0.58 [44]

Table 1.1: Parameters for computation of energy levels as a function of aspect ratio.

Long-range exchange interaction

Until now, the model presented has neglected the influence of long-range exchange interaction, leading to an underestimation of the energy splitting. However, since the model of Efros et al. in 1996 [35], subsequent revisions have incorporated a long-range exchange interaction term to address this limitation [44]. The electron-hole exchange interaction is then given by:

$$\hat{H}^{exch} = \eta \left[\frac{3}{2}\mathcal{I} - (\sigma_e.F) \right] + \bar{\eta}\mathcal{I}, \tag{1.32}$$

where $\mathcal{I}$ is the 8×8 identity matrix and σ_e is the electron Pauli matrix. Unlike Ref. [35], the Hamiltonian of eq. 1.32 describes the absolute position of the energy levels relative to the lowest optical transition in the absence of exchange effects. The first term describes an asymmetric splitting of the 1 and 2 levels and the second term describes an overall shift of all levels from the reference energy.

Two new terms are introduced in this revisited model:

- $\bar{\eta}$, which describes an overall shift of all the fine structures. The long-range exchange does not contribute to the overall shift term $\bar{\eta}$. The exchange shift is written:

$$\bar{\eta} = \hbar\omega_{\mathrm{TF}}\bar{\chi}(\beta)\left(\frac{a_X}{a}\right)^3. \tag{1.33}$$

  Unlike χ, $\bar{\chi}$ vanishes in the limit $\beta \to 1$, which fits the simple band limit where the $1S_{3/2}$ ground hole level is entirely composed of $L = 0$ envelope functions.

- η^{LR}, which is the long-range exchange interaction:

$$\eta^{\mathrm{LR}} = \frac{\hbar\omega_{\mathrm{LT}}}{4}\left(\frac{a_X}{a}\right)^3\left[\xi(\beta) + \left(\frac{\kappa-1}{\kappa+2}\right)\frac{2|Q_0^{(1)}(\beta)|^2}{3}\right] \tag{1.34}$$

  $\hbar\omega_{\mathrm{LT}}$ is the bulk exciton longitudinal transverse splitting, $\xi(\beta)$ and $Q_0^{(1)}(\beta)$ are two dimensionless functions depending only on β and defined in [44], $\kappa = \frac{\epsilon_{in}}{\epsilon_{out}}$ the ratio of the internal ϵ_{in} to the external ϵ_{out} high-frequency dielectric constants.

The total exchange interaction in Eq. 1.32 is then simply the sum of the long and short-range interaction terms:

$$\eta = \eta^{LR} + \eta^{SR} \tag{1.35}$$

According to Eq. 1.32, the levels defined in Eq. 1.31 are shifted by $\frac{3}{2}\eta + \bar{\eta}$, giving:

$$\begin{aligned} E_0^{\mathrm{U,L}} &= \bar{\eta} + 2\eta + \frac{\Delta}{2} \pm 2\eta \\ E_1^{\mathrm{U,L}} &= \bar{\eta} + 2\eta \pm \sqrt{\frac{(2\eta-\Delta)^2}{4} + 3\eta^2} \\ E_2 &= \bar{\eta} - \frac{\Delta}{2} \end{aligned} \tag{1.36}$$

The new energy levels, taking into account the shift due to long-range exchange interaction, are plotted as a function of the aspect ratio of the nanocrystal in Fig. 1.7 for $CdSe$ and InP spheroidal nanocrystals. All the parameters for these plots are given in Table 1.1.

Comparing Fig. 1.7 with Fig. 1.6, one can see that while the overall order of energy levels and their crossing point do not change, their splitting is increased by the addition of the long-range term.

Another correction can be added to the model by accounting for the proximity in energy between the hole ground level $1S_{3/2}$ and the first excited hole level $1P_{3/2}$ in small-size nanocrystals. One may have to consider an energy overlap between the $1S_{3/2}1S_e$ and $1P_{3/2}1S_e$ of the hole state to apprehend better the exciton fine structure splitting. In particular, the important decay time observed in small-sized nanocrystals at room temperature can be partially attributed to the thermal occupation of the optically inactive $1P_{3/2}1S_e$ exciton state [44].

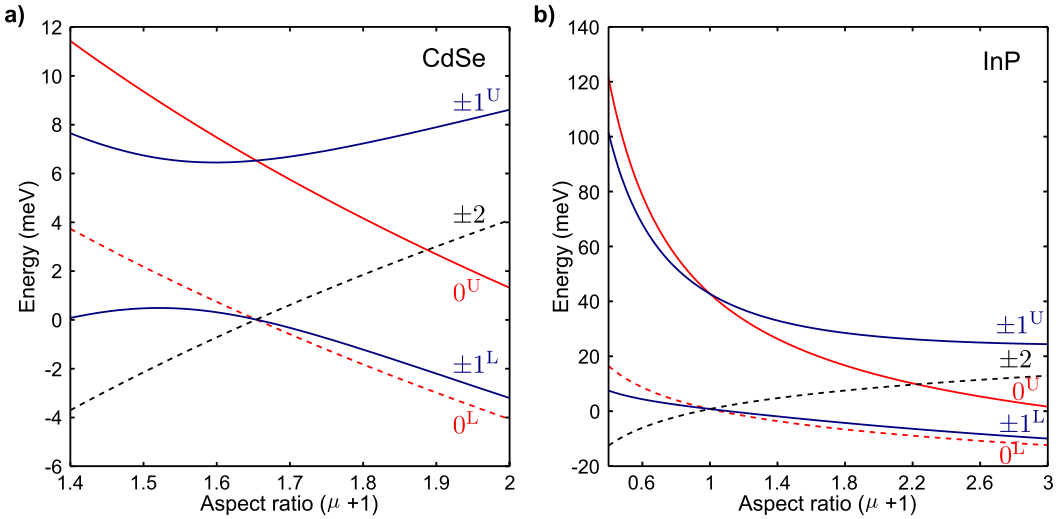

Figure 1.7: Energy levels as a function of aspect ratio of spheroidal nanocrystal calculated taking into account the long-range component of the exchange interaction, **a)** for a $CdSe$ nanocrystal with a radius of 27 Å **b)** for an InP nanocrystal with a radius of 16.5 Å. Dotted lines indicate non-optically active states. All parameters are given in Table 1.1.

1.1.7 Effect of the magnetic field on the exciton fine structure

Experimentally, we use a magnetic field external to the nanocrystal as a tool to identify the fine structure of the exciton. In particular, the magnetic field lifts the spin degeneracy of degenerate states by Zeeman effect, and reveals dark states by inducing coupling between neighboring dark and bright states, modifying their oscillator strength.

The Zeeman Hamiltonian describes the effect of an external magnetic field $\boldsymbol{H}$:

$$\hat{H}_H = g\mu_B \boldsymbol{J}.\boldsymbol{H} \tag{1.37}$$

with g is the Landé factor (g-factor), μ_B the Bohr magneton and $\mathbf{J}$ the total angular momentum. The Zeeman Hamiltonian in semiconductor nanocrystals describes the interaction of the magnetic moment of the electron and hole spins with an external magnetic field:

$$\hat{H}_H = \frac{1}{2} g_e \mu_B \hat{\sigma}.\boldsymbol{H} - g_h \mu_B \hat{\mathcal{K}}.\boldsymbol{H} \tag{1.38}$$

The first term of the sum depicts the interaction between the magnetic field and the electron spin, and the second term describes the interaction with the hole spin, with $\hat{\sigma}$ the Pauli matrix for the electron spin and $\hat{\mathcal{K}}$ the operator of the angular momentum of the hole.

The magnetic interaction is then treated as a perturbation to the initial system. The influence of the magnetic field on an excitonic level $|\Psi_{\alpha',M'}\rangle$ is given by calculating the perturbation matrix elements [35]:

$$E'_H = \langle \Psi_{\alpha,M} | \hat{H}_H | \Psi_{\alpha',M'} \rangle \tag{1.39}$$

with α the projection of the electron spin and M the projection of the angular momentum.

These terms split the energies of the excitonic sublevels through the Zeeman effect, depending on the angle between the nanocrystal main axis and the orientation of the magnetic field θ_H. The expression for the splitting between two sublevels is:

$$\Delta E_i = g_{X,i} \mu_B H cos(\theta_H) \tag{1.40}$$

where i is the excitonic level (±1 or ±2) and $g_{X,i}$ is a combination of the Landé factor of hole and electron. The values of $g_{X,i}$ depend on the relation between the electron-hole exchange interaction and the anisotropy in the nanocrystal, their detailed expressions are given in the case of wurtzite $CdSe$ in reference [35].

In addition to the splitting of the sublevels, adding a magnetic field external to the nanocrystal can enable the optical recombination of a dark state by mixing it with an optically active bright state. The non-diagonal terms of the perturbation Zeeman Hamiltonian involve magnetic field components orthogonal to the nanocrystal quantization axis, which induce coupling between neighboring sublevels. For instance, in $CdSe$, adding a magnetic field mixes the $F = \pm2$ dark exciton states with the optically active $F = \pm1$ states in the oblate case, or the $F = 0^{\mathrm{L}}$ dark exciton state with the optically active $F = \pm1$ in the prolate case.

1.1.8 Exciton fine structure in lead halide perovskites

Part of this thesis will be dedicated to the experimental study of different types of lead halide perovskites nanocrystals. Lead halide perovskites are a crystallographic family with a general formula $APbX_3$ with A a cation and X halide anions. We study in particular the case of cesium lead halide perovskites ($CsPbX_3$) with X being a bromide or chloride atom. The crystal structure of lead halide perovskites can be described as a three-dimensional arrangement of corner-sharing $(PbX_6)^{-4}$ octahedra and is represented in Fig 1.8 **a)** and **b)**.

Lead halide perovskites exhibit a distinct band-edge electronic structure compared to conventional direct band-gap semiconductors like $CdSe$ and InP. They possess an opposite ordering of band-edge states in the sense that they have a s-like valence band and p-like conduction band, unlike semiconductors with zinc-blende and wurtzite crystal phases possessing a p-like valence band and s-like conduction-band states. Thus, in lead halide perovskites, the spin-orbit coupling happens in the conduction band rather than the valence band. This unique band-edge arrangement sets perovskites apart and plays a significant role in their optoelectronic properties.

In this type of structure, the octahedra can rotate and tilt to stabilize the crystal lattice. The cubic crystal phase called α and noted (000) in Glazer notation [47] shows no tilt of the octahedra. The tetragonal phase β possesses an octahedral tilt along the z-axis with an amplitude a, and is noted $(00a^+)$. The orthorhombic phase γ adds to the β structure two antiphase tilts on the x and y axis with amplitude b and is noted $(b^-b^-a^+)$. These different tilts have an important impact on the level of symmetry in these systems and are represented in Fig. 1.8 **c)**.

These three crystallographic phases exist depending on the temperature and the crystal growth process. $CsPbX_3$ has been observed in cubic phase (0_h point group) at high temperature, and in tetragonal phase (D_{4h} point group) and orthorhombic phase (D_{2h} point group) at low temperature. The crystal structure of $CsPbX_3$ nanocrystals is still under investigation and potentially depends on the size and shape of the nanocrystal in addition to the temperature [48, 49].

The electronic band structure of bulk $CsPbX_3$ has been theoretically addressed using density-functional theory (DFT) [50, 51, 52]. The atomic orbitals of lead and halide atoms play a predominant role in the construction of this band structure, with the valence and conduction bands being characterized by the hybridization of these orbitals as shown in Fig. 1.9.

Four-band model

The band edge structure in bulk $CsPbX_3$ can be described in the effective mass model. In a first approximation, the crystal lattice is considered as cubic. Calculated band structures of $CsPbX_3$ reveal that the band edge is situated at the R-point of the first Brillouin zone. The following model is based on the isomorphism of the Γ-point to the R-point in the Brillouin zone for cubic

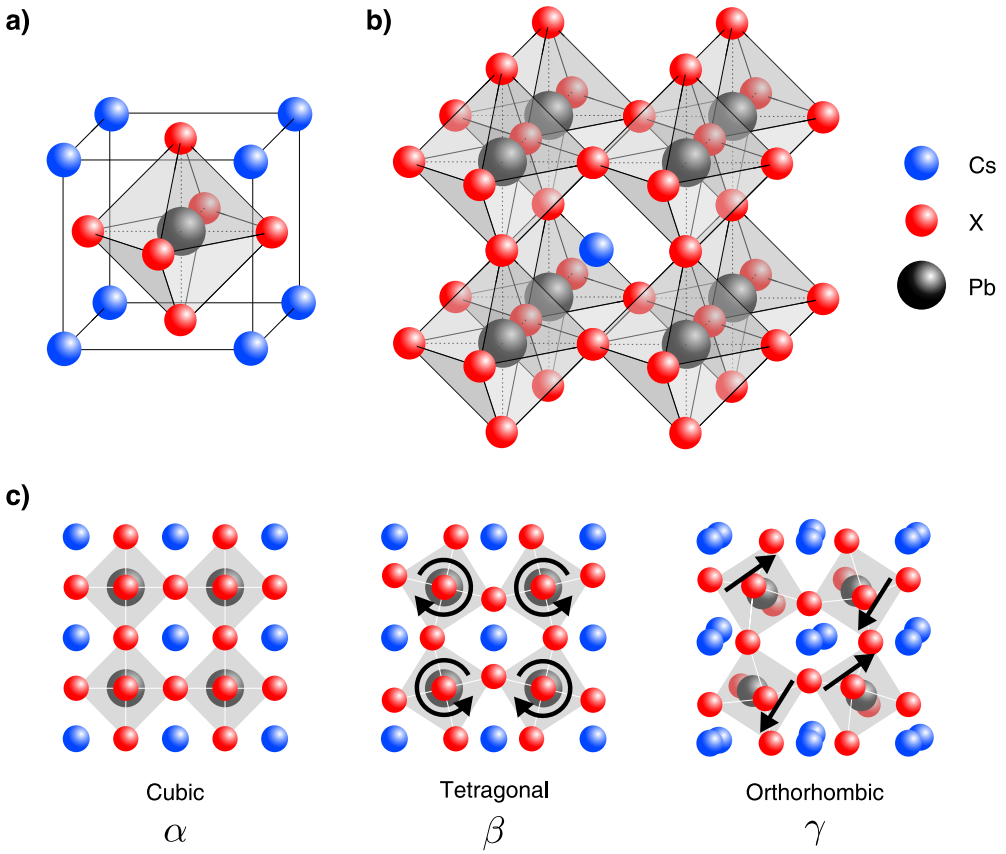

Figure 1.8: Illustration of the crystal structure of $CsPbX_3$ perovskites **a)** in a cubic unit-cell and **b)** with a representation of the corner-sharing $(PbX_6)^{-4}$ octahedra. **c)** Top view of the octahedral network in the cubic, tetragonal and orthorhombic phases showing the octahedral tilting.

semiconductors [38]. Therefore, the R-point can be depicted as the Γ-point, using the eight by eight $k.p$ Hamiltonian matrix introduced earlier in this chapter to describe the dispersion of electrons and holes. The large spin-orbit coupling present in these semiconductors enables the extraction of the four-by-four matrix section associated with the upper valence band and lower conduction bands which significantly simplifies the model [51].

Conduction band

The conduction band of lead halide perovskites comes from the hybridization of the Pb $6p$ orbitals and s orbital of the halide, as represented in Fig. 1.9. This band is affected by strong spin-orbit coupling, splitting the levels into an upper band with a total angular momentum $J_e = 3/2$ with projection $J_z = \pm 3/2$ and $J_z = \pm 1/2$ called, respectively, heavy electron (he) and light electron (le) bands in analogy with the $CdSe$ model, and the lowest split off (so) conduction band doubly degenerate with $J_e = 1/2$. These levels are represented in Fig. 1.10. Due to the p symmetry of the conduction band, there are three orthogonal spatial components (X, Y, Z) for the corresponding Bloch functions. The spin-orbit coupling mixes these three components and the electron Bloch wavefunctions of the conduction band can be written:

$$\begin{aligned} |\Uparrow\rangle_e &= -\frac{1}{\sqrt{3}}\left[(|X\rangle + i\,|Y\rangle)\,|\downarrow\rangle + |Z\rangle\,|\uparrow\rangle\right] \\ |\Downarrow\rangle_e &= \frac{1}{\sqrt{3}}\left[|Z\rangle\,|\downarrow\rangle - (|X\rangle - i\,|Y\rangle)\,|\uparrow\rangle\right] \end{aligned} \tag{1.41}$$

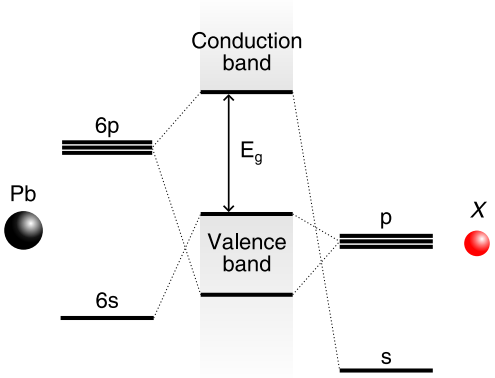

Figure 1.9: Schematic of the hybridization of orbitals of a lead atom with a halide atom leading to the construction of the band-edge structure in lead halide perovskites. The conduction band is constructed from the $6p$ orbital of the lead atom with the s orbital of the halide atom. The valence band is constructed from the hybridization of the $6s$ orbital of the lead atom and the p orbital from the halide atom.

Valence band

The valence band comes from the antibonding hybridization of the Pb $6s$ orbital and the halide p orbital. It has a s-like symmetry with total angular momentum $J_h = 1/2$. The holes' Bloch wavefunctions are simply described by:

$$\begin{aligned} |\uparrow\rangle_h &= |S\rangle\,|\uparrow\rangle \\ |\downarrow\rangle_h &= |S\rangle\,|\downarrow\rangle \end{aligned} \tag{1.42}$$

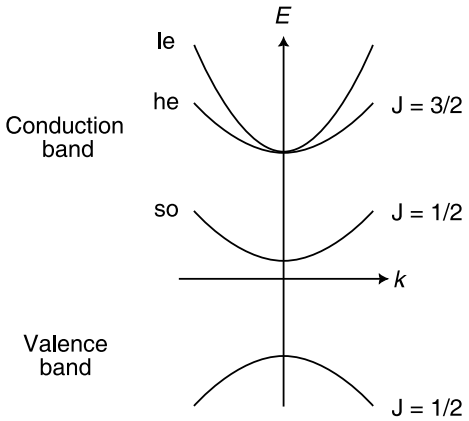

Figure 1.10: Band structure of lead halide perovskite nanocrystals. *le* is the light electron, *he* the heavy electron and *so* the split-off band.

Band-edge exciton

The band-edge exciton is a paired hole in the upper valence band with an electron from the lowest split-off conduction band. In perovskites, it is therefore formed from a hole with angular momentum $J_h = 1/2$ and an electron in a spin-orbit split-off state with angular momentum $J_e = 1/2$ linked by Coulomb interaction, which results in a four-fold degenerate exciton level,

with the following Bloch functions:

$$\begin{aligned} |\Psi_{0,0}\rangle &= \frac{1}{\sqrt{2}}\left(|\Downarrow\rangle_e |\uparrow_h\rangle - |\Uparrow\rangle_e |\downarrow\rangle_h\right) \\ |\Psi_{1,0}\rangle &= \frac{1}{\sqrt{2}}\left(|\Downarrow\rangle_e |\uparrow_h\rangle + |\Uparrow\rangle_e |\downarrow\rangle_h\right) \\ |\Psi_{1,-1}\rangle &= |\Downarrow\rangle_e |\downarrow\rangle_h \\ |\Psi_{1,+1}\rangle &= |\Uparrow\rangle_e |\uparrow\rangle_h \end{aligned} \tag{1.43}$$

The resulting exciton wavefunctions $\Psi_{i,j}$ in a perovskite nanocrystal can be written as the product of the Bloch functions and the envelope function $v(r_e, r_h)$ [51].

Electron-hole exchange interaction

The electron-hole exchange interaction expression is given equation 1.24. For lead-halide perovskites, in the case of a cubic-shaped nanocrystal with a cubic crystal structure, it lifts the degeneracy of the exciton states into a dark ground singlet state $J = 0$ and a bright triplet $J = 1$ with projection $J_z = 0, \pm 1$ along the z-axis. The energy diagram of lead halide perovskite nanocrystals is represented in Fig. 1.11. The energy splitting between the singlet and triplet levels can be expressed [51]:

$$\Delta_{BD} = 4\alpha_{exch}\Omega_0 \int d^3 r v^2(r, r) \tag{1.44}$$

This expression shows a direct link between a stronger spatial confinement and the enhancement of the splitting. The sign of the exchange constant α_{exch} determines the level ordering between triplet and singlet: lead halide perovskites present a strong spin-orbit coupling in the conduction band thus α_{exch} is negative and the singlet exciton state is the lowest.

Splitting of the exciton fine structure

Similar to the model of the exciton fine structure for $CdSe$ and InP nanocrystals, symmetry breaking in both the crystal structure and nanocrystal shape can lift the degeneracy of the exciton levels, resulting in up to four distinct energy levels for the exciton, as represented in Fig 1.11.

The splitting of the bright exciton in inorganic cesium lead halide perovskites nanocrystals has been theoretically addressed by considering the anisotropy of their shape and their crystal structure [53, 54]. As represented in Fig. 1.11, a tetragonal crystal field would split the bright triplet energy level into a singlet state 0_{B} and a doublet state ± 1, while an orthorhombic crystal field would fully split the bright triplet into the X, Y and Z states.

Rashba effect

Semiconductors usually present non-optically active lowest energy sublevels. Consequently, at low temperatures, when the dark state is predominantly populated, the photoluminescence signal is low.

Nevertheless, the first photoluminescence measurements obtained from cesium lead-halide perovskite nanocrystals (such as $CsPbI_3$, $CsPbBr_3$, $CsPbCl_3$) have revealed that they are bright down to low temperatures, where their lifetimes are short [51, 55]. To explain this phenomenon, a hypothesis has been put forth suggesting that the lowest energy state in perovskite nanocrystals was, in fact, the bright triplet level with $J = 1$, as the existence of a dark state had yet to be observed experimentally [51, 56]. This inversion in the energy levels order would be justified by the presence of a strong Rashba effect, which would further split the sublevels and reverse

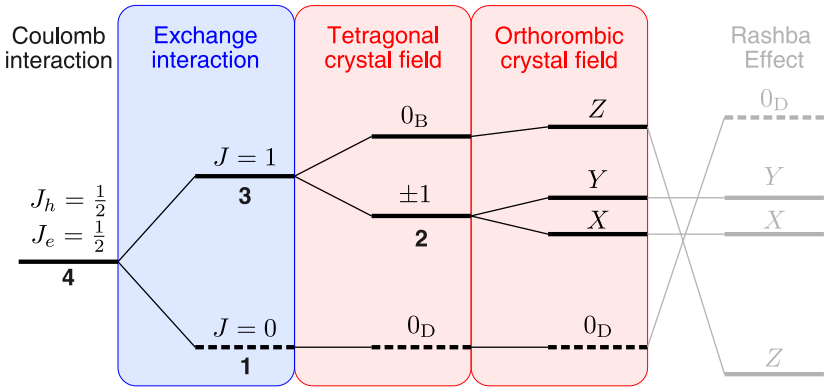

Figure 1.11: Energy level diagram of the band-edge exciton fine structure of lead halide perovskite. The energy levels are split by the exchange interaction and the crystal field asymmetry. The non-optically active state is represented with dotted lines. The hypothetical Rashba effect would reverse the order of the energy levels as represented in grey.

the singlet/triplet order as represented in grey in Fig. 1.11. This effect would be due to a symmetry breaking of the polar lattice, which could be related to non-symmetric cation position instabilities at the nanocrystal surface [51], but has never been demonstrated experimentally and has been much discussed in the scientific community in recent years [57]. Lately, the dark state 0_D has been observed experimentally for formamidinium lead bromide ($FAPbBr_3$) and cesium lead iodide ($CsPbI_3$) perovskites, demonstrating that the Rashba effect has a small impact on the exciton level order and confirming that the ground exciton state is a dark singlet state for those two coumpounds [58, 59]. Nevertheless, the debate over the bright-dark level ordering was still alive at the start of my thesis, in the absence of signature of the dark singlet in $CsPbBr_3$ perovskites, the compound most studied theoretically and experimentally.

1.2 Optical properties of semiconductor nanocrystals

The discretization of exciton energy levels in semiconductor nanocrystals makes them good candidates as tunable light emitters. The following part describes their characteristic optical properties.

1.2.1 Recombination dynamic of the exciton

Photoluminescence spectra of semiconductor nanocrystals are directly linked to the oscillator strength of exciton states, as their photoluminescence comes from the recombination of the band-edge exciton.

Transition oscillator strengths

The electron-hole exchange interaction directly impacts the optical transition probabilities of exciton states. In the case of $CdSe$ and InP, the states $F = \pm 2$ are optically passive as absorbed photons cannot have an angular momentum of ± 2. For other states, the probability P_F of optical transition from an exciton state F is proportional to the square of the matrix element of the polarization vector of the emitted or absorbed light e, and the electric dipole momentum operator $\hat{p}$, between the wavefunctions of the exciton state $|\Psi_F\rangle$ and the vacuum state $|0\rangle = \delta(\boldsymbol{r_e} - \boldsymbol{r_h})$ [35]:

$$P_F = |\langle 0|\boldsymbol{e}\hat{\boldsymbol{p}}|\boldsymbol{\Psi}_F\rangle|^2 \tag{1.45}$$

This equation provides the transition probability from each state of the exciton fine structure. In the case where the excitation is linearly polarized light, for $CdSe$ nanocrystals with a hexagonal crystal lattice, the oscillator strengths are given by the following expressions:
for $F = 0$

$$\begin{aligned} P_0^{\mathrm{U}} &= |\langle 0|\boldsymbol{e}\hat{\boldsymbol{p}}|\boldsymbol{\Psi}_0^{\mathrm{U}}\rangle|^2 = N_0^{\mathrm{U}} cos^2(\theta) = \frac{4KP^2}{3} cos^2(\theta) \\ P_0^{\mathrm{L}} &= |\langle 0|\boldsymbol{e}\hat{\boldsymbol{p}}|\boldsymbol{\Psi}_0^{\mathrm{L}}\rangle|^2 = N_0^{\mathrm{L}} cos^2(\theta) = 0 \end{aligned} \tag{1.46}$$

for $F = \pm 1$

$$\begin{aligned} P_{\pm 1}^{\mathrm{U}} &= |\langle 0|\boldsymbol{e}\hat{\boldsymbol{p}}|\boldsymbol{\Psi}_1^{\mathrm{U}}\rangle|^2 = N_1^{\mathrm{U}} sin^2(\theta) = \left(\frac{2\sqrt{f^2+d} - f + \sqrt{3d}}{6\sqrt{f^2+d}}\right) KP^2 sin^2(\theta) \\ P_{\pm 1}^{\mathrm{L}} &= |\langle 0|\boldsymbol{e}\hat{\boldsymbol{p}}|\boldsymbol{\Psi}_1^{\mathrm{L}}\rangle|^2 = N_1^{\mathrm{L}} sin^2(\theta) = \left(\frac{2\sqrt{f^2+d} + f - \sqrt{3d}}{6\sqrt{f^2+d}}\right) KP^2 sin^2(\theta) \end{aligned} \tag{1.47}$$

with θ the angle between the polarization vector of propagation light and the axis of the crystal, P the Kane interband matrix element and K the square of the overlap integral depending only on β, as defined in Ref. [36]. Based on these equations, it is explicit that the probability of having an optical transition occurring from the lower $F = 0$ exciton state is equal to zero, indicating that this state is always non-optically active.

Dark exciton state in $CdSe$ and InP

The lower exciton state in InP and $CdSe$ (0^{L} or ± 2) is, therefore, always non-optically active. However, radiative recombination from these states can still occur through some intermediate processes. For instance, a dark state can be brightened through optical phonon-assisted transitions. In this case, the polarization properties of the ground exciton state will be influenced by the angular momentum of the phonons involved in the transitions. The ground exciton state can also become radiative under an external magnetic field; the dark state can then potentially mix with an optically active state, which allows direct recombination from the dark exciton state, as shown in section 1.1.7.

The dark nature of the exciton ground state is at the origin of the long lifetime component ($\sim 1\,\mu s$) observed for $CdSe$ at cryogenic temperature [60], which is explained by the relaxation of the exciton into the dark ground state through less efficient phonon-assisted transition, leading to a long emission lifetime.

Dark exciton state in lead halide perovskites

In lead halide perovskites, the calculation of the transition-dipole matrix element between the lowest exciton singlet level 0_D and the vacuum state also shows that the lowest exciton state is non-optically active [51]. The transition-dipole matrix element $\hat{p}$ only acts on the conduction

band:

$$\begin{aligned}\langle 0|\hat{p}|\Psi_{0,0}\rangle &= \int d^3r \frac{1}{\sqrt{2}}\Big((\hat{\mathcal{K}}|S\rangle|\uparrow\rangle)\hat{p}\frac{1}{\sqrt{3}}[|Z\rangle|\downarrow\rangle - (|X\rangle - i|Y\rangle)|\uparrow\rangle] \\ &\quad -(\hat{\mathcal{K}}|S\rangle|\downarrow\rangle)\hat{p}\left(-\frac{1}{\sqrt{3}}[(|X\rangle + i|Y\rangle)|\downarrow\rangle + |Z\rangle|\uparrow\rangle]\right)\Big) \\ &= \frac{1}{\sqrt{6}}\int d^3r\,(\langle S|\langle\downarrow|\hat{p}[|Z\rangle|\downarrow\rangle - (|X\rangle - i|Y\rangle)|\uparrow\rangle] \\ &\quad +\langle S|\langle\uparrow|\hat{p}\,(-[(|X\rangle + i|Y\rangle)|\downarrow\rangle + |Z\rangle|\uparrow\rangle])) \\ &= \frac{1}{\sqrt{6}}\int d^3r\,(\langle S|\hat{p}|Z\rangle - \langle S|\hat{p}|Z\rangle) \\ &= 0\end{aligned} \tag{1.48}$$

with $\mathcal{K}$ the time reversal operator: $\hat{\mathcal{K}}\,|\uparrow\rangle = |\downarrow\rangle$ and $\hat{\mathcal{K}}\,|\downarrow\rangle = -\,|\uparrow\rangle$.
Equivalent calculations on the three states of the exciton triplet X, Y, Z give a nonzero solution, confirming that they are optically active.

1.2.2 Recombination from other complexes of charge

The optical excitation of a nanocrystal can lead to the formation of complex of charges other than the exciton. To correctly interpret the photoluminescence spectra coming from a single nanocrystal, one must also consider the emission from trions and biexcitons, which all exhibit distinct spectral signatures.

Trions

The presence of an additional charge in a nanocrystal gives rise to an excited state called trion. It can be formed when an exciton is created in the presence of an unpaired charge carrier in the core of the nanocrystal and a charge carrier trapped at its surface or in a lattice defect. It consists of two holes in the valence band and one electron in the conduction band (positive trion X^+) or one hole in the valence band and two electrons in the conduction band (negative trion X^-).

In the case of a negative trion, the lowest energy state is composed of two electrons of opposite spin and a hole with two possible spin orientations. The total angular momentum is set by that of the unpaired electron (unpaired hole for X^+). Consequently, the system is composed of a hole interacting with a spin singlet electron pair without exchange interaction of the complex of charges. With no splitting of its states coming from exchange interaction, in the absence of magnetic fields, the trion emission is characterized by a unique emission line on the photoluminescence spectra of a single nanocrystal.

Applying an external magnetic field will cause a Zeeman spin-splitting of the trion states [61]. In the case of $CdSe$ and InP, the trions states split into four levels under a magnetic field of amplitude B, as represented in Fig. 1.12. The four possible transitions lead to a quadruplet on the photoluminescence emission spectra. These four levels are shifted in energy by $\Delta_{\text{trion}} = (\pm g^e \pm g^h)\mu_{\text{B}}B$ from the zero-field trion line [61], with g^e and g^h the g-factor of the electron and hole, respectively. The specific case of trions in lead halide perovskite nanocrystals will be discussed in Chap. 4.

The study of trions emissions is an interesting tool to investigate single charge-carrier spin properties. In particular, the splitting in the magneto-optical spectra of a trion allows direct measurements of both the electron and hole g-factors. The energy of the negative trion is given by:

$$E_{X^-} = E_X + E_{1e} + E_{bX^-} \tag{1.49}$$

where E_{1e} is the energy of a single confined electron, E_X is the energy of the exciton, and E_{bX^-} is the binding energy of the negative trion.

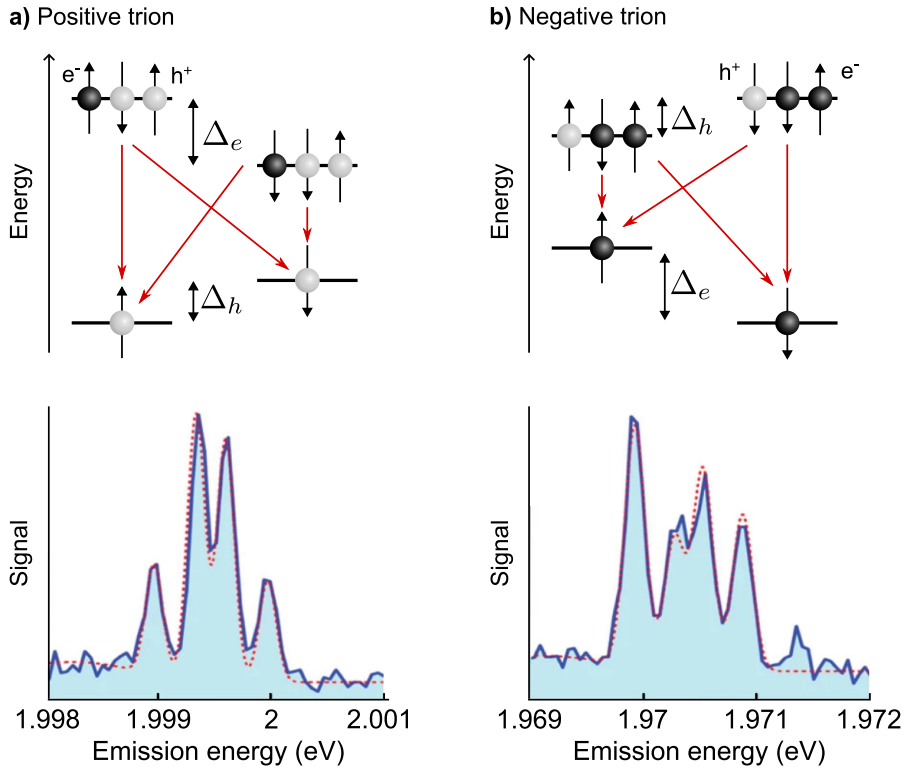

Figure 1.12: Relaxation schemes of **a)** a positive trion and **b)** a negative trion under an external magnetic field of 7 T. Red arrows show the four possible recombination paths. The resultant four-peak spectrum is shown below in the case of $CdSe$. Adapted from Ref. [62].

Biexciton

Another type of quasiparticle appearing in nanocrystals when subjected to optical excitation is the biexciton (XX). It involves the interaction of two electrons and two holes, as it couples two excitons. The recombination from a biexciton leads to the formation of an exciton and the emission of a photon. Notably, the energy carried by this emitted photon is distinct from that produced by exciton recombination due to the influence of the biexciton binding energy E_{bXX}. The energy of a biexciton is therefore given by:

$$E_{XX} = 2E_X - E_{bXX}. \tag{1.50}$$

The probability of forming a biexciton increases with the density of exciton existing in the nanocrystal. Consequently, these complexes are more likely to appear under high laser excitation.

Louyer et al. [63] have studied biexciton emission depending on excitation intensity in the case of $CdSe/ZnS$ nanocrystals. Their results are represented in Fig. 1.13. The integrated intensity of the biexciton emission lines is linearly dependent on the excitation intensity, while for the excitons, it saturates at high intensity as displayed in Fig. 1.13 **b)**. The photoluminescence signal integrated over the full emission spectrum scales linearly with the excitation intensity, as shown in Fig. 1.13 **c)**. A similar evolution has been observed in Ref. [64] for $CdSe/CdS$ core/shell nanocrystals.

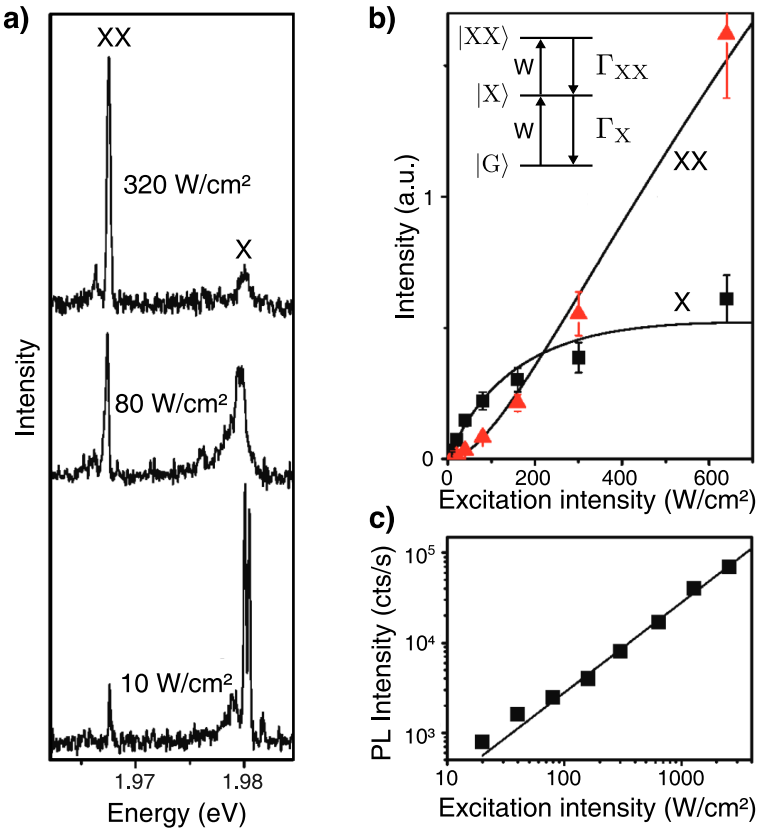

Figure 1.13: **a)** Photoluminescence spectra of a single nanocrystal at 2 K for three different excitation intensities, showing the emission peak coming from the exciton (X) and biexciton (XX). **b)** Integrated intensities of the exciton (black squares) and biexciton (red triangles) as a function of the excitation intensity. **c)** Evolution of the total photoluminescence intensity as a function of excitation intensity. Figure from Ref. [63].

The study of biexcitons is particularly interesting as they display a two-photon cascade emission; they could be used as sources of pairs of correlated photons [65].

1.2.3 Spectral diffusion

When single nanocrystals are optically excited, they often exhibit a photophysical phenomenon known as spectral diffusion. This phenomenon is characterized by a random dynamic shifting of a spectral line. Depending on the acquisition time, spectral diffusion can cause broadening of the photoluminescence line, leading to deviations from theoretical linewidth values. This phenomenon has been mainly studied for $CdSe$ nanocrystals [66, 67, 68] and is attributed to a combination of two mechanisms. The first source is a fluctuation of the electric field in the local environment of the nanocrystal, inducing a shift of the band edge spectra due to the Stark effect [66]. Spectral diffusion can also be thermally assisted and activated by the release of excess excitation energy following the absorption of a photon. In this case, the spectral diffusion strongly depends on excitation power and wavelength [67].

The stability of the spectral peak position has been studied using resonant photoluminescence excitation by Fernée et al. [69]. The fast spectral diffusion process observed in single nanocrystals is attributed to spontaneous local charge fluctuation within the environment surrounding the nanocrystal after excitation.

Spectral diffusion takes part in the causes for nanocrystal spectral instability, which makes it prejudicial for potential applications of semiconductor nanocrystals in quantum technologies.

However, it does not affect the photon's indistinguishability.

1.2.4 Blinking and Auger effect

Even with constant excitation, we experimentally observe emission intermittency in the photoluminescence of individual nanocrystals. This phenomenon is called photoluminescence blinking and was first reported for $CdSe$ nanocrystals in 1996 [70]. Photoluminescence blinking results from a random process of charging and discharging under constant illumination. If the nanocrystal is charged, the extra carrier triggers a process known as nonradiative **Auger recombination**. In the case of semiconductor nanocrystals, the Auger process refers to various non-radiative relaxation processes of the charge complexes, depicted in Fig. 1.14. Because the rate of Auger recombination is faster than the rate of radiative recombination, this process leads to a reduction in the photoluminescence quantum yield. The Auger recombination lifetime decreases significantly with decreasing nanocrystal size, following a cubic dependence on the nanocrystal radius [71].

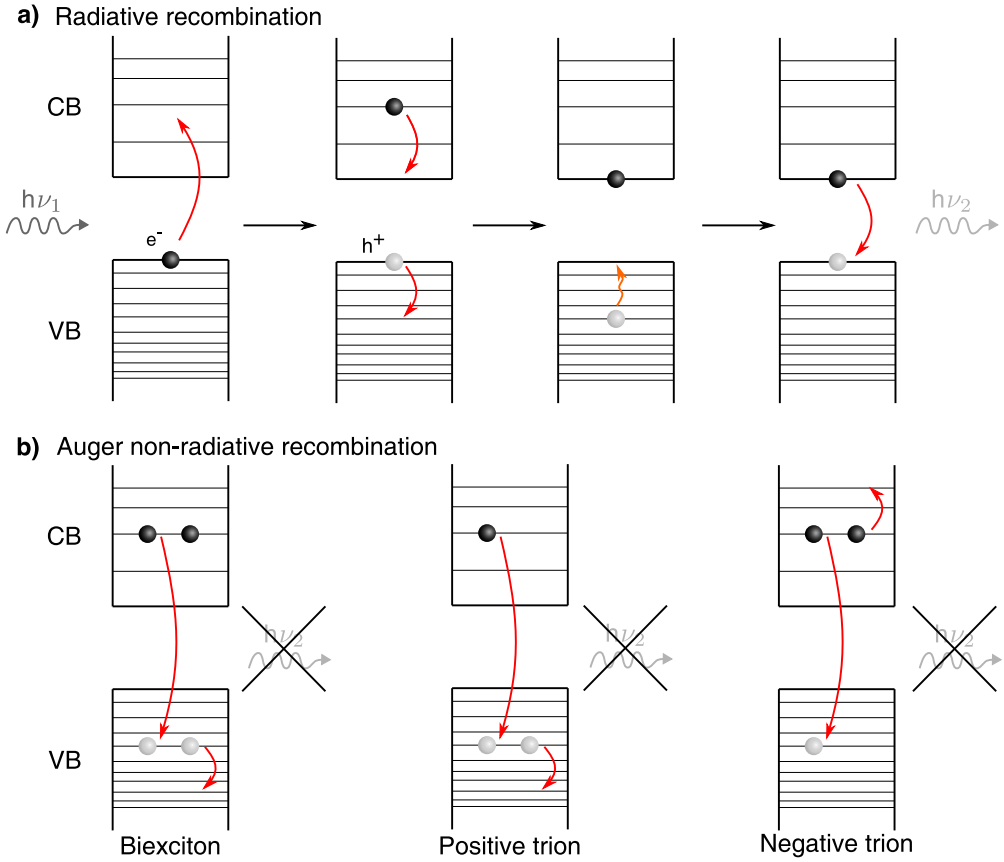

Figure 1.14: a) Relaxation process of an exciton in a nanocrystal with radiative recombination. **b)** Non radiative Auger recombinations of a biexciton (multi excitonic Auger process), a positive trion and a negative trion.

Numerical computations have shown that the abruptness of the confinement potential is an aggravating factor for photoluminescence efficiency. As derived in Ref. [72], using Fermi's golden rule, the rate of the nonradiative Auger recombination for a final hole state is given by:

$$\frac{1}{\tau_{\mathrm{A}}} = \frac{2\pi}{\hbar} \int |M_{\mathrm{if}}|^2 \delta(E_{\mathrm{i}} - E_{\mathrm{f}}) d\mathcal{R}_{\mathrm{f}} \tag{1.51}$$

$E_{\mathrm{i,f}}$ are the initial and final energies of the system, $\mathcal{R}_{\mathrm{f}}$ is the complete set of variables quantifying

the final state of the system and $M_{i,f}$ the electronic transition matrix element of the Coulomb interaction. The main contribution to $M_{i,f}$ is given by the spatial frequency component k_f. As a result, the Auger rate is directly linked to the square of the Fourier amplitude of the initial ground state, which is assessed at the spatial frequency of the final excited state. Smoothing out the confinement within confined structures would decrease the high spatial frequency components in the ground states, which would reduce the Auger rate.

Furthermore, a reduction of the blinking phenomenon has also been documented when increasing the shell thickness of $CdSe/CdS$ core/shell quantum dots [73] as discussed in the following section.

1.2.5 Core/shell nanocrystals

When exciting semiconductor nanocrystals, all the absorbed photons do not lead to an emitted photon due to the different types of nonradiative recombination. The quantum yield of a sample of nanocrystals quantifies the conversion efficiency and corresponds to the ratio of the number of emitted photons to the number of absorbed photons.

To improve the quantum yield and optical properties of semiconductor nanocrystals, one solution is to eliminate surface trapping by embedding the nanocrystal in a shell made of another semiconductor material, forming a core-shell system. There are three categories of core-shell systems depending on the alignment of electronic bands between the core and shell layers as represented in Fig. 1.15.

- **Type I:** In this structure, the shell semiconductor has a wider bandgap than the core. The electron and hole wavefunctions are confined in the core region which reduces the non-radiative processes and improves the quantum yield. It is used, for instance, in the case of $CdSe/ZnS$ [74] and InP/ZnS [75] nanocrystals.

- **Type II**: In this second case, the band alignment between the core and shell is staggered, which partially or entirely spatially separates the hole and electron wavefunctions between the shell and the core of the nanocrystal. As a result, the quantum confinement of the two charges is reduced, leading to a redshift in the photoluminescence emission of the nanocrystal. This configuration also extends the lifetime of excitons. This structure finds application in systems like $CdTe/CdSe$ and $CdSe/ZnTe$ [76].

- **Reverse Type I (or quasi-type II):** In this third case, the shell semiconductor has a smaller bandgap than the core material. Both hole and electron wavefunctions partially or completely delocalize over the shell region. This may facilitate efficient charge transfer to an aqueous medium [77], and can be used in optoelectronic applications such as switchers [78].

This core-shell method has already shown good results in increasing the quantum yield of nanocrystals [79], suppressing non-radiative Auger recombinations and reducing blinking [80, 73]. Core-shell systems are also used to prevent exciton-surface-phonon interaction in order to reduce emission line broadening [81].

Lead halide perovskites usually display a high photoluminescence quantum yield without the requirement of a shell. They possess abundant native defects due to the low energy of their formation, but these defects do not severely affect their photophysics [82]. For instance, the defects with the lower energy of formations in perovskites are vacancies. In $CsPbBr_3$ nanocrystals, a common vacancy occurs on the cesium site; however, as cesium orbitals do not contribute to the near band-edge electronic structure, these vacancies do not influence

the photoluminescence properties of $CsPbBr_3$. Similarly, vacancies on the halide site are not prejudicial to the electronic properties since the corresponding non-bonding lead orbitals are resonant with the conduction and the valence bands [83]. The high defect tolerance of perovskite nanocrystals is one of the characteristics that makes them particularly attractive for diverse applications. While they still have defects inducing nonradiative recombination, the need for extensive passivation is less demanding than for $CdSe$ or InP nanocrystals.

However, perovskite nanocrystals face other instability issues that make their surfaces environmentally vulnerable and can lead to nanocrystal decomposition or transformation. Among these issues, they can undergo surface ligand cleavage, increasing their tendency to disassemble when exposed to polar or proton-donating solvents. Furthermore, using weak protic or polar anti-solvents during purification processes can weaken surface-ligand bonds, resulting in colloidal decomposition. To address these challenges, a shell can act as a physical environmental barrier, preventing interactions between nanocrystals and solvents. However, it is worth noting that research in this area is relatively recent. So far, only limited attempts have succeeded in designing core/shell perovskite structures that leads to an enhancement of the material stability [84].

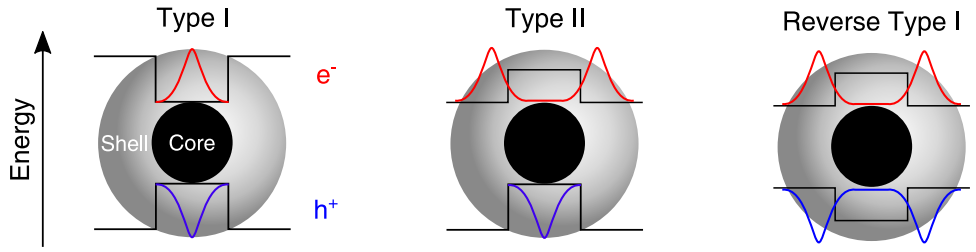

Figure 1.15: Scheme representing the different types of core-shell structures for semiconductor nanocrystals. The red curve represents the wavefunction of the electron and the blue curve represents the wavefunction of the hole. In type I, both the electron and hole wavefunctions are confined in the core of the nanocrystal. In type II, the electron wavefunction is displaced in the shell. In reverse type I, both wavefunctions are in the shell. Scheme adapted from Ref. [85].

1.3 Phonons in nanocrystals

Exciton-phonon interactions are essential to consider in the study of optical properties of semiconductor nanocrystals, as they strongly impact their photoluminescence emission spectra. Interactions with phonons are at the origin of a broadening of the exciton absorption and emission spectra and cause thermal mixing between the exciton fine structure states. Besides governing the emission line broadening of semiconductor nanocrystals, phonon scattering is among the factors setting a fundamental intrinsic limit to the mobility of charge carriers in these materials [86].

In this section, we present the notion of phonons in the framework of bulk crystals and extend it to semiconductor nanocrystals, using the example of $CsPbBr_3$ nanorods.

1.3.1 Lattice vibration in a crystal

In bulk crystals, atoms undergo continuous oscillations around their equilibrium positions on lattice sites. These oscillations increase in amplitude with rising temperature. For a crystal composed of N elementary cells and n atoms in each cell, there are $3nN$ normal modes corresponding to the degree of freedom of all particles, including vibration, rotation, and translation modes. Any crystal state can be described as a superposition of these normal modes. Phonons

are quasi-particles characterizing the vibrational states of a lattice and their interaction with other particles [87].

1.3.2 Types of phonons

There are two main phonon types in a solid, represented in Fig. 1.16:

Acoustic phonons are commonly associated with sound waves propagating within a lattice, representing a coherent movement of atoms out of their equilibrium positions. Longitudinal phonon modes (abbreviated as LA) refer to a displacement direction of atoms aligned with the wave propagation, while transverse modes (abbreviated as TA) occur when the displacement direction is perpendicular to the wave propagation. Acoustic phonons have small frequencies compared to phonon energies for small wave numbers. Due to this energy mismatch, they do not interact with light. However, they can interact with electronic excitation.

Optical phonons are vibrational modes in which neighboring positive and negative ions within a lattice undergo periodic motion towards and away from each other, resulting in an oscillating electric dipole moment. These modes exhibit polarization-dependent interactions with light and can be easily excited by infrared light in ionic solids, which makes them active in Raman spectroscopy. Similar to acoustic phonons, one can define longitudinal (LO) and transverse (TO) optical phonon modes.

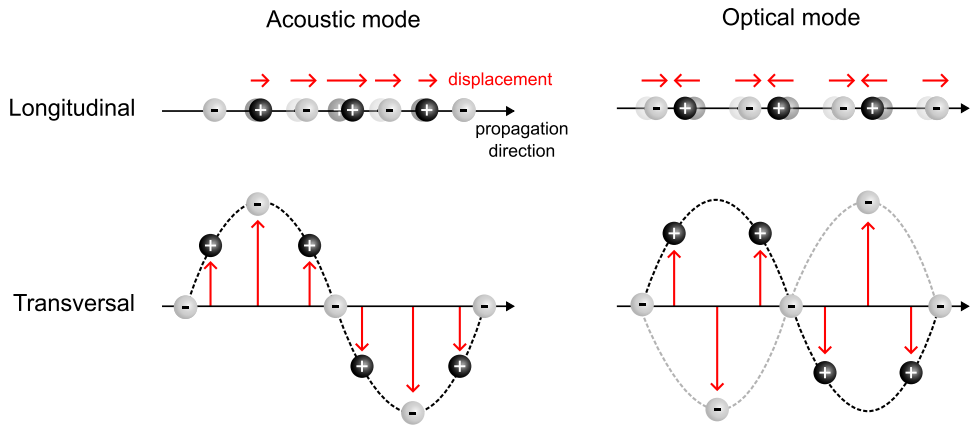

Figure 1.16: Schematic view of acoustic and optical phonon modes.

1.3.3 Phonons behavior in nanoscale crystals

When the size of a nanocrystal is much larger than the lattice period, the properties of nanocrystal lattices do not display significant divergences from bulk crystal properties. In fact, as phonon modes are directly linked to the motion of the different atomic bonds in the crystal, their energies depend only on the chemical composition of the nanocrystal and should not be dependent on its size or shape. Each semiconductor will have characteristic phonon modes with distinct impacts on the exciton recombination dynamics.

However, one disparity between bulk crystals and nanocrystals is the finite nature of the crystal structure at the surface of the particle, leading to the introduction of a third type of phonon called **surface phonons**. Surface phonon modes can couple with charge carriers and affect nanocrystal properties. For instance, a study of surface phonons in $CdSe$ nanocrystals

showed that decreasing nanocrystal sizes increases the surface phonon vibration frequency, having a direct impact on their interactions with electrons [88]. This frequency shift originates from constructive interaction between positive phonon dispersion and lattice contraction.

1.3.4 Phonon bottleneck

Optical phonon bottleneck

Another difference between phonons in bulk crystals and nanocrystals is the phonon bottleneck effect. In bulk crystals, the absorption of a photon of energy $\hbar\omega$, higher than the band gap energy, will lead to the relaxation of an electron accompanied by the emission of phonons, dissipating the excess energy. This recombination process will produce an exciton with an energy independent of the excitation energy.

When the electron energy levels are discretized, the splitting between these levels increases as the nanocrystal size decreases. If the spacing between low-lying levels surpasses typical LO phonon energies, transitions between quantum size levels would occur only through multi-phonon emission, an inefficient process that may slow electron relaxation. For instance, in the case of InP nanocrystals with a size of 26 Å, the energy gap between the first and second electron levels is 410 meV. Given that the energy of an LO phonon in InP is 43 meV, the energy separation corresponds to 10 LO phonon energies [89]. This phenomenon, known as **phonon bottleneck**, is illustrated in Fig. 1.17. Phonon bottleneck could severely affect the electronic and optical properties of nanocrystals.

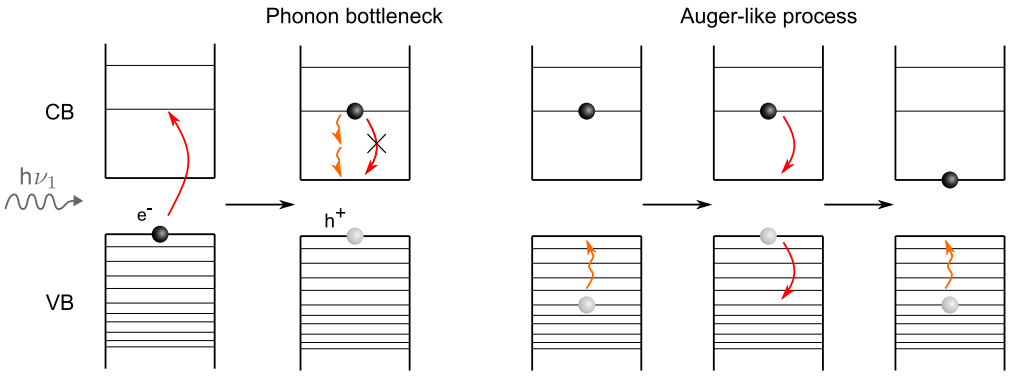

Figure 1.17: Phonon bottleneck and Auger-like relaxation processes.

However, one of the first studies on time-resolved spectroscopy of $CdSe$ nanocrystals showed no optical phonon bottleneck effect, as reported by Woggon (1996) [90]. In this case, the relaxation has been attributed to an Auger-like relaxation mechanism: the electron-hole Coulomb interaction strengthens in smaller structures, and hole-level spacings are smaller than electrons due to the higher effective mass of the hole and the degeneracy of the valence band. Consequently, exciton recombination can occur through an Auger-like process where the excess energy of the electron is transferred to the hole via strong Coulomb coupling. The hole then quickly relaxes through its dense spectrum of states, as illustrated in the right part of Fig. 1.17. This mechanism effectively removes the phonon bottleneck issue in most nanostructures [91].

Nevertheless, the Auger process is inhibited if the hole becomes trapped at the surface of the nanocrystals. In that case, the phonon bottleneck effect can manifest, resulting in slow electron relaxation. This phenomenon has been, for instance, observed for $CdSe$ [92] and InP [89] nanocrystals. In both cases, experimental results indicate a reduction in the electron relaxation

rate by around one order of magnitude when the hole is either absent or trapped at the surface of the structure.

Acoustic phonon bottleneck

Acoustic phonon bottlenecks can also be observed in some nanostructures. In 2012, Fernée et al. showed evidence of an acoustic phonon bottleneck that inhibits spin relaxation in $CdSe$ nanocrystals [62]. Their experimental results show that the acoustic phonon-mediated spin relaxation depends finely on the magnitude of Zeeman splitting, with an onset having a well-defined threshold. For small Zeeman splittings, relaxation between two spin states via the emission of a single acoustic phonon would violate energy conservation, leading to an acoustic phonon bottleneck.

In the case of perovskite nanocrystals, an acoustic phonon bottleneck has been observed for $FAPbI_3$ nanocrystals by Fu et al. in 2018 [93]. Lead halide perovskites are structurally soft semiconductors with a phonon glass character, having their whole acoustic vibrational density of states located at low energies (in the meV range). This weakens the interactions of charge carriers with acoustic phonons, impacting their relaxation and mobility. Moreover, as an acoustic wavelength cannot exceed the nanocrystal size, acoustic phonons with energies lower than 0.5 meV cannot develop in $FAPbI_3$ nanocrystals with a 10 nm size, which blocks the contribution of acoustic phonons to the thermal mixing between fine structure states separated by a few hundreds of μeV.

1.3.5 Exciton-phonons coupling

There are two main contributions to the interaction between excitons and phonons. One is the coupling of excitons to confined acoustic-phonon modes by deformation potential or piezoelectric interaction [94]. The second contribution is the coupling of excitons to optical-phonon modes via the Frölich interaction [95]. This interaction describes the relation between charged particles and phonons in a crystal, which arises due to the polarization of the lattice by charged particles, creating an electric field that can couple to the lattice vibrations [96]. This process is represented in Fig. 1.18.

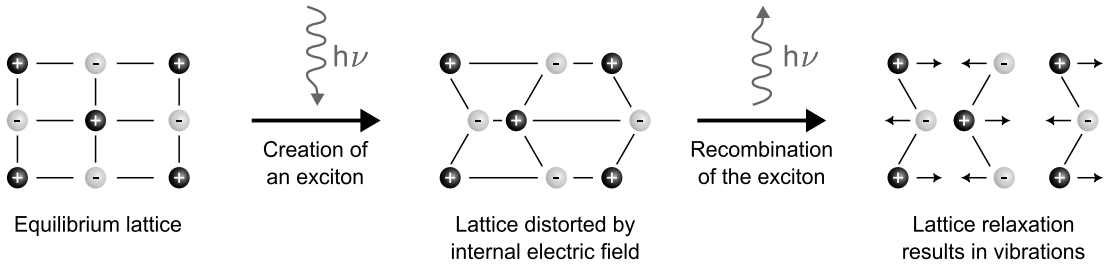

Figure 1.18: Schematic of the Frölich interaction. Initially, the crystal lattice is in an equilibrium position. The creation of an exciton induces an internal electric field, distorting the ionic lattice. After the exciton recombination, the field disappears and atoms return to their equilibrium positions, creating lattice vibrations [97].

The study of phonon-exciton interaction in lead-halide perovskites is still an active area of research. As perovskites are soft and ionic materials, a stronger interaction between exciton and optical phonon modes is expected compared to $CdSe$ or InP. Indeed, lead halide perovskites

are part of the phonon glass electron crystal family [98]. In these materials, the PbX_3^- sublattice forms a crystalline framework where A^+ cations can rotate easily. In such a polar system, the exciton-LO phonon coupling is more important as compared to the coupling with acoustic phonons because of strong Frölich interactions and important lattice anharmonicity.

Coupling between excitons and LO phonon modes directly impacts the photoluminescence spectra of a single nanocrystal. The interaction of the exciton within the lattice vibration causes the formation of a new quasiparticle, which is the exciton dressed by the LO phonon. Its energy and momentum are slightly different from those of the original exciton and will appear as satellite peaks on the spectra, called phonon replica.

Fig. 1.19 shows an example of the photoluminescence spectrum of a single nanorod of $CsPbBr_3$ at low temperature displaying the triplet emission lines of the exciton (X) along with the two first LO phonons replicas LO1 and LO2, with energy shifts of 3.7 and 6.3 meV, matching the values typically observed in the literature for $CsPbBr_3$ [99, 100]. A trion peak (X^*) and its first LO phonon replica can also be observed at lower energy. The LO phonons modes of the exciton and trion in $CsPbBr_3$ nanocrystals have been studied using photoluminescence spectroscopy in Ref. [99]. LO1 phonons can mainly be attributed to the collective vibration of the Cs atoms within the xy plane along with the rotation of the $PbBr_6$ octahedra, with a theoretical phonon energy of 3.94 meV. LO2 phonons can be attributed to a $PbBr_6$ octahedra rotation, with a theoretical energy of 6.67 meV. Although the energies of the LO phonons replicas remain unaffected by the crystal size, their intensities relative to the bright exciton line increase with confinement [99, 100, 101].

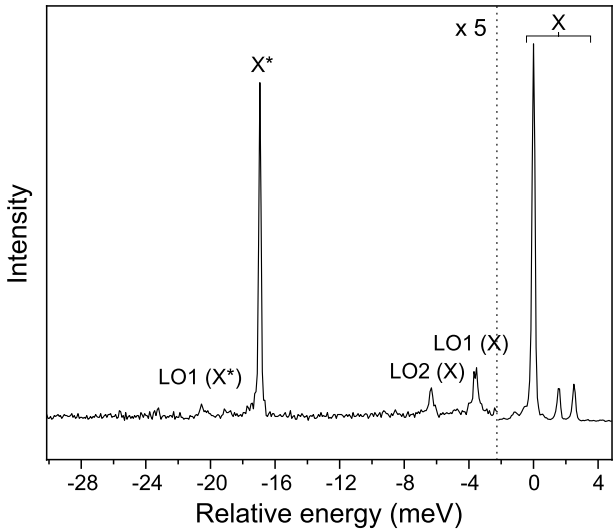

Figure 1.19: Example of photoluminescence spectrum obtained on a single nanorod of $CsPbBr_3$ at low temperature.

Exciton-phonon interactions in nanocrystals are also responsible for the exciton spectral line broadening, as studied for $CsPbBr_3$ in Ref. [102]. Following a similar model to the one developed for $CuCl$ by Itoh and Furumiya [103], the contribution of optical phonons to thermal broadening is proportional to their Bose-Einstein number, whereas the one of acoustic phonons has a linear dependence to temperature. The total contribution of phonons to the thermal broadening of

the homogeneous line as a function of temperature can then be described as:

$$\Gamma(T) = \Gamma_0 + \sigma_{\mathrm{Ac}} T + \frac{\Gamma_{\mathrm{LO}}}{exp(\frac{E_{\mathrm{LO}}}{k_B T}) - 1} \tag{1.52}$$

where Γ_0 is the linewidth at $T = 0$ including spectral diffusion which is not temperature dependent, σ_{Ac} is the coefficient of exciton-acoustic phonon interaction which includes the deformation potential and piezoelectric coupling, Γ_{LO} is the coefficient of exciton-optical phonon interaction and E_{LO} the optical phonon energy.

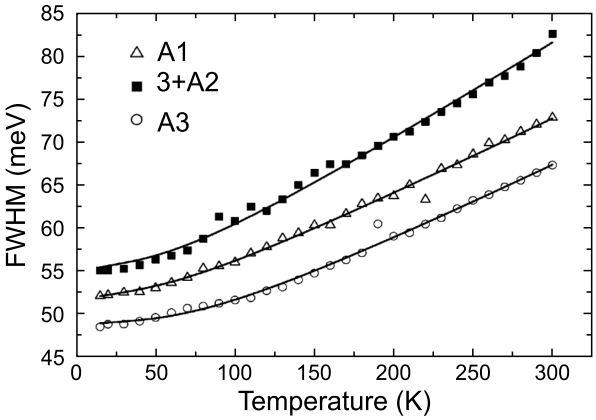

Figure 1.20: FWHM of photoluminescence spectra as a function of temperature for $CdTe$ quantum dots, from Ref. [104]. The results are given for three different samples along with their best-fit curves. The data of the sample A2 are vertically translated by 3 meV.

As an example, Fig. 1.20 presents the temperature dependence of the photoluminescence broadening of three samples of ensemble colloidal $CdTe$ nanocrystals. This study was published in 2007 by Morrello et al. [104]. The average diameters of nanocrystals are 4.2, 4.9, and 5.9 nm for samples A1, A2, and A3, respectively. The Full Width at Half-Maximum (FWHM) have been obtained from a Gaussian fit of the photoluminescence spectra. The experimental data are fitted with Eq. 1.52 with the parameters given in table 1.2. These fitting parameters show that the exciton-acoustic phonons coupling coefficient σ_{Ac} increases when increasing the confinement whereas the exciton-LO phonon coupling coefficient Γ_{LO} decreases. The LO phonon energy does not depend on the size of the quantum dots, and its value is consistent with the bulk value.

Sample	$\boldsymbol{\sigma}_{\mathrm{Ac}}$(µeV/K)	$\boldsymbol{\Gamma}_{\mathrm{LO}}$(meV)	$\boldsymbol{E}_{\mathrm{LO}}$(meV)
A1	31 ± 7	14 ± 3	20 ± 5
A2	33 ± 6	18.3 ± 0.9	20 ± 1.5
A3	14 ± 5	21 ± 4	22 ± 4

Table 1.2: Fit values for Fig. 1.20, from Ref. [104].

1.4 Conclusion

In this chapter, we started by reviewing the foundational models to comprehend the electronic properties of $CdSe$, InP and lead halide perovskite nanocrystals. Starting with a simple particle-in-a-box model and adding complexity to the band-structure material allows us to approach the actual electronic properties of these systems. A good description of the band-edge exciton fine structure is essential for understanding the photoluminescence properties of these materials and must be adapted to the type of nanocrystal under study. Various factors influence this electronic structure such as the crystal structure, shape, and electron-hole exchange interaction, along with external factors like the application of a magnetic field. The difference between InP and $CdSe$ compared to perovskite materials comes from the construction of their electronic band gap structure and has an important impact on their optical properties.

In the second part of this chapter, we presented the particular optical properties of semiconductor nanocrystals. We discussed the recombination dynamics of the different complexes of charges existing in these systems. The emission coming from one nanocrystal also shows peculiar effects, such as spectral diffusion or blinking, that are not observable in ensemble measurement. They lead to non-radiative recombination processes, causing a reduction of the nanocrystals quantum yield. A possible solution is the use of core-shell systems to reduce these phenomena.

Lastly, we introduced the concept of optical and acoustic phonons in a crystal. The finite size of nanocrystals leads to the apparition of surface and interface modes that are not present in bulk crystals. Taking phonon modes into account is essential as they interact with excitons and modify their photoluminescence emission. Lead halide perovskite phonon modes differ from classical semiconductors because of their soft and ionic nature.

Overall, this chapter serves as a theoretical basis for the rest of this thesis and gives a first indication of the fundamental electronic and optical differences between classical nanocrystal semiconductors as InP and $CdSe$, and lead halide perovskites such as $CsPbBr_3$ and $CsPbCl_3$.

Chapter 2

Experimental Methods

As presented in the first chapter of this thesis, the electronic and optical properties of semiconductor nanocrystals are complex and strongly depend on their chemical composition, crystal structure, size, and shape. To explore their properties and, in particular, the spectral signature of the band-edge exciton in these systems, we use the technique of photoluminescence spectroscopy on single nanocrystals at cryogenic temperatures. Spectroscopy on a single nanocrystal provides information about the fundamental photophysical properties of the material without averaging effects observed in ensemble experiments. The measurement of a parameter is then repeated on several nanocrystals, revealing its statistical distribution.

In this chapter, we describe the different experimental methods used throughout this thesis on several types of nanocrystals. We start by depicting the synthesis of semiconductor nanocrystals and the quantum yield measurements of nanocrystals solutions. Then, we present the principles and experimental setup of photoluminescence spectroscopy as a tool to investigate the emission properties of semiconductor nanocrystals.

2.1 Chemical synthesis of semiconductor nanocrystals

Controlled synthesis of colloidal nanocrystals has undergone massive advances in the past two decades. Critical areas for improvement include achieving smaller-sized nanocrystals, ensuring a narrow size distribution, maintaining high stability with minimal defects, and optimizing their quantum yield. Collaborator research groups synthesized the different samples of semiconductor nanocrystals used in this thesis. This section provides a brief overview of their synthesis processes.

2.1.1 InP/ZnS/ZnSe core/shell nanocrystals

The first syntheses of InP nanocrystals with good crystallinity were made in the 1990s [6]. The typical synthesis process for $InP/ZnS/ZnSe$ core/shell structures involves several steps; initially, the InP core is formed at high temperatures, followed by the successive introduction of $ZnSe$ and ZnS precursors to grow shell layers. The thickness of a shell can be controlled by varying the reaction time and precursor concentrations. Afterward, surface passivation is performed by coating nanocrystals with ligands to enhance stability and dispersibility. A purification step usually ends the synthesis by solvent precipitation and centrifugation [75].

Significant degradation of the optical properties of InP nanocrystals comes from oxidative defects due to the oxophilic nature of both indium and phosphorus atoms. They generate defects

such as $InPO_x$ and In_2O_3 in contact with oxygen. Oxygen contamination can come from impurities formed during the reaction or from the presence of oxygen in the solvent, precursors, or surrounding atmosphere.

InP nanocrystals also possess numerous surface defects, making studying their electrical and optical properties challenging. When electrons delocalize upon excitation, they are easily trapped at the nanocrystal surface by ions or vacancies, forming localized defect states within the bandgap. This process quenches band-edge emission through nonradiative recombination of photogenerated carriers. Encapsulating InP nanocrystals within other semiconductor materials allows for the passivation of their surfaces and the prevention of electron and hole entrapment.

The $InP/ZnSe/ZnS$ nanocrystals used in this thesis have been synthesized by Won et al. following the synthesis route presented in Ref. [7]. They developed a method allowing them to obtain uniform InP cores with a quantum yield close to unity. To do so, they used continuous precursor injection during the growth process improving the InP core uniformity. Additionally, the formation of the $ZnSe$ interlayer involved the use of hydrofluoric acid (HF) as an etching method to remove oxide at the surface of the InP core. The large layer of $ZnSe$ also suppresses non-radiative Auger recombination. Moreover, oxygen-free precursors and solvents were employed and a constant flow of nitrogen was maintained during the reaction to create an inert atmosphere, minimizing the presence of oxygen sources throughout the synthesis.

This synthesis results in nanocrystals composed of a nearly spherical zinc-blende InP core with a diameter of 3.3 nm and a $ZnSe$ interlayer with a thickness of around 3 nm, that is further capped by a single layer of ZnS with a thickness of around 0.4 nm. Fig. 2.1 shows a schematic representation of an $InP/ZnSe/ZnS$ nanocrystal along with the size distribution of a sample of nanocrystals showing a size polydispersity as low as 10%.

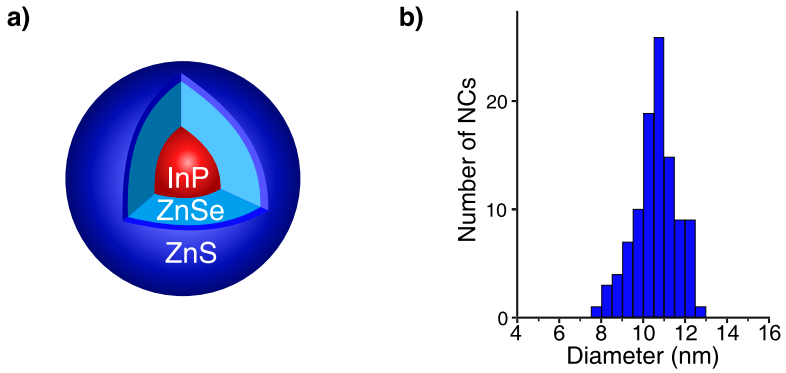

Figure 2.1: **a)** Scheme of a $InP/ZnSe/ZnS$ nanocrystal. **b)** Size distribution of $InP/ZnSe/ZnS$ nanocrystals synthesized by Won et al. [105].

.

2.1.2 Lead halide perovskite nanocrystals

The second type of semiconductor nanocrystals studied in this thesis are lead halide perovskite nanocrystals. Their first significant synthesis was carried out in 2015 by Protesescu et al. [13]. They showed promising systems with narrow emission linewidth and high quantum yields. Unlike InP nanocrystals, lead halide perovskites nanocrystals are less sensitive to surface defects and oxidation. Due to their high defect tolerance, they do not necessitate growing shells, which greatly simplifies their synthesis. In the past few years, the synthesis methods of lead halide perovskite nanocrystals have undergone significant improvements, enabling better control over their size and composition [82]. Furthermore, the stability of the nanocrystals has been greatly

enhanced by incorporating passivation techniques and encapsulation.

Halide perovskite nanocrystals are typically synthesized using a liquid-phase bottom-up approach. The two main methods for synthesizing these nanocrystals are the hot injection method (HI) and the ligand-assisted reprecipitation (LARP) method. The perovskite nanocrystals and nanorods studied in this thesis were synthesized by the group of Kovalenko [13, 106] using one of these two approaches, depending on the type of sample.

The HI method consists of a rapid injection of a precursor in a hot solution containing solvent, ligands, and the rest of the precursors at high temperatures and in an inert atmosphere. It leads to rapid nucleation, followed by a decrease in the concentration of monomers, which terminates the nucleation stage and allows nuclei to continue growing. This method relies on ligands to improve stability and precisely control crystal growth. The size, size distribution, and shape of colloidal nanocrystals can be controlled by adjusting the ratio of ligands to precursors, the injection temperature of cation or anion precursors, the reaction time, and the concentrations of precursors [82].

On the other hand, the LARP method is employed at ambient atmosphere and room temperature. Ions are dissolved in a solvent, and a cosolvent is added. The combination of these two solvents results in an immediate supersaturation, initiating both the nucleation and growth of nanocrystals. Similarly, adding ligands during this phase allows for control of the size and shape of the nanocrystals. In particular, organic capping ligands facilitate the growth of nanometer-sized crystals and effectively passivate surface defects, comparable to the synthesis process employed for more traditional nanocrystals [82].

2.2 Quantum yield measurements

Before conducting single dot spectroscopy, we perform ensemble optical spectroscopic studies to test the overall photostability of nanocrystals by measuring their quantum yield.

Quantum yield measurements are an important tool for evaluating and optimizing the efficiency of photoluminescent processes and for facilitating the development and characterization of semiconductor nanocrystals for their future applications. The quantum yield of a sample of nanocrystals corresponds to the ratio of the number of emitted photons to the number of absorbed photons:

$$\Phi = \frac{\text{Number of photons emitted through fluorescence}}{\text{Number of photons absorbed}} \tag{2.1}$$

Measurements of quantum yields can be done through two different approaches: one involves an absolute measurement of the emitted photons, while the other is based on a relative method [107, 108]. The absolute measurement requires an integrating sphere collecting all emitted photons. In this case, a unique measurement allows for the detection of all the fluorescence coming from a sample. By comparing the total number of emitted photons to the number of absorbed photons, the quantum yield can be directly determined.

To quantify the quantum yield of semiconductor nanocrystals in solution, we employ a relative method, which necessitates the availability of a reference sample with a known quantum yield emitting within the same wavelength range as the target nanocrystals. In the study of InP nanocrystals, we use Rhodamine 6G as our reference dye, which presents a quantum yield of 0.95 at 488 nm [109]. Rhodamine 6G is diluted in ethanol to match the absorbance of the sample of interest. The absorption at 488 nm must be lower than 0.1 to prevent potential non-linear effects arising from inner filters, such as re-absorption, which could introduce deviations in the calculated quantum yield [110]. Absorbances of both solutions are measured between 400 nm

and 800 nm using a single-beam spectrophotometer. To minimize any potential error, we study several solutions with different concentrations. Next, photoluminescence spectra of the sample and reference solution are acquired between 500 and 800 nm with an excitation at 488 nm using a fluorescence spectrophotometer equipped with an InGaAs multi-channel array detector and a 450 W xenon lamp. The quantum yield is calculated by comparing the integrated fluorescence intensity of the sample with the reference solution, taking into account the refractive index of the solvents used for each solution. It is then retrieved using the following formula:

$$\Phi_{sample} = \Phi_{reference} \left(\frac{A_{reference}}{A_{sample}} \right) \left(\frac{E_{sample}}{E_{reference}} \right) \left(\frac{n_{sample}}{n_{reference}} \right)^2, \tag{2.2}$$

with n the refractive index of the solvent, A the absorbance of the solution, E the integrated fluorescence intensity of the emitted light, and $\Phi_{reference}$ the quantum yield of the reference solution. The results of these measured quantum yields can be found in section 3.3.1.

2.3 Single nanocrystal spectroscopy

Since their first synthesis, several techniques have been employed to optimize the characterization of semiconductor nanocrystals, such as transient differential absorption (TDA) spectroscopy [111], also known as pump-probe or hole-burning spectroscopy, photoluminescence excitation (PLE) spectroscopy or fluorescence line narrowing (FLN) spectroscopy [60].

Using single nanocrystal photoluminescence spectroscopy stands as a unique method for examining and grasping the optical characteristics of nanocrystals free from ensemble-averaging influences. This approach provides essential insights for comprehending the underlying physical mechanisms within nanocrystals. Moreover, it reveals distinctive properties not observed in ensemble experiments, such as photoluminescence blinking and spectral diffusion.

In this thesis, we use a homebuilt laser scanning confocal microscope, which will be detailed in the following sections.

2.3.1 Cryogenic measurements

Performing spectroscopy measurements at low temperatures (around 3 K) provides the opportunity to reveal physical properties that remain hidden at room temperature, as the reduced thermal dephasing and diminished populations of acoustic phonons at low temperatures facilitate the acquisition of extremely narrow emission lines from single nanocrystals.

We use a cryostat operating on a helium-based closed-cycle, capable of achieving temperatures below 3 K. This cryostat possesses three layers of radiation shielding with two windows enabling optical access to the sample. Based on pulsed tube technology, this type of cryostat permits reaching and maintaining low temperatures without the need for a continuous supply of liquid helium. Cooling is achieved through a sequence of helium-4 expansions. The operation of the cryostat is illustrated in Figure 2.2. First, during a compression cycle, a compressor increases the gas pressure to approximately 20 bars. The pressurized helium flows to a rotating valve before passing through a pulsed tube and a generator, releasing some of the heat acquired during compression. It then enters the cold exchanger. The valve changes direction, reversing helium flow and initiating a rapid gas expansion, resulting in cooling within the cold exchanger due to the Joule-Thomson effect. The gas then circulates back through the regenerator, recovering the previously transferred heat, and returns to the compressor at a pressure of around 7 bars. The gaseous piston tube and capillary allow for adjustment of the phase between the helium flow and pressure wave in the circuit to maximize the temperature gradient between the

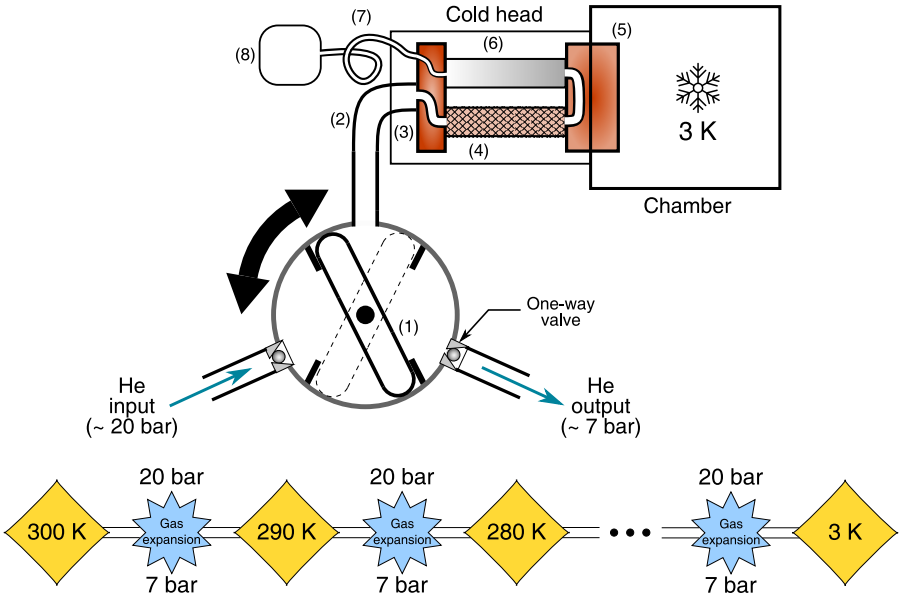

Figure 2.2: Scheme of the functioning of the cryostat. (1) Rotating valve. (2) Pulsed tube. (3,5) Heat exchanger. (4) Regenerator. (6) Gaseous piston tube. (7) Capillary. (8) Buffer space. Figure adapted from Ref. [112] with authorization from the author.

hot and cold parts of the gaseous piston tube. The cooled gas is returned to the compressor, completing the closed-loop cycle. This cycle repeats, gradually lowering the temperature within the cryostat chamber. Thermalization wires between the sample and the cold plate ensure it reaches the desired temperature.

At the beginning of the cool-down process, the cryostat chamber is put under vacuum to diminish thermal conduction with the external environment and prevent water condensation. To achieve a low-pressure environment, we initially use an oil-sealed vacuum pump, followed by a secondary turbomolecular pump reaching a pressure of around 6.10^{-7} bar. The entire cool-down process, including cooling the cryostat and the sample to their respective steady-state temperatures, takes approximately 16 hours with the magnetic coils (made of 13 kg of copper, described in section 2.3.6) and 8 hours without them. Different temperature sensors placed on the cryostat plate, coils, and sample allow us to monitor the temperature.

2.3.2 Sample preparation

Throughout this thesis, we study nanocrystals with different sizes, shapes, and compositions. However, the sample preparation method for single nanocrystal spectroscopy stays consistent for each type of nanocrystal. A solution of nanocrystals in polymer is prepared with a massic concentration between 2 and 3 wt%. The choice of solvent and polymer depends on the type of nanocrystals. In particular, it depends on whether the initial solution has a polar or nonpolar environment based on the used solvent. For InP nanocrystals, we use a solution of 2 wt% PMMA (Poly(methyl methacrylate)) in anhydrous toluene; for $CsPbBr_3$ nanorods we use a solution of 3 wt% SEBS (Polystyrene-block-poly(ethylene-ran-butylene)-block-polystyrene) in cyclohexane and for $CsPb(BrCl)_3$ nanocrystals a solution of 3 wt% polystyrene in anhydrous toluene.

The initial solution is diluted in the polymer solution and spin-coated on a sapphire slide cleaned beforehand using a plasma cleaner. Sapphire is used for its transparency and high thermal conductivity. The spin-coating process is illustrated in Fig. 2.3. The slide is fixed to

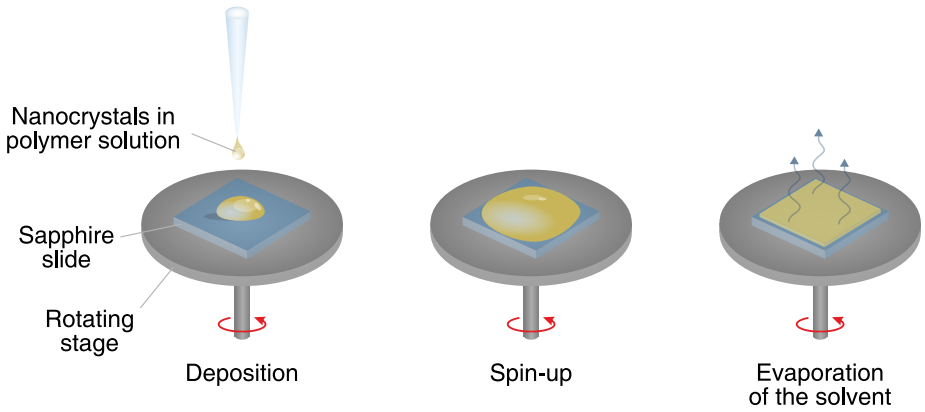

Figure 2.3: Spin-coating process. A drop of 50 µL of a solution containing nanocrystals in polymer and solvent is deposited on a sapphire slide. The acceleration of the rotation of the solution allows for a good dispersion of nanocrystals on the slide surface. During the spinning process, the solvent evaporates.

the rotating stage through suction and rotates at a speed of 2000 rpm for 100 s. During the spin coating process, centrifugal force helps the dispersion of nanocrystals in the polymer matrix, and the solvent is ejected and evaporates. Changing the acceleration and rotation speed allows for control of the thickness of the polymer film created. The sapphire slide is then fixed on an aluminum sample holder using silver paste to allow a good thermal transfer between the sample and the sample holder.

The role of the polymer matrix is to isolate nanocrystals from their environment to minimize interactions that might otherwise lead to spectral instabilities in their photoluminescence. Achieving an appropriate concentration of nanocrystals in the polymer is crucial, as it must be low enough to enable straightforward isolation and imaging of the nanocrystals using confocal microscopy while high enough to facilitate the study of various single nanocrystals within a single confocal image.

2.3.3 Piezoelectric positioners and scanner

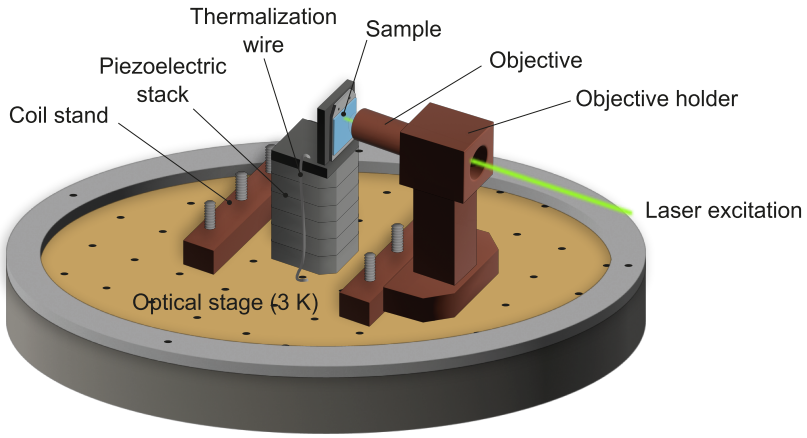

Figure 2.4: Scheme of the cryostat optical stage. The sample is placed on a piezoelectric stack and excited with a laser passing through a microscope objective.

The sample is then placed on a piezoelectric stack set on the optical stage of a cryostat, and excited with a laser as represented in Fig. 2.4. To obtain confocal images, the sample is

scanned using a piezoelectric scanner, procuring images at low temperatures and under a strong magnetic field as detailed hereafter. At low temperatures, applying a voltage up to 150 V to the scanner, an image of 12.8 µm × 12.8 µm can be obtained. At ambient temperature, applying a voltage of 60 V gives an image of around 25 µm × 25 µm.

The scanner is installed on linear nanopositioners with motion in the X and Y directions, enabling a change in the area of interest, and one in the Z direction, allowing adjustment of the objective-to-sample distance to focus the laser beam on the sample.

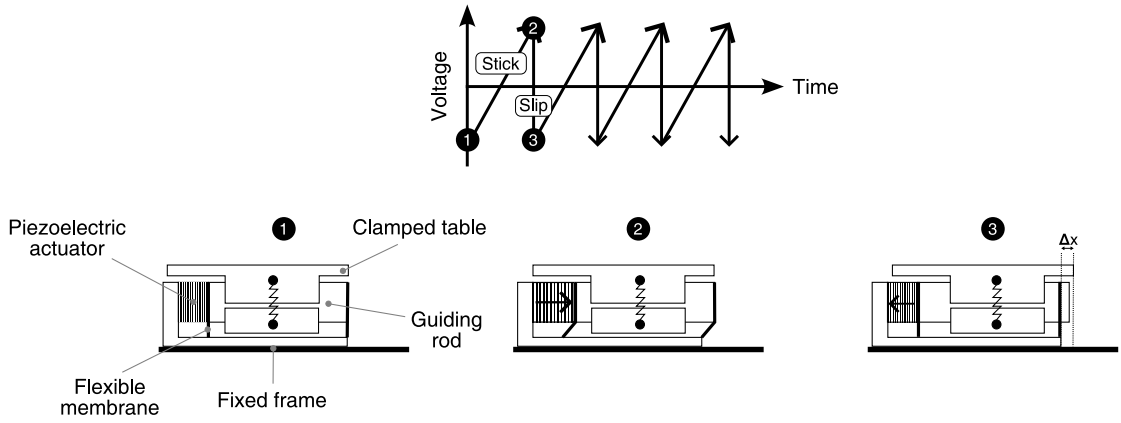

Figure 2.5: Scheme of the slip-stick principle of an Attocube piezoelectric system.

These positioners operate based on a dynamic cyclic process known as the slip-stick principle. The system comprises a stationary base plate, which hosts a piezoelectric actuator linked to a moveable table by a finite holding force. When a sawtooth shape voltage is applied to the piezoelectric material, it gradually expands, causing the table to move along. When reaching the steep edge of the signal, the friction of the finite clamping force is exceeded, resulting in a small net step, as represented in Fig. 2.5. This periodic cycle enables quasi-continuous macroscopic motion. On top of the high precision, this system offers the advantage of voltage returning to zero once the desired position is achieved. This characteristic improves position stability by preventing electrical drift, ensuring that the system remains in its intended position over time.

2.3.4 Excitation sources

The sample of nanocrystals, mounted on the piezoelectric system, is excited using different lasers depending on the type of semiconductor and the experiment. Continuous-wave lasers serve as the excitation source for wide-field images, confocal images, and photoluminescence spectra. For InP nanocrystals, we employ a laser emitting at a wavelength of 561 nm. In the case of lead halide perovskite nanocrystals, a laser emitting at 488 nm is employed. Both lasers are based on Optically Pumped Semiconductor Laser technology (OPSL). For lifetime measurements, we use a tunable femtosecond Ti:Sapphire pulsed laser (150 fs FWHM). This laser is used with frequency doubling or along with an optical parametric oscillator (OPO). The different laser beams are coupled to an optical fiber upstream of the imaging system to facilitate the change of exciting sources during our experiments, as represented in Fig. 2.6.

2.3.5 Imaging methods

A microscope objective with a numerical aperture of 0.95 and a focal length of 2.5 mm is placed on the cryostat optical stage, as shown in Fig. 2.4, focusing the laser on a single nanocrystal in the sample. The choice of a high numerical aperture serves to optimize photoluminescence signal

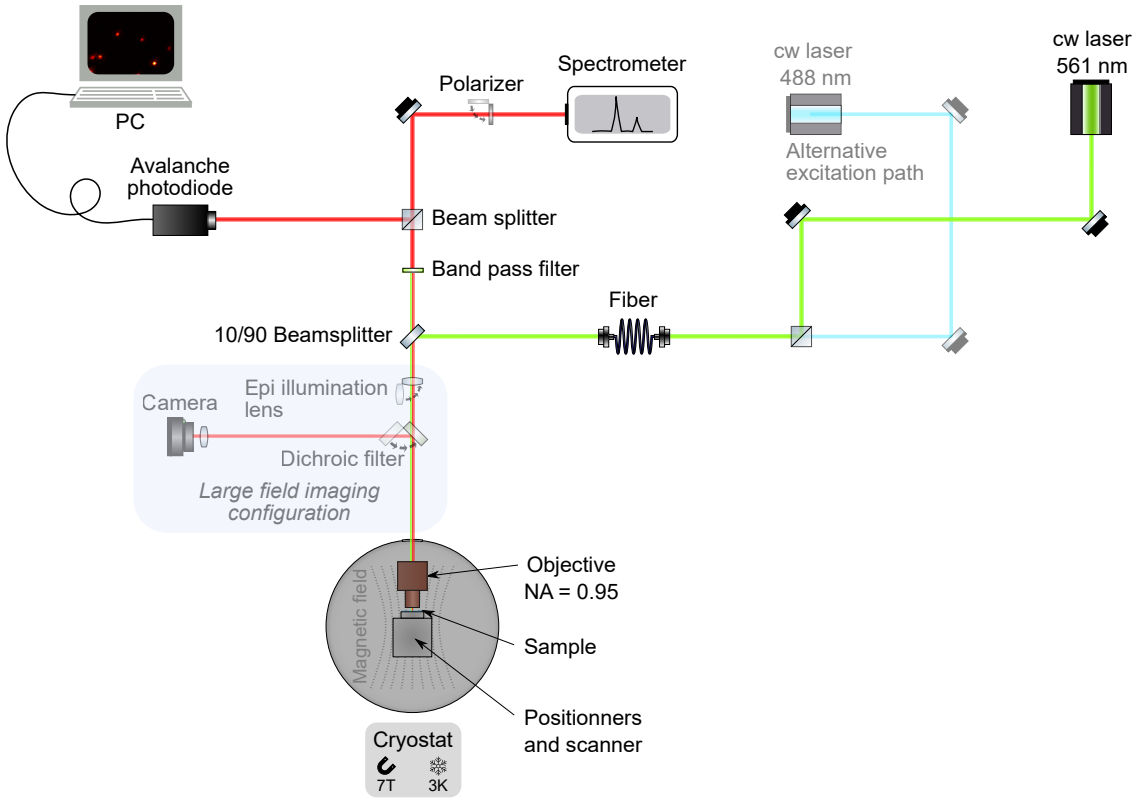

Figure 2.6: Simplified optical scheme of the single nanocrystal spectroscopy set up at low temperature and under magnetic field.

collection efficiency. Furthermore, placing the objective inside the cryostat eliminates spherical aberration that could be induced by the cryostat windows, thereby minimizing background signal interference. The microscope objective is used either in a wide-field or confocal configuration, as shown in Fig. 2.6.

Wide field imaging

Wide-field imaging consists of illuminating a large zone of the sample using a defocussed laser to obtain an ensemble view of the nanocrystal concentration. To do so, an epi-illumination lens is added in the excitation path before the cryostat in order to illuminate a wide area of the sample. A dichroic filter is placed in the emission path to filter and reflect the photoluminescence, which is then collected by an electron-multiplying CCD camera with single-photon sensitivity. The photoluminescence is focused on the camera, where the chip is conjugated to the surface of the sample.

Confocal imaging

In the case of confocal imaging, the laser is focused on the sample by the objective, and the photoluminescence emission is collected and sent to an avalanche photodiode (APD). An image of the region can be obtained by scanning the sample using the scanning piezo stage driven by a Labview program. Fig. 2.7 shows a typical scanned image obtained for a sample of $CsPb(BrCl)_3$ nanocrystals. The detection timescale in this setup is in the millisecond range.

To eliminate the scattered excitation light and diminish any surrounding noise, the emitted photons are filtered by a band-pass filter tailored to the wavelength emission region of the sample under study. For instance, when working with $CsPb(BrCl)_3$ nanocrystals, we used a band-pass

emission filter centered at 538 nm with a bandwidth of 84 nm.

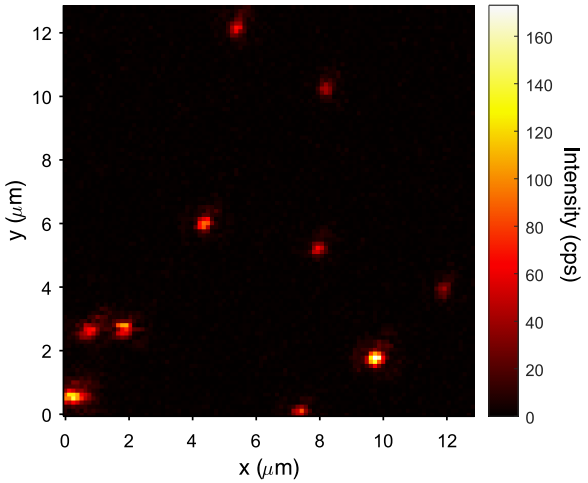

Figure 2.7: Typical confocal image obtained for a sample of $CsPb(BrCl)_3$ nanorods in polystyrene excited with a continuous laser at 488 nm, at 3.4 K. The integration time is 25 ms per pixel.

2.3.6 Magnetic field

We use an external magnetic field to conduct magneto-optical spectroscopy studies on semiconductor nanocrystals. This approach enables splitting the degenerated states through the Zeeman effect and reveals hidden dark states due to the field-induced mixing of states. To do so, we use coils placed around the sample on the cold plate of the cryostat. These coils constitute a superconducting magnet in Helmholtz configuration, capable of generating a magnetic field of up to 7 T at the sample location. It produces a nearly uniform magnetic field region along one axis as shown in Fig. 2.8 **b)**.

Given that the magnetic coils cannot be rotated in the cryostat, a rotation of the sample inside the coil allows access to both the Faraday configuration, where the magnetic field is parallel to the optical axis and perpendicular to the sample, and the Voigt configuration, where the field is perpendicular to the optical axis as represented on Fig. 2.8 **c)**.

2.3.7 Spectroscopy measurements

In the confocal configuration, the photoluminescence emitted from the nanocrystal is directed to a beam splitter, which divides the signal between the APD and a spectrometer to obtain photoluminescence spectra. We use a spectrometer equipped with three gratings (150 g/mm, 300 g/mm, 1800 g/mm) and with a CCD camera, with a focal length of 50 cm. The maximal resolution, obtained with the 1800 g/mm gratings, is around 120 μeV.

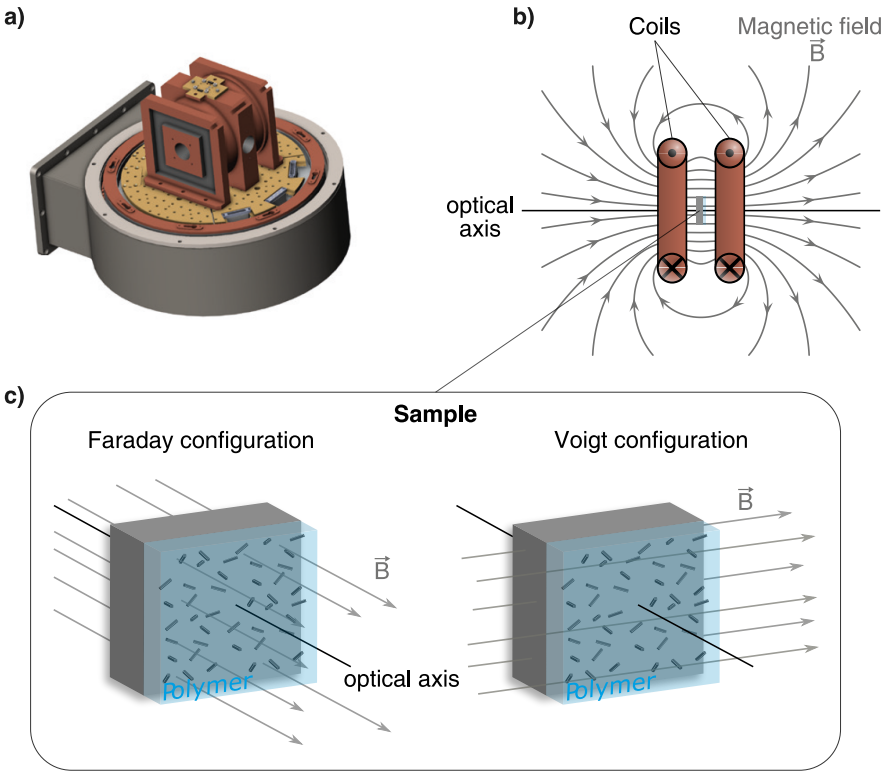

Figure 2.8: a) Scheme of the magnetic coils placed on the cryostat cold plate (from Ref. [113]) **b)** Scheme of the top view of Helmholtz coils showing the magnetic field lines in-plane. **c)** Two configurations for the magnetic field with respect to the sample. In the Faraday configuration, the magnetic field is parallel to the optical axis and perpendicular to the sample. In the Voigt configuration, the magnetic field is perpendicular to the optical axis and parallel to the sample.

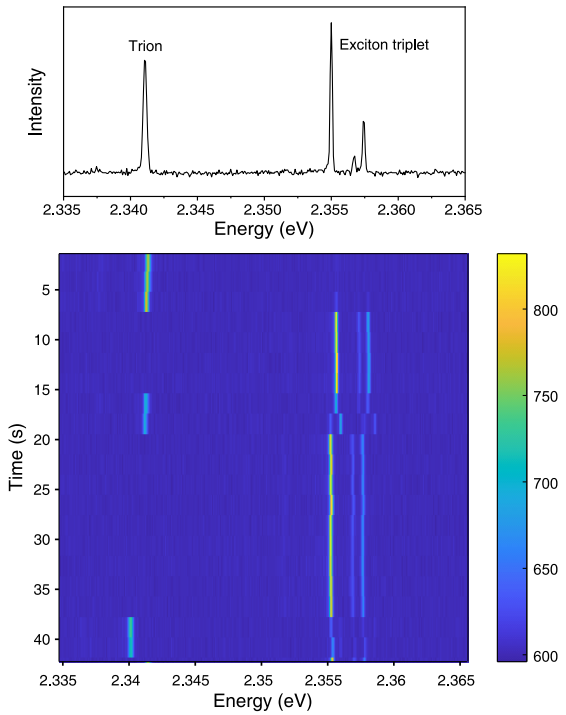

Figure 2.9: Photoluminescence spectrum and spectral trace of a single nanocrystal of $CsPbBr_3$ displaying emission peaks coming from a trion and an exciton recombination.

Several criteria are employed to ensure that the collected signal originates from a single nanocrystal and not a cluster. Firstly, the signal from the avalanche photodiode (APD) is examined. Sudden jumps in intensity, comparable to a step function, indicate blinking behavior or transitions between emissive states characteristic of a single nanocrystal. Secondly, sharp zero-phonon lines that are diffraction-limited provide further evidence of emission coming from a single nanocrystal. Additionally, monitoring the spectral behavior over time allows the observation of typical single nanocrystal phenomena like spectral diffusion or blinking. An example of a spectral trail is given Fig. 2.9 with a photoluminescence emission spectrum coming from a $CsPbBr_3$ nanocrystal presenting switches between trion and exciton emissions.

2.3.8 Polarization study

Analyzing the polarization properties of a nanocrystal photoluminescence emission provides important insight regarding the nanocrystal orientation. Additionally, as the different emitting states in a nanocrystal correspond to distinct transition dipole orientations, the relative polarization of the different photoluminescence peaks offers complementary information about their origin.

The polarization of the emission lines can be studied by simply adding a linear polarizer on the emission optical path before the spectrometer, as displayed in Fig. 2.6. The polarizer is mounted on an automatic rotation, driven by a LabVIEW program. The spectra are collected every 10° or 15° rotation of the polarizer. An example of a polarization study of an exciton

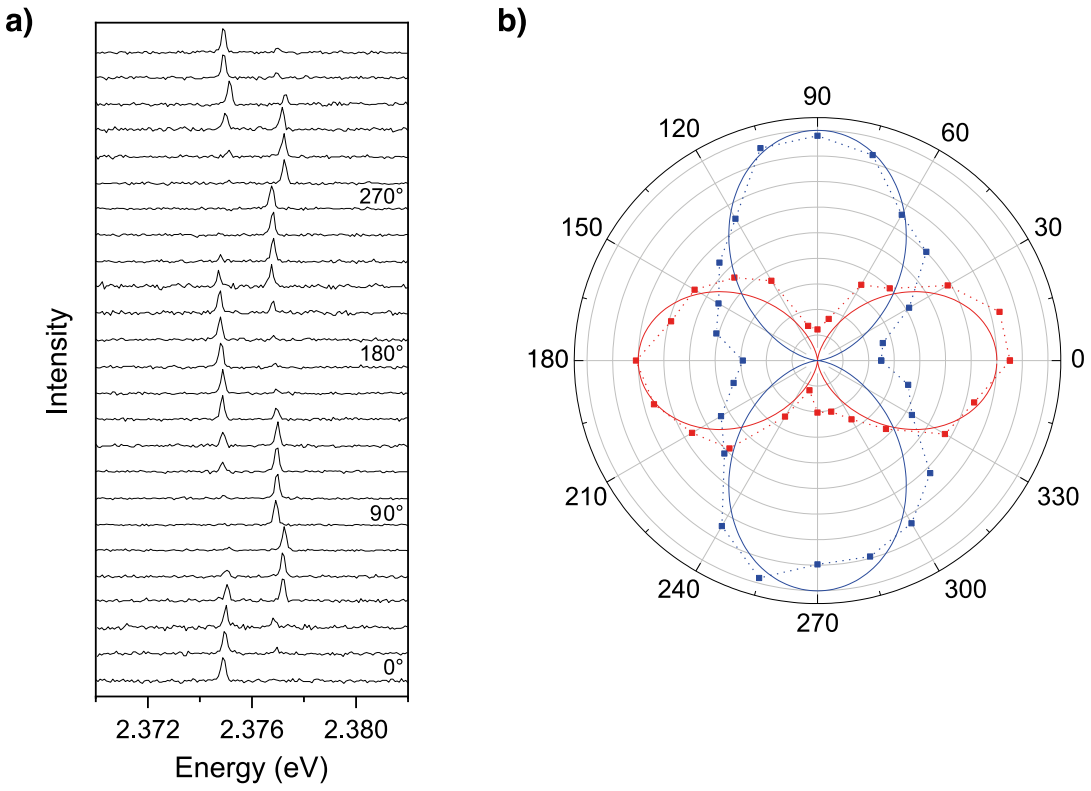

Figure 2.10: Example of polarized spectra. **a)** Photoluminescence spectra as a function of the polarizer angle. **b)** Polar diagram of single $CsPbBr_3$ nanorod showing doublet emission. The spectra are measured every 15° as a function of the polarizer angle.

emission doublet coming from a single $CsPbBr_3$ nanorod is shown Fig. 2.10. Varying the

polarization angle allows observation of the change of weight between the two peaks (Fig. 2.10 **a)**). By integrating each peak and normalizing it by the total area, we can plot the relative weight of each peak as a function of the polarizer angle, which allows us to identify the polarization orientation of each line (Fig. 2.10 **b)**). In this example, the two peaks exhibit orthogonal linear polarization. These measurements provided an additional tool for assigning the emission lines in the study of single nanocrystal photoluminescence.

2.3.9 Lifetime measurements

Studying the photoluminescence decay of single nanocrystals provides valuable information on the relaxation rates of the charge-complex states. Photoluminescence decay measurements are conducted using a time-correlated single photon counting (TCSPC) approach. This method relies on collecting fluorescence signals from multiple cycles of excitation and emission coming from a nanocrystal. It requires a good temporal resolution and the ability to detect single photons. The experimental setup is represented in Fig. 2.11.

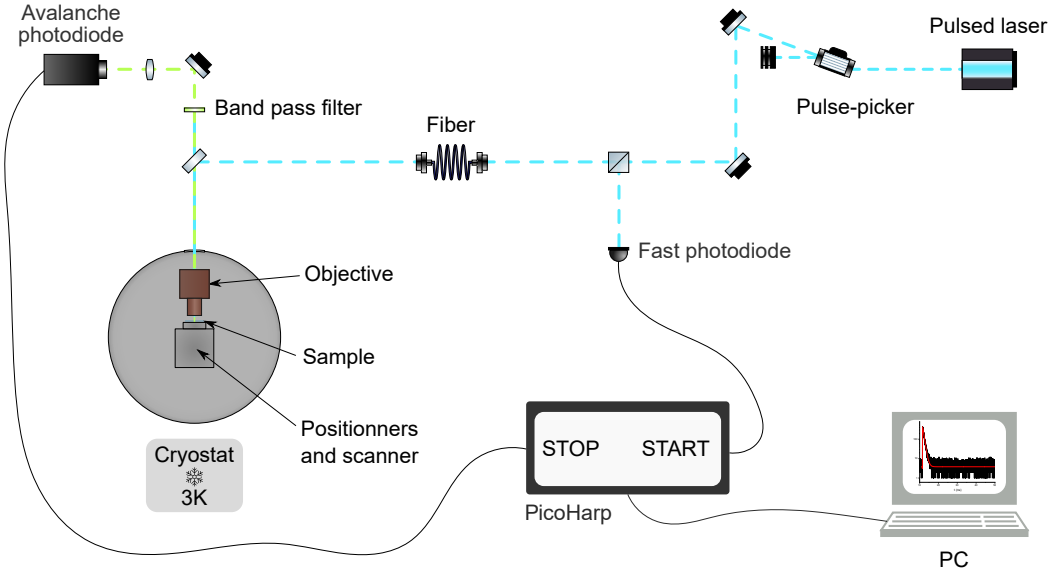

Figure 2.11: Scheme of the experimental setup of time-correlated single photon counting measurement.

The excitation source employed is a pulsed laser. A portion of the excitation beam is directed toward a fast photodiode, which is connected to an event timer and generates a pulse serving as the start signal. Simultaneously, the remaining beam is directed to the sample, exciting a single nanocrystal. The resulting photoluminescence photons, produced within a pulse, are detected by an avalanche photodiode, constituting the stop signal. The time difference between the start and stop signals is collected, allowing the building of a histogram of bins of photons per unit time. To evaluate the decay shape of the nanocrystal, this process must be repeated over multiple excitation-emission cycles with periodic excitation. The excitation repetition rate is adjusted using a pulse picker to ensure a longer delay between two excitation pulses than the nanocrystal lifetime, enabling the study of long decay times. The principle of TCSPC measurements is illustrated Fig. 2.12.

The Instrument Response Function (IRF) is measured at the outset of the experiment by directing the attenuated laser beam onto the single-photon detector while keeping all the other parameters consistent with the experimental conditions. In an ideal system, the IRF signal would be infinitely narrow. However, various factors contribute to the broadening of the signal. It primarily arises from the detector itself, as the synchronization accuracy is constrained by

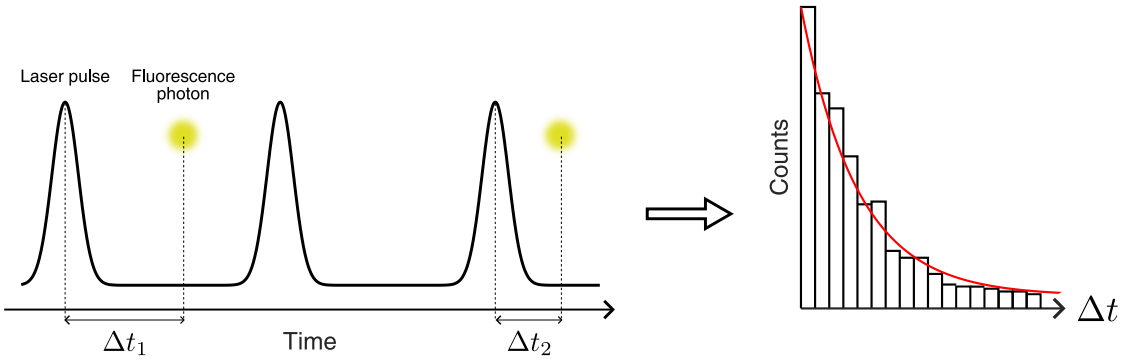

Figure 2.12: Schematics of the principle of a TCSPC experiment.

the inherent time uncertainty associated with converting a photon into an electrical signal. Limitations of the excitation source and timing fluctuations in signals originating from different electronic components also contribute to the broadening. The total IRF is the convolution of all these contributions [114]. An example of IRF is presented in Fig. 2.13. The signal is composed of a biexponential with both a short and a long time component. The width of the IRF is an indicator of the timing resolution of the instrument. In the case of our experiment, the short time component of the exponential decay is mainly limited by the APD having a typical timing accuracy of 35 ps FWHM. We employ an iterative re-convolution technique on

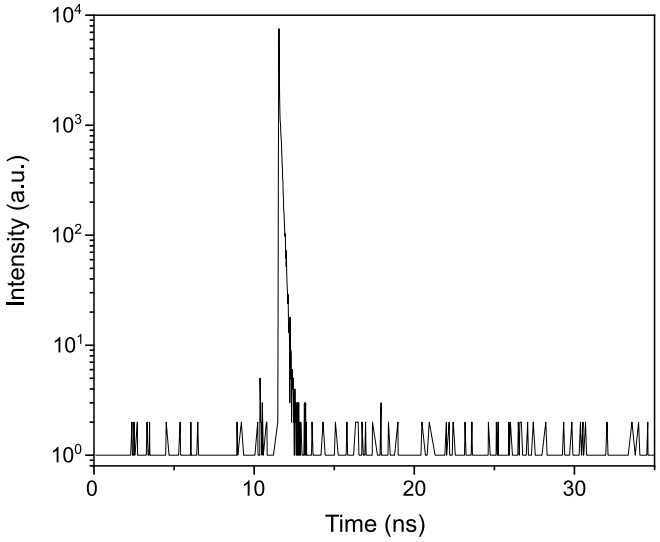

Figure 2.13: Example of an IRF measurement.

the histogram acquired through the IRF to extract the characteristic times of the decay and their associated weights. We typically expect a multiexponential decay when photoluminescence arises from multiple states. The lifetimes of the different emitting states of the nanocrystal can be determined by fitting the measured decay using the following formula:

$$I(t) = \int_{-\infty}^{t} IRF(t') \sum_{i=1}^{n} A_i \mathrm{e}^{-\frac{t-t'}{\tau_i}} dt', \tag{2.3}$$

with A_i the amplitude in counts at time zero of the i^{th} exponential component and τ_i the lifetime of the i^{th} component.

2.4 Conclusion

This chapter described the various experimental methods employed for investigating the photophysical characteristics of both ensemble and single semiconductor nanocrystals. These include quantum yield measurements, single nanocrystal spectroscopy at low temperatures and in the presence of a magnetic field along with polarization studies and lifetime measurements. These different measurements provide some complementary information essential for unraveling the intricate structure of the band-edge exciton and other charge complexes within these systems, as will be presented in the following chapters.

Chapter 3

Band-Edge Exciton Fine Structure of Single InP Nanocrystals

3.1 Introduction

As detailed in the first chapter of this thesis, semiconductor nanocrystals feature quantum confinement effects, leading to size-dependent optical properties that are ideal for tunable absorbers and emitters in various fields of application. Historically, prototypical CdSe-based core/shell nanocrystals were extensively studied as they offer bright luminescence through the whole visible spectrum. However, they present major environmental and toxicity hazards. Their use in optoelectronics, lightning, and photovoltaic can lead to nanocrystal degradation, potentially releasing highly toxic Cd^{2+} ions in the environment. Moreover, various studies have reported the cytotoxic effects of $CdSe$ quantum dots over the past years [115, 116, 117, 118].

Indium phosphide (InP) nanocrystals represent a promising, less toxic alternative to Cd-based nanocrystals [7, 119, 120] while possessing similar photoluminescence properties. They have thus quickly emerged in a variety of technological applications such as nanocrystal-based light-emitting devices [7, 8], solar cells [9], photocatalysts [10, 11], and bioimaging [12]. InP nanocrystals are usually synthesized with robust shells, protecting the nanocrystal from degradation [121].

The development of applications integrating InP nanocrystals requires a deep understanding of the fundamental optical properties of their band-edge excitons, whose recombination is at the origin of the luminescence. In particular, mapping the dark exciton states within the exciton fine structure is crucial in view of potential applications in quantum technologies based on the coherent manipulation of long-lived spin qubits [17, 18].

This chapter investigates the fundamental optical properties of single zinc-blende InP/ZnSe/ZnS nanocrystals using frequency- and time-resolved magneto photoluminescence spectroscopy. We start by giving the structural characteristics of the nanocrystals under study and their ensemble properties. We then present the results obtained from single nanocrystal measurements and propose a theoretical model and interpretation developed to fit these measurements.

The results presented in this chapter have been published in the following paper: *Revealing the Band-Edge Exciton Fine Structure of Single InP Nanocrystals*, Prin, E., Xia, C., Won, Y.-H., Jang, E., Goupalov, S.V., Tamarat, P., Lounis, B., 2023. Nano Lett. 23, 6067–6072 [105].

3.2 InP nanocrystals

The nanocrystals investigated in this study were synthesized by Yu-Ho Won and Eunjoo Jang at the *Samsung Advanced Institute of Technology* as developed in Ref. [7], and detailed in Section 2.1.1. They have a nearly spherical InP core with a diameter of 3.3 nm and a zinc-blende structure, which derives from a face-centered cubic structure. This core is embedded in an interlayer shell of $ZnSe$ with a thickness of around 3 nm and a single layer of ZnS of around 0.4 nm. Strong deviations from a spherical shape are observed in the TEM images (Fig. 3.2) due to the difficulty of growing uniform shells; the layers have a polyhedron shape with an average size of around 10.5 nm.

The semiconductor material shells are chosen depending on the alignment of the electronic bands between the core and shell layers. In the case of $InP/ZnS/ZnSe$, the shells have a wider bandgap than the core, corresponding to a type I core/shell structure as represented Fig. 3.1. Therefore, the electron and hole wavefunctions are confined in the core of the nanocrystal. Those epitaxial shells also significantly improve the photoluminescence quantum yield through surface passivation and by reducing direct contact with oxygen. Overall, it allows for a better quantum yield and more stable quantum dots.

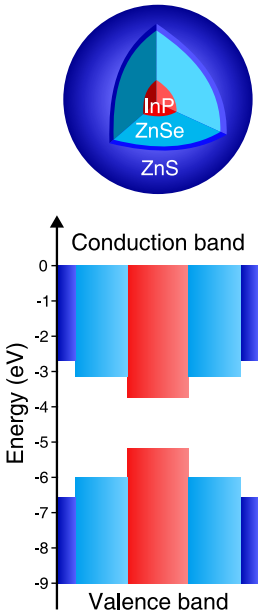

Figure 3.1: Core-shell structure of a $InP/ZnSe/ZnS$ nanocrystal. The energy values are given for bulk materials, relative to the vacuum level [122].

In InP nanocrystals, the electron ground $1S_e$ level is doubly degenerate with respect to its spin projection of $\pm 1/2$, and the hole ground $1S_{3/2}$ level is 4-fold degenerate with respect to projections $3/2$, $1/2$, $-1/2$, and $-3/2$ of its total angular momentum $J = 3/2$ [35]. The electron-hole exchange interaction [44] splits the 8-fold degenerate exciton state of spherical nanocrystals with a cubic lattice structure into an optically passive 5-fold degenerate ground state with a total angular momentum of $F = 2$ and an optically active 3-fold degenerate upper state with $F = 1$, as depicted in Fig. 3.3. Breaking the spherical symmetry in spheroidal-shaped nanocrystals leads to five band-edge exciton sublevels $F_z = \pm 2$, $\pm 1^{\mathrm{L}}$, $\pm 1^{\mathrm{U}}$, 0^{L} and 0^{U}, where F_z is the projection of the total exciton angular momentum onto the spheroid cylindrical z-axis. The deformation of the nanocrystal can happen along the z axis or perpendicularly to it. In both cases, the ground exciton level is optically forbidden, with $F_z = \pm 2$ for an oblate nanocrystal or $F_z = 0^{\mathrm{L}}$ for a prolate nanocrystal, as shown in Fig. 3.3.

Pioneering spectroscopic and time-resolved studies on ensembles of InP-based core/shell nanocrystals [123, 124, 125], suggest the presence of a dark exciton ground level located well below ($\sim$ 5-10 meV) the lowest bright exciton level for InP nanocrystals with a core size of $\sim$3 nm. These levels were respectively attributed to the ± 2 and $\pm 1^{\mathrm{L}}$ states of oblate nanocrystals [124, 125]. However, averaging over nanocrystal sizes and shapes, as well as limited spectral resolution inherent in these ensemble spectroscopic methods, may hide subtle spectral features, making the assignments of the lines to the exciton fine structure states questionable. From single-dot spectroscopic measurements coupled to fluorescence line narrowing (FLN) on InP nanocrystal ensembles [42], it was instead proposed that the band-edge exciton fine structure

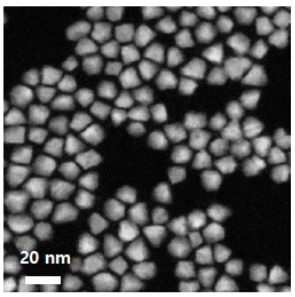

Figure 3.2: Transmission electron microscopy images of $InP/ZnSe/ZnS$ nanocrystals.

lies in the nearly spherical regime and that the single-nanocrystal emission lines stem from upper bright states $\pm 1^{\mathrm{U}}$ and 0^{U} located around 6 meV above the $F = 2$ quintuplet. However, these assignments remain elusive in the absence of spectral signatures of dark- and bright-exciton recombination measured on single InP nanocrystals, which is the focus of the following experimental study.

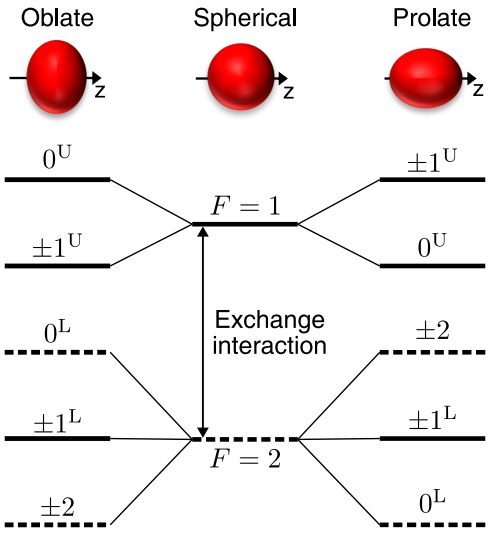

Figure 3.3: Energy-level scheme of the band-edge exciton fine structure of a zinc-blende nearly spherical InP nanocrystal. The dark levels are marked with dotted lines. While states ± 2 and 0^{L} are truly dark states, states $\pm 1^{\mathrm{L}}$ are predicted to have a reduced (respectively zero) oscillator strength for a nearly spherical (respectively spherical) nanocrystal.

3.3 Experimental results

3.3.1 Optical properties of ensemble InP nanocrystals

As a start, measurements were conducted on ensembles of nanocrystals. Performing ensemble optical spectroscopic studies, such as analyzing quantum yield, photoluminescence peak energy, linewidth, and Stokes shift, enables assessing the sample quality in terms of brightness and photostability. Ensemble optical measurements also provide valuable information on the trends in photoluminescence spectra, exciton recombination dynamics, and temperature-dependent decay mechanisms. They offer an initial insight into the mechanisms at the origin of the photoluminescence.

Absorbance and photoluminescence emission

The absorbance and emission spectra of ensemble $InP/ZnSe/ZnS$ nanocrystals at room temperature are presented in Fig. 3.4. The absorbance spectrum is characterized by an absorption peak at 2.02 eV and a dramatic absorbance increase at energies greater than 2.8 eV, caused by the thick $ZnSe$ shell. The photoluminescence emission spectrum is well-fitted by a Gaussian profile with a linewidth as narrow as 126 meV, which indicates a high degree of uniformity of the InP cores.

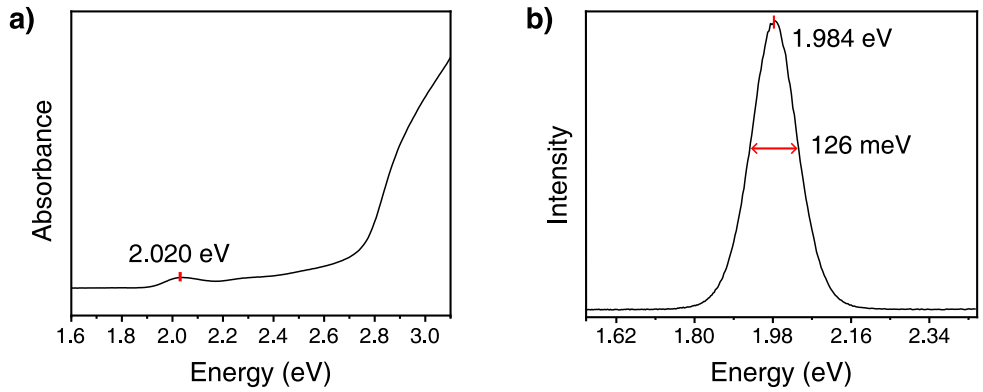

Figure 3.4: a) Room-temperature absorbance and **b)** photoluminescence spectra of ensemble $InP/ZnSe/ZnS$ nanocrystals dispersed in toluene.

Quantum yield measurements

To investigate the photoluminescence stability of the nanocrystal samples, we measured their quantum yield using a relative measurement method with Rhodamine 6G as a reference dye. We studied different batches of nanocrystals, which differed only in their processing methods. Their quantum yields were measured first right after their synthesis at the *Samsung Advanced Institute of Technology*, then a second time upon arrival at the *LP2N*, and a third time two months later. The results are presented in Table 3.1. A significant decrease in the quantum yields was observed across all samples. This drop is likely due to the oxidation of InP at the core/shell interface, as InP is highly oxophilic and prone to oxidize in the presence of water or air. This decrease in the quantum yield seems to have appeared during sample transportation, as two samples exhibited stable quantum yields when measured two months after the second measurement.

Sample	PL peak (nm)	FWHM (nm)	PLQY before shipment	PLQY day 0	PLQY day 58
1	625	39	88%	64%	64%
2	622	38	94%	49%	38%
3	624	38	85%	37%	37%

Table 3.1: Quantum yield measurements on different samples of $InP/ZnSe/ZnS$ nanocrystals.

Temperature-dependent photoluminescence spectra and decay curve

Fig. 3.5 **a)** shows ensemble photoluminescence spectra of these nanocrystals when lowering the temperature from 250 to 3.4 K. As temperature decreases, the photoluminescence peak positions show a pronounced blue shift down to 50 K. This shift is attributed to crystal contraction inducing a stronger quantum confinement effect [126, 127].

A first evaluation of the exciton recombination dynamics in these InP nanocrystals can be derived from the evolution of their photoluminescence decay with temperature. As shown in Fig. 3.5 **b)**, close to room temperature, the photoluminescence lifetime is short ($\sim$ 20 ns), which is comparable to that of prototypical $CdSe$ nanocrystals. At cryogenic temperatures, the photoluminescence decay becomes multiexponential, with a long component of ~ 1 μs at 3.4 K. As previously observed on $CdSe$ nanocrystals [128], this behavior is a signature of the thermal redistribution of populations between a long-lived, ground exciton state and the neighboring bright states.

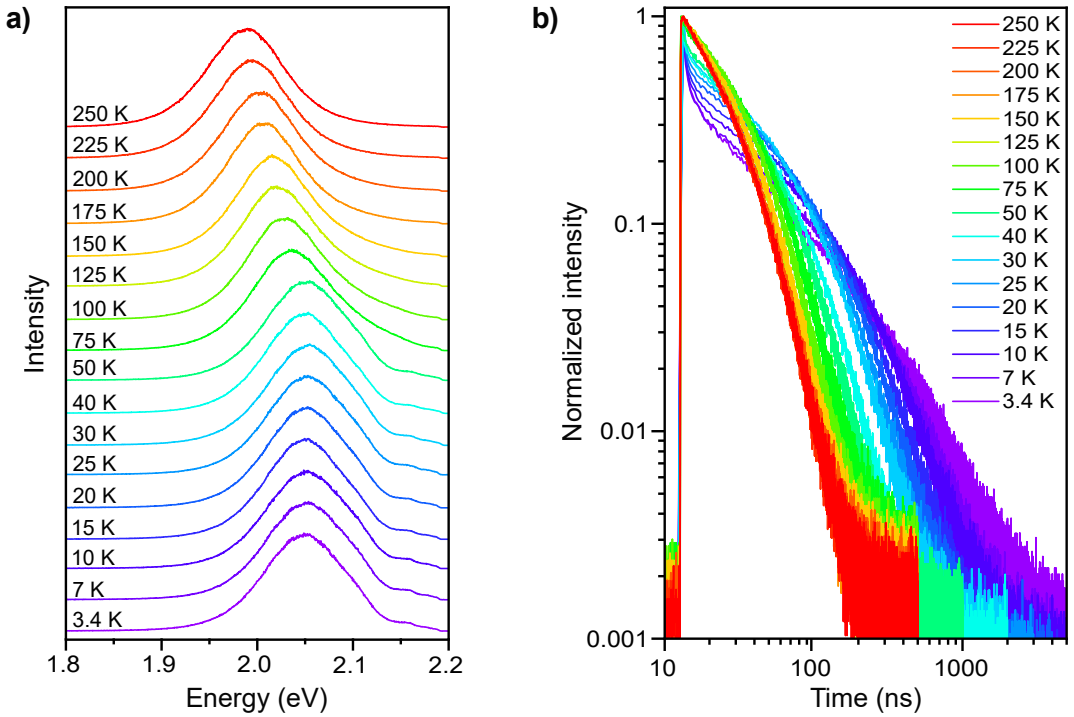

Figure 3.5: a) Photoluminescence spectra and **b)** photoluminescence decay of an ensemble of $InP/ZnSe/ZnS$ nanocrystals displayed for temperatures ranging from 250 to 3.4 K.

3.3.2 Single nanocrystal measurements

In order to investigate the band-edge exciton fine structure of these nanocrystals at the single dot level and thus get rid of inhomogeneities in sizes and shapes, we performed single nanocrystal spectroscopy measurements. The nanocrystals are dispersed in a PMMA thin film spin-cast on a sapphire coverslip and then photoexcited with a continuous laser with a wavelength of 561 nm. The sample is cooled to liquid helium temperature to reduce the population of phonons responsible for the homogeneous broadening of the emission lines. We start by studying the photoluminescence emission of these nanocrystals without any magnetic field. We then apply a magnetic field up to 7 T to the sample in the Faraday configuration.

At zero magnetic fields, the photoluminescence spectrum of a single InP nanocrystal is composed of two sharp resolution-limited lines, as shown in Fig. 3.6 **a)**. The spectral trajectories of these doublets, built with consecutive photoluminescence spectra (Fig. 3.6 **c)**), show evidence of identical spectral excursions and intensity fluctuations over time. We thus conclude that these lines stem from the same single nanocrystals and attribute them to the zero phonon recombination lines (ZPLs) of the two lowest bright exciton sublevels. As an exception, the nanocrystal whose photoluminescence spectrum and spectral trail are displayed in Fig. 3.6 **b)**

and **d)** presents a single ZPL in zero field. Overall, the bright exciton doublet splittings are distributed in the range from 0 to 1.1 meV and are presented in Fig. 3.7 as a function of their exciton recombination energy. The apparent lack of correlation between these splittings and the emitted photon energies suggests that the doublet splittings may not depend on the nanocrystal diameter but originate from nanocrystal shape anisotropy effects, as will be discussed below.

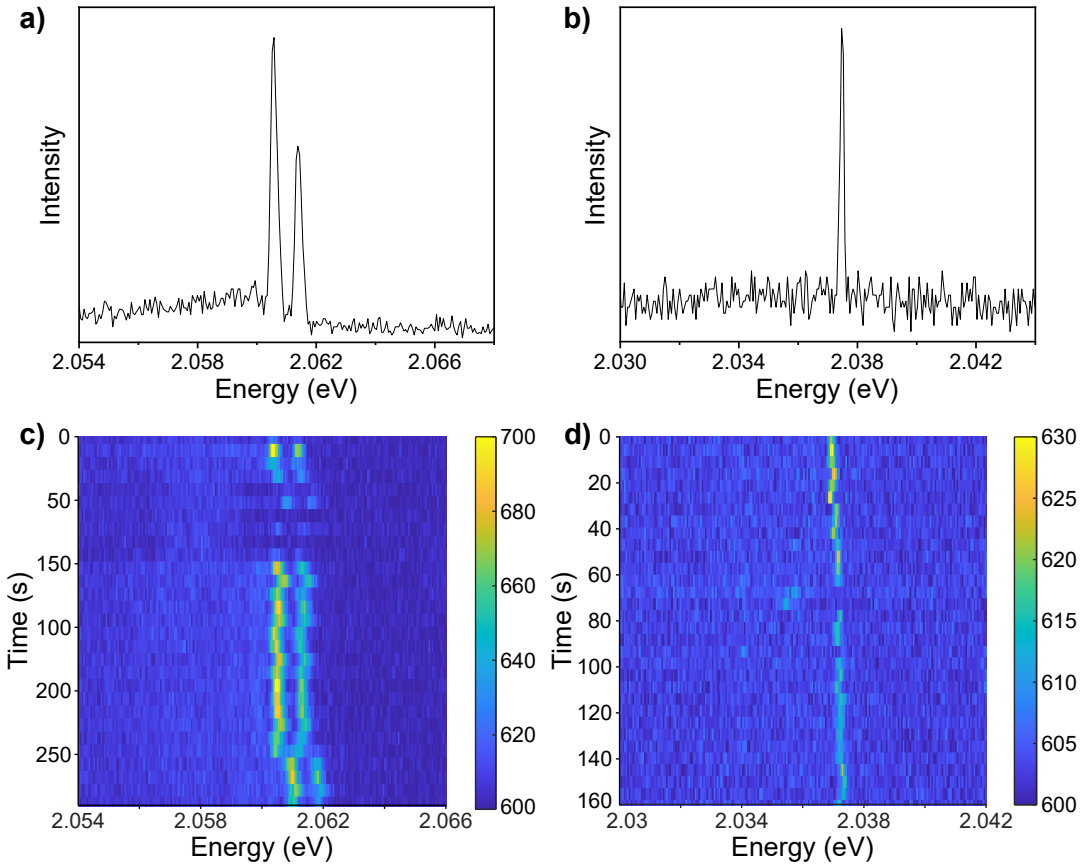

Figure 3.6: Bright exciton splittings in a zero magnetic field. The photoluminescence spectra **a)** and **b)** of two different single InP nanocrystals show doublet and singlet emission lines at 3.5 K, respectively. The spectral trails of these nanocrystals over time are displayed in **c)** and **d)**.

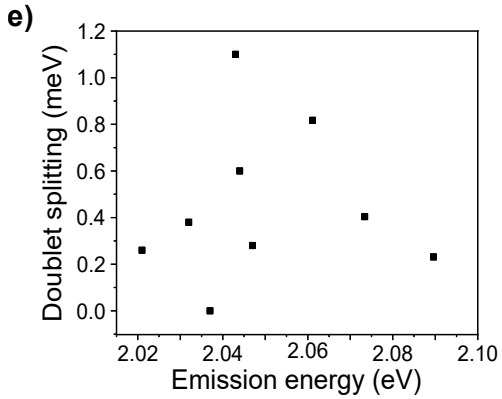

Figure 3.7: Energy splittings of spectral doublets as a function of the emission energy. The degeneracy of the doublet with emission energy 2.037 eV is strengthened by the evolution of the photoluminescence spectrum of this nanocrystal under magnetic fields, as shown in Fig. 3.8 **b)**.

Under external magnetic fields, a third line emerges on the low-energy side of the doublet and gains weight with increasing fields, as shown in Fig. 3.8 **a)** and **b)**. Other examples are presented in Fig. 3.9 and exhibit similar behaviors. As observed in single prolate $CdSe$ nanocrystals [129, 130] and single perovskite nanocrystals [58, 59, 131], the onset of a new, single ZPL under magnetic fields is the hallmark of magnetic brightening of a nondegenerate ground dark exciton level [61]. We thus rule out the possibility that the ± 2 dark level, which would split under magnetic fields [132], is the ground exciton level in these nanocrystals. The three ZPLs revealed by magneto-photoluminescence spectroscopy are therefore assigned to the nondegenerate ground exciton state 0^{L} topped by the bright exciton doublet $\pm 1^{\mathrm{L}}$ split by nanocrystal shape anisotropy [130, 133, 134]. The state ± 1 is split into two sublevels, labeled X and Y, polarized along the x and y directions at zero magnetic field (see section 3.4).

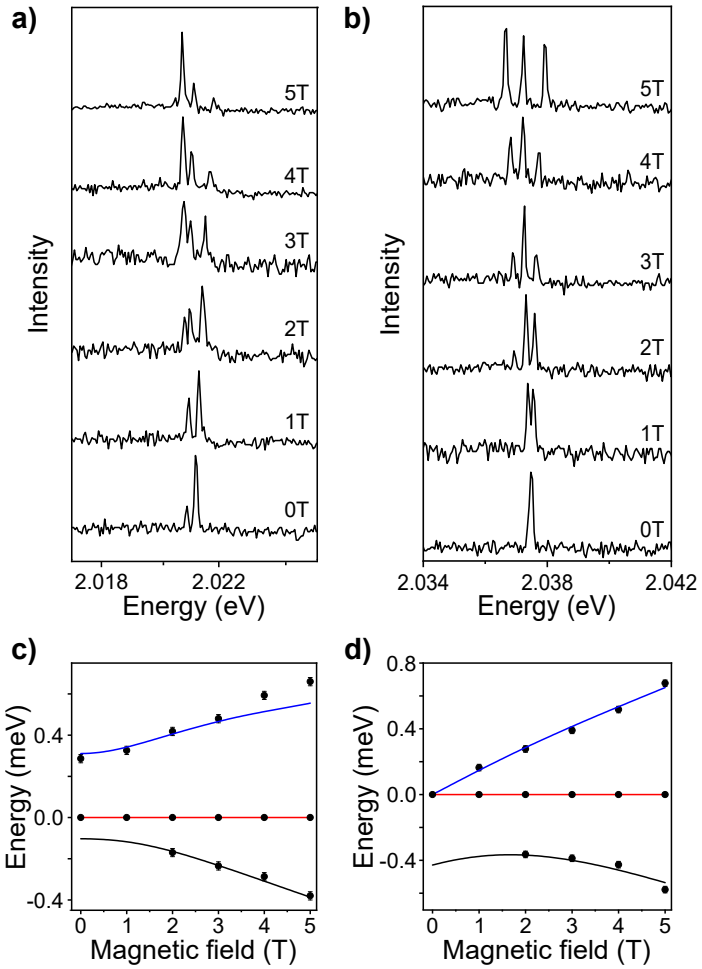

Figure 3.8: Magnetic brightening of the lowest dark exciton state of individual InP nanocrystals. **a)** and **b)** Evolution of the photoluminescence spectrum of two different single nanocrystals as a function of applied magnetic fields up to 5 T. The new line emerging on the low-energy side of the spectrum is assigned to the dark ground exciton state. The relative spectral positions of the ZPLs with respect to the ZPL assigned to the lowest bright state are respectively displayed in **c)** and **d)** as a function of the applied magnetic field. The fitting curves displayed in **c)** and **d)** are obtained in section 3.4 using the following parameters of nanocrystal nonsphericity and magnetic field orientation: $\mu_z = 0.015$, $\mu_{xy} = 3.4 \times 10^{-3}$, and $(\theta, \Phi) = (55°, 10°)$ for **c)** and $\mu_z = 0.031$, $\mu_{xy} = 0$, and $(\theta, \Phi) = (32°, 0)$ for **d)**, with (θ, Φ) being respectively the polar and azimuthal angles.

For the nanocrystal displaying a single line in zero field (the same nanocrystal as in Fig. 3.6

b)), the application of magnetic fields actually reveals that this line consists of a bright doublet with a zero-field splitting much less than the resolution limit of the spectrograph ($\sim$ 100 µeV), as demonstrated in Fig. 3.8 **b)**. Over the studied single nanocrystals, the energy splittings between the lowest dark exciton level and the center of the bright doublet range from 300 to 600 µeV, which is an order of magnitude less than those extracted from ensembles of InP-based quantum dots ($\sim$ 6 meV) [42, 123, 124, 125].

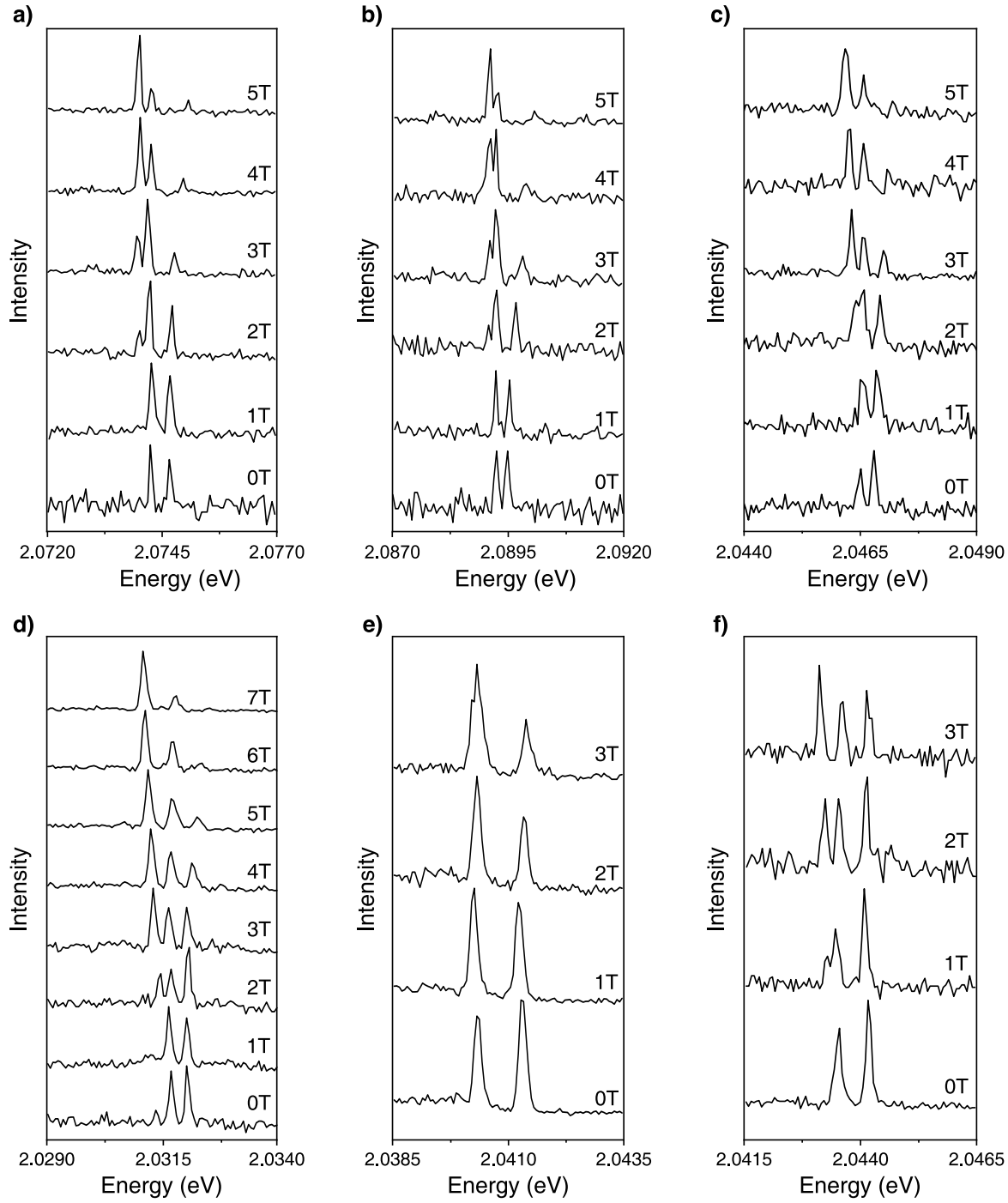

Figure 3.9: Magnetic brightening of the lowest dark exciton state of various single $InP/ZnSe/ZnS$, at T = 3.4 K. For these six nanocrystals, a new spectral line grows under the application of a magnetic field.

The magnetic brightening of the dark ground exciton is also evidenced by the field dependence of the low-temperature photoluminescence decay of single nanocrystals, as shown in Fig. 3.10 **a)**. In zero field, the decay is biexponential with a long component possessing a lifetime of around 400 ns, which is assigned to the dark exciton recombination. With increasing fields, the long-time component drastically shortens and gains weight in the photoluminescence decay, as the magnetic coupling opens a radiative recombination channel for the ground exciton via admixture in the dark state of the bright states [58] as previously observed in *CdSe* single nanocrystals [63]. The increase of the long-component decay rate Γ_L with the amplitude B of the magnetic field is displayed in Fig. 3.10 **b)**. As the splittings between the three exciton lowest states are less than 1 meV, we could consider the thermal redistribution between these three states even at liquid helium temperature. A complete model of thermal mixing between bright and dark states involves the energy splittings between the three levels, the orientation of the nanocrystal with respect to the magnetic field, the relaxation rates of these levels as well as the phonon density of states in the core-shell nanocrystal.

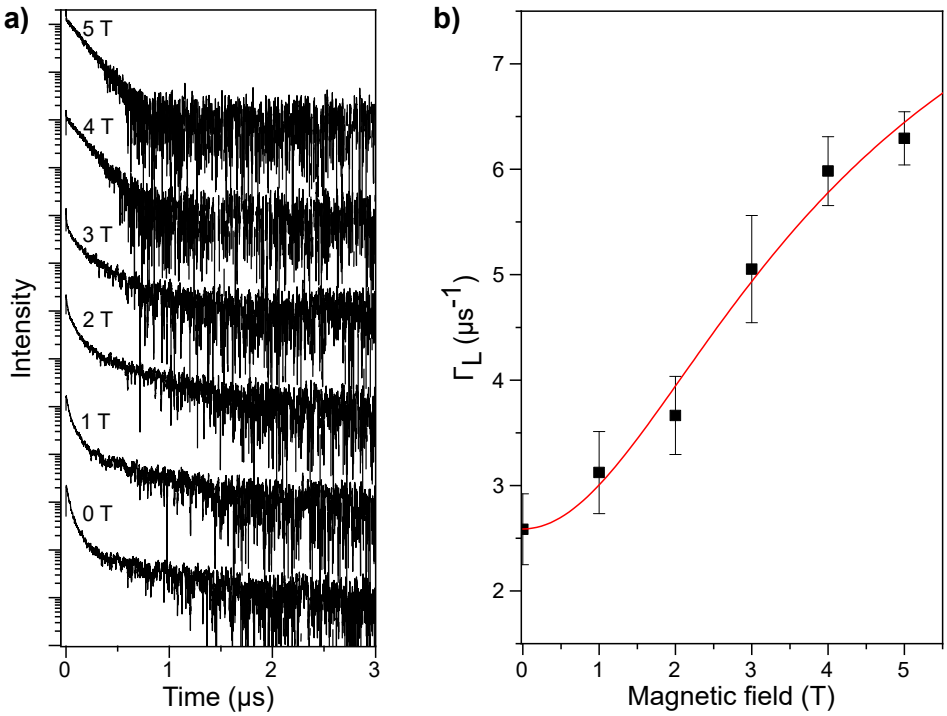

Figure 3.10: a) Photoluminescence decay curves of a single *InP* nanocrystal under various magnetic fields. The corresponding photoluminescence spectra are displayed in Fig. 3.9 **b)**. The increase in the long component decay rate Γ_L displayed in **b)** is a signature of magnetic coupling of the long-lived dark exciton state with the neighboring bright states. This evolution is modeled within the framework of the magnetic coupling model described in section 3.4 and accounts for the ground dark state (0^L) and the lowest bright exciton state (Y), having exciton recombination rates of Γ_{0L} and Γ_Y.

3.4 Theoretical model

3.4.1 Evolution of the photoluminescence decay with a magnetic field

The photoluminescence spectra show a magnetic coupling between the dark state (0^L) and the lowest bright exciton state (Y). We propose here a simplified two-level model for magnetic

coupling. The splitting between these two levels is very weak ($\sim$ 0.2 meV). Low-energy acoustic phonon modes with energy corresponding to this splitting are nonexistent in the studied nanocrystals. An acoustic phonon with such energy would necessitate a wavelength on the order of a hundred nanometers, significantly larger than the nanocrystal size, thereby creating an acoustic phonon bottleneck [62]. Considering a velocity of sound of 4500 ms^{-1} in $ZnSe$ [135], which is the most abundant material in the core-shell nanocrystal, and a core-shell nanocrystal radius of 5 nm, a rough estimation for the energy of the first acoustic phonon mode is ~ 0.6 meV, following Ref. [62]. Therefore, thermal mixing assisted by acoustic phonon modes between the lowest exciton states 0^{L} and Y is discarded. Moreover, thermal mixing between the states 0^{L} and X, which are split by 0.5 to 1 meV, is negligible at the temperature $\sim$3 K. Indeed, with $k_B T \sim 0.26$ meV, the Bose-Einstein number varies between 0.17 and 0.02 for this range of phonon energies.

To model the evolution of the photoluminescence decay with a magnetic field, we use a one-phonon thermal mixing model between the bright and the dark states, similar to the approach used for $CdSe$ nanocrystals [128]. This model involves the absorption and emission of a phonon whose energy matches the bright-dark splitting. The populations of the 0^{L} and Y states can be deduced based on the rate equations [136, 58]:

$$\begin{cases} \dot{p}_{0^{\mathrm{L}}}(t) &= \gamma_{\downarrow} p_Y - (\gamma_{\uparrow} + \Gamma_{0^{\mathrm{L}}}) p_{0^{\mathrm{L}}} \\ \dot{p}_Y(t) &= \gamma_{\uparrow} p_{0^{\mathrm{L}}} - (\gamma_{\downarrow} + \Gamma_Y) p_Y \end{cases} \tag{3.1}$$

where $p_{0^{\mathrm{L}}}(t)$ and $p_Y(t)$ are the populations at time t of the 0^{L} and Y states respectively, with initial populations $p_{0^{\mathrm{L}}}(0) = a$ and $p_Y(0) = 1 - a$, and $\Gamma_{0^{\mathrm{L}}}$ and Γ_Y are the recombination rates of the dark and first bright exciton states. $\gamma_{\uparrow}$ and $\gamma_{\downarrow}$ are the uphill and downhill thermal mixing rates between bright and dark states:

$$\begin{cases} \gamma_{\uparrow} &= \gamma_0 N_{\mathrm{B}} \\ \gamma_{\downarrow} &= \gamma_0 (N_{\mathrm{B}} + 1) \end{cases} \tag{3.2}$$

where γ_0 is a characteristic mixing rate, and N_{B} is the Bose-Einstein phonon number

$$N_{\mathrm{B}} = \frac{1}{\exp\left(\frac{E_\varphi}{k_{\mathrm{B}} T}\right) - 1}. \tag{3.3}$$

The fluorescence signal is given by:

$$S(t) = \Gamma_{0^{\mathrm{L}}} \beta^2 p_{0^{\mathrm{L}}}(t) + \Gamma_Y \alpha^2 p_Y(t), \tag{3.4}$$

with

$$\begin{aligned} \beta^2 &= \frac{1}{2}(1 - f(B)) \\ \alpha^2 &= \frac{1}{2}(1 + f(B)). \end{aligned} \tag{3.5}$$

Following the derivation of Ref. [128, 58], we get:

$$\Gamma_{\mathrm{S,\,L}} = \frac{1}{2}\left(\Gamma_Y + \Gamma_{0^{\mathrm{L}}} + \gamma_{\downarrow} + \gamma_{\uparrow} \pm \sqrt{[(\Gamma_Y - \Gamma_{0^{\mathrm{L}}}) f(B) + \gamma_{\downarrow} - \gamma_{\uparrow}]^2 + 4\gamma_{\downarrow}\gamma_{\uparrow}}\right). \tag{3.6}$$

At low temperatures, we use the approximation $\gamma_\uparrow = 0$ and $\gamma_\downarrow = 1$

$$\Gamma_{\mathrm{L}}(B) = \frac{1}{2}\left(\Gamma_Y[1 - f(B)] + \Gamma_{0^{\mathrm{L}}}[1 + f(B)]\right), \tag{3.7}$$

where $f(B)$ is a field-dependent coefficient involving the oscillator strengths of the sublevels. Assuming that the electron-hole exchange dominates the shape anisotropy splittings ($\Delta << \eta$), and that the field azimuthal angle $\varphi = 0$, the simplified Hamiltonian matrix H in the basis $\{0^{\mathrm{L}}, X, Y\}$ writes:

$$H = \begin{pmatrix} 0 & -ib\sin(\theta)\sin(\phi) & b\sin(\theta)\cos(\theta) \\ ib\sin(\theta)\sin(\phi) & \delta_0 - \frac{\Delta_{XY}}{2} & -\frac{b\cos\theta}{\sqrt{3}} \\ b\sin(\theta)\cos(\phi) & -\frac{b\cos(\theta)}{\sqrt{3}} & \delta_0 + \frac{\Delta_{XY}}{2} \end{pmatrix} \tag{3.8}$$

with $b = \frac{\sqrt{3}}{4}(g_e - 3g_h)\mu_B$, (θ, ϕ) being the polar and azimuthal angles of the magnetic field with respect to the nanocrystal z- and x-axis, respectively, δ_0 the zero-field splitting between 0^{L} and the center of the $(X,\ Y)$ sublevels and Δ_{XY} the anisotropy splitting between X and Y. The magnetic coupling $b\sin(\theta)$ between 0^{L} and Y leads to:

$$f(B) = \frac{\delta_0 - \frac{\Delta_{XY}}{2}}{\sqrt{\left(\delta_0 - \frac{\Delta_{XY}}{2}\right)^2 + 4[b\sin(\theta)]^2}}. \tag{3.9}$$

The evolution of $\Gamma_{\mathrm{L}}(B)$ is well reproduced in Fig. 3.10 **b)** using the two fitting parameters $\Gamma_Y = 0.021\,ns^{-1}$ and $\Gamma_{0^{\mathrm{L}}} = 2.5\,\mu s^{-1}$. We use electron and hole Landé factors $g_{\mathrm{e}} = 1.55$ and $g_{\mathrm{h}} = -1.5$ close to those calculated in a recent study [137] as well as a common set of field orientation angles and level splittings to reproduce both the ZPL spectral shifts of Fig. 3.11 and the photoluminescence decay of this nanocrystal.

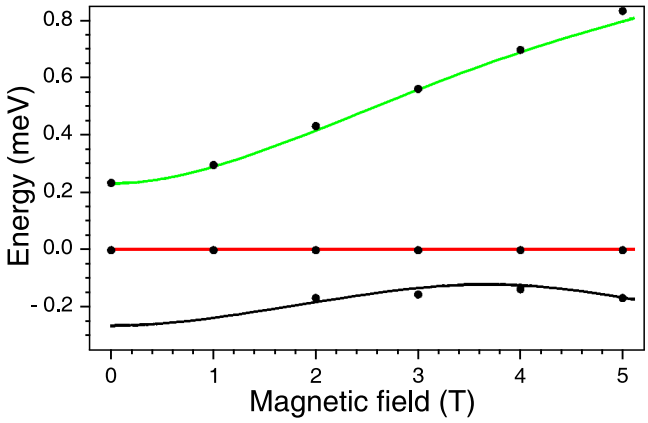

Figure 3.11: Spectral shifts as a function of the magnetic field, for the same nanocrystal than Fig. 3.10. The fits are made using the same set of parameters $\Gamma_{\mathrm{Y}} = 0.021\,ns^{-1}$, $\Gamma_{0^{\mathrm{L}}} = 2.5\,\mu s^{-1}$, $\theta = 10°$; $\varphi = 0°$, $\Delta_{XY} = -0.23$ meV, $g_e = 1.55$ and $g_h = -1.5$.

3.4.2 Effect of shape anisotropy

In order to theoretically reproduce our experimental spectroscopic findings, we model the band-edge exciton fine structure of zinc-blende InP nanocrystals with a spin Hamiltonian, in a similar manner that the model developed for $CdSe$ quantum dots in Ref. [130], by including the effect of shape anisotropy on the valence band energy but neglecting the anisotropy exchange interac-

tion [35, 138, 139, 140]:

$$\hat{H} = \underbrace{-\eta(\hat{\boldsymbol{\sigma}}.\hat{\boldsymbol{J}})}_{\textcircled{1}} \underbrace{-\frac{\Delta}{2}\left(\hat{J}_z^2 - \frac{5}{4}\right)}_{\textcircled{2}} \underbrace{+\frac{C}{\sqrt{3}}\left(\hat{J}_x^2 - \hat{J}_y^2\right)}_{\textcircled{3}} \underbrace{+\mu_B \frac{g_e}{2}(\hat{\boldsymbol{\sigma}}.\boldsymbol{B}) - \mu_B g_h(\hat{\boldsymbol{J}}.\boldsymbol{B})}_{\textcircled{4}} \tag{3.10}$$

In this expression, $\hat{\sigma}_\alpha$ ($\alpha = x, y, z$) are the Pauli matrices, $\hat{J}_\alpha$ represents the matrices of the angular momentum $J = 3/2$, g_e and g_h are the electron and hole effective Landé factors, μ_B is the Bohr magneton, and $\mathbf{B}$ is the magnetic field. The characteristic energies η, Δ, and C are calculated using the nanocrystal material and shape parameters as detailed hereafter.

The first term ❶ of Eq. 3.10 serves spherical symmetry and describes the electron-hole exchange interaction [44, 139, 140], which splits the band-edge exciton into the 3-fold degenerate bright level with $F = 1$ and the 5-fold degenerate dark level with $F = 2$, as depicted in Fig. 3.3. The parameter η consists of the short-range and long-range contributions of the electron-hole exchange interaction in a spherical nanocrystal. It can be expressed as [139, 140]:

$$\eta = \left(\frac{a_B}{R}\right)^3 \left(\chi(\beta)\hbar\omega_{TF} + \frac{\pi}{9}\zeta(\beta)\hbar\omega_{LT}\right) \tag{3.11}$$

where $a_B = 9.6$ nm is the bulk exciton Bohr radius [141] and R is the nanocrystal radius. $\hbar\omega_{TF}$ and $\hbar\omega_{LT}$ are, respectively, the short-range and longitudinal-transverse splittings of the exciton-polariton in bulk InP, with the following expressions [139]:

$$\hbar\omega_{TF} = \frac{2}{\pi}\left(\frac{a_0}{a_B}\right)^3 \varepsilon_{exch} \tag{3.12}$$

$$\hbar\omega_{LT} = \frac{4}{\kappa_b a_B^3}\left(\frac{e\hbar p_{cv}}{m_0 E_g}\right)^2 \tag{3.13}$$

We use the values $\hbar\omega_{TF} = 0.04$ meV and $\hbar\omega_{LT} = 0.17$ meV from Ref. [141]. The dimensionless parameters $\chi(\beta) = 0.180$ and $\zeta(\beta) = 0.072$ are defined following Ref. [139]:

$$\chi(\beta) = \frac{\pi R^3}{3}\int_0^1 dx\, x^2 \psi_e^2(x)\left(f_0^2(x) + \frac{1}{5}f_2^2(x)\right), \tag{3.14}$$

$$\zeta(\beta) = \frac{1}{(2\pi)^3}\int_0^\infty dy\, y^2 \left[I_0(y) + I_2(y)\right]^2, \tag{3.15}$$

$$I_\ell(y) = 4\pi R^{\frac{3}{2}}(-1)^{\frac{\ell}{2}}\int_0^1 dx\, x^2 f_\ell(x)\psi_e(x) j_\ell(xy), \tag{3.16}$$

where $\beta = 0.156$ is the light-to-heavy hole effective mass ratio $\beta = \frac{\gamma_1 - 2\gamma}{\gamma_1 + 2\gamma}$ with $\gamma = \frac{2\gamma_2 + 3\gamma_3}{5}$. γ_1, γ_2 and γ_3 are the Luttingers parameters with values taken from Ref. [142] for InP: $\gamma_1 = 4.6$, $\gamma_2 = 1.6$ and $\gamma_3 = 1.73$. The expression of $\chi(\beta)$ has been derived in Ref. [35], those of $\zeta(\beta)$ and $I_\ell(y)$ in Ref. [139]. Here $f_\ell(x)$ is the radial part of the hole wave function corresponding to the orbital angular momentum ℓ ($\ell = 0, 2$) and depends on the dimensionless radial coordinate $x = r/R$. $j_\ell(xy)$ is the spherical Bessel function and $\psi_e(x)$ is the electron envelope wave function.

The electron envelope wavefunction of a particle in a spherical box for core-only nanocrystals is given by [139]:

$$\psi_e(x) = \frac{1}{\sqrt{2\pi R^3}}\frac{\sin(\pi x)}{x}. \tag{3.17}$$

Core/shell $InP/ZnSe$ nanocrystals have a conduction band offset of about $V_c = 770$ meV [143]. Therefore, the electron can tunnel into the shell, while we assume that the hole is localized within the core. The electron envelope wavefunction should therefore be replaced by:

$$\psi_e(x) = \frac{A}{\sqrt{2\pi R^3}} \frac{\sin(\phi_e x)}{x}, \tag{3.18}$$

where ϕ_e is the root of the equation from the interval $\left[\frac{\pi}{2}, \pi\right]$:

$$\sin(x) = \sqrt{\frac{\hbar^2}{2m_e R^2 V_c}} x, \tag{3.19}$$

m_e is the electron effective mass and

$$A = \sqrt{\frac{\kappa R}{\kappa R + 1}}, \tag{3.20}$$

with

$$\hbar\kappa = \sqrt{2m_e V_c - \frac{\hbar^2 \phi_e^2}{R^2}}. \tag{3.21}$$

Given the conduction and valence band offsets between the InP core and the $ZnSe$ shell [143], it is assumed that $0 \leq x \leq 1$; the hole essentially resides in the core, while the electron, having a much lower effective mass, is distributed over the core-shell nanocrystal. This effect reduces the electron-hole overlap compared to core-only nanocrystals and, thus, the strength η of the electron-hole exchange interaction. Fig. 3.12 illustrates the difference in the electron envelope wavefunctions between the core-only and core/shell structures.

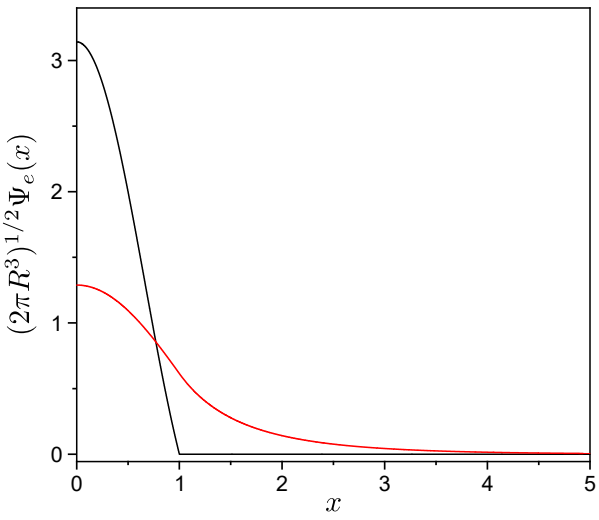

Figure 3.12: Electron envelope wavefunction in a spherical box model (black curve) and in a spherical well with a finite barrier (red curve).

For core/shell nanocrystals, we must also consider the difference in the dielectric permittivities of the nanocrystal core $\varepsilon_{\text{core}}$ and its environment $\varepsilon_{\text{shell}}$ in the expression of η. The new expression η', derived in Ref. [139] is given by:

$$\eta' \left(\frac{R}{a_B}\right)^3 = \eta \left(\frac{R}{a_B}\right)^3 + \frac{1}{3}\hbar\omega_{LT} \frac{\varepsilon_{\text{core}} - \varepsilon_{\text{shell}}}{\varepsilon_{\text{core}} + 2\varepsilon_{\text{shell}}} \left[\int_0^1 f_0(x) sin(\pi x) x dx\right]^2 \tag{3.22}$$

Here, we take $\varepsilon_{\text{core}} = 9.6$ for the InP core [40] and $\varepsilon_{\text{shell}} = 5.7$ for the $ZnSe$ shell [144] leading to $\eta' = 2.42$ meV.

The second term ❷ of Eq. 3.10 introduces a cylindrically symmetric perturbation resulting from a uniaxial deformation that transforms the nanocrystal shape from spherical to spheroidal [5]. As sketched in Fig. 3.3, this term further splits the exciton sublevels with respect to the quantum number $|F_z|$. It also mixes states $\pm 1^{\text{L}}$ and $\pm 1^{\text{U}}$, leading to the partial brightening of $\pm 1^{\text{L}}$. The resulting energy levels for these $InP/ZnSe$ core/shell nanocrystals are shown in Fig. 3.13 with blue dashed lines as functions of the parameter $\mu_z = 2\frac{c-a}{c+a}$, where $a \equiv b$ and c are the semiaxes along x, y, z of the InP spheroid core having the same volume as a sphere of diameter 3.3 nm. The parameter Δ is the net splitting of the hole state as defined in Chap.1 for a deformation along one axis [5].

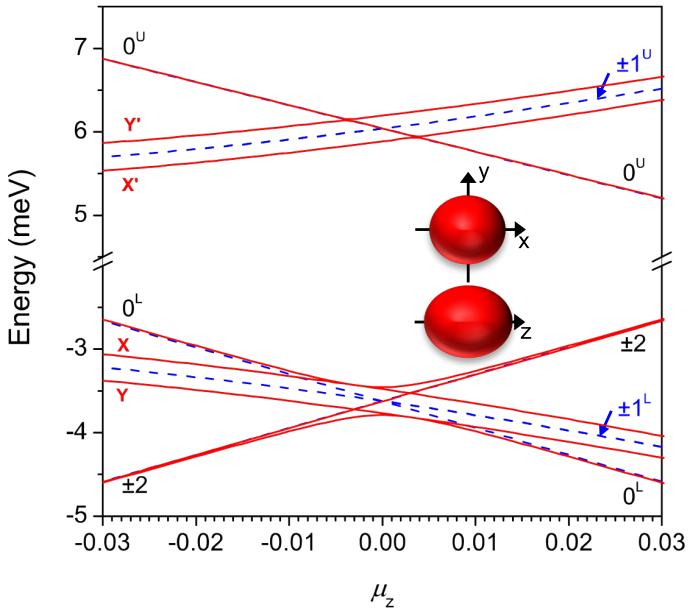

Figure 3.13: Band-edge exciton fine structure of a core-shell InP nanocrystal with a zinc-blende crystal structure. The band-edge exciton fine structure is calculated as a function of the nanocrystal core aspect ratio μ_z around the region where the heavy-hole and light-hole exciton branches cross. The nanocrystal core has the same volume as a sphere with a diameter of 3.3 nm. The blue dashed lines give the fine structure of a nanocrystal with no shape anisotropy in the (x, y) plane ($\mu_{xy} = 0$), while the solid red curves correspond to the case where $\mu_{xy} = 0.003$. Shape anisotropy in the (x, y) plane ($\mu_{xy} \neq 0$) introduces splittings of the $\pm 1^{\text{L}}$ sublevel (into states denoted X and Y) and the $\pm 1^{\text{U}}$ sublevel (into states denoted X' and Y') as well as complex level anticrossings within the $F = 2$ quintuplet. The inset illustrates the spheroidal perturbations for $\mu_z > 0$ and $\mu_{xy} > 0$.

The third term ❸ of Eq. 3.10 is responsible for further reduction of the nanocrystal shape symmetry, whereby the nanocrystal shape is stretched along the x direction and simultaneously squeezed along the y direction while preserving its elongation along the z direction [138]. It leads to the splitting of the sublevels with $F_z = \pm 1$ into states X and Y polarized along the x and y directions in zero magnetic field. The energy levels calculated for such nanocrystals are shown in Fig. 3.13 with red solid lines for an x, y anisotropy parameter $\mu_{xy} = 2\frac{a-b}{a+b} = 0.003$, with a and b now being distinguished for a triaxial ellipsoid. Unlike the first part of Eq. 3.10, parameters Δ and C only refer to the valence-band hole and remain the same for core-only and

core-shell nanocrystals.

Let us note that our choice of z for the main deformation axis of the nanocrystal shape implies that $|\mu_{xy}| \ll |\mu_z|$. The splittings due to nanocrystal shape nonsphericity are further affected by the anisotropic exchange interaction [138], which can be neglected for the exciton quintuplet $F = 2$ with low oscillator strength. The definition of the parameter C can be found in Ref. [138]:

$$C = \frac{\sqrt{3}}{2}\mu_{xy} v(\beta) E_h(\beta). \tag{3.23}$$

$v(\beta)$ is given by

$$v(\beta) = -\frac{1}{3\varphi(h)^2}\frac{1}{(2\pi)^3}\int_0^\infty dy\, y^4 \left[\frac{1-\beta}{2\beta}\left(\mathcal{I}_2^0(y) - \frac{1}{5}\mathcal{I}_2^2(y)\right) + \frac{2}{5}\frac{1+\beta}{\beta}\mathcal{I}_0(y)\mathcal{I}_2(y)\right], \tag{3.24}$$

with

$$\mathcal{I}_0(y) = 4\pi\int_0^1 dx\, x^2 j_0(xy) f_0(x), \tag{3.25}$$

and

$$\mathcal{I}_2(y) = -4\pi\int_0^1 dx\, x^2 j_2(xy) f_2(x). \tag{3.26}$$

Here its value is $v(\beta) = -0.066$.
$E_h(\beta)$ is the energy of the hole level in a perfectly spherical nanocrystal of radius R:

$$E_h(\beta) = \frac{\hbar^2 \varphi_h^2(\beta)}{2 m_{hh} R^2}, \tag{3.27}$$

where $\varphi(\beta)$ is the first root of equation [35]:

$$j_0(\varphi) j_2(\sqrt{\beta}\varphi) + j_2(\varphi) j_0(\sqrt{\beta}\varphi) = 0 \tag{3.28}$$

with $j_n(x)$ the spherical Bessel functions of order n. Here we use $\frac{C}{\mu_{x,y}} = 55.6$ meV.

Finally, the last two terms ❹ of Eq. 3.10 account for Zeeman splitting in external magnetic fields [35] and are used to fit the experimental evolutions of the photoluminescence spectra and photoluminescence decay under increasing magnetic fields in Fig. 3.8 **c)** and **d)**, Fig. 3.10 **b)** and Fig. 3.11.

In light of the energy-level diagrams of Fig. 3.13, our spectroscopic findings over a variety of single nanocrystals show evidence that the magnetically brightened exciton state is the non-degenerate ground dark 0^L state, which points to a prolate regime of the InP cores ($\mu_z > 0$). Moreover, the bright-dark splittings ranging from 300 to 600 µeV are consistent with the fine structure regime of slightly prolate nanocrystals with $\mu_z < 0.03$. The X-Y splittings with an average 400 µeV point to a tiny shape anisotropy in the (x, y) plane with an average $\mu_{x,y} \approx 0.003$. These results highlight the power of single-nanocrystal spectroscopy to unveil subtle deviations in nanocrystal morphologies and confirm that the InP nanocrystal cores prepared with this synthesis method [7] are highly uniform and almost spherical.

Interestingly, our findings and modeling provide an alternative interpretation of the previous FLN experiments conducted on an ensemble of similar nanocrystals in Ref. [124]. In this study, they investigate $InP/ZnSe$ core/shell nanocrystals with core diameters ranging from 2.9 to 3.6 nm. They use photoluminescence decay at different temperatures, Raman spectroscopy, and the FLN method at 4 K to perform size-selective spectroscopy under high magnetic fields. In

FLN spectroscopy, a monochromatic laser resonantly excites a small subensemble of nanocrystals to the bright states of the exciton branch $F = 1$. Employing circularly polarized excitation predominantly excites either the $F = -1$ or $+1$ states.

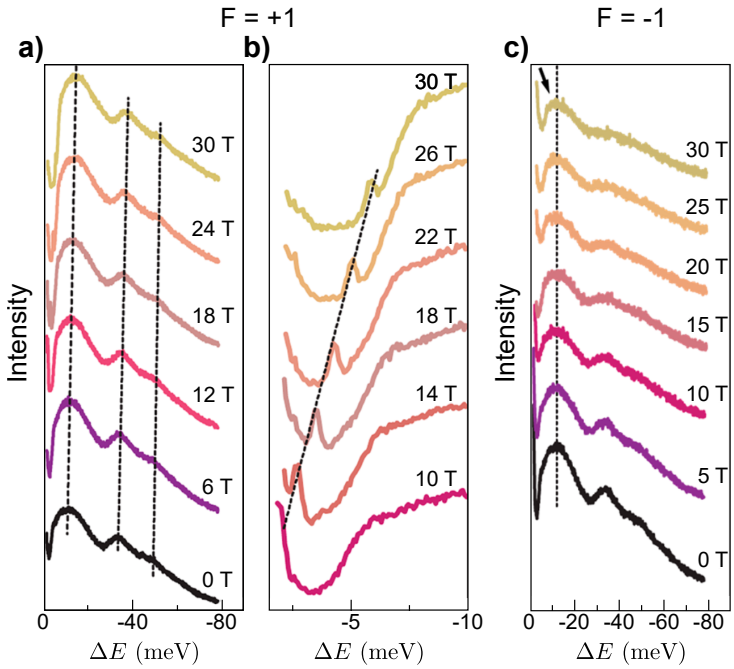

Figure 3.14: Figure from Ref. [124]. **a)** FLN spectra at 4 K upon excitation of the bright $F = +1$ state with σ^+ light of 2.1 eV, at variable magnetic fields. The excited state at 2.1 eV (the excitation laser energy) is taken as a reference and set to 0 meV. **b)** Zoom-in of the spectra at small ΔE. **c)** FLN spectra at 4 K upon excitation of the bright $F = -1$ with σ^- light of 2.1 eV.

Fig. 3.14 **a)** and **b)** illustrate the results of their FLN experiments, obtained with σ^+ circularly polarized excitation light and with detection of the σ^- circularly polarized emission. This configuration predominantly excites the upper $F = +1$ state. In these spectra, the bright $F = +1$ state is set as the energy zero reference. Fig 3.14 **c)** presents the outcomes obtained through excitation of the bright state with σ^- circularly polarized light and detection of the σ^+ circularly polarized emission. In this case, the $F = -1$ level is predominantly excited and serves as the reference energy in the spectra.

In the FLN spectra, the energy separation observed between the $F = \pm 1$ state and the peak with the highest intensity ranges from 6 to 16 meV, depending on the InP core diameter. They attribute the most intense FLN peak to a phonon replica of the dark state (which is, for them, the ± 2 state). Therefore, they estimate the splitting between the $F = \pm 1$ state and the dark state to range from 2 to 9 meV. However, our interpretation is as follows: after rapid nonradiative relaxation to the lowest branch $F = 2$, the emission stems from states $\pm 1^{\mathrm{L}}$ having weaker oscillator strengths. The reported shifts between the excitation photon energy and the narrow photoluminescence line correspond to the splitting between branches $F = 1$ and $F = 2$, following our calculations of the fine structure.

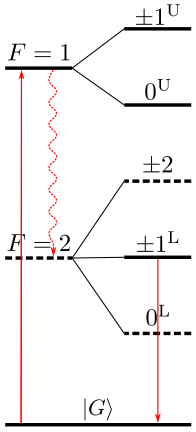

3.5 Complementary observations

It should be noted that during our experimental spectroscopic study, another photoluminescence emission behavior was observed in single nanocrystals. Many of the studied nanocrystals displayed a single emission line at zero magnetic fields, without any further splitting as the magnetic field increased. Fig. 3.15 illustrates this behavior for three different nanocrystals. This phenomenon is unexpected and challenging to explain, as no similar behaviors have been reported in the literature. This type of spectra has been consistently observed for all studied InP samples and constitutes around 70% of the observed nanocrystals. While a single exciton emission line under a magnetic field could be explained by the misalignment of the crystal orientation with respect to the magnetic field, this is highly unlikely to happen to such a high percentage of nanocrystals.

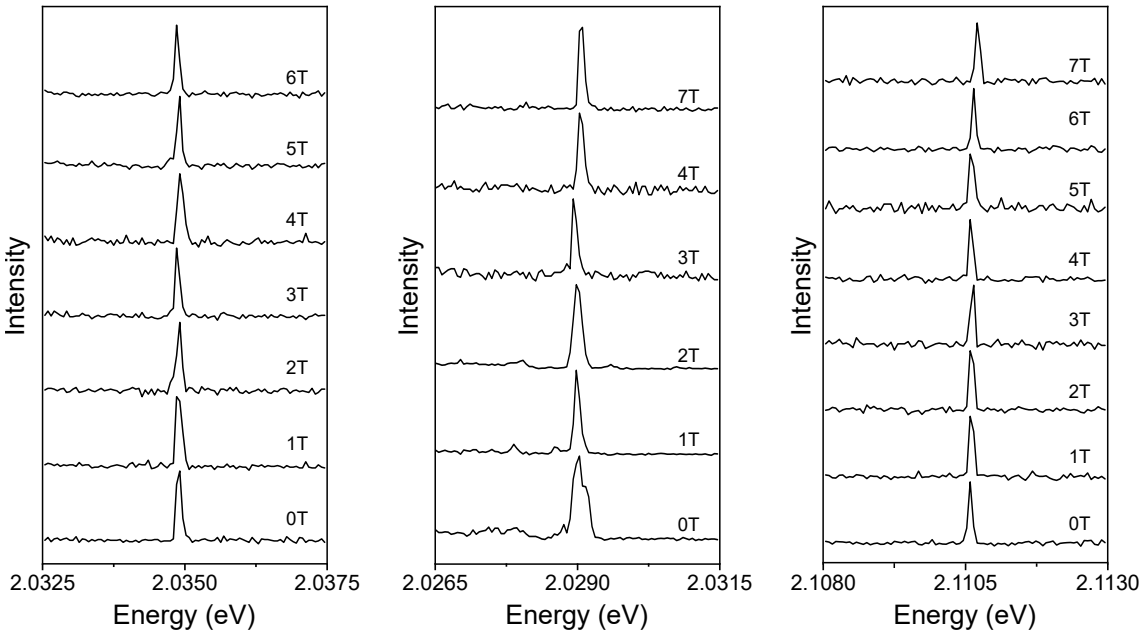

Figure 3.15: Example of spectra from three nanocrystals presenting a single line emission with no splitting and no new line appearing under an external magnetic field.

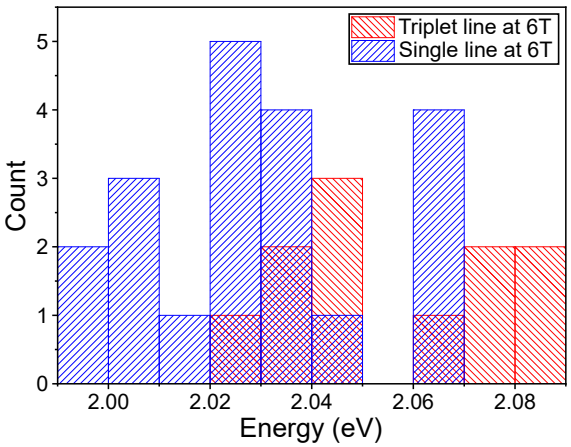

Figure 3.16: Histogram of the emission energy for nanocrystals presenting a single line under magnetic field (in blue) and nanocrystals presenting three lines with a 6 T magnetic field (in red).

Fig. 3.16 shows the distribution of emission energy for nanocrystals exhibiting a single line under a magnetic field of 6 T, compared to nanocrystals displaying three lines. The repartition of the emission energies is comparable for both cases. Therefore, it suggests that both emission behaviors originate from the same chemical species.

One possible explanation is that the single line observed may correspond to the emission from a positive trion. If the relaxation rate from the highest trion state is high enough to produce emission from the lowest trion state and if $\Delta_h \approx 0$, we would not observe a splitting under a magnetic field of 7T, as schematized in Fig. 3.17. A study of the photoluminescence decay with a magnetic field would allow verifying this hypothesis, as we would expect a monoexponential decay (instead of a biexponential decay in the case of exciton emission due to the existence of the lower dark state).

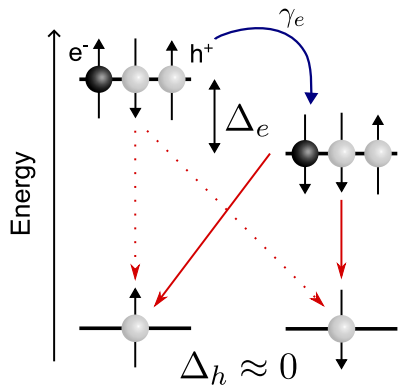

Figure 3.17: Scheme of the recombination path of a positive trion.

3.6 Conclusion

In this chapter, we presented the results obtained for photoluminescence measurements on ensemble and single $InP/ZnS/ZnSe$ core/shell nanocrystals. Magneto-photoluminescence investigations of single $InP/ZnSe/ZnS$ at liquid helium temperatures revealed highly resolved spectral fingerprints of the three lowest exciton fine structure states. We provide evidence that they stem from the recombination of the ground dark exciton 0^{L} and the lowest bright $\pm 1^{\mathrm{L}}$ states, whose degeneracy is lifted by the nanocrystal shape anisotropy. The 0^{L} ground state seems to be a truly dark state from which luminescence is evidenced only under magnetic fields, as in prolate $CdSe$ nanocrystals [129]. The evolutions of the energy levels and photoluminescence decays with applied magnetic fields are well reproduced with a band-edge exciton fine structure model accounting for the InP core shape anisotropy. Our spectral fingerprints are extremely sensitive to nanocrystal morphologies and unveil highly uniform shapes with prolate deviations of less than 3 % from perfect sphericity. These spectroscopic results and calculations set the foundations of refined theoretical models of the exciton fine structure and its magnetic properties in these nanostructures.

Chapter 4

Band-Edge Exciton Fine Structure of Lead Halide Perovskites Nanocrystals

4.1 Introduction

Lead halide perovskite nanocrystals open great prospects for a multitude of applications ranging from photovoltaics to optoelectronics [106, 19, 145, 146] and potential applications as quantum light sources [147, 148, 149, 150, 59, 151]. While intense experimental and theoretical efforts have been made to explore their unique optical and electronic properties, the physics of band-edge charge complexes, whose recombination is at the origin of the photoluminescence, remains unclear. For instance, the ordering of bright and dark sublevels in the exciton fine structure was a subject of debate at the beginning of my Ph.D. thesis, though essential for the development of quantum light sources [20, 21, 22], and for spin-based technologies [23, 24, 25]. Among lead halide perovskite, cesium lead bromide ($CsPbBr_3$) perovskite nanocrystals are the test bench materials for next-generation devices. The band-edge exciton of $CsPbBr_3$ is expected to split by electron-hole exchange interaction into a dark ground singlet state (with zero angular momentum) and a bright triplet (with angular momentum unity) [152, 153, 154, 155]. However, since cesium lead halide perovskite nanocrystals exhibit strong photoluminescence with triplet line emission at cryogenic temperatures [102, 55, 156, 157, 51], it has been proposed that a Rashba effect reverses the fine structure level ordering and places the dark singlet above the bright triplet as detailed in Section 1.1.8 [51, 56, 158, 159], making perovskites an exception among all bulk semiconductors and all existing semiconductor heterostructures. Before my Ph.D. thesis, low-temperature single-nanocrystal magneto-optical spectroscopy provided direct signatures of the dark singlet exciton emission in hybrid organic-inorganic formamidinium lead bromide $FAPbBr_3$ [58] and inorganic cesium lead iodide $CsPbI_3$ [59] nanocrystals showing that the singlet is positioned a few meV below the bright triplet. These findings align with theoretical estimations of confined exchange interaction. However, the observation of dark singlet emission from $CsPbBr_3$ was still pending.

In addition, no general picture is available for many-body Coulomb interactions in perovskites, besides investigations of the size dependence of the biexciton and trion binding energies in single $FAPbBr_3$ nanocrystals [101]. The biexciton binding energy has important consequences in the development of perovskite-based light-emitting technologies since a large shift of the biexciton recombination lines with respect to those of the band-edge exciton would reduce the emission color purity under high-flux excitation. Its sign also fixes the transition

that may sustain population inversion and nanocrystal gain for lasing applications [160]. For $CsPbBr_3$ perovskites, contradictory results have been reported on the amplitude and sign of the biexciton energy shift in the range -100 meV to 100 meV, using time- and spectrally- resolved photoluminescence [161, 162, 163], transient absorption [164, 165, 166, 167] or nonlinear [168] spectroscopic methods on nanocrystal ensembles. Single-nanocrystal spectroscopy on $CsPbBr_3$ and $CsPbI_3$ perovskites lead to estimations of the biexciton binding energy at room-temperature with inherently low spectral precision and even uncertainties on the sign of the interaction [169].

In this chapter, we present the results of low-temperature magneto-optical spectroscopy on nearly bulk $CsPbBr_3$ and $CsPb(BrCl)_3$ single nanocrystals to reveal their entire band-edge exciton fine structure and charge-complex binding energies. We then combine these results with spectroscopic measurements on various perovskite nanocrystal compounds to develop universal scaling laws relating the exciton fine structure splitting, the trion and biexciton binding energies to the band-edge exciton energy in lead-halide perovskite nanostructures, regardless of their chemical composition.

The results presented in this chapter have been published in the following paper: *Universal scaling laws for charge-carrier interactions with quantum confinement in lead-halide perovskites*, Tamarat, P., Prin, E., Berezovska, Y., Moskalenko, A., Nguyen, T.P.T., Xia, C., Hou, L., Trebbia, J.-B., Zacharias, M., Pedesseau, L., Katan, C., Bodnarchuk, M.I., Kovalenko, M.V., Even, J., Lounis, B., 2023. Nat Commun 14, 229 [131].

4.2 Structural and optical properties

The samples of $CsPbBr_3$ and $CsPb(BrCl)_3$ used in this study have been prepared by Y. Berezovska, A. Moskalenko, M. I. Bodnarchuk and M. V. Kovalenko in the Empa-Swiss Federal Laboratories for Materials Science and Technology and Institute of Inorganic Chemistry, at ETH Zürich.

4.2.1 Nearly-bulk $CsPbBr_3$ nanocrystals

Magnetic brightening of the dark exciton state is challenging in $CsPbBr_3$ perovskite nanocrystals as the photoluminescence intensity of the dark state is inversely proportional to the square of the bright-dark energy splitting, while the bulk electron-hole exchange interaction in this material is particularly strong among lead-halide perovskites [59]. Moreover, confinement effects in nanocrystals enhance the exciton fine structure splittings, which makes magnetic brightening of the dark singlet even more difficult. The $CsPbBr_3$ nanocrystals specifically prepared for this study are nanorods with sides that largely exceed the bulk exciton Bohr radius a_B ~3.1 nm in order to minimize quantum confinement effects on the dark-bright exciton splittings.

These large nanocrystals are synthesized under ambient conditions employing the ligand-assisted reprecipitation (LARP) approach, using a novel ligand molecule, oleylguanidinium bromide (OGB), to obtain dispersible and large $CsPbBr_3$ perovskite nanocrystals. First, for the synthesis of OGB ligands, Oleylamine (1 eq) was added to S-ethylisothiourea hydrobromide (1.2 eq) suspended in tetrahydrofurane (THF). The resulting mixture was stirred at room temperature overnight. Then THF was evaporated under reduced pressure and the resulting residue was recrystallized with diethylether (Et_2O). The obtained precipitate was washed several times with Et_2O and dried under reduced pressure overnight at 50 °C. The structural formula of OGB is given in Fig. 4.1.

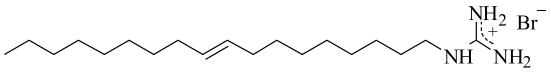

Figure 4.1: Structural formula of N-(octadec-9-en-1-yl)guanidinium hydrobromide (oleylguanidinium bromide, OGB) ligands.

For the synthesis of OGB-capped $CsPbBr_3$ nanocrystals, the hybrid precursor solution was prepared by mixing solutions of 90 µL of $PbBr_2$ (0.67 M in DMF), 465 µL of $CsBr$ (0.043 M in DMF-DMSO in ratio 1:1) and 300 µL of OGB (1 M in DMF), where DMF denotes dimethyl formamide and DMSO dimethyl sulfoxide. 75 µL of the hybrid precursor solution was injected into a 4 mL vial containing 2.5 mL of vigorously stirred mesitylene to initiate fast nucleation of the $CsPbBr_3$ nanorods. The green solution with bright green luminance could be observed in 15-20 s. To purify the $CsPbBr_3$ nanocrystals, 0.25 mL of ethyl acetate was added to 0.5 mL of the crude solution, followed by centrifugation for 4 min at 4250 × g. The supernatant was discarded and the precipitate was dispersed in 0.4 mL of toluene. The solution of $CsPbBr_3$ nanocrystals was then diluted 50 times into a solution of polystyrene (1 wt%) in toluene, and 25 µL of the resulting solution was spin-coated on a clean sapphire substrate for low-temperature magneto-optical spectroscopic measurements, as described in Section 2.3.2.

The 3D size and shape of these OGB-capped $CsPbBr_3$ nanocrystals are characterized using 45°-tilted scanning electron microscopy (Fig. 4.2). With average base lengths of 195 ± 18 nm,

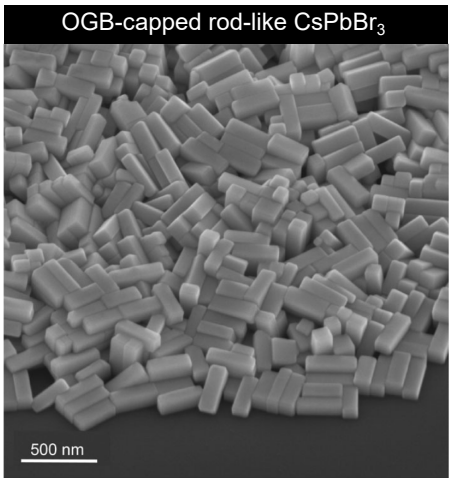

Figure 4.2: Scanning electron microscopy image of large OGB-capped $CsPbBr_3$ nanocrystals.

41 ± 8.5 nm and a thickness of ∼40 nm, these nanocrystals are nearly bulk-like particles with reduced quantum confinement. The crystal phase of the $CsPbBr_3$ nanocrystals purified by ethyl acetate was investigated by powder X-ray diffraction, revealing an orthorhombic crystal phase, as shown in Fig. 4.3 **a)**. The ensemble absorption spectrum presents a threshold at ∼2.38 eV (see Fig. 4.3 **b)**), which roughly corresponds to the room-temperature bulk electronic bandgap. Under light excitation at 405 nm, these nanocrystals exhibit a bright green photoluminescence centered at 2.36 eV, with a high color purity (full width at half maximum (FWHM) of 77 meV) and a photoluminescence quantum yield of 32 %.

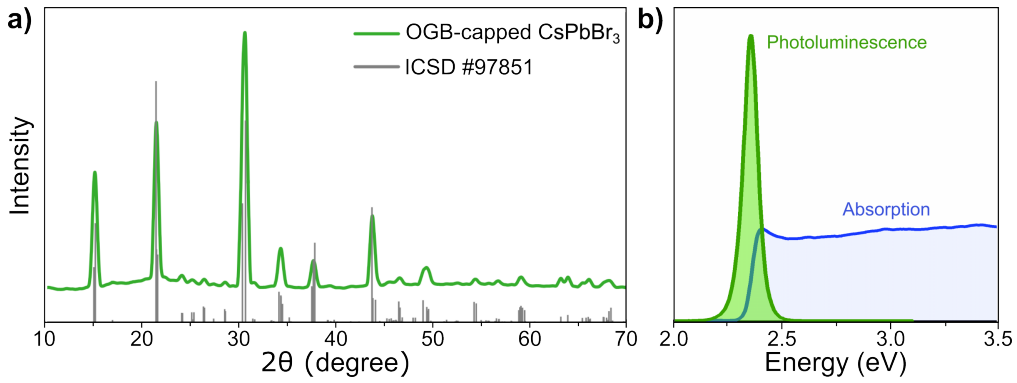

Figure 4.3: a) Powder X-ray diffraction pattern of OGB-capped $CsPbBr_3$ nanocrystals purified by ethyl acetate, and reference pattern of orthorhombic crystal structure (Inorganic Crystal Structure Database #97851). **b)** Their room-temperature absorption and emission spectra.

4.2.2 Spheroidal $CsPb(BrCl)_3$ nanocrystals

Spheroidal $CsPb(ClxBr_{1-x})_3$ nanocrystals with x ∼0.3 and with size ∼ 30 nm were synthesized by partial anion exchange on $CsPbBr_3$ nanocrystals [170, 171].

First, ∼30 nm-sized $CsPbBr_3$ nanocrystals were synthesized with the following modifications compared to the synthesis presented in Ref. [172]. The injection of Cs oleate and further annealing were conducted at 225 °C. These large $CsPbBr_3$ nanocrystals were colloidally stabilized by lecithin as a capping ligand. While the reaction mixture was cooling down, at 50 °C, 2 ml of lecithin in toluene (0.01 M) was added, and the solution was stirred for 30 min. The crude solution was centrifuged for 5 min at 1600 × g. The resulting supernatant was discarded and

the precipitate was dispersed in a lecithin/toluene mixture (0,01 M, 2 mL) and kept undisturbed for one hour. Then, the solution was centrifuged a second time for 4 min at 1600 × g. The precipitate was redispersed in toluene/ 1,2-dichlorobenzene.

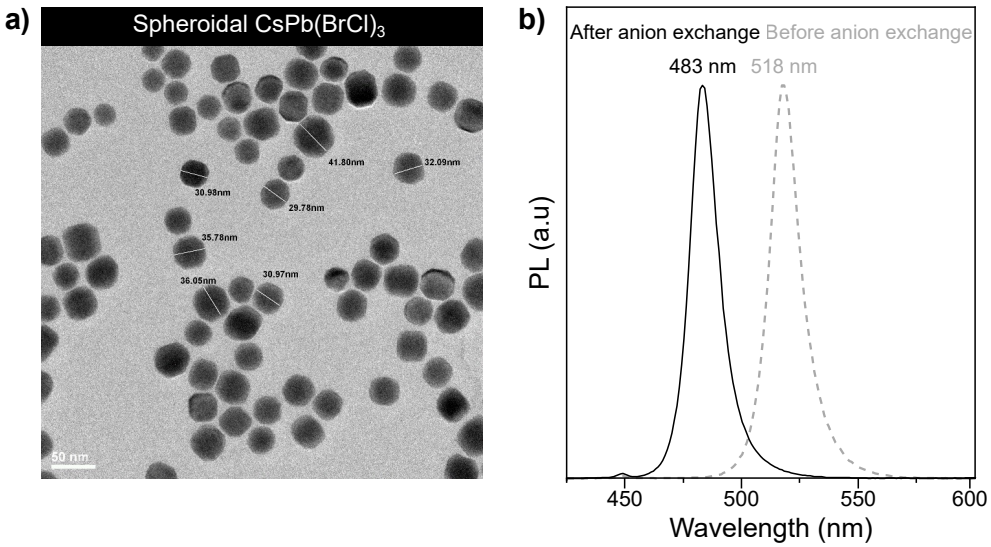

Figure 4.4: a) Scanning electron microscopy image of spheroidal $CsPb(BrCl)_3$ nanocrystals. **b)** Photoluminescence of ensemble nanocrystals at ambient temperature before and after anion exchange.

The anion exchange reaction was conducted at room temperature. A mixture of didodecyldimethylammonium chloride (DDAC)/$PbCl_2$ in toluene was used as a source of chloride ions. It was prepared by mixing 42 mg DDAC and 13.8 mg $PbCl_2$ with 7.5 mL toluene under moderate heating. 200 µL of $CsPbBr_3$ nanocrystal colloid prepared as described above were mixed with 6.5 µL of the $DDAC/PbCl_2$ mixture. A scanning electron microscopy image of the obtained nanocrystals is presented in Fig. 4.4 **a)**. The average size of these nanocrystals is evaluated at ∼30 nm. Fig. 4.4 **b)** shows the photoluminescence spectra of the synthesized nanocrystals before and after anion exchange, showing an emission blueshift due to the presence of Cl ions in the crystal lattice. An estimation x ∼0.3 for the relative amount of chloride atoms in $CsPb(Cl_xBr_{1-x})_3$ nanocrystals is derived from the empirical Vegard's law [173, 174] using the room temperature bandgap of this alloy $E_{\text{gap}}(x) = 2.57$ eV measured from the absorption spectrum.

4.3 Band-edge exciton fine structure

The band-edge fine structure of single $CsPbBr_3$ was investigated using the photoluminescence spectroscopy experimental setup described in Section 2.3. At low temperatures (3.5 ± 0.3 K) and under continuous-wave laser excitation with a wavelength of 488 nm (2.54 eV), the photoluminescence spectra of single $CsPbBr_3$ nanocrystals are characterized by a triplet of resolution-limited zero phonon lines (ZPLs) corresponding to the recombination of the bright triplet exciton, followed by optical phonon replica, as exemplified on Fig. 4.5. The photon energy of these recombination lines is distributed in the range 2.3-2.35 eV, that is across the low-temperature electronic bandgap $E_{\text{gap}} = 2.342$ eV of bulk $CsPbBr_3$ [175].

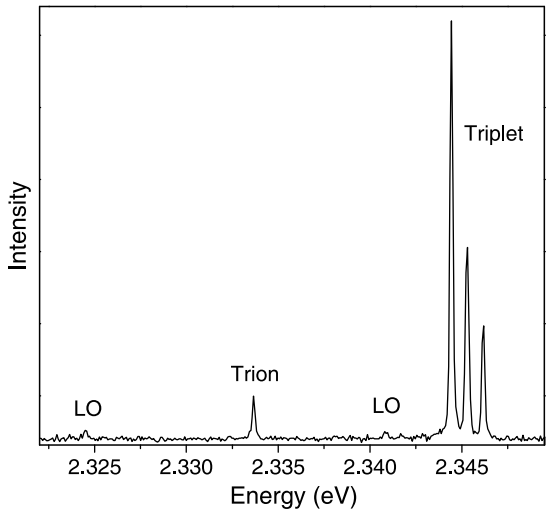

Figure 4.5: Representative photoluminescence spectrum of a single nanocrystal of $CsPbBr_3$ at 3.5 K under continuous laser excitation with wavelength 488 nm, an intensity of $50\,\text{W.cm}^{-2}$ and an integration time of 10 s. It displays the bright exciton triplet ZPLs, the trion recombination line as well as longitudinal optical (LO) phonon replicas.

4.3.1 Bright triplet splitting

All triplets observed in this study are non-degenerate, which is consistent with triplet splittings mainly set by the nanocrystal anisotropic crystal phase for such large crystals [55, 176, 53]. The triplet splittings between extreme lines range from 0.5 to 2.3 meV (Fig. 4.6), with an average of 1.2 meV that matches the theoretical estimations for nearly-bulk $CsPbBr_3$ nanocrystals with an orthorhombic crystal structure [53]. The overall variation in emission energies among the nearly-bulk $CsPbBr_3$ nanocrystals seen in Fig. 4.6 may result from differences in charge distribution inside or at the surface of nanocrystals.

One can also notice in Fig. 4.6 that the triplet splittings have a slight correlation with the nanocrystal emission energies, which points to residual effects of exciton quantum confinement. The observation of triplet emission in perovskite nanocrystals indicates that acoustic-phonon-assisted relaxation between triplet sublevels is much longer than the exciton recombination lifetime [93]. This is due to the strong lattice anharmonicity in these soft materials, where the acoustic vibrational density of states is that of a glassy state [98].

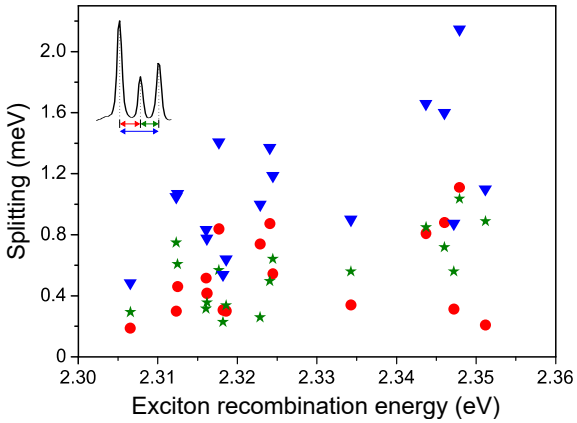

Figure 4.6: Statistics of bright triplet splittings of nearly-bulk $CsPbBr_3$ nanocrystals. The red disks ● (resp. green stars ⋆) are the splittings between the two lowest (resp. highest) energy ZPLs, while the blue triangles ▼ are the splittings between the extreme triplet ZPLs. These splittings are plotted as a function of the exciton recombination energy, taken at the central ZPL.

4.3.2 Magnetic brightening of the dark ground state

Adding an external magnetic field to the spectroscopy study reveals the entire band-edge exciton fine structure of the nearly-bulk $CsPbBr_3$ nanocrystals. While the triplet further splits under increasing fields, a red-shifted line develops in the photoluminescence spectrum, as shown in Fig. 4.7 for four different nanocrystals. The emergence of a red-shifted ZPL under magnetic fields is the hallmark of a field-induced mixing between an optically forbidden state and a neighboring bright state. This red-shifted ZPL is attributed to the ground dark singlet exciton state of $CsPbBr_3$ nanocrystals. Due to the magnetic field being limited to 7 T, the ZPL of the dark state is often very weak and its observation requires photoluminescence spectra with good quality, which requires excellent photostability and long acquisition times. The relative weights of the ZPLs not only depend on the corresponding radiative lifetimes and state populations but also on the collection efficiency of the associated dipole radiation patterns. As a consequence, the weight of the singlet ZPL under magnetic brightening results from many factors: (1) the population of the singlet state, which is set by the nonradiative relaxation from the high-energy photo-excited states, (2) the bright-dark magnetic coupling, which depends on the orientation of the nanocrystal with respect to the magnetic field and (3) the collection efficiency for the corresponding transition-dipole radiation pattern, which depends on the nanocrystal orientation with respect to the optical axis. These factors explain the large distribution of singlet-ZPL weights throughout our study.

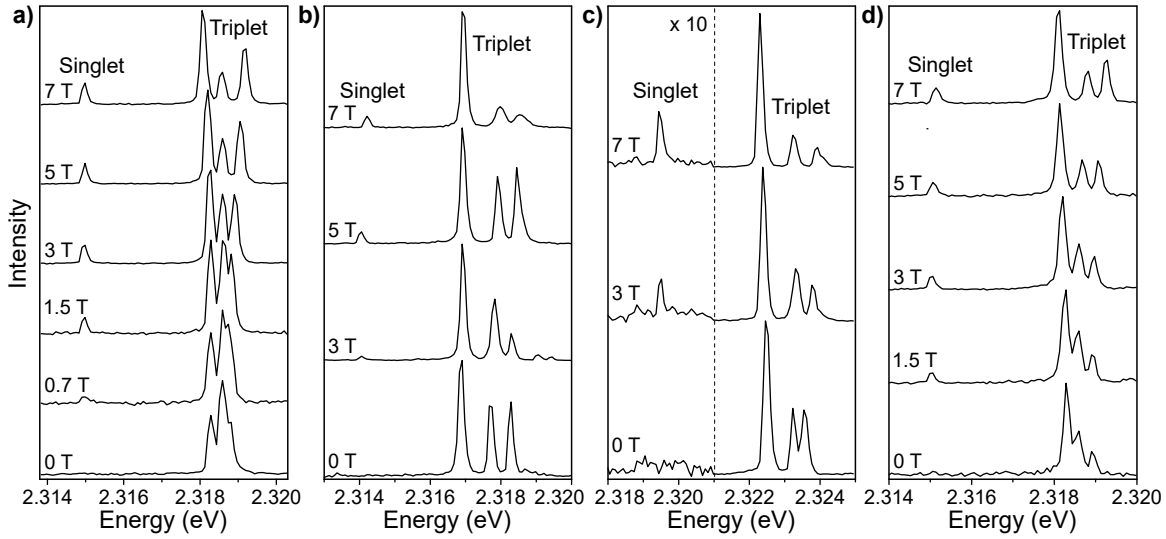

Figure 4.7: **a)**, **b)**, **c)**, **d)**, Evolution of photoluminescence spectra of four different single nanocrystals with magnetic field. The spectra displayed in **a)** have been recorded on the same nanocrystal as the one presented in Fig. 4.11.

The dark singlet lays 3.6 meV to 5 meV below the middle bright triplet sublevel in these $CsPbBr_3$ nanocrystals (Fig.4.8). These results invalidate recent models of exciton fine structure predicting a bright-dark exciton level inversion for weakly confined $CsPbBr_3$ nanocrystals caused by the Rashba effect [51, 56, 158]. The strong triplet luminescence of lead halide bulk-like perovskites nanocrystals at liquid helium temperatures is actually a signature of reduced phonon-assisted relaxation to the dark ground exciton [177], even if the dark-bright splittings coincide with the LO-phonon energies.

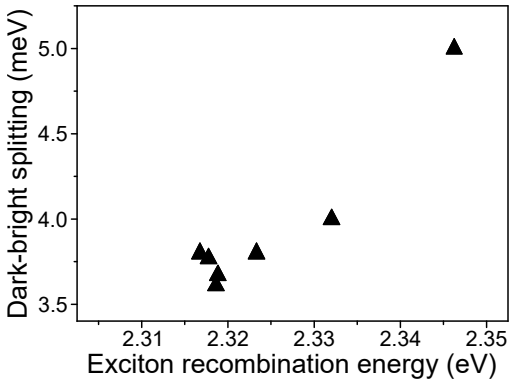

Figure 4.8: Dark-bright exciton splittings of nearly-bulk $CsPbBr_3$ nanocrystals as a function of the exciton recombination energy.

Triplet-to-singlet relaxation with a LO-phonon is indeed inhibited since phonons do not carry angular momentum [178, 179]. The ground singlet exciton can nevertheless be populated by relaxation from high-energy continuum states excited at 2.54 eV, with important consequences on the statistics of photons emitted by individual bulk-like nanocrystals. While a flat correlation is expected for bulk-like particles with Poissonian photon statistics, strong photon bunching is evidenced in the low-temperature photoluminescence intensity autocorrelation function of these nanocrystals (Fig. 4.9). Magnetic coupling of dark and bright states leads to the shortening of the long component of the photoluminescence decay and the weakening of the photon bunching, as shown in Fig. 4.9 and modeled in Fig. 4.10. These observations indicate that the population of

the long-lived ground exciton state favors the formation of biexcitons in perovskites [59]. These behaviors have been observed for all nearly-bulk $CsPbBr_3$ nanocrystals. The slight asymmetry of the autocorrelation histograms **m)** and **o)** may be due to a residual cross-talk effect between the two avalanche photodiodes.

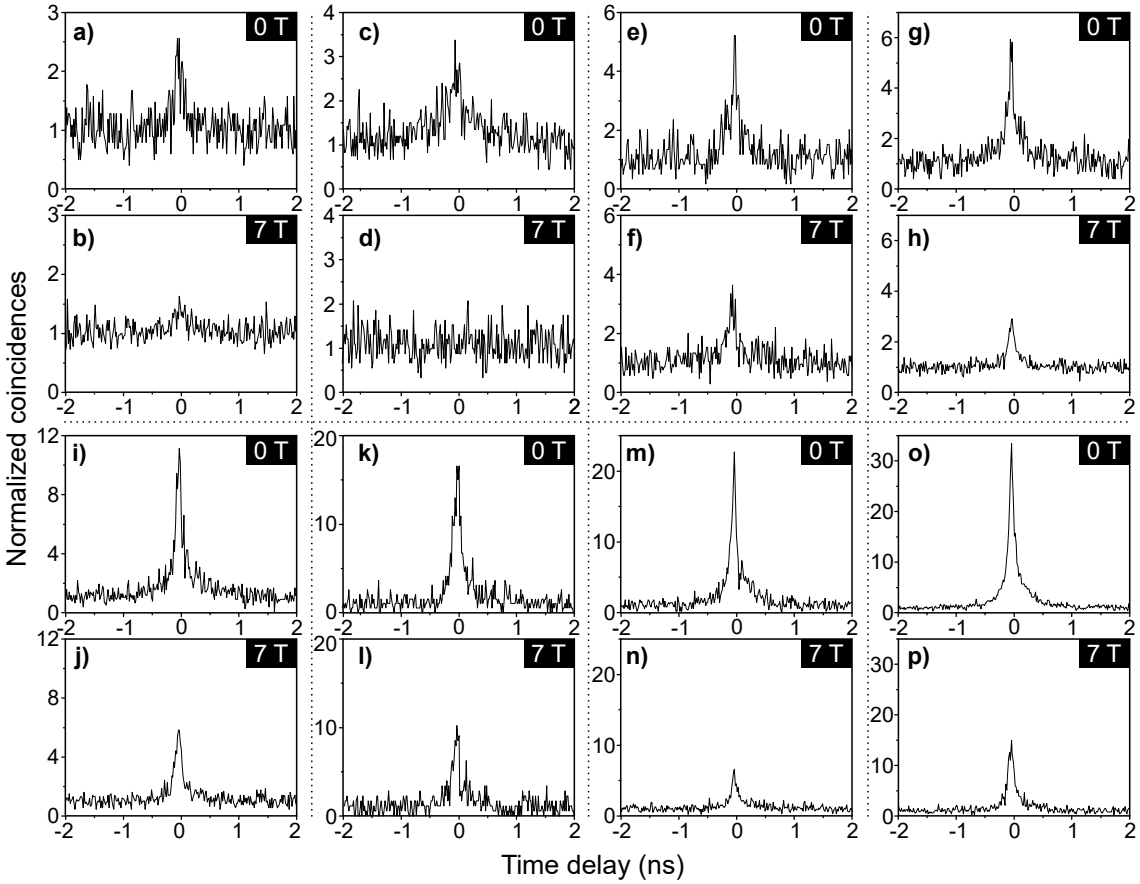

Figure 4.9: Photon correlation histograms of single nearly-bulk $CsPbBr_3$ nanocrystals. The photoluminescence intensity autocorrelation functions of eight single nanocrystals measured at 3.5 K and in zero field are sorted in ascending order of zero-delay autocorrelation $g^{(2)}(0)$ in **a)**, **c)**, **e)**, **g)**, **i)**, **k)**, **m)**, **o)**. The values of $g^{(2)}(0)$ range from 2.5 up to 32. Their corresponding autocorrelation functions at 7 T are presented in **b)**, **d)**, **f)**, **h)**, **j)**, **l)**, **n)**, **p)** with the same vertical scales, showing evidence for a reduction of photon bunching effect under magnetic field. As explained and modeled in Ref. [17], photon bunching takes its origin in the fact that the long-lived ground state stores the exciton for its long lifetime, which promotes the generation of biexcitons in the nanocrystal, followed by biexciton to zero-exciton two-photon cascades. The weakening of photon bunching with the application of magnetic fields results from the shortening of the dark state lifetime.

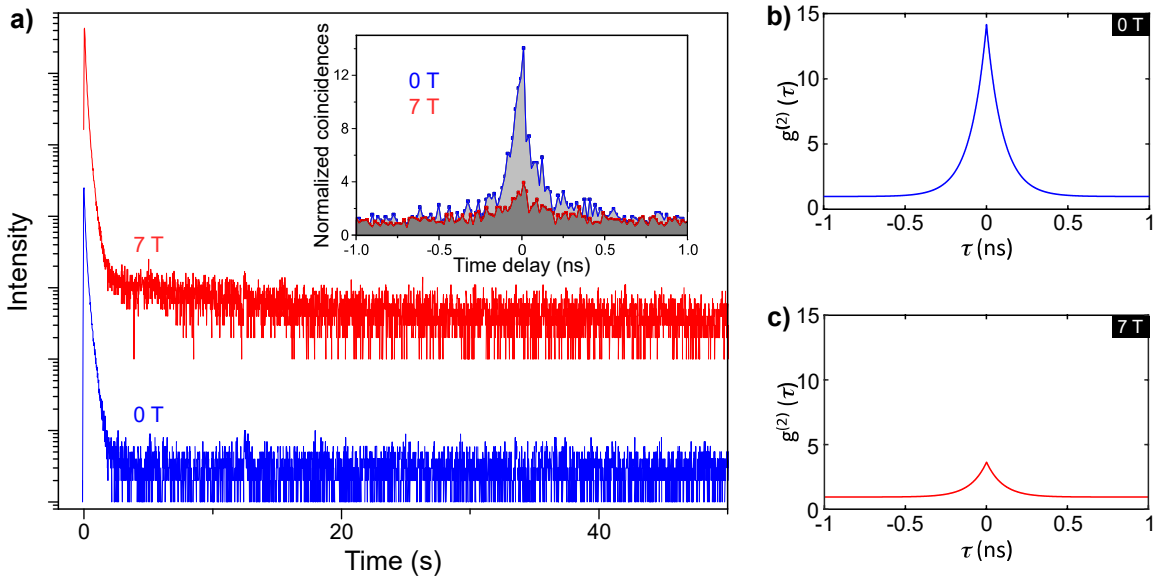

Figure 4.10: **a)** Correlated photoluminescence decays and photon coincidence histograms for the same single nanocrystal at 0 T and at 7 T, at 3.5 K. This nanocrystal is the one whose photoluminescence spectra are displayed in Fig. 4.7 **b)**. The correlations are well reproduced in **b)** and **c)** with the model developed in Ref. [59], taking $\Gamma_B = 10\ ns^{-1}$, $\gamma_0 = 0.1$ ns^{-1}, W = 0.025 ns^{-1}, $\eta_{XX} = 0.12$, $\Gamma_D = 0.01$ ns^{-1} at 0 T **b)** and $\Gamma_D = 0.125$ ns^{-1} at 7 T **c)**, i.e. a lifetime of 8 ns given by the long component of the photoluminescence decay in **a)**.

4.4 Magneto-optical properties of trions

Applying a magnetic field also allows for studying the trion emission. A complete example of a spectrum obtained at 7 T is displayed in Fig. 4.11. The spectral trail from this nanocrystal shows the singlet and triplet lines undergoing identical variations of their photoluminescence intensities. Since the nanocrystals are either in the neutral or in the charged state, the exciton and trion spectral features are inherently measured on different emission spectra. Spectral jumps occurring during these emission switches are frequent and may lead to dispersion in the measured trion binding energies. Charge complexes such as trions are indeed highly sensitive to the local dielectric environment and to charge redistributions located at the surface of the nanocrystal. The intensity variations of the doublet and the exciton manifold are anti-correlated, showing evidence that they belong to different charge complexes of the same nanocrystal.

For most of the nanocrystals studied here, the emission switches over time between the neutral exciton triplet and trion emission. The latter is characterized by a single, red-shifted ZPL, which invariably splits into two Zeeman components when an external magnetic field is applied, as depicted in Fig 4.11 and Fig. 4.12 **a)**. These spectra are consistent with previous experimental results indicating that, under a magnetic field, the trion line of nanocrystals undergoes Zeeman splitting in only two components [55, 180] in contrast to the four-line splitting observed in $CdSe$ nanocrystals [61]. This difference can be explained if the value of either the electron (g^e) or the hole (g^h) g-factors are close to zero. Here, the g-factor associated with the trion doublet is narrowly distributed around 2.4 (Fig. 4.12 **c)**). This value is in broad agreement with measurements on $CsPbBr_3$ crystals with time-resolved Kerr rotation [181]. It is also very similar to the trion g-factors measured for $\sim$ 10 nm sized $CsPbBr_3$ nanocrystals [55], $FAPbBr_3$ nanocrystals [58] and $CsPbI_3$ nanocrystals [59]. This suggests that the electron g-factor is close to 2, the value for a free electron, while the hole has a reduced g-factor, close to zero. This observation is in

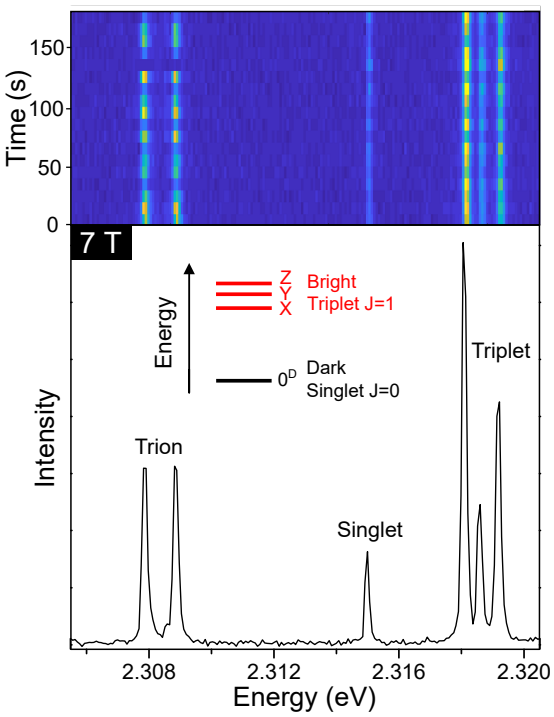

Figure 4.11: The upper panel shows the spectral trail of a single $CsPbBr_3$ nanocrystal at 7 T, showing switches between the entire exciton fine structure manifold (triplet + singlet) and the trion Zeeman doublet. The lower panel displays the spectrum integrated over the spectral trail. The inset indicates the band-edge exciton fine-structure sublevels, where X, Y, Z arbitrarily refer to linear and orthogonal emission dipoles associated with the nanocrystal axes.

line with the calculations of the g-factor derived from effective mass calculations [182] where g^h is significantly smaller than g^e.

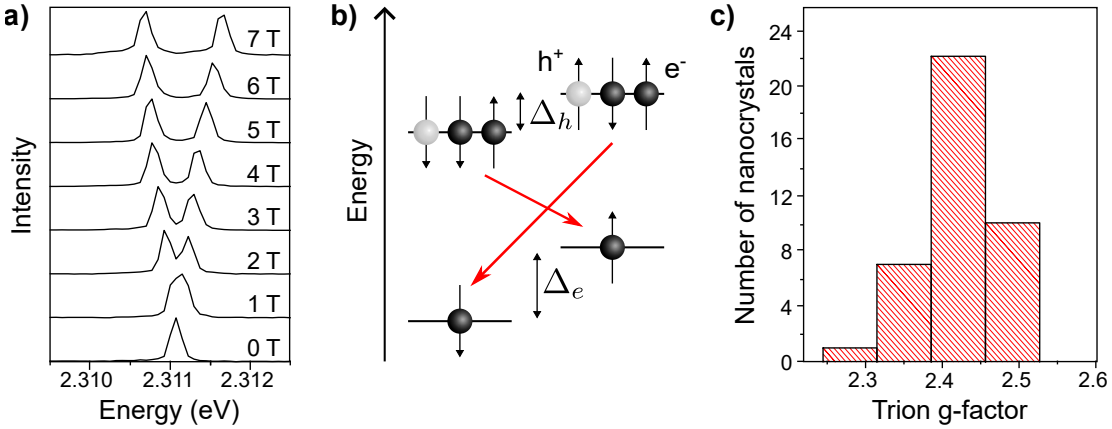

Figure 4.12: **a)** Representative magnetic field dependence of the photoluminescence spectrum of a $CsPbBr_3$ nanocrystal displaying trion emission. **b)** Scheme of energy levels and recombination transitions for a negative trion under magnetic fields. The black spheres represent the spin states of electrons, and the white spheres are the ones of holes. The level splitting associated with the hole and the electron are noted as Δ_h and Δ_e, respectively. **c)** Histogram of the trion g-factors of 41 single nanocrystals.

Overall, these results point to a nearly isotropic character of the magnetic response of charged perovskite nanocrystals, regardless of their size and chemical composition. The red shift of the

trion line from the central triplet line provides a measure of the trion binding energy and spans from 3 to 18 meV among the studied nanocrystals, as shown in Fig. 4.13. A correlation emerges between the trion binding energy and the exciton recombination energy. This correlation becomes obvious when adding to this dataset the trion binding energy measured on smaller $CsPbBr_3$ nanocrystals having sizes 14.5 nm, 9 nm, and 5.5 nm (in blue in Fig. 4.13). Their corresponding low-temperature emission energies are respectively 2.355 eV, 2.40 eV [55] and 2.434 eV, as a signature of increasing charge-carrier confinement.

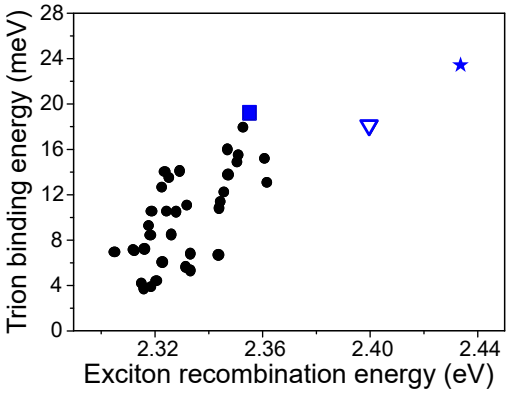

Figure 4.13: Distribution of trion binding energies in $CsPbBr_3$ single nanocrystals as a function of the exciton recombination energy taken at the central triplet ZPL. The black dots • correspond to nearly-bulk $CsPbBr_3$ nanocrystals, the blue triangle ▽ to 9 nm sized nanocrystals [55]. The blue star ⋆ and the blue square ■ respectively correspond to 5.5 nm sized and 14.5 nm sized nanocrystals.

4.5 Biexciton binding energy

Our spectroscopic investigations of single perovskite nanocrystals also reveal the spectral fingerprint of the biexciton-to-exciton transitions. Raising the excitation intensity leads to the onset of a spectral triplet (XX) that is red-shifted with respect to the exciton (X) bright triplet (Fig. 4.14), and whose temporal variations in photoluminescence intensity are correlated with those of the X triplet. Fig. 4.15 shows a typical example of a spectral trail allowing to identify the exciton emission lines, the trion, and the biexciton.

Moreover, the ratio of the integrated intensities of the XX and X triplets is proportional to the intensity of the X triplet, as a distinctive signature of XX biexciton emission [63, 156] (Fig. 4.16). Additionally, the XX triplet components XX_i perfectly match the X triplet components X_i (i = 1,2,3) under mirror symmetry and are attributed to the three transitions that link the ground zero-angular-momentum biexciton state to the bright exciton triplet sublevels (Fig. 4.14 **a)**).

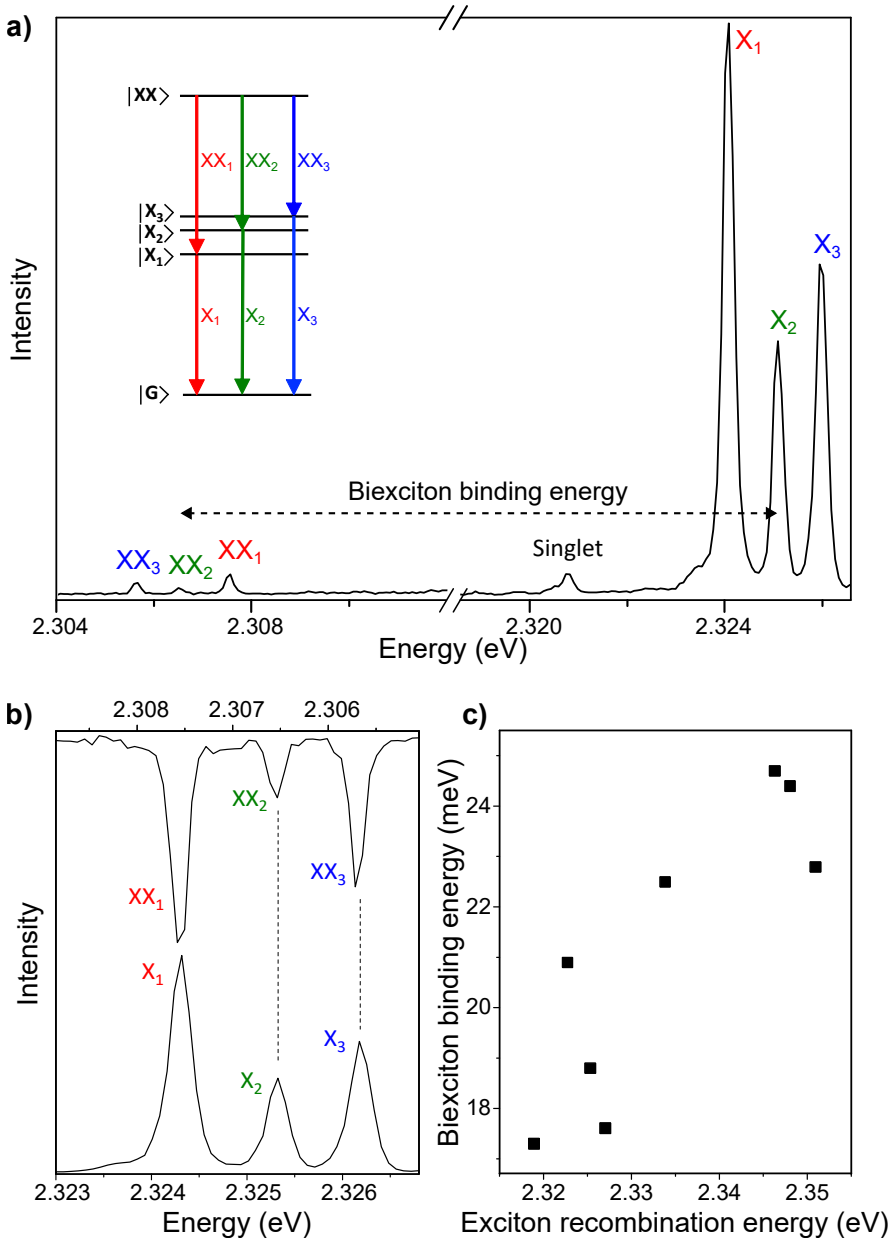

Figure 4.14: **a)** Low-temperature photoluminescence spectrum of a single nanocrystal of $CsPbBr_3$ at high excitation intensity (50 kW cm^{-2}) and at 7 T. The four lines at energies higher than 2.32 eV are assigned to recombination ZPLs of the triplet (named X_1, X_2, X_3) and the dark ground singlet. The red-shifted lines named XX_1, XX_2, XX_3 are assigned to the biexciton-to-exciton transitions, as shown in the inset. **b)** The biexciton-to-exciton transitions perfectly map onto the exciton triplet ZPLs under mirror image allowing a straightforward correspondence of the transition lines. The spectral trail of this nanocrystal over time is shown in Fig. 4.15. **c)** Distribution of the biexciton binding energy, measured as the energy offset of the XX_2 line with respect to the X_2 line, as a function of the exciton recombination energy (taken at the X_2 line).

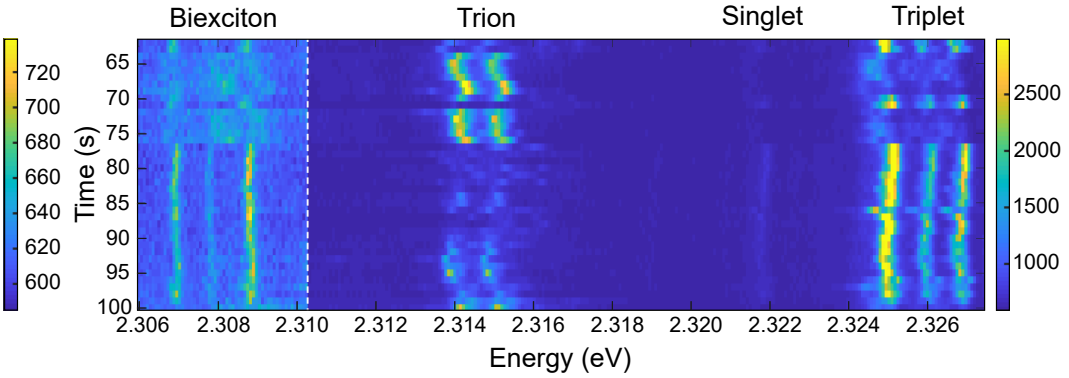

Figure 4.15: Spectral trail of a nanocrystal at 7 T under high excitation intensity. These series of consecutive photoluminescence spectra were recorded at 50 kW cm^{-2} on the same nanocrystal as in Fig. 4.14 **a)**. One can notice that the trion binding energies experience a much larger spread than the biexciton one.

Importantly, the red shift of the XX triplet with respect to the X triplet indicates that the biexciton interaction is attractive. In the large $CsPbBr_3$ particles, the biexciton binding energy ranges from 17 to 25 meV with a trend of correlation with the corresponding exciton recombination energy (Fig. 4.14 **c)**), as in the case of trion emission. These measurements provide the bulk $CsPbBr_3$ biexciton binding energy ∼17 meV, a key parameter for the development of refined models of many-body Coulomb interactions in perovskites [183]. This value is in good agreement with those extrapolated from two-dimensional electronic spectroscopic measurements performed on small $CsPbBr_3$ nanocrystal ensembles [168].

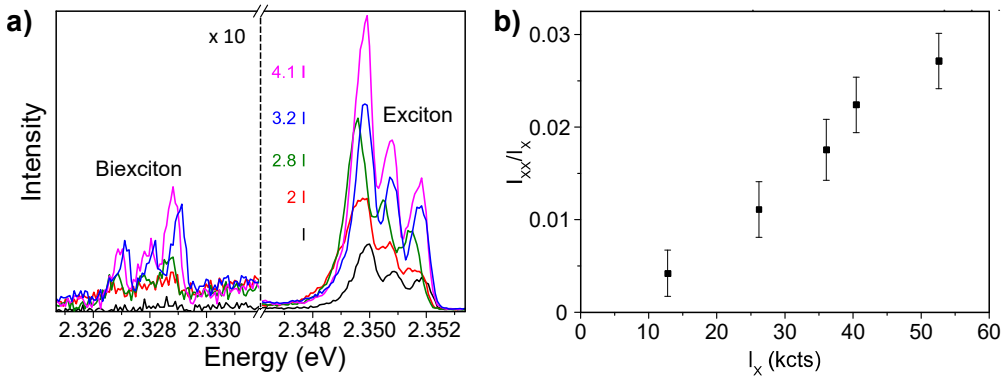

Figure 4.16: **a)** Evolution of the spectral features assigned to the exciton triplet and the biexciton-to-exciton triplet under increasing excitation intensities ranging from I = 0.8 $kW cm^{-2}$ to 4.1 I. **b)** Ratio of the integrated intensities of the XX and X spectral structures plotted as a function of the integrated intensities of the X triplet and showing a linear behavior, as a distinctive signature of XX biexciton emission.

4.6 Magneto-optical spectroscopy of spheroidal $CsPb(BrCl)_3$

To strengthen the generality of these findings, we have also conducted magneto-optical spectroscopic investigations of mixed-halide $CsPb(ClxBr_{1-x})_3$ single nanocrystals with an average size ∼ 30 nm. A typical spectra obtained under a magnetic field of 6 T presenting exciton and biexciton emission is displayed Fig. 4.17. These perovskites follow the same behaviors as $CsPbBr_3$ in terms of exciton sublevel ordering and signs of the interactions within trion and biexciton charge complexes.

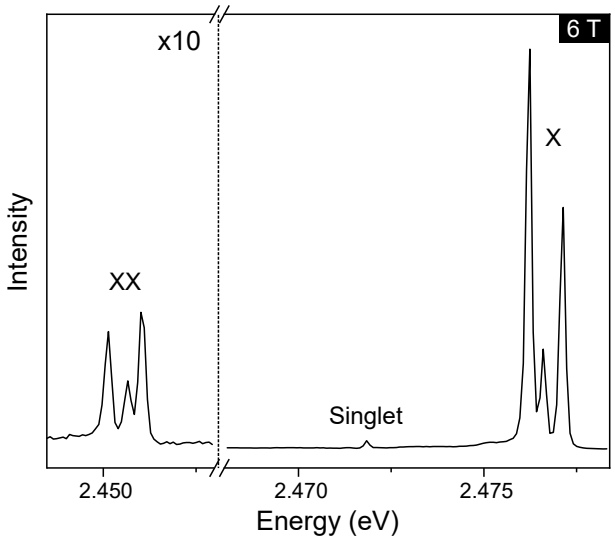

Figure 4.17: Photoluminescence spectra of a $CsPb(BrCl)_3$ spheroidal nanocrystal at 6 T showing the entire band edge exciton structure as well as the biexciton emission (XX).

In our spectroscopy study, with no magnetic field, around 2/3 of nanocrystals presented triplet emission lines, 1/3 presented doublet emission lines and one nanocrystal presented a single emission line associated with exciton emission. These three behaviors relate to the level of anisotropy of the spheroidal nanocrystal. The repartition of the doublet and triplet splitting show no correlation to the nanocrystal emission energies (Fig. 4.18) due to the size of these nanocrystals, leading to reduced quantum confinement.

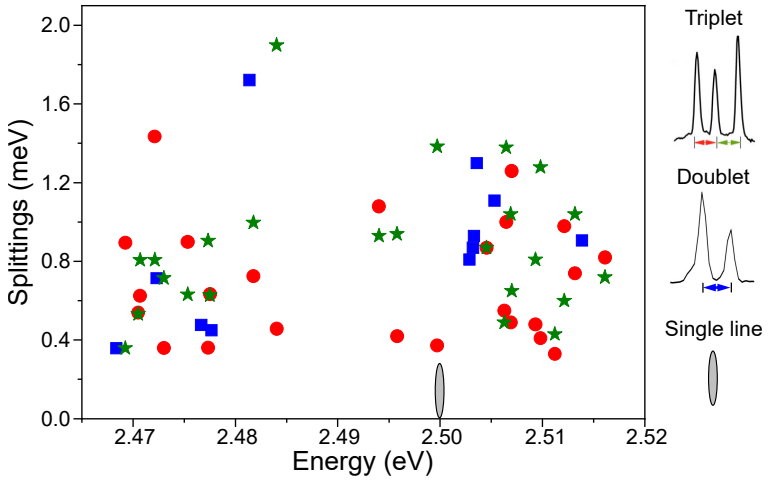

Figure 4.18: Splitting of the doublet (blue square ■) and the triplet (green stars ⋆ and red disks ●) emission lines from $CsPb(BrCl)_3$ single spheroidal nanocrystal as a function of their emission energies. The single-line energy value is limited by the spectral resolution.

The lower dark exciton state was also observed in these nanocrystals when applying a magnetic field in the Faraday configuration. The spectra of Fig. 4.19 **a)** show the exciton doublet emission lines splitting into a triplet while a new line appears at lower energy when applying a magnetic field. For these nanocrystals, the exciton dark-bright splittings are found in the range 4-6 meV, while their trion and biexciton binding energies are respectively of the order of 5 meV and 24 meV (Fig. 4.19 **b)**, **c)**, **d)**).

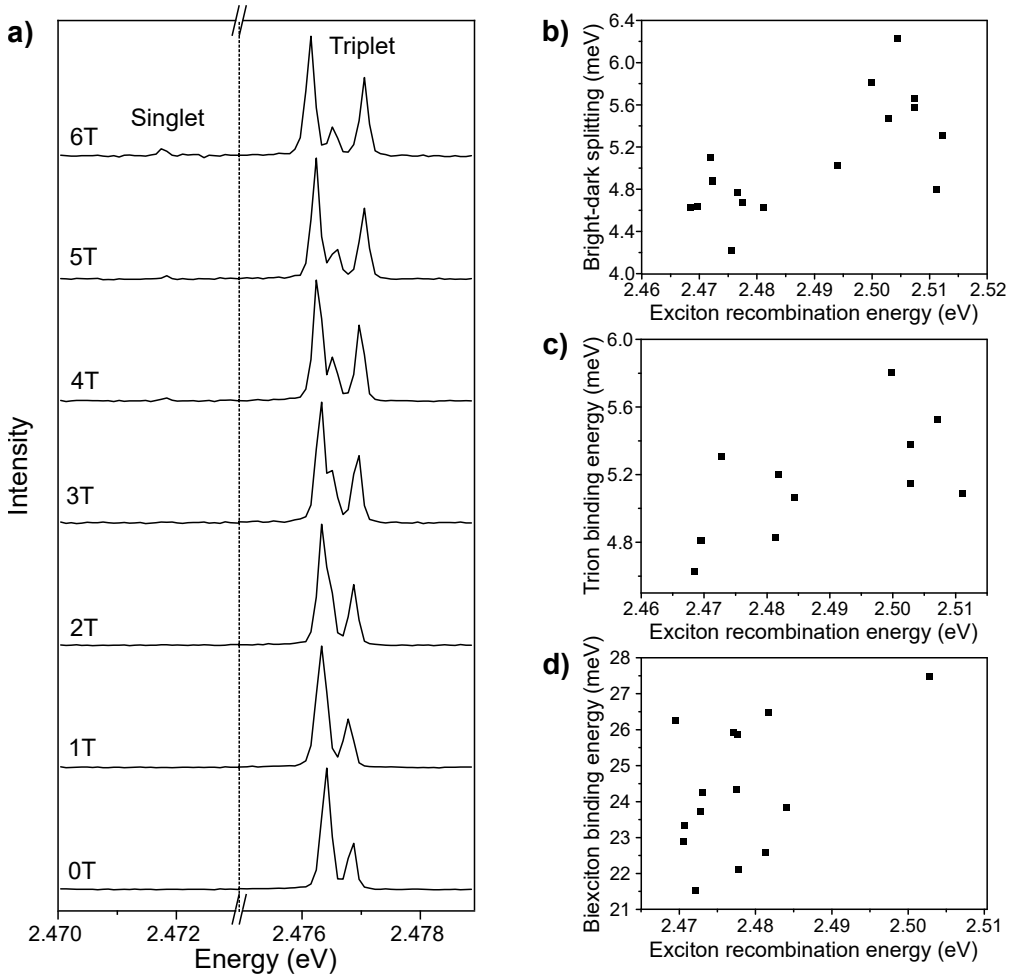

Figure 4.19: Magneto optical spectroscopic data on single $CsPb(BrCl)_3$ nanocrystals. **a)** Example of low-temperature photoluminescence spectra of a single nanocrystal under magnetic fields, showing evidence for magnetic brightening of the ground dark singlet state. **b)** Exciton bright-dak splittings as a function of emission energy. **c)** Distribution of trion binding energies, measured from the red shift of the trion line with respect to the central exciton triplet line. **d)** Distribution of biexciton binding energies, measured from the red-shift of the biexciton triplet with respect to the central exciton triplet line.

The excellent spectral stability of these nanocrystals and their good signal-to-noise ratio allow for studying the polarization of the biexciton. As shown in Fig. 4.20, for this nanocrystal, the transition dipoles associated with X_1 and X_3 (as well as XX_1 and XX_3), have nearly linear and orthogonal polarizations in the focal plane, while X_2 (as well as XX_2) with weak intensity and polarization character is assigned to a transition dipole oriented along the optical axis. The striking similarity between the polar plots provides further evidence of the correspondence between the biexciton-to-exciton and exciton-to-zero-exciton transitions, as XX_i and X_i transitions involving the same bright state have identical polarizations.

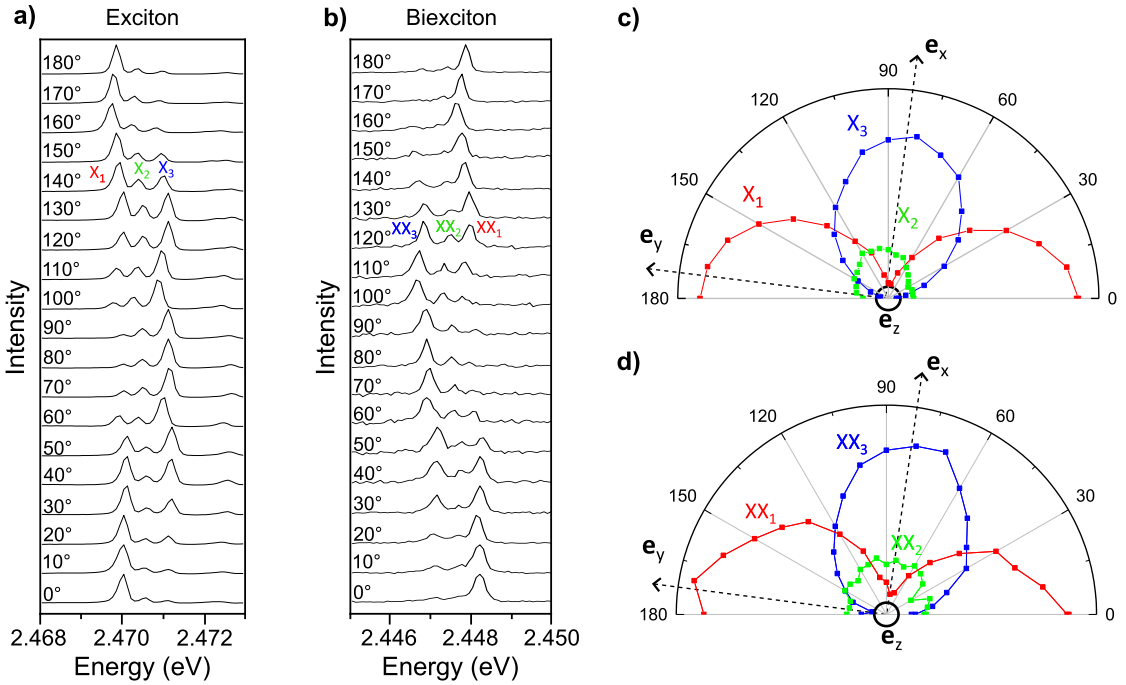

Figure 4.20: Polarization of the exciton and biexciton recombination lines. **a)**, **b)** Polarized photoluminescence spectra of a single $CsPb(Cl_xBr_{1-x})_3$ single nanocrystal with x∼0.3 and size ∼30 nm, for various analyzer angles ranging from 0° to 180°. The series of spectra in **a)** are zoomed on the exciton line triplet (X_1, X_2, X_3 ZPLs), while those in **b)** are zoomed on the biexciton recombination ZPLs (named XX_1, XX_2, XX_3). The evolutions of the exciton and biexciton ZPL intensities as a function of the polarizer angle are displayed in the polar plots **c)** and **d)**, respectively.

The correlation between polarizations of the biexciton-to-exciton and exciton-to-ground-state transition lines (Fig. 4.20) can be explained through symmetry considerations. As discussed in Ref. [55], the double group irreducible representations of the D_{2h} point group are suitable for the orthorhombic bulk phase of $CsPbBr_3$ and lead to the following decomposition of the exciton fine structure:

$$E_{1/2,u} \otimes E^*_{1/2,g} = A_\mathrm{u} \oplus B_{1u} \oplus B_{2u} \oplus B_{3u} \tag{4.1}$$

For biexciton states related to the same bulk Bloch states, one obtains:

$$E_{1/2,u} \otimes E^*_{1/2,g} \otimes E_{1/2,u} \otimes E^*_{1/2,g} = 4(A_g \oplus B_{1g} \oplus B_{2g} \oplus B_{3g}) \tag{4.2}$$

The A_g irreducible representation is the only one related to a total momentum equal to zero corresponding to a complete filling of the doubly degenerated conduction band edge, and thus to the biexciton ground state. A transition from the A_g biexciton ground state to one of the three bright exciton states as described by $< \varphi_\mathrm{biexc} | H_\mathrm{D.E.} | \varphi_\mathrm{exc} >$ corresponds to an optical transition with polarization along one of the three (x, y, z) crystallographic axes since the vectorial representation V relevant for the dipolar electric Hamiltonian $H_\mathrm{D.E.}$ is $V = B_{1u}(z) \oplus B_{2u}(y) \oplus B_{3u}(x)$. This transition is, therefore, followed by an optical transition from an exciton state to the ground state $< \varphi_\mathrm{biexc} | H_\mathrm{D.E.} | \varphi_\mathrm{exc} >$ with the same polarization, as the ground state also behaves as the totally symmetric representation A_g.

4.7 Scaling laws of charge-complex energies

We now aim at giving a general and predictive picture for the exciton dark-bright energy splittings as well as the trion and biexciton binding energies in lead halide perovskite nanocrystals from various compositions, on the basis of single-nanocrystal spectroscopic data gathered in this study and from previous reports [59, 55, 156, 51, 58, 101, 184]. As compared to II-VI and III-V semiconductors, perovskites exhibit a simpler band structure (a single valence band, and a single conduction band due to the giant spin-orbit coupling). Moreover, for each perovskite compound, the electron and the hole have nearly identical effective masses m^* [153, 51] and confinement potentials.

The Hamiltonian $\mathcal{H}$ describing the kinetic and Coulomb energies of the charge carriers in a nanocrystal, where the confinement potential with infinitely high barriers is taken to zero, can be written

$$\begin{aligned}\mathcal{H} &= \mathcal{H}_{\text{kin}} + \mathcal{H}_{\text{Coul}} \\ &= \sum_A \frac{-\hbar^2}{2m^* a_{\text{B}}^2} \frac{1}{\left(L_{\text{eff}}/a_{\text{B}}\right)^2} \hat{\nabla}_{\text{A}}^2 + \sum_{A<B} \frac{e^2}{4\pi\varepsilon_0\varepsilon a_{\text{B}}} \frac{c_{\text{A}}c_{\text{B}}}{\left(L_{\text{eff}}/a_{\text{B}}\right)} \frac{1}{|\hat{r}_{\text{A}} - \hat{r}_{\text{B}}|} \\ &= R_y \left(\sum_{\text{A}} \frac{-1}{2\left(L_{\text{eff}}/a_{\text{B}}\right)^2} \hat{\nabla}_{\text{A}}^2 + \frac{2}{\left(L_{\text{eff}}/a_{\text{B}}\right)} \sum_{A<B} c_{\text{A}}c_{\text{B}} \frac{1}{|\hat{r}_{\text{A}} - \hat{r}_{\text{B}}|} \right),\end{aligned} \tag{4.3}$$

where L_{eff} is the effective nanocrystal confinement size, $\hat{\nabla}_i$ and $\hat{r}_i$ the dimensionless (normalized to L_{eff}) Nabla-operators and coordinates of the charge carriers i ($i = A, B...$), c_i the signs of their charges having absolute value e, and $R_y = \hbar^2/(m^* a_{\text{B}}^2)$ the bulk exciton Rydberg energy, ε being the perovskite dielectric constant. Such normalization in Rydberg's units makes interaction energies independent of the material and shows that trion and biexciton binding energies are essentially set by the quantum confinement regime, i.e. the dimensionless ratio L_{eff}/a_B. This simple statement explains the universal laws relating, in Rydberg's units, the experimental trion and biexciton binding energies to the exciton recombination energy E_{X}, once the bandgap of the material is subtracted (Fig. 4.21 **a)**, **b)**). Indeed, using these scales, the experimental points strikingly spread along a trend line from the bulk limit (abscissa approaching -1) to the strong confinement regime (abscissa of several units), regardless of the perovskite compositions.

The dark-bright exciton energy splitting Δ_{BD} measured on single nanocrystals of $CsPbBr_3$, $CsPb(Cl_xBr_{1-x})_3$, $CsPbI_3$ [59] and $FAPbBr_3$ [58] also displays a universal scaling law as a function of the exciton quantum confinement. The dark-bright splitting Δ_{BD} is mainly set by the long-range contribution of the electron-hole exchange interaction, which is directly related to the dimensionless ratio $L_{\text{eff}}/a_{\text{B}}$ and to the difference between the energies of longitudinal and transverse excitonic polaritons $\hbar\omega_{\text{LT}}/3$ where

$$\hbar\omega_{\text{LT}} = \frac{2}{3\pi\varepsilon a_{\text{B}}^3} \left(\frac{e\hbar p_{\text{cv}}}{m_0 E_{\text{gap}}} \right)^2, \tag{4.4}$$

p_{cv} being the Kane interband momentum matrix element and m_0 the electron mass [140]. As transverse and longitudinal excitons are connected to the exchange interaction [185, 186], the exciton Rydberg energy R_y is not an adequate normalization factor for $\hbar\omega_{\text{LT}}$. However, this quantity can be related to R_y and E_{gap} considering the Kane energy $E_{\text{Kane}} = p_{\text{cv}}^2/(2m_0)$ introduced as a fundamental constant of 2D [187] and 3D [187] perovskites. It was experimentally shown that a single Kane energy is enough to describe the evolution of the effective masses with bandgaps for various compositions of 3D bulk metal halide perovskites [188, 175]. Using

$E_{\mathrm{Kane}}/E_{\mathrm{gap}} \propto \mu^{-1}$ leads to

$$\hbar\omega_{\mathrm{LT}} \propto \frac{E_{\mathrm{Kane}}}{E_{\mathrm{gap}}^2\,\varepsilon a_{\mathrm{B}}^3} \propto \frac{1}{\mu E_{\mathrm{gap}}\varepsilon a_{\mathrm{B}}^3} \propto \frac{R_y^2}{E_{\mathrm{gap}}}, \tag{4.5}$$

the proportionality coefficients being material independent. Therefore, using the dimensionless quantity $\Delta_{\mathrm{BD}}/\left(R_y^2/E_{\mathrm{gap}}\right)$ should lead to a universal dependence of the exciton dark-bright splitting as a function of the quantum confinement. This is demonstrated in Fig. 4.21 **c)**, where a clear correlation between the dimensionless bright-dark splitting and the exciton recombination energy after bandgap subtraction is evidenced.

To justify the applicability of a scaling factor designed to account for the long-range exchange interaction to an experimental quantity related to the sum of the short-range and long-range contributions, we have numerically inspected the bulk limits of both contributions for various perovskites. In order not to rely on only a few values of short-range component spread in the literature [51], we use the general bulk formula proposed by Ben Aich et al. [155] and derived from Rössler et al. [189].

$$\Delta_{\mathrm{SR,BD}} = \frac{2}{3}D = \frac{2}{3}\frac{C}{\pi a_B^3}. \tag{4.6}$$

This formula aligns with the same approach as the present work and aims at proposing a law based on an empirical factor $C = 107.6\,\mathrm{meV.nm^3}$. This contribution is computed in Table 4.1, together with the bulk limit of the long-range part $\Delta_{\mathrm{LR,BD,bulk}} = \frac{\hbar\omega_{\mathrm{LT}}}{3}$, for all compounds relevant to perovskite nanostructures.

	$CsPbI_3$	$MAPbI_3$	$FAPbI_3$	$CsPbBr_3$	$MAPbBr_3$	$FAPbBr_3$	$CsPb(Br,Cl)_3$ ($x_{Cl}=0.24$)
$\Delta_{SR,BD}$ (meV)	0.22917	0.20950	0.13795	0.79542	0.58725	0.39425	1.44394
$\Delta_{SR,BD}/(R_y^2/E_{\mathrm{gap}})$	1.6359	1.34511	1.05199	1.79446	1.67507	1.80153	2.05704
$\Delta_{LR,BD}/(R_y^2/E_{gap})$ (meV)	0.61302	0.64849	0.52006	1.57754	1.18363	0.75214	2.48142
$\Delta_{LR,BD,bulk}/(R_y^2/E_{\mathrm{gap}})$	4.37597	4.16367	3.96570	3.55891	3.37618	3.43692	3.53503
$\Delta_{BD,bulk} = \Delta_{SR,BD} + \Delta_{LR,BD,bulk}$ (meV)	0.84220	0.85799	0.65801	2.37296	1.77088	1.14639	3.92536
$\Delta_{BD,bulk}/(R_y^2/E_{\mathrm{gap}})$	6.01190	5.50878	5.01769	5.35337	5.05125	5.23845	5.59207

Table 4.1: Contributions of the short-range and long-range electron-hole exchange interactions, using the normalization factor R_y^2/E_{gap}.

Interestingly, when the proper scaling factor R_y^2/E_{gap} is introduced, all these perovskites yield very similar dimensionless bulk limits of the exchange energy in the 5-6 range, in reasonable agreement with the bulk limit extrapolation of the experimental master curve (Fig. 4.21 **c)**). Moreover, since the short-range and long-range contributions of the exchange interaction are predicted to have the same nanocrystal size-dependence in the strongly confined regime [140], the applicability of the scaling factor R_y^2/E_{gap} over the whole range of confinement regimes is strengthened.

We have thus plotted the normalized splitting $\Delta_{BD}/\left(\frac{R_y^2}{E_{\mathrm{gap}}}\right)$ of all these nanocrystals as a function of the corresponding exciton recombination energies in Rydberg's units, after bandgap subtraction Fig. 4.21 **c)**. This figure shows evidence that the data points line up on a same curve, regardless of the cation and halide contained in the perovskite.

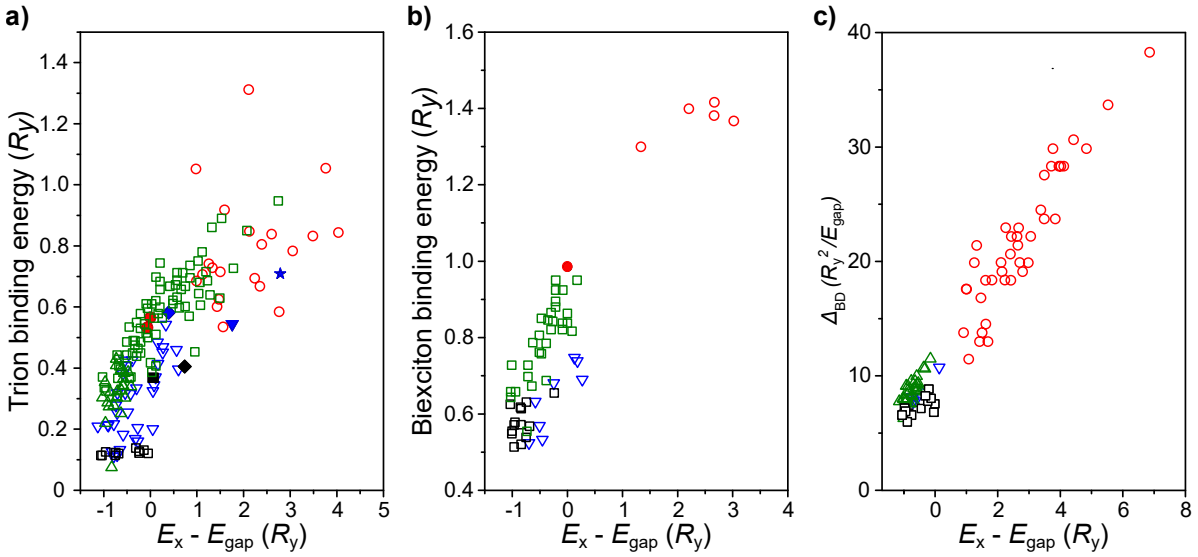

Figure 4.21: **a)** Evolutions of the single-nanocrystal trion binding energies in R_y units, **b)** biexciton binding energies in R_y units and **c)** dark-bright exciton energy splittings in R_y^2/E_{gap} units, as a function of the exciton recombination energy expressed in R_y units after bandgap subtraction. The splittings and binding energies are measured with respect to the central line of the exciton triplet. Open blue triangles ▽: $CsPbBr_3$ nanocrystals; Open black squares □: $CsPb(ClxBr_{1-x})_3$ nanocrystals; Green triangles △: $FAPbBr_3$ nanocrystals [58]; Red circles ○: $CsPbI_3$ nanocrystals [59]. Green squares □: $FAPbBr_3$ nanocrystals (data extracted from Ref. [101]). Plain blue triangle ▼ in **a)**: average data for 9 nm sized $CsPbBr_3$ nanocrystals [55]. Blue star ★ in **a)**: $CsPbBr_3$ nanocrystal with 5.5 nm size. Blue diamond ◆ in **a)**: $CsPbBr_3$ nanocrystal with 14.5 nm size. Plain black square ■ in **a)**: $CsPbClBr_2$ nanocrystals [51]. Black diamond ◆ in **a)**: $CsPb(ClBr)_3$ nanocrystals from Ref. [184]. Red disks ● in **a)** and **b)**: $CsPbI_3$ nanocrystals [156]. For these perovskites, the low-temperature bandgaps and bulk exciton binding energies taken for the normalization are deduced from Refs. [175, 188, 190] (See Table 4.2) : E_{gap} = 2.342 eV and R_y = 33 meV for $CsPbBr_3$, E_{gap} = 1.723 eV and R_y = 15 meV for $CsPbI_3$, E_{gap} = 2.233 eV and Ry = 24 meV for $FAPbBr_3$, E_{gap} = 2.513 eV and R_y = 42 meV for $CsPb(ClxBr_{1-x})_3$ with x = 0.24. This value of x was adjusted using empirical interpolations of the bandgaps of bulk $CsPbCl_3$ and $CsPbBr_3$ materials composing the alloy. It matches reasonably well the estimation $x \sim 0.3$ after the growth procedure. The trion binding energies in **a)** experience a larger spread than the biexciton ones in **b)**, as a result of spectral jumps accompanying the neutral-to-charged switches of the nanocrystals, as illustrated in Fig. 4.15.

Overall, the dimensionless experimental dark-bright exciton splitting, as well as trion and biexciton binding energies, are evidenced to display a universal behavior mainly set by the quantum confinement of the charge carriers in perovskite nanostructures without the need for prior characterization of the nanocrystal size or composition. Beyond settling the debate on the bright and dark exciton sublevel ordering and its main origin in lead halide perovskites, the laws unraveled by single nanocrystal spectroscopy offer a general predictive picture for the interaction energies within charge complexes photo-generated in these materials. They also pave the way for the development of accurate models of charge complex interactions in lead halide perovskites, which share common physics and form a unique class of semiconductors.

Material	Band gap $E_{\text{gap}}(eV)$	Binding energy R_y (meV)	Eff. Bohr radius a_{B} (nm)	Reduced mass μ (m_e)	Eff. dielectric constant ε
$FAPbBr_3$ (2K)	2.233 [188]	24 [188]	3.87	0.115 [188]	8.4 [188]
$CsPbI_3$	1.723 [175]	15 ± 1 [175]	4.64	0.114 [175]	10.0 [175]
$CsPbBr_3$	2.342 [175]	33 ± 1 [175]	3.07	0.126 [175]	7.3 [175]
$CsPb(Cl_{0.24}Br_{0.76})_3$	2.513	42	2.51	0.148	7.1
$CsPbCl_3$	3.056 [190]	64 ± 1.5 [190]	1.72	0.202 [190]	6.6 [190]

Table 4.2: Fundamental parameters used for the normalization of the charge-complex binding energies and the dark-bright exciton splitting. This table indicates the electronic band gap E_{gap}(eV), the bulk exciton binding energy R_y (meV), the effective Bohr radius a_{B}(nm), the reduced mass μ given in electron mass (m_{e}) units, and the effective dielectric constant ε. Except for $CsPb(Cl_{0.3}Br_{0.7})_3$ with mixed halides, the values of E_{gap} and R_y are taken from low-temperature magneto-optical measurements [188, 175, 190]. The effective mass and the effective dielectric constant were derived from the hydrogen model combined with either (i) the approximation $\mu = (m_{\text{e}}E_{\text{gap}})/4P^2$, using estimations of the Kane momentum P [188, 175] or (ii) the dependence of the exciton diamagnetic-shift coefficient on μ and ε_{eff} [190]. For the mixed halide compound $CsPb(ClxBr_{1-x})_3$ with $x \sim 0.24$, the low-temperature band gap is estimated using a linear Vegard's interpolation law $E_{\text{gap}}(x) = xE_{\text{gap}}(CsPbCl_3) + (1-x)E_{\text{gap}}(CsPbBr_3)$. The values of R_y and a_{B} are obtained from the empirical relations [190] $R_y \propto E_{\text{gap}}^{1.6}$ and $a_{\text{B}} \propto E_{\text{gap}}^{-1.33}$. Similarly, $\mu \propto E_{\text{gap}}$ and $\varepsilon \propto (R_{\text{y}}a\text{B})^{-1} \propto E_{\text{gap}}^{-0.29}$ provide estimates for the reduced mass and effective dielectric constant.

4.8 Conclusion

In this chapter, we revealed the entire band-edge exciton fine structure and charge-complex binding energies of nearly bulk $CsPbBr_3$ and $CsPb(BrCl)_3$ nanocrystals using low-temperature magneto-optical photoluminescence spectroscopy on single nanocrystals.

We established that the ground exciton state is dark and lays several millielectronvolts below the lowest bright exciton sublevels at variance with the models based on the Rashba effect [51, 56, 158]. This settles the debate on the bright-dark exciton level ordering in halide perovskite nanostructures. Moreover, the spectral fingerprint of biexciton recombination was also evidenced in these materials and provides precise measurements of the biexciton binding energy.

Combining our results with spectroscopic measurements on various perovskite nanocrystal previously investigated compounds [59, 55, 156, 51, 58, 101, 184], we have shown evidence for universal scaling laws relating the exciton fine structure splitting, the trion and biexciton binding energies to the band edge exciton energy in lead-halide perovskite nanostructures, regardless of their chemical composition. Additional measurements on single $CsPb(Cl_xBr_{1-x})_3$ nanocrystals further extend the validity of these dependences over a broader emission spectral range. These scaling laws, solely based on quantum confinement effects and dimensionless energies, offer a general predictive picture for the interaction energies within charge-carrier complexes photogenerated in these emerging semiconductor nanostructures.

Chapter 5

Conclusion and Perspectives

5.1 Conclusion

The work completed in this thesis was dedicated to studying the optical properties of semiconductor nanocrystals, with a particular focus on investigating the fine structure of band edge excitons in these materials. This experimental work relies on magneto-optical photoluminescence spectroscopy on single nanocrystals, enabling the reach of highly resolved spectral fingerprints of the exciton fine structure and other charge complexes in nanocrystals of different compositions.

We started this manuscript by providing an introduction to the theoretical framework of the electronic and optical properties of $CdSe$, InP, and lead halide perovskite nanocrystals alongside a precise description of the experimental methods used in this work.

The first object of study was indium phosphide nanocrystals with zinc selenide and zinc sulfide shells. The exciton recombination dynamics were initially evaluated through ensemble measurements from the evolution of their photoluminescence decay with temperature. At cryogenic temperatures, the photoluminescence decay exhibits multiexponential behavior, characterized by a long component that provides a signature of the thermal redistribution of populations between a long-lived ground exciton state and the neighboring bright states. Using a magneto-photoluminescence technique on single nanocrystals, we then experimentally resolved the spectra of the three lower exciton states. Importantly, we were able to evidence the dark ground state of the exciton using a magnetic field to allow its recombination through optical mixing with an optically active state. These experimental results were successfully reproduced using a band-edge structure model with a spin Hamiltonian, which accounted for the effect of shape anisotropy of the InP core on the valence band energy but neglected the anisotropy exchange interaction. These findings highlight the strong sensitivity of single nanocrystal photoluminescence spectra to the nanocrystal morphology.

The second part of this work was devoted to the investigation of lead halide perovskite nanocrystals. Applying the same spectroscopy method to samples of both $CsPbBr_3$ and $CsPb(BrCl)_3$ revealed their entire band-edge structure, including the spectral fingerprint of the exciton, biexciton, and trion recombinations. Photoluminescence studies of $CsPbBr_3$ nanocrystals have shown a non-degenerate triplet of resolution-limited zero-phonon lines (ZPLs) attributed to the recombination from the bright triplet emission of the exciton. Studying nearly-bulk nanocrystals of $CsPbBr_3$ allowed field-induced mixing between the optically forbidden exciton ground state and a neighboring bright state. These results settled the debate on the bright-dark exciton level ordering in lead halide perovskite nanostructures by experimentally showing that the ground exciton state is dark and lays several millielectronvolts below the lowest bright

exciton sub-levels. Spectroscopic investigations also revealed the magneto-optical properties of trions and spectral fingerprints of the biexciton-to-exciton transitions. These results enabled the measurement of the binding energies of these complexes of charges. Additional measurements on single $CsPb(Cl_xBr_{1-x})_3$ nanocrystals further extended the analysis. They follow the same behaviors as $CsPbBr_3$ in terms of exciton sublevel ordering and interactions with trion and biexciton complex of charges. These results were combined with spectroscopic measurements on various perovskite nanocrystals to demonstrate universal scaling laws relating the exciton fine structure splitting, the trion and biexciton binding energies to the band-edge exciton energy in lead-halide perovskite nanostructures, regardless of their chemical composition.

Overall, the results obtained on InP and lead halide perovskites nanocrystals demonstrate the benefits of low-temperature magneto-optical photoluminescence spectroscopy as an important and versatile tool to gain a deeper understanding of the band-edge exciton fine structure in single nanocrystals.

5.2 Perspectives

Quantum sources producing indistinguishable photons play a fundamental role in various photonic quantum technologies. Diverse quantum emitters are currently being investigated, including color centers in diamonds [191], single-walled carbon nanotubes [192] and defects in 2D materials like hexagonal boron nitride [193]. Nevertheless, these sources present several challenges, such as difficulties in their nanofabrication, inconsistent emission wavelengths, or incomplete suppression of dephasing [194].

Lead halide perovskite nanocrystals exhibit promising potential as quantum emitters. Theoretically, they can generate single photons on demand through pulsed excitation of the nanocrystal, followed by spectral filtering of the emitted light to isolate one photon with desired properties. Quantum emission at room temperature has already been demonstrated with $CsPbI_3$ and $CsPbBr_3$ in 2015 [147]. However, these systems lacked stability due to blinking, bleaching, and low count rates. Using semiconductor nanocrystals as quantum emitters still requires material development and better optimization.

Nevertheless, perovskite nanocrystals possess a unique potential to serve as tunable sources of indistinguishable photons, thanks to their ease of synthesis and the progress made in recent years to achieve better control of their shape, size homogeneity, and aspect ratio. Recently, the observation of two-photon quantum interference (also called Hong–Ou–Mandel interference) from the emission of $CsPbBr_3$ nanocubes has been reported [195]. The recombination of excitons in these nanocubes leads to triplet ZPLs corresponding to the exciton bright triplet emission, possessing linear orthogonal polarizations. Consequently, using nanocubes as a single photon emitter requires suppressing two emission lines using polarization filtering.

$CsPbBr_3$ nanorods offer a promising alternative to nanocubes due to their potential for single-line emission, depending on their aspect ratio. In the next section, we will present some preliminary spectroscopy analysis on $CsPbBr_3$ nanorods, suggesting their suitability as a quantum source candidate.

5.2.1 Spectroscopy analysis of $CsPbBr_3$ nanorods

Recent advances in chemical fabrication techniques for nanocrystals have enabled better control of their sizes and growth processes and allowed the obtention of perovskite nanorods with high aspect ratios. The nanorods studied here have been synthesized by Kovalenko Lab - Functional Inorganic Materials at ETH Zurich using a controllable slow injection method to create monodisperse one-dimensional $CsPbBr_3$ nanorods. Their new synthesis route is based on the simultaneous injection of cesium salt of single-chain acids and $PbBr_2$-trioctylphosphine oxide (TOPO) precursors into nonpolar solvents. The injection rate, the amount of precursors injected (i.e. the Cs:Pb ratio), the reaction temperature, and the introduction of amines as co-ligands help control the size and aspect ratio of the nanorods.

This crystal growth method is based on the anisotropy of the orthorhombic perovskite crystal structure. Ligands that specifically bind to different lattice planes [196, 197] are used to control the anisotropic growth of the nanorods. The direction of elongation corresponds to the crystallographic [001] direction (*Pbnm* space group) of $CsPbBr_3$ crystals [198]. In the following, the z-axis is taken along the deformation direction, corresponding to the orthorhombic primitive c-axis, and the x- and y-axes are taken normal to the lateral orthorhombic facets containing

the crystallographic c-axis. These newly synthesized nanorods are characterized by their aspect ratio, $AR = \frac{L_z}{\sqrt{L_x L_y}}$, and effective size, $L_e = \sqrt[3]{L_x L_y L_z}$, with L_x, L_y and L_z the lengths of the nanorods along the x, y and z directions.

In the next section, we present spectroscopy analyses of $CsPbBr_3$ nanorods with two different aspect ratios.

Photoluminescence spectroscopy on $CsPbBr_3$ nanorods with small AR

The nanorods in this study measure 8.5 nm ×19.5 nm ($AR = 2.3$, $L_e = 11.2$ nm). They are diluted in a solution of styrene-ethylene-butylene-styrene (SEBS) in cyclohexane. A TEM image of the sample is shown in Fig. 5.1 **a)**. We conduct a photoluminescence spectroscopy study at 3.5 K, using continuous laser excitation at 488 nm and a bandpass filter 538/84 nm.

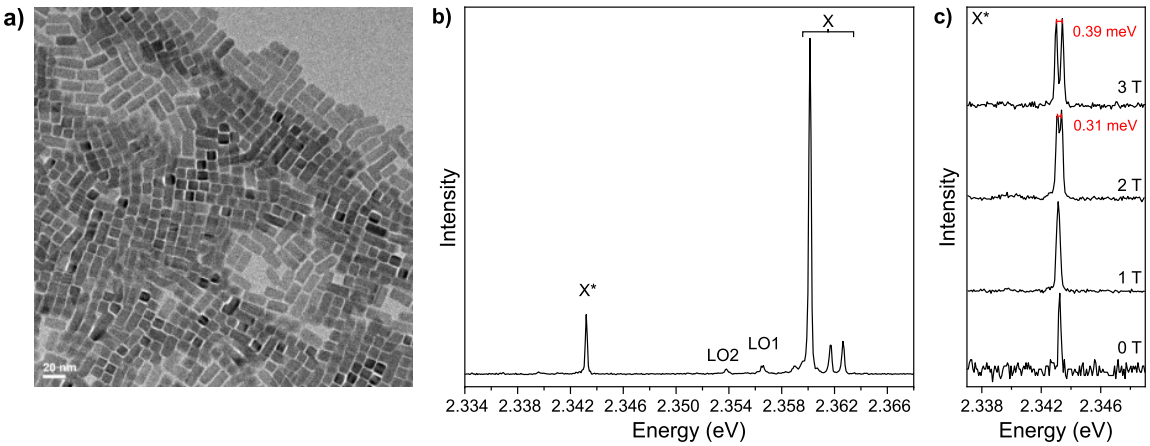

Figure 5.1: **a)** Transmission electron microscopy of $CsPbBr_3$ nanorods measuring 8.5 nm ×19.5 nm. **b)** Photoluminescence emission spectrum of a single nanorod at 3.5 K. **c)** Splitting of the trion emission line with a magnetic field.

Fig. 5.1 **b)** shows an example of a photoluminescence spectrum obtained at low temperature from a single nanorod with a long integration time. The exciton emission (X) consists of three lines attributed to the recombination of the bright triplet state. Two lines are observed with energy shifts of 3.6 and 6.3 meV with respect to the exciton emission, corresponding to the first two replicas of longitudinal optical phonons (LO1 and LO2). These values are close to those reported in the literature for $CsPbBr_3$ [99, 100], as discussed in section 1.3.5.

The lowest energy peak is identified as a trion emission line. Fig. 5.1 **c)** shows its evolution with a magnetic field. Among the three trion emissions studied with a magnetic field in this sample, the mean value for the trion g-factor is 2.28. Additionally, their mean binding energy is around 16.1 meV. These values are consistent with what has been observed in section 4.4 for cuboidal lead halide perovskites nanocrystals with exciton emission energy around 2.36 eV.

Of the 50 nanorods studied, 34 exhibited two emission lines, 14 presented three, and 2 showed single emission lines from exciton recombination. Given the size and aspect ratio of these nanorods, we aimed to verify that the sample preparation technique did not lead to a preferred orientation of the nanorods in the sample with respect to the optical axis. Therefore, the magnetic field was applied both in Faraday and Voigt configurations. No significant statistical changes were observed between the two configurations, suggesting no preferred orientation of

the nanorods in the sample.

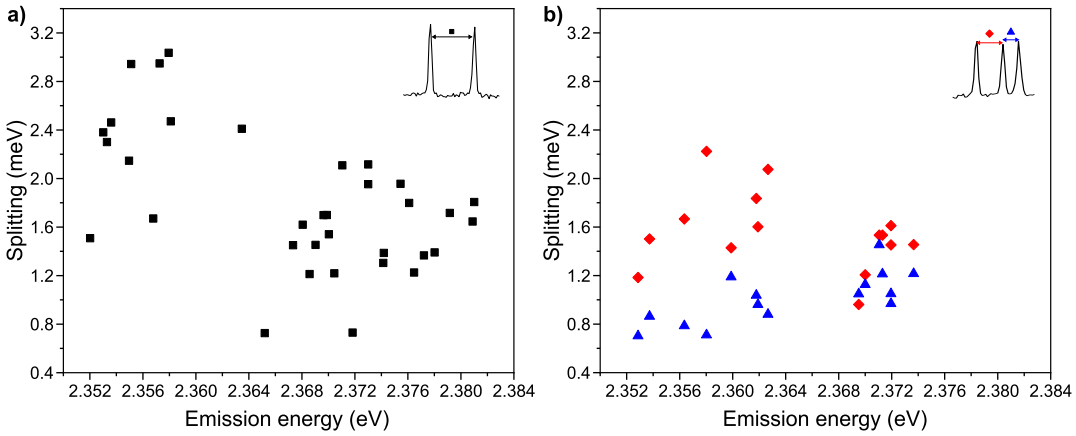

Figure 5.2: **a)** Splitting energy of the doublet emission line ■ and **b)** of the triplet emission lines between the two lowest energy lines ◆ and between the two highest energy lines ▲ as a function of the exciton emission energy.

The energy splittings of the two and three exciton emission lines are given in Fig. 5.2. They span between 0.7 and 3 meV for the two ZPLs and between 0.7 and 2.4 meV for the triplet ZPLs, with no apparent correlations between the splitting values and the emission energy. The splitting ranges are similar to the ones observed for cubic nanocrystals of $CsPbBr_3$, for equivalent effective sizes, in Ref. [199]. The mean energy splitting values are: $\bar{\Delta}_{\text{doublet}}$(■) = 1.81 meV, $\bar{\Delta}_1$(◆) = 1.56 meV and $\bar{\Delta}_2$(▲)= 1.02 meV. To better understand the structure of these spectra, we analyze the weight of the lines hereafter.

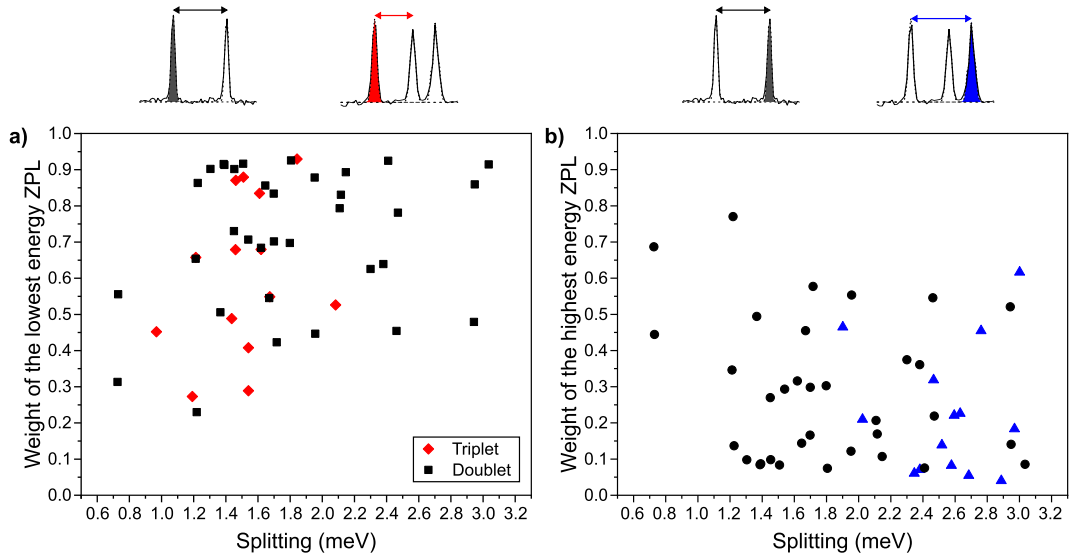

Figure 5.3: **a)** Weight of the lowest-energy line as a function of the splitting energy between the two lowest-energy lines for ■ doublet and ◆ triplet emission lines. **b)** Weight of the highest-energy line as a function of the splitting energy between the lowest- and highest-energy lines for doublet ● and triplet ▲ emission lines.

The weight of the different emission lines varies from one nanorod to another, both for two and three ZPLs spectra. Fig. 5.3 **a)** and **b)** display the weight of the lowest-energy (respectively highest-energy) line as a function of the splitting energy of the two lowest-energy (respectively

lowest and highest) lines, in the case of nanorods presenting two and three ZPLs. The relative weights of the triplet ZPLs generally depend on the orientation of the nanorod with respect to the optical axis, as well as on the population and the oscillator strength of the state at the origin of emission. Fig. 5.3 shows a large dispersion of the different ZPLs weights, reflecting the variety of nanorods orientations. Nevertheless, the weight of the lowest-energy line mostly dominates: its average weight for both doublet and triplet is 0.68, whereas the highest-energy line of the triplet has an average weight of 0.22. The thermalization of state populations is ruled out, considering that the energy splittings of the lines are high compared to the thermal energy ($k_{\mathrm{B}}T \approx 0.3$ meV) and that there is no apparent correlation between the weight of a line and its splitting energy. Therefore, the dominance of the lowest-energy line weight suggests a variation of oscillator strengths between the different exciton bright states.

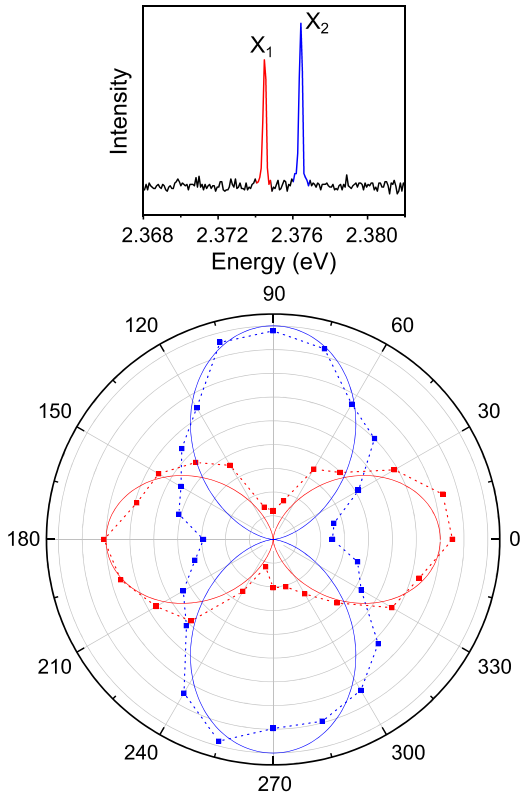

Figure 5.4: Polarization-dependent optical spectroscopy of a single nanorod. The area of each emission line is plotted as a function of the polarization angle.

Fig. 5.4 displays the polarization study for a two-line emission spectrum. The two lines exhibit clear orthogonal polarization, indicating that the emitting states correspond to distinct transition dipole orientations, which indicates that each of the two emission lines is non-degenerate. Therefore, a line from one of the bright exciton triplets is missing in the doublet spectra. The observation of two ZPLs instead of three likely results from a very low oscillator strength of the third state. To try and highlight all the triplet lines, we apply a magnetic field to lift any possible degeneracy and change the weight of the lines [55], and we increase the temperature to change the population of the states.

Fig. 5.5 **a)** and **b)** depict the evolution of photoluminescence spectra with magnetic field in the case of two and three emission lines, respectively. Increasing the magnetic field does not lead to the observation of new emission lines for all 32 nanorods studied under a magnetic field. However, a change in the weight of the emission lines is clearly observed as a result of field-coupling

of the fine structure states. Fig. 5.5 **c)** and **d)** show the evolution of photoluminescence spectra with temperature. As the temperature rises, the emission line exhibits a broadening attributed to electron-phonon coupling, along with a blue-shift due to the stabilization of the valence band maximum with lattice expansion [200] as previously observed for $FAPbBr_3$ [58, 201]. Of the four nanocrystals with doublet ZPLs studied with temperature, only one presented a new line appearing between the two lines at 30 K, as shown in Fig. 5.5 **c)**, while the others only display two emission lines regardless of the temperature, as exemplified in Fig. 5.5 **d)**.

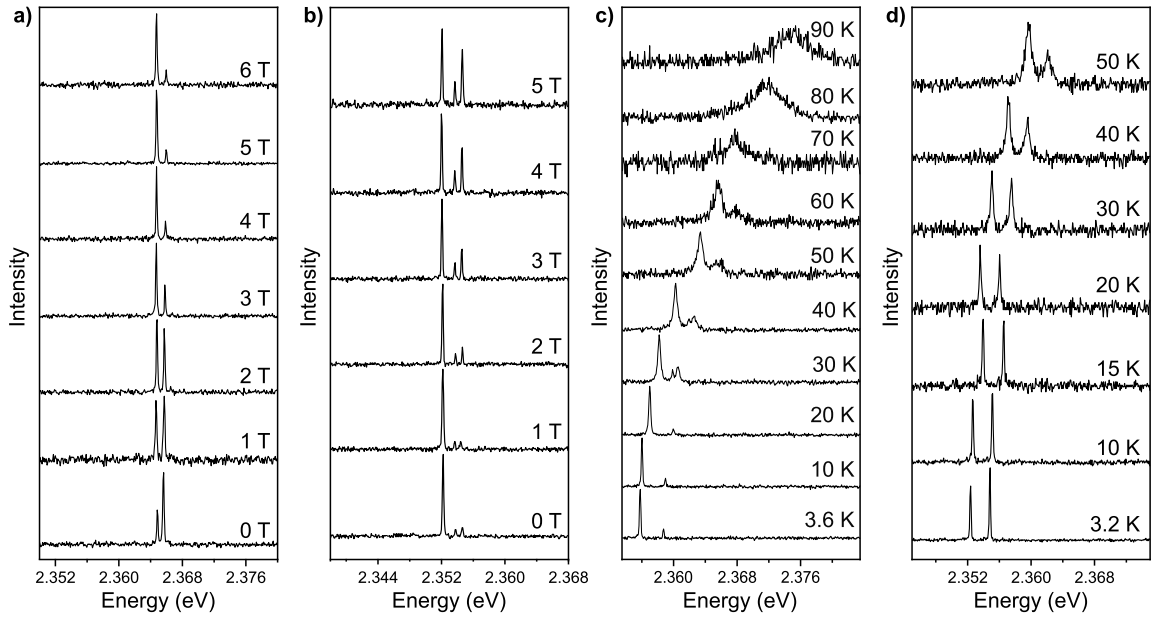

Figure 5.5: Magneto-optical study at 3.5 K and temperature study at 0 T for **a)**, **c)** and **d)** two emission lines and **b)** triplet emission lines.

Next, we investigate $CsPbBr_3$ nanorods with higher aspect ratios to explore the modification of their photoluminescence spectra.

Photoluminescence spectroscopy on $CsPbBr_3$ nanorods with large AR

We now study a sample of $CsPbBr_3$ nanorods, measuring $5.3 \pm 0.5 \times 29.8 \pm 3.5$ nm ($AR = 5.6$, $L_e = 9.4$ nm). A TEM image of these nanocrystals is given in Fig. 5.6. Our spectroscopy results are presented in Fig. 5.7.

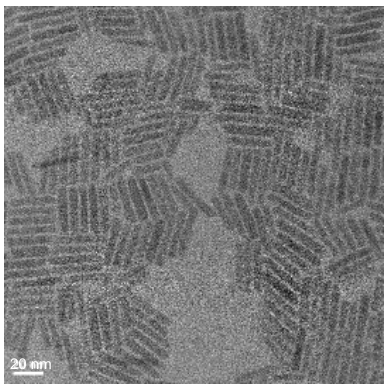

Figure 5.6: Transmission electron microscopy of $CsPbBr_3$ nanorods measuring 5.3×29.8 nm.

Of the 34 nanorods studied, each exhibited a single ZPL in the absence of magnetic fields. Applying an external magnetic field to the nanocrystals does not change their emission spectra, as shown in Fig. 5.7 **a)**. There is no emergence of a new line nor splitting of the single line, suggesting that the emission originates from one non-degenerate energy state.

This hypothesis is validated by the polarization study conducted on the same nanorod, displayed in Fig. 5.7 **b)**. The area of the emission line relative to the polarizer angle confirms that this nanocrystal presents a linearly polarized emission.

We also studied the emission spectra of a single nanorod as a function of temperature up to 80 K. The results are presented in Fig. 5.7 **c)**. Similarly observed in section 5.2.1, the emission line exhibits a broadening along with a blue shift when increasing the temperature. However, no new lines emerge, indicating that no new energy level is thermally populated even at higher temperatures.

All of the studied nanorods of this sample exhibit a single emission line, matching the typical results presented in Fig. 5.7. This observation suggests that one of the exciton bright triplet states has a significantly larger oscillator strength compared to the other states. Based on the results from the previous section, where the lowest-energy line has the highest weight for 77% of the nanorods, it is likely that the emission comes from the lowest bright exciton state.

The consistency of spectra across all nanocrystals reinforced their potential as indistinguishable photon sources. Unlike nanocubes, they would not require any polarization filtering but only optical filtering for potential trion and biexciton recombination and LO replicas. Additionally, these samples demonstrate robust spectral stability over time.

These data should fuel the development of refined theoretical models to explain the evolution of the fine structure and the oscillator strengths with the nanorod aspect ratio.

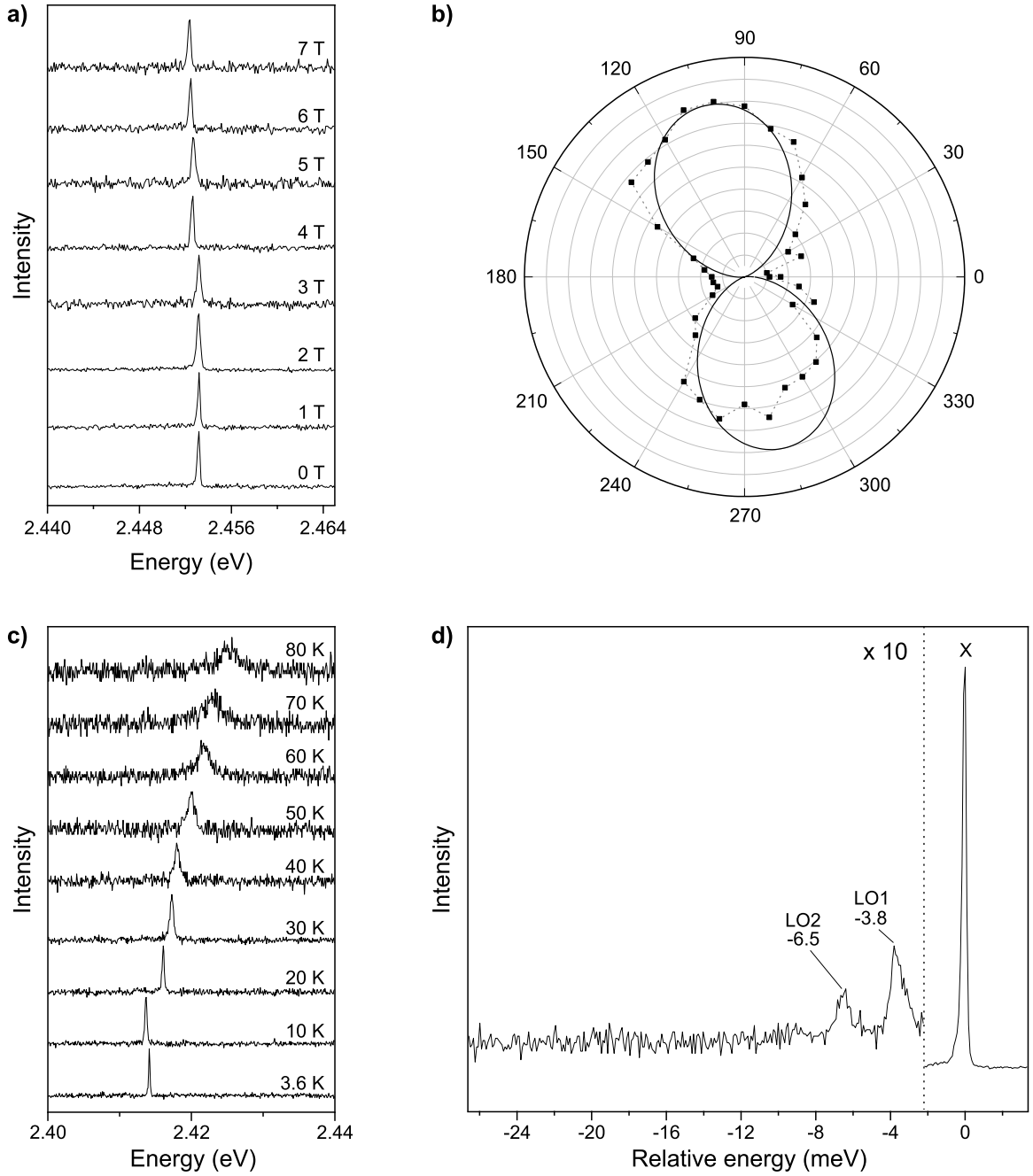

Figure 5.7: a) Photoluminescence emission spectra at low temperature of a single nanocrystal as a function of external magnetic field applied in Faraday configuration. **b)** Polarization study of the same nanocrystal as in a) showing a linearly polarized emission. **c)** Photoluminescence emission as a function of temperature. **d)** Photoluminescence spectra at high excitation intensity showing two LO phonon lines, with a shift of 3.8 and 6.5 meV from the exciton emission; these values are similar to those observed in the previous section for nanorods with smaller AR. Their emission constitutes 9% and 6% of the total emission, respectively.

Bibliography

[1] A. Ekimov, Al. L. Efros, and A. Onushchenko. "Quantum Size Effect in Semiconductor Microcrystals". *Solid State Communications* 56.11 (Dec. 1985), pp. 921–924.

[2] A. I. Ekimov and A. A. Onushchenko. "Size Quantization of the Electron Energy Spectrum". *Jetp Lett.* 40.8 (1984), pp. 1136–1139.

[3] L. E. Brus. "Electron–Electron and Electron-hole Interactions in Small Semiconductor Crystallites: The Size Dependence of the Lowest Excited Electronic State". *The Journal of Chemical Physics* 80.9 (May 1984), pp. 4403–4409.

[4] C. B. Murray, D. J. Norris, and M. G. Bawendi. "Synthesis and Characterization of Nearly Monodisperse CdE (E = Sulfur, Selenium, Tellurium) Semiconductor Nanocrystallites". *J. Am. Chem. Soc.* 115.19 (Sept. 1, 1993), pp. 8706–8715.

[5] Al. L. Efros and A. V. Rodina. "Band-Edge Absorption and Luminescence of Nonspherical Nanometer-Size Crystals". *Phys. Rev. B* 47.15 (Apr. 15, 1993), pp. 10005–10007.

[6] O. I. Micic et al. "Synthesis and Characterization of InP Quantum Dots". *J. Phys. Chem.* 98.19 (May 1994), pp. 4966–4969.

[7] Y.-H. Won et al. "Highly Efficient and Stable InP/ZnSe/ZnS Quantum Dot Light-Emitting Diodes". *Nature* 575.7784 (Nov. 28, 2019), pp. 634–638.

[8] Y. Shirasaki et al. "Emergence of Colloidal Quantum-Dot Light-Emitting Technologies". *Nature Photon* 7.1 (Jan. 2013), pp. 13–23.

[9] R. W. Crisp et al. "Highly Photoconductive InP Quantum Dots Films and Solar Cells". *ACS Appl. Energy Mater.* 1.11 (Nov. 26, 2018), pp. 6569–6576.

[10] I. N. Chakraborty et al. "InP/ZnS Quantum Dots as Efficient Visible-Light Photocatalysts for Redox and Carbon–Carbon Coupling Reactions". *Chem. Mater.* 31.7 (Apr. 9, 2019), pp. 2258–2262.

[11] S. Yu et al. "Efficient Photocatalytic Hydrogen Evolution with Ligand Engineered All-Inorganic InP and InP/ZnS Colloidal Quantum Dots". *Nat Commun* 9.1 (Dec. 2018), p. 4009.

[12] L. Zhang et al. "*In Vivo* Tumor Active Cancer Targeting and CT-fluorescence Dual-Modal Imaging with Nanoprobe Based on Gold Nanorods and InP/ZnS Quantum Dots". *J. Mater. Chem. B* 6.17 (2018), pp. 2574–2583.

[13] L. Protesescu et al. "Nanocrystals of Cesium Lead Halide Perovskites (CsPbX3, X = Cl, Br, and I): Novel Optoelectronic Materials Showing Bright Emission with Wide Color Gamut". *Nano Lett.* 15.6 (June 10, 2015), pp. 3692–3696.

[14] H. Zhou et al. "Interface Engineering of Highly Efficient Perovskite Solar Cells". *Science* 345.6196 (Aug. 2014), pp. 542–546.

[15] W. Sun et al. "Lead Halide Perovskite Vortex Microlasers". *Nat Commun* 11.1 (Sept. 25, 2020), p. 4862.

[16] Y. He et al. “CsPbBr3 Perovskite Detectors with 1.4% Energy Resolution for High-Energy γ-Rays”. *Nat. Photonics* 15.1 (Jan. 2021), pp. 36–42.

[17] E. Poem et al. “Accessing the Dark Exciton with Light”. *Nature Phys* 6.12 (Dec. 2010), pp. 993–997.

[18] I. Schwartz et al. “Deterministic Generation of a Cluster State of Entangled Photons”. *Science* 354.6311 (Oct. 28, 2016), pp. 434–437.

[19] F. Yan et al. “Light Generation in Lead Halide Perovskite Nanocrystals: LEDs, Color Converters, Lasers, and Other Applications”. *Small* 15.47 (2019), p. 1902079.

[20] B. Lounis and M. Orrit. “Single-Photon Sources”. *Rep. Prog. Phys.* 68.5 (Apr. 2005), p. 1129.

[21] O. Benson et al. “Regulated and Entangled Photons from a Single Quantum Dot”. *Phys. Rev. Lett.* 84.11 (Mar. 13, 2000), pp. 2513–2516.

[22] R. M. Stevenson et al. “A Semiconductor Source of Triggered Entangled Photon Pairs”. *Nature* 439.7073 (7073 Jan. 2006), pp. 179–182.

[23] M. Kim et al. “Switchable S = 1/2 and J = 1/2 Rashba Bands in Ferroelectric Halide Perovskites”. *Proceedings of the National Academy of Sciences* 111.19 (May 13, 2014), pp. 6900–6904.

[24] F. Zheng et al. “Rashba Spin–Orbit Coupling Enhanced Carrier Lifetime in CH3NH3PbI3”. *Nano Lett.* 15.12 (Dec. 9, 2015), pp. 7794–7800.

[25] M. Kepenekian et al. “Rashba and Dresselhaus Effects in Hybrid Organic–Inorganic Perovskites: From Basics to Devices”. *ACS Nano* 9.12 (Dec. 22, 2015), pp. 11557–11567.

[26] N. W. Ashcroft and N. D. Mermin. *Solid State Physics*. Fort Worth: Harcourt Brace, 1976.

[27] V. I. Klimov, ed. *Semiconductor and Metal Nanocrystals: Synthesis and Electronic and Optical Properties*. Optical Engineering 87. New York, NY Basel: Dekker, 2004. 484 pp.

[28] Al. L. Efros and A. L. Efros. “Interband Absorption of Light in a Semi-conductor Sphere.” *Sov. Phys. Semicond.* 16 (1982), pp. 772–775.

[29] L. E. Brus. “A Simple Model for the Ionization Potential, Electron Affinity, and Aqueous Redox Potentials of Small Semiconductor Crystallites”. *The Journal of Chemical Physics* 79.11 (Dec. 1983), pp. 5566–5571.

[30] Al. L. Efros and M. Rosen. “The Electronic Structure of Semiconductor Nanocrystals”. *Annu. Rev. Mater. Sci.* 30.1 (Aug. 2000), pp. 475–521.

[31] C. Kittel. *Quantum Theory of Solids*. 2. rev. print. New York, NY: Wiley, 1987. 425 pp.

[32] J. M. Luttinger and W. Kohn. “Motion of Electrons and Holes in Perturbed Periodic Fields”. *Phys. Rev.* 97.4 (Feb. 15, 1955), pp. 869–883.

[33] E. O. Kane. “Band Structure of Indium Antimonide”. *Journal of Physics and Chemistry of Solids* 1.4 (Jan. 1, 1957), pp. 249–261.

[34] C. R. Pidgeon and R. N. Brown. “Interband Magneto-Absorption and Faraday Rotation in InSb”. *Phys. Rev.* 146.2 (June 10, 1966), pp. 575–583.

[35] Al. L. Efros et al. “Band-Edge Exciton in Quantum Dots of Semiconductors with a Degenerate Valence Band: Dark and Bright Exciton States”. *Phys. Rev. B* 54.7 (Aug. 15, 1996), pp. 4843–4856.

[36] Al. L. Efros. “Luminescence Polarization of CdSe Microcrystals”. *Phys. Rev. B* 46.12 (Sept. 15, 1992), pp. 7448–7458.

[37] G. E. Pikus and G. L. Bir. “Exchange Interaction in Excitons in Semiconductors”. *Zh. Eksp. Theor. Fiz.* 60 (1971), pp. 195–208.

[38] G. L. Bir and G. E. Pikus. *Symmetry and Strain-induced Effects in Semiconductors*. Wiley, 1974. 484 pp.

[39] R. S. Knox. *Theory of Excitons*. 2. print. Solid State Physics Supplement 5. New York: Academic Pr, 1972. 207 pp.

[40] M. Levinshtein, S. Rumyantsev, and M. Shur. *Handbook Series on Semiconductor Parameters: Volume 1: Si, Ge, C (Diamond), GaAs, GaP, GaSb, InAs, InP, InSb*. Vol. 1. World Scientific, Nov. 1996.

[41] Y.-S. Kim, K. Hummer, and G. Kresse. “Accurate Band Structures and Effective Masses for InP, InAs, and InSb Using Hybrid Functionals”. *Phys. Rev. B* 80.3 (July 13, 2009), p. 035203.

[42] A. Brodu et al. “Fine Structure of Nearly Isotropic Bright Excitons in InP/ZnSe Colloidal Quantum Dots”. *J. Phys. Chem. Lett.* 10.18 (Sept. 19, 2019), pp. 5468–5475.

[43] H. Fu, L.-W. Wang, and A. Zunger. “Excitonic Exchange Splitting in Bulk Semiconductors”. *Phys. Rev. B* 59.8 (Feb. 15, 1999), pp. 5568–5574.

[44] P. C. Sercel and A. L. Efros. “Band-Edge Exciton in CdSe and Other II–VI and III–V Compound Semiconductor Nanocrystals - Revisited”. *Nano Lett.* 18.7 (July 11, 2018), pp. 4061–4068.

[45] O. Madelung. *Semiconductors: Data Handbook*. Berlin, Heidelberg: Springer Berlin Heidelberg, 2004.

[46] W. Ekardt, K. Lösch, and D. Bimberg. “Determination of the Analytical and the Nonanalytical Part of the Exchange Interaction of InP and GaAs from Polariton Spectra in Intermediate Magnetic Fields”. *Phys. Rev. B* 20.8 (Oct. 15, 1979), pp. 3303–3314.

[47] A. M. Glazer. “The Classification of Tilted Octahedra in Perovskites”. *Acta Crystallogr B Struct Crystallogr Cryst Chem* 28.11 (Nov. 15, 1972), pp. 3384–3392.

[48] M. C. Brennan, M. Kuno, and S. Rouvimov. “Crystal Structure of Individual CsPbBr3 Perovskite Nanocubes”. *Inorg. Chem.* 58.2 (Jan. 22, 2019), pp. 1555–1560.

[49] D. Weinberg et al. “Size-Dependent Lattice Symmetry Breaking Determines the Exciton Fine Structure of Perovskite Nanocrystals”. *Nano Lett.* 23.11 (June 14, 2023), pp. 4997–5003.

[50] K. Heidrich et al. “Electronic Structure, Photoemission Spectra, and Vacuum-Ultraviolet Optical Spectra of CsPbCl3 and CsPbBr3”. *Phys. Rev. B* 24.10 (Nov. 15, 1981), pp. 5642–5649.

[51] M. A. Becker et al. “Bright Triplet Excitons in Caesium Lead Halide Perovskites”. *Nature* 553.7687 (Jan. 2018), pp. 189–193.

[52] M. Hussain et al. “Spin–Orbit Coupling Effect on Energy Level Splitting and Band Structure Inversion in CsPbBr3”. *J Mater Sci* 56.1 (Jan. 2021), pp. 528–542.

[53] R. Ben Aich et al. “Bright-Exciton Splittings in Inorganic Cesium Lead Halide Perovskite Nanocrystals”. *Phys. Rev. Applied* 11.3 (Mar. 18, 2019), p. 034042.

[54] A. Ghribi et al. “Dielectric Effects, Crystal Field, and Shape Anisotropy Tuning of the Exciton Fine Structure of Halide Perovskite Nanocrystals”. *Phys. Rev. Materials* 6.10 (Oct. 3, 2022), p. 106001.

[55] M. Fu et al. “Neutral and Charged Exciton Fine Structure in Single Lead Halide Perovskite Nanocrystals Revealed by Magneto-optical Spectroscopy”. *Nano Lett.* 17.5 (May 10, 2017), pp. 2895–2901.

[56] P. C. Sercel et al. “Exciton Fine Structure in Perovskite Nanocrystals”. *Nano Lett.* (2019), p. 10.

[57] M. Sajedi et al. “Absence of a Giant Rashba Effect in the Valence Band of Lead Halide Perovskites”. *Phys. Rev. B* 102.8 (Aug. 21, 2020), p. 081116.

[58] P. Tamarat et al. “The Ground Exciton State of Formamidinium Lead Bromide Perovskite Nanocrystals Is a Singlet Dark State”. *Nat. Mater.* 18.7 (July 2019), pp. 717–724.

[59] P. Tamarat et al. “The Dark Exciton Ground State Promotes Photon-Pair Emission in Individual Perovskite Nanocrystals”. *Nat Commun* 11.1 (Dec. 2020), p. 6001.

[60] M. Nirmal et al. “Observation of the "Dark Exciton" in CdSe Quantum Dots”. *Phys. Rev. Lett.* 75.20 (Nov. 13, 1995), pp. 3728–3731.

[61] M. Bayer et al. “Fine Structure of Neutral and Charged Excitons in Self-Assembled In(Ga)As/(Al)GaAs Quantum Dots”. *Phys. Rev. B* 65.19 (May 7, 2002), p. 195315.

[62] M. J. Fernée et al. “Magneto-Optical Properties of Trions in Non-Blinking Charged Nanocrystals Reveal an Acoustic Phonon Bottleneck”. *Nat Commun* 3.1 (Jan. 2012), p. 1287.

[63] Y. Louyer et al. “Efficient Biexciton Emission in Elongated CdSe/ZnS Nanocrystals”. *Nano Lett.* 11.10 (Oct. 12, 2011), pp. 4370–4375.

[64] H. Htoon et al. “Highly Emissive Multiexcitons in Steady-State Photoluminescence of Individual “Giant” CdSe/CdS Core/Shell Nanocrystals”. *Nano Lett.* 10.7 (July 14, 2010), pp. 2401–2407.

[65] Y. Arashida, Y. Ogawa, and F. Minami. “Polarization-Correlated Photon Pairs from Charged Biexciton in a Single GaAs Quantum Dot”. *Physica E: Low-dimensional Systems and Nanostructures* 43.3 (Jan. 2011), pp. 804–807.

[66] S. A. Empedocles and M. G. Bawendi. “Quantum-Confined Stark Effect in Single CdSe Nanocrystallite Quantum Dots”. *Science* 278.5346 (Dec. 19, 1997), pp. 2114–2117.

[67] S. A. Empedocles and M. G. Bawendi. “Influence of Spectral Diffusion on the Line Shapes of Single CdSe Nanocrystallite Quantum Dots”. *J. Phys. Chem. B* 103.11 (Mar. 1, 1999), pp. 1826–1830.

[68] M. J. Fernée et al. “Spontaneous Spectral Diffusion in CdSe Quantum Dots”. *J. Phys. Chem. Lett.* 3.12 (June 21, 2012), pp. 1716–1720.

[69] M. J. Fernée et al. “The Ultimate Limit to the Emission Linewidth of Single Nanocrystals”. *Nanotechnology* 24 (Oct. 24, 2013), 465703 (1.

[70] M. Nirmal et al. “Fluorescence Intermittency in Single Cadmium Selenide Nanocrystals”. *Nature* 383.6603 (Oct. 1996), pp. 802–804.

[71] V. I. Klimov et al. “Quantization of Multiparticle Auger Rates in Semiconductor Quantum Dots”. *Science* 287.5455 (Feb. 11, 2000), pp. 1011–1013.

[72] G. E. Cragg and A. L. Efros. “Suppression of Auger Processes in Confined Structures”. *Nano Lett.* 10.1 (Jan. 13, 2010), pp. 313–317.

[73] B. Mahler et al. “Towards Non-Blinking Colloidal Quantum Dots”. *Nature Mater* 7.8 (Aug. 2008), pp. 659–664.

[74] B. O. Dabbousi et al. “(CdSe)ZnS Core-Shell Quantum Dots: Synthesis and Characterization of a Size Series of Highly Luminescent Nanocrystallites”. *J. Phys. Chem. B* 101.46 (Nov. 1, 1997), pp. 9463–9475.

[75] M. D. Tessier et al. “Economic and Size-Tunable Synthesis of InP/ZnE (E = S, Se) Colloidal Quantum Dots.” *Chem. Mater.* 27.13 (July 14, 2015), pp. 4893–4898.

[76] S. Kim et al. “Type-II Quantum Dots: CdTe/CdSe(Core/Shell) and CdSe/ZnTe(Core-/Shell) Heterostructures”. *J. Am. Chem. Soc.* 125.38 (Sept. 1, 2003), pp. 11466–11467.

[77] X. Yang et al. “Synthesis of In2O3–In2S3 Core–Shell Nanorods with Inverted Type-I Structure for Photocatalytic H2 Generation”. *Phys. Chem. Chem. Phys.* 15.30 (2013), p. 12688.

[78] T. Baran et al. “Reverse Type I Core - CuI /Shell - CuO: A Versatile Heterostructure for Photoelectrochemical Applications”. *Electrochimica Acta* 266 (Mar. 10, 2018), pp. 441–451.

[79] A. B. Greytak et al. “Alternating Layer Addition Approach to CdSe/CdS Core/Shell Quantum Dots with near-Unity Quantum Yield and High on-Time Fractions”. *Chem. Sci.* 3.6 (2012), p. 2028.

[80] Y.-S. Park et al. “Effect of the Core/Shell Interface on Auger Recombination Evaluated by Single-Quantum-Dot Spectroscopy”. *Nano Lett.* 14.2 (Feb. 12, 2014), pp. 396–402.

[81] G. Rainò et al. “Ultra-Narrow Room-Temperature Emission from Single CsPbBr3 Perovskite Quantum Dots”. *Nat Commun* 13.1 (Dec. 2022), p. 2587.

[82] J. Shamsi et al. “Metal Halide Perovskite Nanocrystals: Synthesis, Post-Synthesis Modifications, and Their Optical Properties”. *Chem. Rev.* 119.5 (Mar. 13, 2019), pp. 3296–3348.

[83] M. V. Kovalenko and M. I. Bodnarchuk. “Lead Halide Perovskite Nanocrystals: From Discovery to Self-assembly and Applications”. *Chimia* 71.7-8 (Aug. 9, 2017), p. 461.

[84] G. H. Ahmed et al. “Successes and Challenges of Core/Shell Lead Halide Perovskite Nanocrystals”. *ACS Energy Lett.* 6.4 (Apr. 9, 2021), pp. 1340–1357.

[85] B. Chen, D. Li, and F. Wang. “InP Quantum Dots: Synthesis and Lighting Applications”. *Small* 16.32 (Aug. 2020), p. 2002454.

[86] P. Y. Yu and M. Cardona. *Fundamentals of Semiconductors: Physics and Materials Properties*. Graduate Texts in Physics. Berlin, Heidelberg: Springer, 2010.

[87] S. V. Gaponenko. *Optical Properties of Semiconductor Nanocrystals*. 1st ed. Cambridge University Press, Oct. 28, 1998.

[88] Y.-N. Hwang, S.-H. Park, and D. Kim. “Size-Dependent Surface Phonon Mode of CdSe Quantum Dots”. *Phys. Rev. B* 59.11 (Mar. 15, 1999), pp. 7285–7288.

[89] J. L. Blackburn et al. “Electron Relaxation in Colloidal InP Quantum Dots with Photogenerated Excitons or Chemically Injected Electrons”. *J. Phys. Chem. B* 107.1 (Jan. 1, 2003), pp. 102–109.

[90] U. Woggon et al. “Ultrafast Energy Relaxation in Quantum Dots”. *Phys. Rev. B* 54.24 (Dec. 15, 1996), pp. 17681–17690.

[91] Al. L. Efros, V. Kharchenko, and M. Rosen. "Breaking the Phonon Bottleneck in Nanometer Quantum Dots: Role of Auger-like Processes". *Solid State Communications* 93.4 (Jan. 1995), pp. 281–284.

[92] V. I. Klimov et al. "Mechanisms for Intraband Energy Relaxation in Semiconductor Quantum Dots: The Role of Electron-Hole Interactions". *Phys. Rev. B* 61.20 (May 15, 2000), R13349–R13352.

[93] M. Fu et al. "Unraveling Exciton–Phonon Coupling in Individual FAPbI3 Nanocrystals Emitting near-Infrared Single Photons". *Nat Commun* 9.1 (Dec. 2018), p. 3318.

[94] U. Woggon. *Optical Properties of Semiconductor Quantum Dots*. Springer Tracts in Modern Physics 136. Berlin Heidelberg: Springer, 1997. 251 pp.

[95] H. Fröhlich, H. Pelzer, and S. Zienau. "XX. Properties of Slow Electrons in Polar Materials". *The London, Edinburgh, and Dublin Philosophical Magazine and Journal of Science* 41.314 (Mar. 1950), pp. 221–242.

[96] V. I. Klimov. *Nanocrystal Quantum Dots*. 2nd ed. Boca Raton: CRC press, 2010.

[97] S. A. Empedocles et al. "Photoluminescence from Single Semiconductor Nanostructures". *Adv. Mater.* 11.15 (Oct. 1999), pp. 1243–1256.

[98] K. Miyata, T. L. Atallah, and X.-Y. Zhu. "Lead Halide Perovskites: Crystal-liquid Duality, Phonon Glass Electron Crystals, and Large Polaron Formation". *Sci. Adv.* 3.10 (Oct. 6, 2017), e1701469.

[99] K. Cho et al. "Exciton–Phonon and Trion–Phonon Couplings Revealed by Photoluminescence Spectroscopy of Single CsPbBr3 Perovskite Nanocrystals". *Nano Lett.* 22.18 (Sept. 28, 2022), pp. 7674–7681.

[100] M.-R. Amara et al. "Spectral Fingerprint of Quantum Confinement in Single CsPbBr3 Nanocrystals". *Nano Lett.* 23.8 (Apr. 26, 2023), pp. 3607–3613.

[101] K. Cho et al. "Luminescence Fine Structures in Single Lead Halide Perovskite Nanocrystals: Size Dependence of the Exciton–Phonon Coupling". *Nano Lett.* 21.17 (Sept. 8, 2021), pp. 7206–7212.

[102] J. Ramade et al. "Exciton-Phonon Coupling in a CsPbBr $_3$ Single Nanocrystal". *Appl. Phys. Lett.* 112.7 (Feb. 12, 2018), p. 072104.

[103] T. Itoh and M. Furumiya. "Size-Dependent Homogeneous Broadening of Confined Excitons in CuC1 Microcrystals". *Journal of Luminescence* 48 (1991), pp. 704–708.

[104] G. Morello et al. "Temperature and Size Dependence of Nonradiative Relaxation and Exciton-Phonon Coupling in Colloidal CdTe Quantum Dots". *J. Phys. Chem. C* 111.16 (Apr. 1, 2007), pp. 5846–5849.

[105] E. Prin et al. "Revealing the Band-Edge Exciton Fine Structure of Single InP Nanocrystals". *Nano Lett.* 23.13 (July 12, 2023), pp. 6067–6072.

[106] M. V. Kovalenko, L. Protesescu, and M. I. Bodnarchuk. "Properties and Potential Optoelectronic Applications of Lead Halide Perovskite Nanocrystals". *Science* 358.6364 (Nov. 10, 2017), pp. 745–750.

[107] J. Laverdant et al. "Experimental Determination of the Fluorescence Quantum Yield of Semiconductor Nanocrystals". *Materials* 4.7 (June 30, 2011), pp. 1182–1193.

[108] C. Würth et al. "Relative and Absolute Determination of Fluorescence Quantum Yields of Transparent Samples". *Nat Protoc* 8.8 (Aug. 2013), pp. 1535–1550.

[109] R. Kubin and A. Fletcher. “Fluorescence Quantum Yields of Some Rhodamine Dyes”. *Journal of Luminescence* 27.4 (Dec. 1982), pp. 455–462.

[110] S. Dhami et al. “Phthalocyanine Fluorescence at High Concentration: Dimers or Reabsorption Effect?” *Photochemistry and Photobiology* 61.4 (1995), pp. 341–346.

[111] C. D. Sonnichsen et al. “Polaronic Quantum Confinement in Bulk CsPb Br 3 Perovskite Crystals Revealed by State-Resolved Pump/Probe Spectroscopy”. *Phys. Rev. Research* 3.2 (May 26, 2021), p. 023147.

[112] Q. Deplano. “Manipulations optiques ultra-rapides de molécules organiques fluorescentes et étude de l’intrication moléculaire pour deux émetteurs quantiques couplés à températures cryogéniques”. Bordeaux, 2023.

[113] *Cryostats for quantum technology*. MyCryoFirm. URL: https://www.mycryofirm.com.

[114] M. Wahl. *Time-Correlated Single Photon Counting*.

[115] A. M. Derfus, W. C. W. Chan, and S. N. Bhatia. “Probing the Cytotoxicity of Semiconductor Quantum Dots”. *Nano Lett.* 4.1 (Jan. 1, 2004), pp. 11–18.

[116] H. Soo Choi et al. “Renal Clearance of Quantum Dots”. *Nat Biotechnol* 25.10 (Oct. 2007), pp. 1165–1170.

[117] J. Geys et al. “Acute Toxicity and Prothrombotic Effects of Quantum Dots: Impact of Surface Charge”. *Environ Health Perspect* 116.12 (Dec. 2008), pp. 1607–1613.

[118] C. Kirchner et al. “Cytotoxicity of Colloidal CdSe and CdSe/ZnS Nanoparticles”. *Nano Lett.* 5.2 (Feb. 1, 2005), pp. 331–338.

[119] V. Brunetti et al. “InP/ZnS as a Safer Alternative to CdSe/ZnS Core/Shell Quantum Dots: In Vitro and in Vivo Toxicity Assessment”. *Nanoscale* 5.1 (2013), pp. 307–317.

[120] R. Yadav et al. “Narrow Near-Infrared Emission from InP QDs Synthesized with Indium(I) Halides and Aminophosphine”. *J. Am. Chem. Soc.* 145.10 (Mar. 15, 2023), pp. 5970–5981.

[121] F. Dussert et al. “Physico-Chemical Transformation and Toxicity of Multi-Shell InP Quantum Dots under Simulated Sunlight Irradiation, in an Environmentally Realistic Scenario”. *Nanomaterials* 12.20 (Oct. 21, 2022), p. 3703.

[122] D. J. Norris, A. L. Efros, and S. C. Erwin. “Doped Nanocrystals”. *Science* 319.5871 (Mar. 28, 2008), pp. 1776–1779.

[123] L. Biadala et al. “Band-Edge Exciton Fine Structure and Recombination Dynamics in InP/ZnS Colloidal Nanocrystals”. *ACS Nano* 10.3 (Mar. 22, 2016), pp. 3356–3364.

[124] A. Brodu et al. “Exciton Fine Structure and Lattice Dynamics in InP/ZnSe Core/Shell Quantum Dots”. *ACS Photonics* 5.8 (Aug. 15, 2018), pp. 3353–3362.

[125] A. Brodu et al. “Exciton-Phonon Coupling in InP Quantum Dots with ZnS and (Zn , Cd) Se Shells”. *Phys. Rev. B* 101.12 (Mar. 13, 2020), p. 125413.

[126] Y. P. Varshni. “Temperature Dependence of the Energy Gap in Semiconductors”. *Physica* 34 (1967), pp. 149–154.

[127] R. Pässler. “Basic Model Relations for Temperature Dependencies of Fundamental Energy Gaps in Semiconductors”. *phys. stat. sol. (b)* 200.1 (Mar. 1997), pp. 155–172.

[128] O. Labeau, P. Tamarat, and B. Lounis. “Temperature Dependence of the Luminescence Lifetime of Single CdSe/ZnS Quantum Dots”. *Phys. Rev. Lett.* 90.25 (June 26, 2003), p. 257404.

[129] M. J. Fernée, P. Tamarat, and B. Lounis. “Cryogenic Single-Nanocrystal Spectroscopy: Reading the Spectral Fingerprint of Individual CdSe Quantum Dots”. *J. Phys. Chem. Lett.* 4.4 (Feb. 21, 2013), pp. 609–618.

[130] C. Sinito et al. “Tailoring the Exciton Fine Structure of Cadmium Selenide Nanocrystals with Shape Anisotropy and Magnetic Field”. *ACS Nano* 8.11 (Nov. 25, 2014), pp. 11651–11656.

[131] P. Tamarat et al. “Universal Scaling Laws for Charge-Carrier Interactions with Quantum Confinement in Lead-Halide Perovskites”. *Nat Commun* 14.1 (Jan. 16, 2023), p. 229.

[132] L. Biadala et al. “Band-Edge Exciton Fine Structure of Single CdSe / ZnS Nanocrystals in External Magnetic Fields”. *Phys. Rev. Lett.* 105.15 (Oct. 5, 2010), p. 157402.

[133] H. Htoon et al. “Linearly Polarized ‘Fine Structure’ of the Bright Exciton State in Individual CdSe Nanocrystal Quantum Dots”. *Phys. Rev. B* 77.3 (Jan. 22, 2008), p. 035328.

[134] H. Htoon et al. “Anomalous Circular Polarization of Photoluminescence Spectra of Individual CdSe Nanocrystals in an Applied Magnetic Field”. *Phys. Rev. Lett.* 102.1 (Jan. 9, 2009), p. 017402.

[135] H. Ozaki et al. “Photoluminescence and Raman Scattering of ZnSe-ZnTe Superlattices”. *physica status solidi (a)* 133.2 (1992), pp. 523–532.

[136] M. Gandil et al. “Spectroscopic Signatures of Spin-Orbit Coupling and Free Excitons in Individual Suspended Carbon Nanotubes”. *Phys. Rev. B* 100.8 (Aug. 26, 2019), p. 081411.

[137] M. A. Semina, A. A. Golovatenko, and A. V. Rodina. “Influence of the Spin-Orbit Split-off Valence Band on the Hole g Factor in Semiconductor Nanocrystals”. *Phys. Rev. B* 104.20 (Nov. 18, 2021), p. 205423.

[138] S. V. Goupalov. “Anisotropy-Induced Exchange Splitting of Exciton Radiative Doublet in CdSe Nanocrystals”. *Phys. Rev. B* 74.11 (Sept. 11, 2006), p. 113305.

[139] S. V. Gupalov and E. L. Ivchenko. “The Fine Structure of Excitonic Levels in CdSe Nanocrystals”. *Phys. Solid State* 42.11 (Nov. 2000), pp. 2030–2038.

[140] S. Goupalov and E. Ivchenko. “Electron—Hole Long-Range Exchange Interaction in Semiconductor Quantum Dots”. *Journal of Crystal Growth* 184–185 (Feb. 1998), pp. 393–397.

[141] Y. Chen et al. “Exciton-Polaritons in InP: Magnetoreflectance Investigation”. *Phys. Rev. B* 36.3 (July 15, 1987), pp. 1510–1518.

[142] W. Hackenberg, R. T. Phillips, and H. P. Hughes. “Investigation of the Luttinger Parameters for InP Using Hot-Electron Luminescence”. *Phys. Rev. B* 50.15 (Oct. 15, 1994), pp. 10598–10607.

[143] R. Toufanian et al. “Bandgap Engineering of Indium Phosphide-Based Core/Shell Heterostructures Through Shell Composition and Thickness”. *Front. Chem.* 6 (Nov. 20, 2018), p. 567.

[144] S. Adachi and T. Taguchi. “Optical Properties of ZnSe”. *Phys. Rev. B* 43.12 (Apr. 15, 1991), pp. 9569–9577.

[145] A. K. Jena, A. Kulkarni, and T. Miyasaka. “Halide Perovskite Photovoltaics: Background, Status, and Future Prospects”. *Chem. Rev.* 119.5 (Mar. 13, 2019), pp. 3036–3103.

[146] J. Y. Kim et al. “High-Efficiency Perovskite Solar Cells”. *Chem. Rev.* 120.15 (Aug. 12, 2020), pp. 7867–7918.

[147] Y.-S. Park et al. “Room Temperature Single-Photon Emission from Individual Perovskite Quantum Dots”. *ACS Nano* 9.10 (Oct. 27, 2015), pp. 10386–10393.

[148] F. Hu et al. “Superior Optical Properties of Perovskite Nanocrystals as Single Photon Emitters”. *ACS Nano* 9.12 (Dec. 22, 2015), pp. 12410–12416.

[149] G. Rainò et al. “Superfluorescence from Lead Halide Perovskite Quantum Dot Superlattices”. *Nature* 563.7733 (Nov. 2018), pp. 671–675.

[150] H. Utzat et al. “Coherent Single-Photon Emission from Colloidal Lead Halide Perovskite Quantum Dots”. *Science* 363.6431 (Mar. 8, 2019), pp. 1068–1072.

[151] S. Feng et al. “Universal Existence of Localized Single-Photon Emitters in the Perovskite Film of All-Inorganic CsPbBr3 Microcrystals”. *Advanced Materials* 34.1 (2022), p. 2106278.

[152] K. Tanaka et al. “Comparative Study on the Excitons in Lead-Halide-Based Perovskite-Type Crystals CH3NH3PbBr3 CH3NH3PbI3”. *Solid State Communications* 127.9 (Sept. 1, 2003), pp. 619–623.

[153] J. Even. “Pedestrian Guide to Symmetry Properties of the Reference Cubic Structure of 3D All-Inorganic and Hybrid Perovskites”. *J. Phys. Chem. Lett.* 6.12 (June 18, 2015), pp. 2238–2242.

[154] J. Ramade et al. “Fine Structure of Excitons and Electron–Hole Exchange Energy in Polymorphic CsPbBr3 Single Nanocrystals”. *Nanoscale* 10.14 (2018), pp. 6393–6401.

[155] R. Ben Aich et al. “Multiband K · p Model for Tetragonal Crystals: Application to Hybrid Halide Perovskite Nanocrystals”. *J. Phys. Chem. Lett.* 11.3 (Feb. 6, 2020), pp. 808–817.

[156] C. Yin et al. “Bright-Exciton Fine-Structure Splittings in Single Perovskite Nanocrystals”. *Phys. Rev. Lett.* 119.2 (July 11, 2017), p. 026401.

[157] M. Isarov et al. “Rashba Effect in a Single Colloidal CsPbBr3 Perovskite Nanocrystal Detected by Magneto-Optical Measurements”. *Nano Letters* 17.8 (July 5, 2017), pp. 5020–5026.

[158] P. C. Sercel et al. “Quasicubic Model for Metal Halide Perovskite Nanocrystals”. *J. Chem. Phys.* 151.23 (Dec. 21, 2019), p. 234106.

[159] M. W. Swift et al. “Rashba Exciton in a 2D Perovskite Quantum Dot”. *Nanoscale* 13.39 (Oct. 14, 2021), pp. 16769–16780.

[160] V. I. Klimov et al. “Single-Exciton Optical Gain in Semiconductor Nanocrystals”. *Nature* 447.7143 (7143 May 2007), pp. 441–446.

[161] Y. Wang et al. “All-Inorganic Colloidal Perovskite Quantum Dots: A New Class of Lasing Materials with Favorable Characteristics”. *Advanced Materials* 27.44 (2015), pp. 7101–7108.

[162] J. A. Castañeda et al. “Efficient Biexciton Interaction in Perovskite Quantum Dots Under Weak and Strong Confinement”. *ACS Nano* 10.9 (Sept. 27, 2016), pp. 8603–8609.

[163] K. E. Shulenberger et al. “Setting an Upper Bound to the Biexciton Binding Energy in CsPbBr3 Perovskite Nanocrystals”. *J. Phys. Chem. Lett.* 10.18 (Sept. 19, 2019), pp. 5680–5686.

[164] N. S. Makarov et al. “Spectral and Dynamical Properties of Single Excitons, Biexcitons, and Trions in Cesium–Lead-Halide Perovskite Quantum Dots”. *Nano Lett.* 16.4 (Apr. 13, 2016), pp. 2349–2362.

[165] J. Aneesh et al. “Ultrafast Exciton Dynamics in Colloidal CsPbBr3 Perovskite Nanocrystals: Biexciton Effect and Auger Recombination”. *J. Phys. Chem. C* 121.8 (Mar. 2, 2017), pp. 4734–4739.

[166] M. N. Ashner et al. “Size-Dependent Biexciton Spectrum in CsPbBr3 Perovskite Nanocrystals”. *ACS Energy Lett.* 4.11 (Nov. 8, 2019), pp. 2639–2645.

[167] J. Dana et al. “Unusually Strong Biexciton Repulsion Detected in Quantum Confined CsPbBr3 Nanocrystals with Two and Three Pulse Femtosecond Spectroscopy”. *ACS Nano* 15.5 (May 25, 2021), pp. 9039–9047.

[168] X. Huang et al. “Inhomogeneous Biexciton Binding in Perovskite Semiconductor Nanocrystals Measured with Two-Dimensional Spectroscopy”. *J. Phys. Chem. Lett.* 11.23 (Dec. 3, 2020), pp. 10173–10181.

[169] G. Lubin et al. “Resolving the Controversy in Biexciton Binding Energy of Cesium Lead Halide Perovskite Nanocrystals through Heralded Single-Particle Spectroscopy”. *ACS Nano* 15.12 (Dec. 28, 2021), pp. 19581–19587.

[170] G. Nedelcu et al. “Fast Anion-Exchange in Highly Luminescent Nanocrystals of Cesium Lead Halide Perovskites (CsPbX3, X = Cl, Br, I)”. *Nano Lett.* 15.8 (Aug. 12, 2015), pp. 5635–5640.

[171] E. Scharf et al. “Ligands Mediate Anion Exchange between Colloidal Lead-Halide Perovskite Nanocrystals”. *Nano Lett.* 22.11 (June 8, 2022), pp. 4340–4346.

[172] S. Bera, R. K. Behera, and N. Pradhan. “α-Halo Ketone for Polyhedral Perovskite Nanocrystals: Evolutions, Shape Conversions, Ligand Chemistry, and Self-Assembly”. *J. Am. Chem. Soc.* 142.49 (Dec. 9, 2020), pp. 20865–20874.

[173] T. G. Liashenko et al. “Electronic Structure of CsPbBr3-xClx Perovskites: Synthesis, Experimental Characterization, and DFT Simulations”. *Phys. Chem. Chem. Phys.* 21.35 (Sept. 11, 2019), pp. 18930–18938.

[174] M. K. Hossain et al. “Controllable Optical Emission Wavelength in All-Inorganic Halide Perovskite Alloy Microplates Grown by Two-Step Chemical Vapor Deposition”. *Nano Res.* 13.11 (Nov. 1, 2020), pp. 2939–2949.

[175] Z. Yang et al. “Impact of the Halide Cage on the Electronic Properties of Fully Inorganic Cesium Lead Halide Perovskites”. *ACS Energy Lett.* 2.7 (July 14, 2017), pp. 1621–1627.

[176] M. O. Nestoklon et al. “Optical Orientation and Alignment of Excitons in Ensembles of Inorganic Perovskite Nanocrystals”. *Phys. Rev. B* 97.23 (June 6, 2018), p. 235304.

[177] M.-R. Amara et al. “Impact of Bright-Dark Exciton Thermal Population Mixing on the Brightness of CsPbBr3 Nanocrystals”. *Nano Lett.* 24.14 (Apr. 10, 2024), pp. 4265–4271.

[178] Y. Benny et al. “Electron-Hole Spin Flip-Flop in Semiconductor Quantum Dots”. *Phys. Rev. B* 89.3 (Jan. 31, 2014), p. 035316.

[179] H. Wei, G.-C. Guo, and L. He. “Slow Exciton Spin Relaxation in Single Self-Assembled In(1-x)Ga(x)As/GaAs Quantum Dots”. *Phys. Rev. B* 89.24 (June 16, 2014), p. 245305.

[180] L. Hou, P. Tamarat, and B. Lounis. “Revealing the Exciton Fine Structure in Lead Halide Perovskite Nanocrystals”. *Nanomaterials* 11.4 (Apr. 20, 2021), p. 1058.

[181] V. V. Belykh et al. “Coherent Spin Dynamics of Electrons and Holes in CsPbBr3 Perovskite Crystals”. *Nat Commun* 10.1 (Feb. 8, 2019), p. 673.

[182] Z. G. Yu. “Effective-Mass Model and Magneto-Optical Properties in Hybrid Perovskites”. *Sci Rep* 6.1 (Sept. 2016), p. 28576.

[183] T. P. T. Nguyen, S. A. Blundell, and C. Guet. "Calculation of the Biexciton Shift in Nanocrystals of Inorganic Perovskites". *Phys. Rev. B* 101.12 (Mar. 25, 2020), p. 125424.

[184] G. Rainò et al. "Single Cesium Lead Halide Perovskite Nanocrystals at Low Temperature: Fast Single-Photon Emission, Reduced Blinking, and Exciton Fine Structure". *ACS Nano* 10.2 (Feb. 23, 2016), pp. 2485–2490.

[185] Y. Onodera and Y. Toyozawa. "Excitons in Alkali Halides". *J. Phys. Soc. Jpn.* 22.3 (Mar. 15, 1967), pp. 833–844.

[186] M. M. Denisov and V. P. Makarov. "Longitudinal and Transverse Excitons in Semiconductors". *physica status solidi (b)* 56.1 (1973), pp. 9–59.

[187] J. Even et al. "Electronic Model for Self-Assembled Hybrid Organic/Perovskite Semiconductors: Reverse Band Edge Electronic States Ordering and Spin-Orbit Coupling". *Phys. Rev. B* 86.20 (Nov. 5, 2012), p. 205301.

[188] K. Galkowski et al. "Determination of the Exciton Binding Energy and Effective Masses for Methylammonium and Formamidinium Lead Tri-Halide Perovskite Semiconductors". *Energy Environ. Sci.* 9.3 (Mar. 9, 2016), pp. 962–970.

[189] U. Rössler and H.-R. Trebin. "Exchange and Polaron Corrections for Excitons in the Degenerate-Band Case". *Phys. Rev. B* 23.4 (Feb. 15, 1981), pp. 1961–1970.

[190] M. Baranowski et al. "Exciton Binding Energy and Effective Mass of CsPbCl3 : A Magneto-Optical Study". *Photon. Res.* 8.10 (Oct. 1, 2020), A50.

[191] C. Santori et al. "Nanophotonics for Quantum Optics Using Nitrogen-Vacancy Centers in Diamond". *Nanotechnology* 21.27 (July 9, 2010), p. 274008.

[192] A. Högele et al. "Photon Antibunching in the Photoluminescence Spectra of a Single Carbon Nanotube". *Phys. Rev. Lett.* 100.21 (May 27, 2008), p. 217401.

[193] T. T. Tran et al. "Quantum Emission from Defects in Single-Crystalline Hexagonal Boron Nitride". *Phys. Rev. Applied* 5.3 (Mar. 10, 2016), p. 034005.

[194] I. Aharonovich, D. Englund, and M. Toth. "Solid-State Single-Photon Emitters". *Nature Photon* 10.10 (Oct. 2016), pp. 631–641.

[195] A. E. K. Kaplan et al. "Hong–Ou–Mandel Interference in Colloidal CsPbBr3 Perovskite Nanocrystals". *Nat. Photon.* 17.9 (Sept. 2023), pp. 775–780.

[196] C. Zhang et al. "Metal Halide Perovskite Nanorods: Shape Matters". *Adv Mater* 32.46 (Nov. 2020), e2002736.

[197] F. Bertolotti et al. "Crystal Structure, Morphology, and Surface Termination of Cyan-Emissive, Six-Monolayers-Thick CsPbBr3 Nanoplatelets from X-ray Total Scattering". *ACS Nano* 13.12 (Dec. 24, 2019), pp. 14294–14307.

[198] H. Zhu et al. "Synthesis of Zwitterionic CsPbBr3 Nanocrystals with Controlled Anisotropy Using Surface-Selective Ligand Pairs". *Adv Mater* 35.39 (Sept. 2023), e2304069.

[199] M.-R. Amara. "Optical Spectroscopy of Single Perovskite Nanocrystals for Quantum Photonics". 2022.

[200] M. I. Dar et al. "Origin of Unusual Bandgap Shift and Dual Emission in Organic-Inorganic Lead Halide Perovskites". *Sci. Adv.* 2.10 (Oct. 7, 2016), e1601156.

[201] A. D. Wright et al. "Electron–Phonon Coupling in Hybrid Lead Halide Perovskites". *Nat Commun* 7.1 (May 26, 2016), p. 11755.